Effects of Pore-Scale Heterogeneity on Continuum-Scale Multiphase Flow Properties for Subsurface Carbon Dioxide Storage Applications

Nihal Mohamed Mounir Taha Darraj

Imperial College London
Department of Earth Science and Engineering
Faculty of Engineering

Submitted in part fulfilment of the requirements for the degree of Doctor of Philosophy

Supervised by Professor Samuel Krevor, Professor Martin J. Blunt and Professor Ronny Pini

March, 2026

بِسْمِ ٱللَّهِ ٱلرَّحْمَٰنِ ٱلرَّحِيْمِ

رَبِّ أَوْزِعْنِي أَنْ أَشْكُرَ نِعْمَتَكَ الَّتِي أَنْعَمْتَ عَلَيَّ وَعَلَىٰ وَالِدَيَّ وَأَنْ أَعْمَلَ صَالِحًا تَرْضَاه
وَأَدْخِلْنِي بِرَحْمَتِكَ فِي عِبَادِكَ الصَّالِحِينَ

[النمل: 19]

In the name of Allah, the most gracious, the most merciful

“My Lord! Inspire me to ˹always˺ be thankful for Your favours which You have blessed me and my parents with, and to do good deeds that please you. Admit me, by Your mercy, into ˹the company of˺ Your righteous servants.”

Surat An-Naml (19)

Declarations

Declaration of originality

I declare that this thesis, submitted for the degree of Doctor of Philosophy at Imperial College London and Associateship of the Royal School of Mines, is original research that has been completed by me, and carried out under the supervision of Professor Samuel Krevor, Professor Martin Blunt and Professor Ronny Pini. All published and unpublished material used in this thesis has been appropriately referenced. None of this work has previously been submitted to Imperial College London or any other academic institution for a degree or diploma, or for any other qualification.

Nihal Mounir Darraj

28th January 2026

Copyright declaration

The copyright of this thesis rests with the author. Unless otherwise indicated, its contents are licensed under a Creative Commons Attribution-NonCommercial 4.0 International Licence (CC BY-NC).

Under this licence, you may copy and redistribute the material in any medium or format. You may also create and distribute modified versions of the work. This is on the condition that: you credit the author and do not use it, or any derivative works, for a commercial purpose.

When reusing or sharing this work, ensure you make the licence terms clear to others by naming the licence and linking to the licence text. Where a work has been adapted, you should indicate that the work has been changed and describe those changes.

Please seek permission from the copyright holder for uses of this work that are not included in this licence or permitted under UK Copyright Law.

Nihal Mounir Darraj, 2026

Abstract

Geological CO_2 storage relies on multiple trapping mechanisms to ensure long-term subsurface containment. In depleted gas fields, structural trapping is the main mechanism and usually is sufficient, but in saline aquifers and settings where lateral migration poses risks, hence, additional trapping mechanisms are needed to slow and ultimately halt CO_2 migration. Among these, residual trapping is particularly important. It immobilises CO_2 after injection through pore-scale snap-off and capillary trapping behind regions of high capillary entry pressure. Although pore-scale residual trapping is well established in reservoir models, the influence of spatial heterogeneity in pore structure and capillary properties across larger length scales remains poorly constrained.

This thesis investigates how heterogeneity from pore to core scales controls multiphase flow and trapping under conditions relevant to geological CO_2 storage. A multiscale experimental approach combines steady-state coreflooding, X-ray computed tomography imaging, and pore-network analysis to directly observe displacement and trapping in heterogeneous sandstone and carbonate rocks under capillary-dominated flow regimes representative of saline aquifers and depleted hydrocarbon fields.

The first part examines sandstone samples from a Dutch offshore CO_2 storage site. Two samples taken only about 2 cm apart, from the same facies and with similar bulk porosity and permeability, display contrasting saturation profiles, displacement patterns, and residual trapping. Imaging shows that subtle differences in cementation and porosity distribution create capillary barriers and preferential flow paths in one sample, while the other behaves more uniformly.

The second and third parts show that, in Indiana limestone and Edwards Brown dolomite, heterogeneity interacts strongly with flow rate, connectivity, and capillary entry pressure,

controlling saturation distribution, relative permeability, and trapping. Overall, the thesis demonstrates that routine core analysis alone cannot capture flow behaviour in heterogeneous rocks, and that capillary heterogeneity must be considered in more physically representative upscaling approaches for CO_2 storage.

Acknowledgements

I am deeply grateful to my family for their love and support throughout this journey. Most of all, I want to thank my daughter for her patience during the many late nights at the lab, the missed playtimes, and the moments when this PhD had to come first. Her understanding, love, and presence kept me going, and this work carries a part of those shared sacrifices.

I am sincerely thankful to my supervisors, Sam and Martin, for their time, support, and guidance throughout this PhD. I am especially grateful for the trust they placed in me, for giving me the freedom to shape my own research path, and for encouraging me to pursue opportunities beyond the core project, including conferences, collaborations, and wider professional engagement, all of which were central to my development during this journey. I am equally deeply grateful to Steffen Berg for his exceptional guidance and generosity with his time, for always coming back to me promptly, for engaging with my work, and for taking the time to explain and teach, even when he was very busy. My thanks go as well to Jeroen Snippe and Panteha Bolourinejad for their support, input, and collaboration throughout the project.

A heartfelt thank you goes to my unofficial supervisors, Sojwal Manoorkar and Catherine Spurin. They taught me so much of what I know, and their support went far beyond mentorship. Through their generosity, encouragement, and constant willingness to help, they became not only trusted guides but friends, and, in many ways, family.

I am likewise grateful to my dear friends for being by my side throughout this journey. We shared so many moments together, moments of support, laughter, and growth, that I will cherish forever. I am deeply grateful to Mahmoud ElYamani, Sajjad Foroughi, Idris Bukar, Mohamed Saleh, Catrin Harris, Alex Smith, Flowra Zhang, and Nele Wenck for their friendship and for making this journey so meaningful.

I would like to thank Vincenzo Cunsolo for his help in the lab, which was truly invaluable. I am equally thankful to my lab colleagues, Hussain AlZahrani and Waleed Dokhn, whom I constantly

flooded with questions and who always took the time to answer and help. Their patience and support made a real difference throughout this work.

Last but definitely not least, I would like to thank Gareth Oliver, Tony Rocha, and Francios van Schalkwyk for their incredible support when ICT failed. From fixing my computer to spending countless hours making sure everything worked when it mattered most, their help made it possible for me to finish this work.

Dedication

This thesis is dedicated to my father. Although he is not here today, this work exists because of him.

Dad, this is for you. I love you, and I hope I made you proud.

It is also dedicated to my mother, for fighting for me and with me on multiple fronts, for giving everything she could.

Mom, I hope this honours everything you gave and everything you endured for me.

Funding Acknowledgements

We gratefully acknowledge the UKRI Engineering and Physical Sciences Research Council and Shell for providing funding for this project [Project reference: EP/R513052/1].

Publications

Darraj, N., Manoorkar, S., Spurin, C., Foroughi, S., Saleh, M., Berg, S., Blunt, M.J. and Krevor, S. 2025 (b). Heterogeneity driven trapping at the pore-network scale in Edwards Brown Dolomite. Energy & Fuels, 40(1), pp. 528–542. https://doi.org/10.1021/acs.energyfuels.5c04544

Darraj, N., Manoorkar, S., Spurin, C., Foroughi, S., Berg, S., Blunt, M. J., and Krevor, S., (2026). Impact of Pore-Scale Heterogeneity on Continuum-Scale Multiphase Flow Properties: Insights from Indiana Limestone. Impact of pore-scale heterogeneity on continuum-scale multiphase flow properties: Insights from Indiana limestone, International Journal of Greenhouse Gas Control, Volume 151, 2026, https://doi.org/10.1016/j.ijggc.2026.104623.

Darraj, N., Nikolaev, P., Spurin, C., Manoorkar, S., Berg, S., Snippe, J., Bolourinejad, P., Blunt, M. and Krevor, S., Heterogeneity-Driven Multiphase Flow Behaviour in a Dutch Offshore CO_2 Storage Site. *(submitted).*

Spurin, C., Callas, C., **Darraj, N**., Rücker, M. and Benson, S. (2025). Importance and challenges of multi-scale heterogeneity. InterPore Journal, 2(1), IPJ260225. DOI: https://doi.org/10.69631/ipj.v2i1nr76

Ni, H., Li, B., **Darraj, N.**, Ren, B., Harris, C., Krishnamurthy, P.G., Bukar, I., Berg, S., Snippe, J., Ringrose, P., Meckel, T.A., Krevor, S., Benson, S., 2025. The impact of capillary heterogeneity on CO_2 flow and trapping across scales. Earth-Sci. Rev. 270, 105257. https://doi.org/10.1016/J.EARSCIREV.2025.105257

Aboulrous, A.A., **Darraj, N.M**., Cunsolo, V., Uko, D., Trusler, J.P.M. and Blunt, M.J. (2025) Effect of imidazolium-based ionic liquid on CO_2 sequestration: A study on solubility, interfacial properties, and X-ray imaging in water-wet formations. Journal of Molecular Liquids, 435, 128111. https://doi.org/10.1016/j.molliq.2025.128111

Hosseini, S., Chen, J., Cavanagh, A., Chen, B., **Darraj, N.,** Doster, F., Ennis-King, J., Flemisch, B., Gunning, J., Moodie, N., Tavagh M., Tenthorey, E.,. An International Perspective on Modelling and Simulation for Geological CO_2 Storage Assessment. http://dx.doi.org/10.2139/ssrn.5943295 (*Under review in the international journal of Green House Gas Control)*

Nikolaev, P.V., **Darraj, N.,** Bolourinejad, P., Berg, S., Snippe, J. and Krevor, S,. Impact of capillary pressure heterogeneity on CO_2–brine flow through porous media at centimetre scale. *(In Preparation).*

Krevor, S., Orr., F. M., Blunt, M. J., Muggeridge, A., **Darraj, N.** Gao, X., Kivi, I. (2025) Gigatonnes of CO_2 storage with enhanced oil recovery: a phantom of climate peril. *In Preparation.*

Conference Proceedings:

Darraj, N,. Spurin, C., Manoorkar, S., Berg, S., Blunt, M. J.,Pini, R., Cunsolo, V., Krevor, S. C., Pore-Scale Dynamics in Carbonate Reservoirs: The Influence of Heterogeneity on CO_2 Storage in Indiana Limestone (October 1, 2024). Proceedings of the 17th Greenhouse Gas Control Technologies Conference (GHGT-17) 20-24 October 2024, http://dx.doi.org/10.2139/ssrn.5069647

Darraj, N., Spurin, C., Manoorkar, S., Berg, S., Snippe, J., Bolourinejad, P., Cunsolo, V., Pini, R., Blunt, M. and Krevor, S. 2025 (a). Characterising Rock Heterogeneity from an Offshore Dutch CO_2 Storage Site. In: World CCUS Conference 2025, September 2025. European Association of Geoscientists & Engineers, pp. 1–5. https://doi.org/10.3997/2214-4609.202522098

Darraj, N., Manoorkar, S., Spurin, C., Foroughi, S., Saleh, M., Cunsolo, V., Berg, S., Pini, R., Blunt, M.J. and Krevor, S. (2025) Pore-scale investigation of heterogeneity effects on

saturation and trapping for geological CO_2 storage in dolomites. Paper presented at the SPE Europe Energy Conference and Exhibition, Vienna, Austria, June. https://doi.org/10.2118/225555-MS

Conference Presentations

- InterPore 2023: Poster presentation (Edinburgh, UK)
- SPE/AAPG/SEG CCUS Conference 2024: Oral presentation (Houston, USA)
- SPE International Executive Symposium: Innovation for Low Carbon Energy Solution 2024: Oral presentation (Abu Dhabi, UAE)
- GHGT-17 2024: Poster presentation (Calgary, Canada)
- AGU 2024: Oral presentation (Washington DC, USA)
- SPE/AAPG/SEG CCUS Conference 2025: Oral presentation (Houston, US) – **Awarded best student presentation.**
- SPE EUROPEC 2025: Oral presentation (Vienna, Austria)
- World CCUS 2025: Poster presentation (Bergen, Norway)
- SLB EUREKA Energy Transition Technologies Special Interest Group (ETT SIG) 2025: (Online)

Table of Contents

DECLARATIONS ..... **II**

ABSTRACT ..... **V**

ACKNOWLEDGEMENTS ..... **VII**

DEDICATION ..... **IX**

FUNDING ACKNOWLEDGEMENTS ..... **X**

PUBLICATIONS ..... **XI**

CONFERENCE PRESENTATIONS ..... **XIII**

CONTENTS ..... **XIV**

LIST OF FIGURES ..... **XIX**

APPENDIX A LIST OF FIGURES ..... **XXIII**

APPENDIX B LIST OF FIGURES ..... **XXIV**

APPENDIX C LIST OF FIGURES ..... **XXV**

LIST OF TABLES ..... **XXVI**

APPENDIX A LIST OF TABLES ..... **XXVI**

CHAPTER ONE: SCIENTIFIC BACKGROUND AND MOTIVATION **1**

1.1 Motivation - Geological CO_2 Storage 1

1.1.1 Subsurface CO_2 Storage 1

1.1.2 Reservoir Simulation CO_2 Storage 1

1.1.3 Representing Heterogeneity in Grid Blocks 2

1.1.4 Sub-grid Block Heterogeneity 2

1.1.5 Effective Relative Permeability and Capillary Pressure Saturation Functions 4

1.1.6 Practical Workflow for Representing Continuum-Scale Properties in the Presence of Small-Scale Heterogeneity 5

1.2 Thesis outline 9

CHAPTER TWO: LITERATURE REVIEW…….. 13

2.1 Geological CO_2 Storage Contexts: Depleted Hydrocarbon Reservoirs and Saline Aquifers 13

2.2 Fluid Flow from pore-scale to continuum scale 18

2.2.1 Darcy's Law 18

2.2.2 Relative Permeability 20

2.2.3 Capillary Pressure 22

2.3 Trapping Mechanisms in Geological CO_2 Storage 25

2.4 Impact of Pore-Scale (Small-Scale) Heterogeneity 28

2.4.1 The Effect of Heterogeneity on Saturation 28

2.4.2 The Effect of Heterogeneity on Relative Permeability 30

2.4.3 The Effect of Heterogeneity on Capillary Pressure 32

2.4.4 The Effect of Heterogeneity on Trapping 33

2.5 Upscaling Continuum Scale Properties in Heterogenous Rock Samples 36

2.6 Pore-to-Core-to-Field Scale Transitions and Upscaling 38

2.7 Why Structural Heterogeneity Characterisation Alone is Insufficient 39

CHAPTER THREE: EXPERIMENTAL METHODOLOGY AND IMAGE PROCESSING ……...41

3.1 Medical X-ray CT Imaging 41

3.2 Medical-CT Image Processing 45

3.3 Micro-CT Imaging 46

3.4 Micro-CT Image Processing 48

3.5 Pore Network Extraction and Capillary Entry Pressure Mapping 48

3.6 Rationale for Imaging Strategy and Resolution Selection 51

3.7 Methodological Limitations and Uncertainty 53

CHAPTER FOUR: HETEROGENEITY CONTROLS ON MULTIPHASE FLOW PROPERTIES IN A DUTCH OFFSHORE CO_2 STORAGE SITE 56

4.1 Introduction 57

4.2 Materials and Methods 58

4.2.1 Rocks 58

4.2.2 Fluids, Interfacial Tension and Viscosity 61

4.2.3 Pore Network Modelling 63

4.3 Results and Discussion 64

4.3.1 Saturation along the samples after drainage and imbibition 64

4.3.2 Pore network modelling and local heterogeneity 70

4.3.3 Trapping efficiency 74

4.3.4 Relative permeability 76

4.4 Conclusions 78

CHAPTER FIVE: MILLIMETRE-SCALE HETEROGENEITY IN CARBONATES: INDIANA LIMESTONE 80

5.1 Introduction 80

5.2 Methods and Materials 81

5.2.1 Rock and Fluids 82

5.2.2 Experimental Methodology 84

5.2.3 Image Segmentation 87

5.2.4 Characterisation of Heterogeneity 89

5.3 Results and Discussion 89

5.3.1 Saturation Profile 89

5.3.2 Relative Permeability and Trapping 93

5.3.3 Pore Network and Pore Occupancy 95

5.4 Conclusions 100

CHAPTER SIX CENTIMETRE-SCALE TO DECIMETRE-SCALE HETEROGENEITY IN CARBONATES: EDWARDS BROWN DOLOMITE 103

6.1 Introduction 103

6.2 Materials and Methods 105

6.2.1 Rock Sample and Fluids 105

6.2.2 Experimental Methodology 108

6.2.3 Image Processing and Analysis 111

6.3 Results and Discussion 114

6.3.1 Fluid Saturation Profiles and Phase Distribution 114

6.3.2 Relative Permeability 118

6.3.3 Trapping Behaviour 120

6.3.4 Pore Network Occupancy and Connectivity 123

6.3.5 Entry Capillary Pressure 128

6.4 Implications for larger scale flow 131

6.5 Conclusions 133

CHAPTER SEVEN: CONCLUSIONS AND FUTURE WORK 136

7.1 Thesis Summary 136

7.2 Thesis Contributions 140

7.3 Recommendations for Future Research 143

7.3.1 Representativity and sampling across centimetre-scale reservoir variability 143

7.3.2 Protocol limitations 144

7.3.3 Improved segmentation, uncertainty quantification, and reproducibility 144

7.3.4 Dissolution in equilibrated fluids and its interaction with residual trapping 145

7.3.5 Pressure fluctuations and pore-scale invasion events 146

7.3.6 Coupling pore-scale structure to continuum descriptions 146

BIBLIOGRAPHY 148

APPENDIX A 163

A.1. Low Permeability Sample (Sample 3) 163

A.2. Viscous limit relative permeability 166

A.3. Tabulated relative permeability values 170

A.4. Pressure data 171

A.5. 3D saturation profiles during imbibition 172

APPENDIX B: SUPPORTING CHAPTER 5 176

B.1. Saturation Profile 176

B.2. Trapping 177

B.3. Ganglia Analysis 179

B.4. Investigation of wettability 180

APPENDIX C: SUPPORTING CHAPTER 6 182

C.1. Wavelet Analysis 183

List of Figures

Figure 1.1 The different length scales of depositional geological heterogeneities. Adapted from Fitch et al. (2015). 3

Figure 1.2: Typical X-ray CT core flooding sample sizes illustrated using Bentheimer sandstone cores. The sample size used in this thesis is highlighted in the middle. (Reproduced from Jackson et al,. 2020). 7

Figure 1.3: conceptual overview of how pore-scale to core-scale and small-scale heterogeneity is translated into continuum-scale inputs for reservoir simulation. A cartoon of a storage complex is shown at the top, with the numerical reservoir grid superimposed. One coarse grid block is enlarged to illustrate sub-grid heterogeneity and the resulting non-uniform fluid distribution. A further conceptual refinement indicates how this same block would appear if resolved with a much finer grid, highlighting fluid configurations that cannot be explicitly represented at reservoir scale due to computational constraints. The workflow then illustrates how intrinsic relative permeability functions, in combination with heterogeneity, are upscaled to obtain effective relative permeability and capillary pressure descriptions at the grid-block scale. The green dashed frame marks the part of the overall workflow that is addressed in this thesis, namely the experimental and image-based characterisation of small-scale heterogeneity and its impact on effective parameters. 8

Figure 1.4 Conceptual organisation of the experimental programme in Chapters 4 to 6, showing a systematic progression in both geological complexity and heterogeneity length scale. 10

Figure 2.1 Options for storing CO_2 in deep underground geological formations (Source: IPCC, 2005). 14

Figure 2.2 Schematic representation of A) saline aquifer and B) depleted gas field used for CO_2 storage (Source: Worden, 2024). 16

Figure 2.3 Time at which mobile gaseous CO_2 reaches selected modelling fractions (85%; 50%; 15%), 22 depleted gas fields models and 19 saline aquifer models were simulated, however, not every model reaches a selected percentage within the 10,000 year timeframe, (e.g. only 3 out of 22 depleted structurally closed models reach 15%) (Source: Snippe and Tucker, 2014). 17

Figure 2.4 The impact of layers orientated a) parallel to the principal axis of flow on the relative permeabilities, b) perpendicular to the principal axis of flow on the relative permeabilities. (Modified from: Boon and Benson, 2021). 21

Figure 2.5 Schematic diagram of trapping mechanisms in field-scale CO_2 storage. 25

Figure 2.6 Comparing modeling results of CO_2 saturation front advancement in a core with (right) and without (middle) capillary pressure heterogeneity. The modeling results with heterogeneity added to capillary pressure (right) matches the experimental results (left) better. Figure taken from Berg et al. (2013). 29
Figure 2.7 An example of anisotropic and flow-rate dependent effective (i.e., upscaled) relative permeability curve in the presence of small-scale capillary heterogeneity during drainage. Note that both the shape and the end point (i.e., critical CO_2 saturation) have changed as flow rate varies. r1 and r2 are correlation lengths of the media in different directions. Figure taken from Li and Benson (2015). 31
Figure 2.8 An illustration showing the effect of heterogeneous capillary pressure curves on CO_2 saturation under viscous-dominated (green) vs. capillary-dominated (purple) flow regimes with transition (blue). (modified from Reynolds and Krevor (2015)). 33
Figure 2.9 CO_2/water core flooding experimental results demonstrating a significant amount of CHT. (a) Porosity map and CO_2 saturation map (after 100% CO_2 drainage and 100% water imbibition) of the center slice of the core. (b) Initial-residual (IR) plot comparing the difference in capillary trapping with and without the cross-laminated capillary barrier at the end of the core. Figure taken from Krevor et al. (2011). 35
Figure 3.1 The experimental apparatus for the flow experiments with imaging using medical X-ray CT. 42
Figure 3.2 1D slice average saturation along Bentheimer sandstone sample for all fractional flows. 44
Figure 3.3 Micro-CT experimental apparatus. 47
Figure 3.4 2D slice of 3D image of Silurian dolomite rock samples. 54
Figure 4.1 Porosity profiles along the length of the two sandstone samples used in this study, derived from medical X-ray CT imaging. (a) One-dimensional porosity profiles along the core length, obtained by averaging porosity over cross-sectional slices and plotted as a function of distance from the inlet. (b) Three-dimensional renderings illustrate the spatial distribution of porosity of Sample 1. (c) Three-dimensional renderings illustrate the spatial distribution of porosity of Sample 2. 61
Figure 4.2 1D slice average saturation along Sample 1 after drainage (a) and imbibition (b) for all fractional flows. 66
Figure 4.3 1D slice average saturation along Sample 2 after drainage (a), and imbibition (b) for all fractional flows. 68
Figure 4.4 3D saturation profile of Sample 1 for all drainage fractional flow steps. 69
Figure 4.5 3D saturation profile of Sample 2 for all drainage fractional flow steps. 70

Figure 4.6 3D rendering of the micro-CT porosity for a) Sample 1,and b) Sample 2. 71
Figure 4.7 Capillary pressure as a function of saturation in (a) Sample 1 and (b) Sample 2, derived from pore network modelling. In each panel, region 1 corresponds to the upstream half of the core and region 2 to the downstream half. 73
Figure 4.8 Slice average initial saturation versus residual saturation along the samples' length (red) in comparison with homogenous Bentheimer sandstone (black). a) Sample 1. b) Sample 2. 76
Figure 4.9 Relative permeabilities showing drainage and imbibition cycles for wetting and non-wetting phases a) Sample 1, b) Sample 2. 78
Figure 5.1 (a) Two-dimensional cross- section (xy direction) of three-dimensional micro-CT image: grey is grain, black is pores. (b) MICP-derived capillary pressure indicating multiple entry pressures throughout the sample. 83
Figure 5.2 (a and b) Cross-sections of the medical CT (left) and micro-CT (right) scans. (c and d) The one-dimensional porosity profiles averaged along the flow direction for each imaging method. 86
Figure 5.3 Two-dimensional cross-sections (xy direction) of three-dimensional micro-CT images of the middle slice at 0 brine fractional flow (gas injection). (a) Raw image where grey is grain, black is gas, and white is brine, (b) masked image, where black is the masked grain, dark grey is gas, and white is brine, and (c) segmented image, where green is gas and purple is brine. 88
Figure 5.4 One-dimensional slice averaged gas saturation profile in the flow direction at the end of drainage (brine fractional flow of 0). Lines represent the average saturation value across the sample for both flow rates. 91
Figure 5.5 (a) Two-dimensional voxel porosity and saturation maps for end of drainage (f_w =0) at (q= 0.1ml/min and q= 0.2 ml/min). (b) 3-D segmented gas phase at end of drainage (f_w =0) at (q= 0.1ml/min and q= 0.2 ml/min) 92
Figure 5.6 Relative permeability measured during drainage; black is 0.2 ml/min and grey 0.1 ml/min. 94
Figure 5.7 Amount of residual trapping as a function of the initial saturation, black is 0.2 ml/min and grey is 0.1 ml/min. 95
Figure 5.8 (a) Throat size distribution (radius) of six sub-volumes across the sample. (b) Three-dimensional segmented gas phase at end of drainage (f_w =0, q= 1ml/min). The boxes show the location of the sub-volumes taken. 97

Figure 5.9 Pore occupancy for the six sub-volumes analysed. Panels (1-3) corresponds to regions with low capillary entry pressures, while panels (4-6) represent regions with high capillary pressures. 98
Figure 5.10 Estimated capillary entry pressures for the six sub-volumes, calculated using average pore throat diameters obtained from pore network modelling and the Young–Laplace equation..... 99
Figure 6.1 The top panel is a one-dimensional porosity profile along the sample's length (averaged over cross-sectional slices) indicating the low porosity region with the shading. The bottom image shows the middle slice of a representative two-dimensional cross-section of a 3D micro-CT image through a region of interest (grey is the rock matrix, black is the pore space, and white is mineral). 106
Figure 6.2 Mercury intrusion capillary pressure data that has been converted to show the distribution of pore-throat radius, normalized such that the maximum value is 1. Throats of radius below the voxel size of the image (5.6 µm) cannot be resolved. 109
Figure 6.3 Two-dimensional cross-sections of a 3D micro-CT images at the end of drainage (f_w =0): (a) dry scan, rock in grey and pores in black; (b) filtered flow scan, showing rock in grey, decane in black, and brine in white; (c) segmented image, with rock represented in black, decane in blue, and brine in green. 113
Figure 6.4 a) 1D saturation profiles across the length of the sample during drainage (the legend indicates the imposed brine fractional flow). b) 1D saturation profiles across the length of the sample during imbibition (the legend indicates the imposed brine fractional flow). 115
Figure 6.5 Representative 2D cross-sections segmented images extracted from 3D micro-CT images at the end of drainage (f_w =0) and imbibition (f_w =1), captured from two distinct regions of the sample. Panels (a) and (b) correspond to a higher-porosity zone, while panels (c) and (d) are taken from a lower-porosity region, illustrating spatial variability in fluid distribution as a function of local porosity (black is grain, green is brine, and blue is decane). 117
Figure 6.6 A voxel-by-voxel visualisation of the sample along its central axis of the centre-slice micro-CT images captured at key experimental stages: (a) dry scan, illustrating pore space distribution (porosity); (b) drainage, showing non-wetting phase (oil) saturation at a water fractional flow (fw= 0); and (c) imbibition, displaying oil saturation at water fractional flow (fw= 1). Panel (d) presents the corresponding one-dimensional saturation profiles along the sample length at the end of drainage and imbibition, highlighting changes in fluid distribution in the direction of flow. 118

Figure 6.7 Relative permeabilities showing drainage and imbibition cycles for wetting and non-wetting phases. 119
Figure 6.8 Slice average initial saturation versus residual saturation along the sample (grey is at the partial capillary barrier and black is the rest of the sample). 121
Figure 6.9 Analysis of non-wetting phase ganglia across the core after drainage and imbibition. (a) Three-dimensional renderings of the segmented non-wetting phase, superimposed on greyscale micro-CT images of the rock matrix. The image on the left shows the distribution at the end of drainage, where a single large, continuous ganglion (green) spans most of the sample length, with smaller disconnected clusters appearing near the barrier. The image on the right shows the distribution after imbibition, where the non-wetting phase has fragmented into multiple smaller ganglia. Each disconnected ganglion is assigned a unique colour for clarity. The grey-scale image shows the dry image, included to give spatial reference of the barrier region. (b) Histograms showing the number of ganglia (left) and their volume (right) along the core length at the end of drainage. (c) Histograms showing the number of ganglia (left) and their volume (right) along the core length at the end of Imbibition. Figure b highlights an increase in the number of disconnected clusters away from the barrier region and retention of ganglia count around the barrier region after brine re-invasion. While figure c illustrates the breakdown of the large ganglia at the end of drainage to smaller ones after imbibition. 123
Figure 6.10 a) Spatial distribution of selected sub-volumes across the sample, used for detailed analysis. 1 and 2 denotes the barrier zone characterised by reduced porosity and distinct flow behaviour; 3 and 4 corresponds to a higher porosity zone located away from the heterogeneity barrier. b) throat-size distribution of sub-volumes 1, 2, 3 and 4. 124
Figure 6.11 Pore and throat occupancy analysis comparing barrier and non-barrier regions. Panels 1, 2, 3, and 4 correspond to sub-volumes 1, 2, 3, and 4, respectively shown in Figure 6.10. 126
Figure 6.12 a) Distribution of coordination number and b) aspect ratio. These distributions are evaluated for the four sub-volumes shown in Figure 6.10. 128
Figure 6.13 Entry capillary pressure in the barrier region and away from the barrier. The four sub-volumes shown in Figure 6.10 are analysed. 129

APPENDIX A List of Figures

Figure A. 1 1D and 3D porosity profile of Sample 3. 163

Figure A. 2 1D saturation profile for Sample 3. 164
Figure A. 3 3D gas saturation distributions obtained from medical X-ray CT imaging during multiphase flow for Sample 3. The rendering highlights complex heterogeneity expressed both parallel and perpendicular to the primary flow direction..... 165
Figure A. 4 Trapping efficiency showing a slight increase in trapping with cyclic injection for Sample 3. 166
Figure A. 5 1-D and 3-D porosity profiles for Sample 1 after the first set of experiments. 167
Figure A. 6 1-D saturation profile for Sample 1 (2nd experiment). 168
Figure A. 7 3D saturation profile at the end of drainage of Sample 1 (2nd experiment). 168
Figure A. 8 Drainage relative permeability of Sample 1 (2nd experiment). 169
Figure A. 9 Pressure-time series for Sample 1 (2nd experiment). 169
Figure A. 10 Pressure time series for Sample 1 during (a) drainage and (b) imbibition. 171
Figure A. 11 Pressure time series for Sample 2 during (a) drainage and (b) imbibition. 172
Figure A. 12 3D saturation profile for Sample 1 imbibition fractional flow steps. 172
Figure A. 13 3D saturation profile for Sample 2 imbibition fractional flow steps. 173
Figure A. 14 Two-dimensional saturation maps of the central horizontal slice in Sample 1 at the end of drainage and imbibition. 173
Figure A. 15 Two-dimensional saturation maps of the central vertical slice in Sample 1 at the end of drainage and imbibition. 174
Figure A. 16 Two-dimensional saturation maps of the central horizontal slice in Sample 2 at the end of drainage and imbibition. 174
Figure A. 17 Two-dimensional saturation maps of the central vertical slice in Sample 2 at the end of drainage and imbibition. 175

APPENDIX B List of figures

Figure B. 1 The two sub-volumes selected. 176
Figure B. 2 (a) High entry pressure region sub-volume. All pores image is the segmented brine phase when the rock was completely filled with brine. The 0.1 ml/min and 0.2 ml/min are the segmented gas phase at these two total flow rates, respectively. (b)Low entry pressure region sub-volume. All pores image is the segmented brine phase when the rock was completely filled with brine. The 0.1 ml/min and 0.2 ml/min are the segmented gas phase at these two total flow rates, respectively. 177

Figure B. 3 Low flow rate (Q=0.1 ml/min). (a) Segmented gas phase at the end of drainage and imbibition in the low entry pressure region. (b) Segmented gas phase at the end of drainage and imbibition in the high entry pressure region. (c) Residual versus initial saturation for low entry pressure (black) and high entry pressure (red) regions. 178
Figure B. 4 High flow rate (Q=0.2 ml/min). (a) Segmented gas phase at the end of drainage and imbibition in the low entry pressure region. (b) Segmented gas phase at the end of drainage and imbibition in the high entry pressure region. (c) Residual versus initial saturation for low entry pressure (black) and high entry pressure (red) regions. 178
Figure B. 5 (a) Ganglia distribution across the sample in the low and high flow rates at the end of drainage and imbibition respectively. (b) A comparison of the ganglia size and cumulative count (frequency) between the low and high flow rates for drainage and imbibition. Red is the high flow rate while black is the low flow rate. 179
Figure B. 6 Contact angle histogram in both low and high entry pressure regions. 181

APPENDIX C List of figures

Figure C. 1 Mercury invasion capillary pressure (MICP). It highlights multiple entry pressure values. 182
Figure C. 2 Two-dimensional cross-sections from a three-dimensional micro-CT image, zoomed in on the downstream heterogeneous region of the core. Panel (a) shows the fluid distribution at the end of drainage, while panel (b) captures the same region at the end of imbibition. Panel (c) displays the corresponding one-dimensional non-wetting saturation profile, illustrating the contrast in saturation before and after the heterogeneity. Notably, the non-wetting phase saturation remains unchanged within the heterogeneous zone, indicating limited displacement. 182
Figure C. 3 Segmentation workflow visualised for Edwards Brown dolomite. After imaging, the grey-scale image was segmented to separate pore space and grain phases. Finally, the fluid phases were segmented into wetting (dark blue) and non-wetting (light blue) phases and then calculated from the total pore-space to determine the saturation 183
Figure C. 4 Wavelet analysis of the pressure signal for a brine fractional flow of 100% (f_w =1). 184
Figure C. 5 Wavelet analysis of the measured pressure signal for a brine fractional flow of 75% (f_w =0.75).... 185
Figure C. 6 Wavelet analysis of the measured pressure signal for a brine fractional flow of 50% (f_w =0.5)..... 185
Figure C. 7 Wavelet analysis of the measured pressure signal for a brine fractional flow of 5% (f_w =0.05)..... 186

List of Tables

Table 2-1 Recent contributions in Trapping Mechanisms..... 26

Table 4-1 Photographs, 3D Medical CT porosity and 2D Micro CT dry image of the centre slice of all rock samples..... 59

Table 4-2 The properties of the non-wetting and the wetting phases used in this work (NIST Chemistry Webbook, 2018). 62

Table 4-3 Properties of the rock samples used in the study and associated experimental conditions. 63

Table 5-1 Summary of pore network model–derived porosity, absolute permeability, and average capillary entry pressure for each of the six analysed subvolumes highlighted in figure 5.8b. 100

Table 6-1 Average non-wetting phase saturation during the experiment. 116

Table 6-2 Summary of the pore network analysis for the four sub-volumes (barrier region and away from the barrier)..... 131

Table 7-1: Comparative summary of the samples, heterogeneity characteristics, and principal findings across Chapters 4 to 6…….138

Appendix A List of Tables

Table A- 1 Tabulated relative permeability data for drainage in Sample 1. 170

Table A- 2 Tabulated relative permeability data for imbibition in Sample 1. 170

Table A- 3 Tabulated relative permeability data for drainage in Sample 2. 170

Table A- 4 Tabulated relative permeability data for imbibition in Sample 2. 171

Chapter One Scientific Background and Motivation

1.1 Motivation - Geological CO_2 Storage

1.1.1 Subsurface CO_2 Storage

Limiting anthropogenic warming requires deep and sustained reductions in carbon dioxide (CO_2) emissions. Across mitigation pathways assessed by the Intergovernmental Panel on Climate Change (IPCC), carbon capture and storage (CCS) is a key option for reducing emissions from sectors where electrification and direct substitution are constrained, particularly where residual emissions persist and industrial process streams are hard to abate (IPCC, 2022; IPCC, 2005; Darraj and Bender, 2022).

Among geological storage options, saline aquifers are especially important due to their geographic distribution and large potential storage capacity, making them viable for large-scale deployment in many regions (Michael et al., 2010). Depleted hydrocarbon reservoirs are also attractive because they often come with what saline aquifers frequently lack: a long history of subsurface characterisation, a demonstrated trap and seal that has retained buoyant fluids over geological time, and in some cases re-usable infrastructure.

1.1.2 Reservoir Simulation CO_2 Storage

Field-scale prediction of plume migration, pressure evolution, and trapping efficiency in geological CO_2 storage projects is typically performed using continuum-scale reservoir simulators (Juanes et al., 2006; Boon, 2021). These numerical models solve multiphase flow equations to forecast storage efficiency, assess containment, and support risk assessment over injection and post-injection timescales spanning decades to millennia. Reliable simulation is

therefore essential for site selection, operational planning, regulatory approval, and long-term stewardship of CO_2 storage sites.

1.1.3 Representing Capillary Heterogeneity in Grid Blocks

Reservoir simulators operate on discretised computational grids, where each grid block represents a volume of porous rock characterised by effective properties: porosity, absolute permeability, and crucially, saturation-dependent constitutive functions—relative permeability and capillary pressure (including hysteresis). The choice of grid resolution is constrained by computational cost and by the availability of subsurface data. In practice, grid blocks at field scale typically range from metres to tens of metres in lateral extent, a scale far coarser than the centimetre-scale core plugs on which multiphase flow properties are measured (Li and Benson, 2015; Ni et al., 2025). Each grid block therefore requires upscaled or effective parameters that are assumed to represent the integrated behaviour of heterogeneous rock volumes within that block. Laboratory experiments and imaging studies provide an opportunity to directly observe these processes and to examine how pore-scale structure manifests at the core scale, which is essential for interpreting experimental measurements and informing the assignment of flow properties in reservoir-scale simulations (Yin et al., 2024; Elizarev et al., 2024; Gauteplass, 2015).

1.1.4 Sub-grid Block Capillary Heterogeneity

As seen in (Figure 1.1), storage formations commonly exhibit heterogeneity at multiple length scales: from pore-scale variations in throat size and connectivity (micrometres to millimetres), through bedding, lamination, and diagenetic textures (centimetres to decimetres), to facies architecture and stratigraphic layering (metres to kilometres) (Ni et al., 2025). Much of this variability occurs at scales smaller than the simulation grid resolution—referred to as sub-grid or small-scale heterogeneity. When variability in capillary entry pressure occurs at length

scales comparable to or smaller than the displacement front, it can promote preferential invasion, stratified advance, and non-uniform saturation profiles that are not captured by treating the grid block as homogeneous (Aslannezhad et al., 2024; Berg et al., 2013). Consequently, spatially organised capillary heterogeneity at the sub-grid scale can impose first-order control on effective relative permeability, capillary pressure behaviour, and residual trapping, even when bulk porosity and permeability appear uniform (Krevor et al., 2015; Jackson and Krevor, 2020; Li and Benson, 2015).

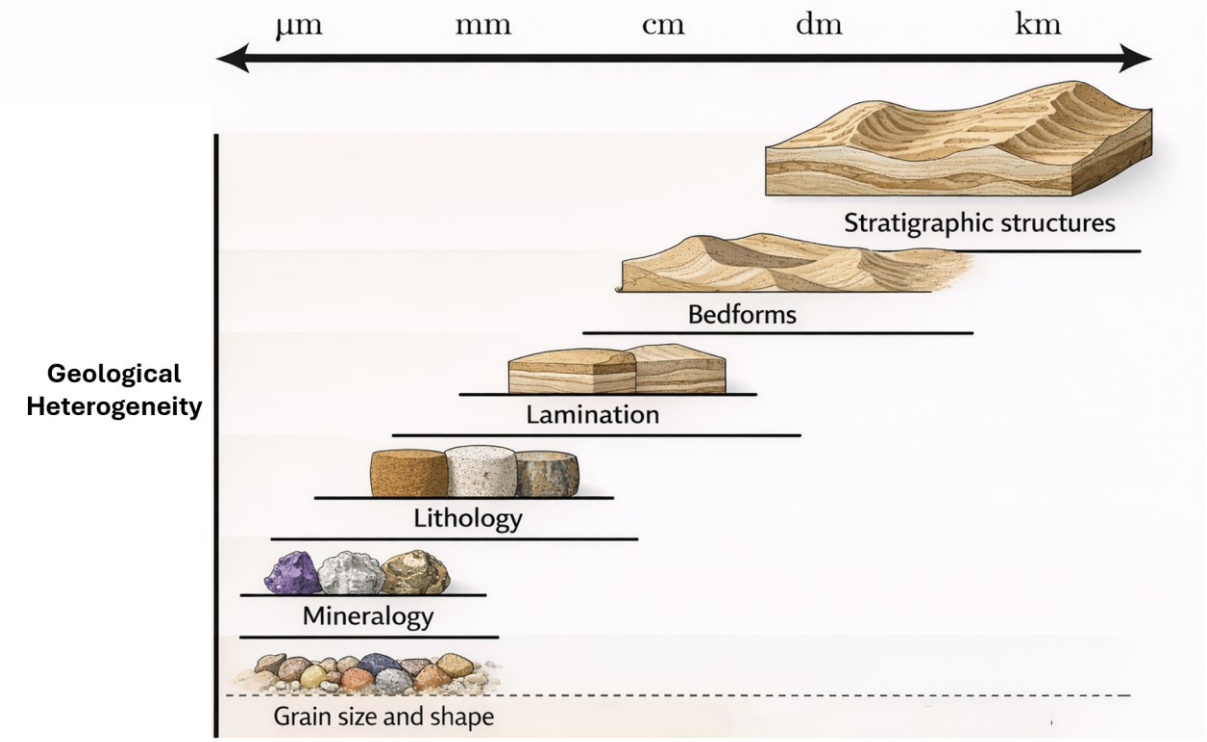


Figure 1.1 The different length scales of depositional geological heterogeneities. Adapted from Fitch et al. (2015).

As storage performance and long-term security are governed by multiphase flow and the immobilisation of CO_2 by trapping processes (Akbarabadi et al., 2013). During injection, buoyant CO_2 invades the pore space and displaces resident brine under drainage conditions, establishing saturation pathways shaped by viscous forces, buoyancy, and capillary pressure. After injection ceases, the system transitions toward redistribution and imbibition-dominated

behaviour, where hysteresis in capillary pressure and relative permeability controls remobilisation or immobilisation of the non-wetting phase (Aslannezhad et al., 2025). Over these stages, CO_2 may be retained by structural and stratigraphic trapping, residual (capillary) trapping, dissolution into brine, and longer-term mineralisation (Bachu et al., 2007).

Field-scale prediction of plume migration, pressure evolution, and trapping efficiency is typically performed using continuum simulators parameterised by constitutive functions, most notably relative permeability and capillary pressure (including hysteresis) (Juanes et al., 2006; Boon, 2021). These functions are commonly measured on core plugs and then upscaled or transferred to reservoir-scale models, where they are assumed to represent larger rock volumes. The reliability of this workflow rests on assumptions about representativity, scale separation, and how heterogeneity is treated within the numerical grid, whether through explicit facies architecture, effective properties, or homogenisation. While the impact of pore-scale processes on residual trapping is relatively well understood, the role of heterogeneity at larger, yet still sub-seismic (below 10s m), scales remains less well constrained (Harris et al., 2021; Elizarev et al., 2024). In many modelling workflows, such heterogeneity is simplified or averaged, despite growing evidence that it can exert strong control on saturation distribution and trapping behaviour. Improving confidence in geological CO_2 storage therefore requires a better understanding of how spatial variability in rock properties influences multiphase flow and trapping in ways that persist under upscaling.

1.1.5 Effective Relative Permeability and Capillary Pressure Saturation Functions

To represent the influence of sub-grid heterogeneity without explicitly resolving every pore, layer, or textural feature, the conventional approach is to assign effective (upscaled) saturation functions to each grid block (Pickup et al., 2000; Virnovsky et al., 2004). These functions are

intended to encapsulate the integrated multiphase flow response of a heterogeneous rock volume. In principle, effective relative permeability and capillary pressure curves account for pore-scale displacement mechanisms, connectivity, and trapping while remaining computationally tractable. However, the validity of this approach depends on whether the measured or assigned saturation functions are truly representative of the heterogeneous volumes they are meant to describe. Growing evidence suggests that when capillary heterogeneity is spatially organised, effective saturation functions can become anisotropic, flow-rate dependent, and non-unique—meaning that a single set of constitutive relationships may not adequately represent all flow conditions or orientations within a given rock type or interval (Boon and Benson, 2021; Li and Benson, 2015).

1.1.6 Practical Workflow for Representing Continuum-Scale Properties in the Presence of Small-Scale Heterogeneity

In practice, relative permeability and capillary pressure functions are most commonly measured on centimetre-scale core plugs extracted from reservoir intervals, using steady-state or unsteady-state coreflood experiments combined with imaging techniques such as X-ray computed tomography (CT) to monitor in-situ saturation distributions (Krevor et al., 2011; Perrin and Benson, 2010). These laboratory-scale measurements are then upscaled—either directly or through numerical modelling—to populate field-scale simulation grids (Jackson and Krevor, 2020; Ni et al., 2025). The reliability of this workflow rests on three key assumptions:

i. that core plugs are representative of the larger interval or facies from which they are drawn;
ii. that the measured saturation functions remain valid when transferred across scales; and
iii. that sub-core heterogeneity, if present, is either negligible or already "averaged out" in the effective properties measured at the core scale.

Laboratory experiments and imaging studies increasingly show that sub-core-scale heterogeneity can produce non-uniform saturation distributions, alter effective flow properties, and create trapping that persists even after apparent steady state is reached as shown in Chapters 4 to 6 and by (Berg et al., 2013; Manoorkar et al., 2021). This raises three critical questions:

1. How do different types, orientations, and magnitudes of small-scale heterogeneity translate into saturation changes, effective relative permeability, and trapping behaviour?
2. Under what combinations of heterogeneity, orientation relative to flow, and flow regime does capillary heterogeneity generate layered or channelised displacement, and how does this modify saturation distributions during drainage and imbibition?
3. To what extent can small-scale variability within a single reservoir interval, as evidenced by closely spaced samples, produce divergent saturation profiles and trapping curves, and what are the implications for assigning saturation functions in reservoir simulation?

In the experimental workflow presented in this thesis, we adopt an optimised sample size that balances two competing requirements: sufficiently small diameter and length to enable micron-resolution CT imaging across multiple representative volumes, thereby resolving fluid–fluid interfaces and phase connectivity, while remaining large enough to measure continuum-scale multiphase flow properties including relative permeability, capillary pressure, and residual trapping as seen in Figure 1.2.



Figure 1.2: Typical X-ray CT core flooding sample sizes illustrated using Bentheimer sandstone cores. The sample size used in this thesis is highlighted in the middle. (Reproduced from Jackson et al., 2020).

Figure 1.3, position the experimental workflow within the multiscale framework. The figure situates the experimental workflow developed in this thesis within the broader pore-scale to continuum-scale description of multiphase flow in geological formations. It highlights how laboratory-scale experiments and image-based analyses link pore-scale fluid configurations and heterogeneity to effective continuum-scale parameters used in reservoir simulation, clarifying the specific scope addressed by this thesis relative to the full modelling and upscaling chain.

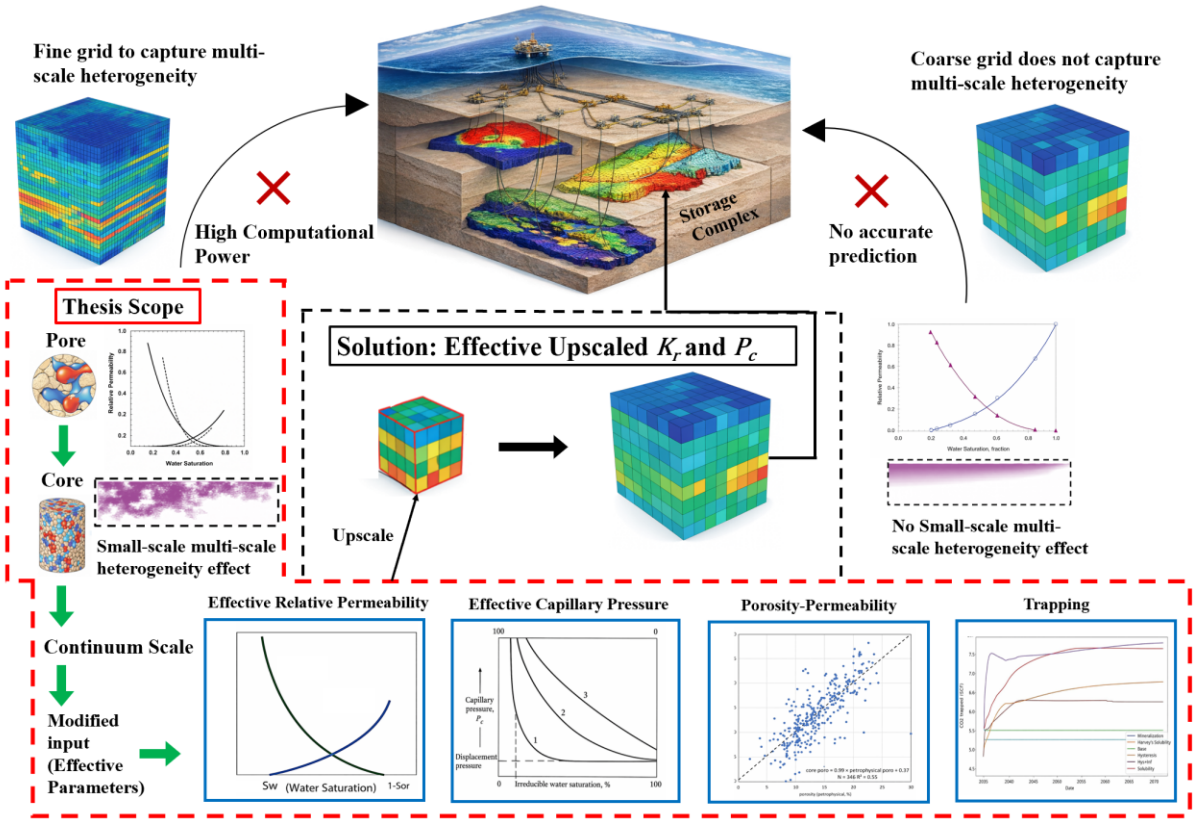


Figure 1.3: Conceptual overview of how pore-scale to core-scale and small-scale heterogeneity is translated into continuum-scale inputs for reservoir simulation. A cartoon of a storage complex is shown at the top, with numerical reservoir model superimposed. One coarse and one fine grid block is enlarged to illustrate the inclusion and exclusion effect of sub-grid heterogeneity and the resulting non-uniform fluid distribution. The red dashed frame marks the part of the overall workflow that is addressed in this thesis, namely the experimental characterisation of small-scale heterogeneity in pore-scale and its upscaling to continuum-scale and its impact on effective parameters. The workflow then illustrates the next steps where, effective parameters are upscaled to be included at the grid-block scale which is outside the scope of this thesis but covered in other sources (Elizarev et al., 2024).

1.2 Thesis outline

The aim of this thesis is to quantify how pore-scale heterogeneity controls continuum-scale multiphase flow properties relevant to geological CO_2 storage, with a particular focus on how capillary heterogeneity and connectivity translate into saturation distributions, relative permeability behaviour, and residual trapping. The central hypothesis is that spatially organised pore-scale and small-scale heterogeneity can impose first-order control on these properties.

To address this challenge systematically, the thesis adopts a scale-progression experimental strategy that moves from less complex sandstone to inherently more complex carbonate rocks. The move is made from centimetre-scale within-interval variability in reservoir sandstone, through millimetre-scale capillary heterogeneity in carbonate, to centimetre-to-decimetre heterogeneity in a more complex carbonate (Figure 1.4). Together, this progression bridges from field-relevant reservoir variability to systematically controlled outcrop analogues, enabling interpretation of how heterogeneity scale and organisation translate into continuum-scale flow properties across the pore-to-core transition.

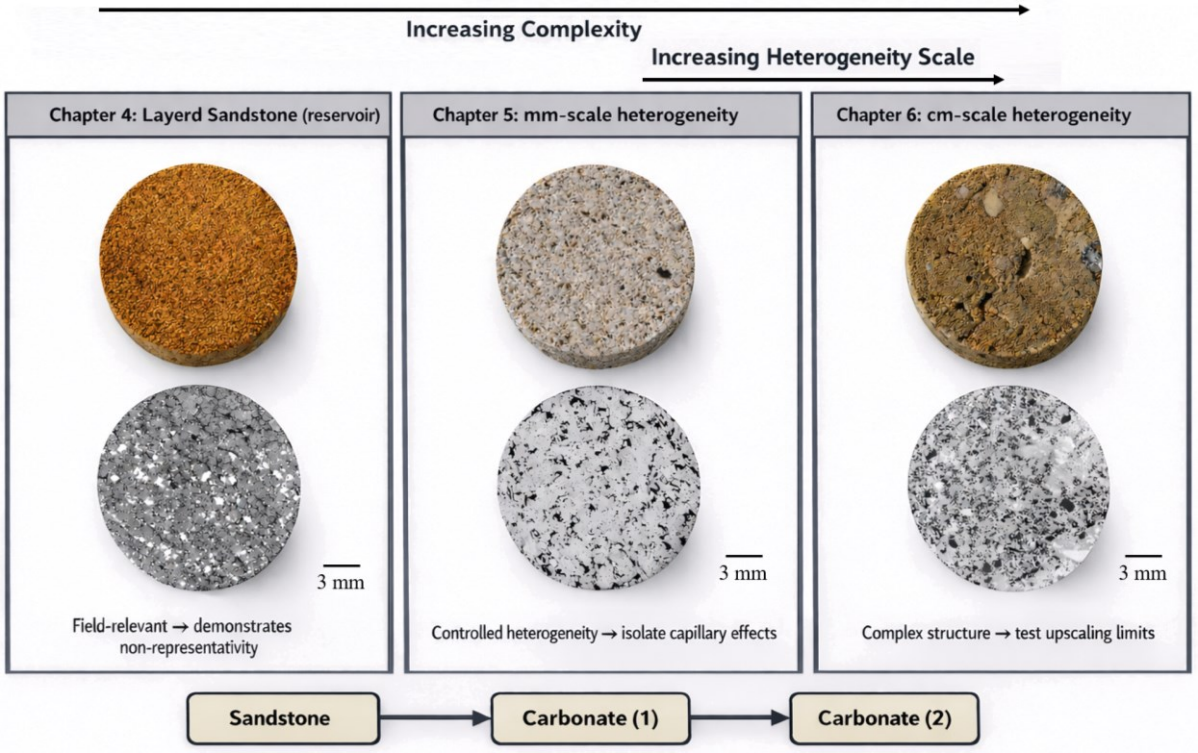


Figure 1.4 Conceptual organisation of the experimental programme in Chapters 4 to 6, showing a systematic progression in both geological complexity and heterogeneity length scale.

Chapter 2 reviews the background literature on multiphase flow and trapping in CO_2 storage, including constitutive relationships (relative permeability and capillary pressure), and the role of heterogeneity across length scales. The chapter identifies the specific gap addressed in this thesis, namely that continuum parameterisations commonly assume representativity within a rock type or interval, while spatially organised capillary heterogeneity can produce non-uniform saturation and trapping responses that challenge this assumption.

Chapter 3 presents the experimental and analysis workflow used throughout the thesis. It details the steady-state drainage and imbibition coreflood protocols, pressure and flow control, and the integrated imaging approach combining medical X-ray CT for core-scale saturation profiling with micro-CT for pore-scale structural characterisation. Image-processing, segmentation, and uncertainty considerations are documented to support defensible interpretation of saturation, connectivity, and trapping.

Chapter 4 investigates centimetre-scale variability within a reservoir sandstone by comparing two core plugs taken in close proximity within a single interval. Using the common methodology established in Chapter 3, the chapter demonstrates that modest differences in pore structure and capillary architecture can produce distinct saturation profiles and trapping relationship. This provides a demonstration of how within-interval heterogeneity can undermine the assumption that a single set of saturation functions is transferable across an interval.

Chapter 5 examines Indiana limestone to look at the influence of millimetre-scale heterogeneity and capillary controls on displacement and trapping. The chapter uses micro-CT imaging and sub-volume analysis to link local entry-pressure variability and connectivity to layered or preferential invasion behaviour at two flow rates, and then to the resulting shifts in effective relative permeability and residual trapping.

Chapter 6 extends the analysis to Edwards Brown dolomite, a highly heterogeneous carbonate. The chapter shows how low-connectivity regions and higher entry pressures act as partial barriers that restructure saturation pathways and enhance heterogeneity-driven trapping. This tests how the heterogeneity length scale and organisation influence the emergence of effective continuum-scale behaviour.

Chapter 7 synthesises findings across the sandstone and carbonate case studies, restating the central claim in terms of heterogeneity effects. It consolidates the novel contributions of the thesis and outlines future work needed to improve representativity and upscaling of multiphase flow functions, including targeted sampling strategies, and approaches to incorporate heterogeneity-informed parameter bounds into field-scale CO_2 storage simulations.

Additional technical detail, supporting analysis, and supplementary material is included in Appendices A, B, and C, which correspond to Chapters 4, 5, and 6 respectively. Appendix A

provides extended analysis and additional saturation maps for the sandstone samples. Appendix B includes an additional sub-volume analysis for flow-rate effects, and ganglia analysis in Indiana limestone. Appendix C presents wavelet pressure analysis for Edwards Brown dolomite.

Chapter Two Literature Review

Some of this material has been published in Ni et al., (2025).

2.1 Geological CO_2 Storage Contexts: Depleted Hydrocarbon Reservoirs and Saline Aquifers

The majority of the geologically sequestered CO_2 is primarily injected into two main reservoir types: saline aquifers and depleted hydrocarbon reservoirs (Figure 2.1). Both provide porous rock volumes at depth that can retain the injected CO_2 beneath a sealing unit, but they differ in the amount of pre-existing data, the initial state, and the way heterogeneity is expressed and parameterised for flow prediction (Bentham and Kirby, 2005; Worden et al., 2024). Saline aquifers have been used for dedicated CO_2 storage since the mid-1990s, with Sleipner in the North Sea commonly cited as the first commercial-scale saline-aquifer storage project (Holloway, 2005; Worden et al., 2024). While the injection of CO_2 in oil and gas fields has been practiced since the 1970s but primarily for enhanced oil recovery (EOR) (Golzapour et al., 2005; Drax 2025).

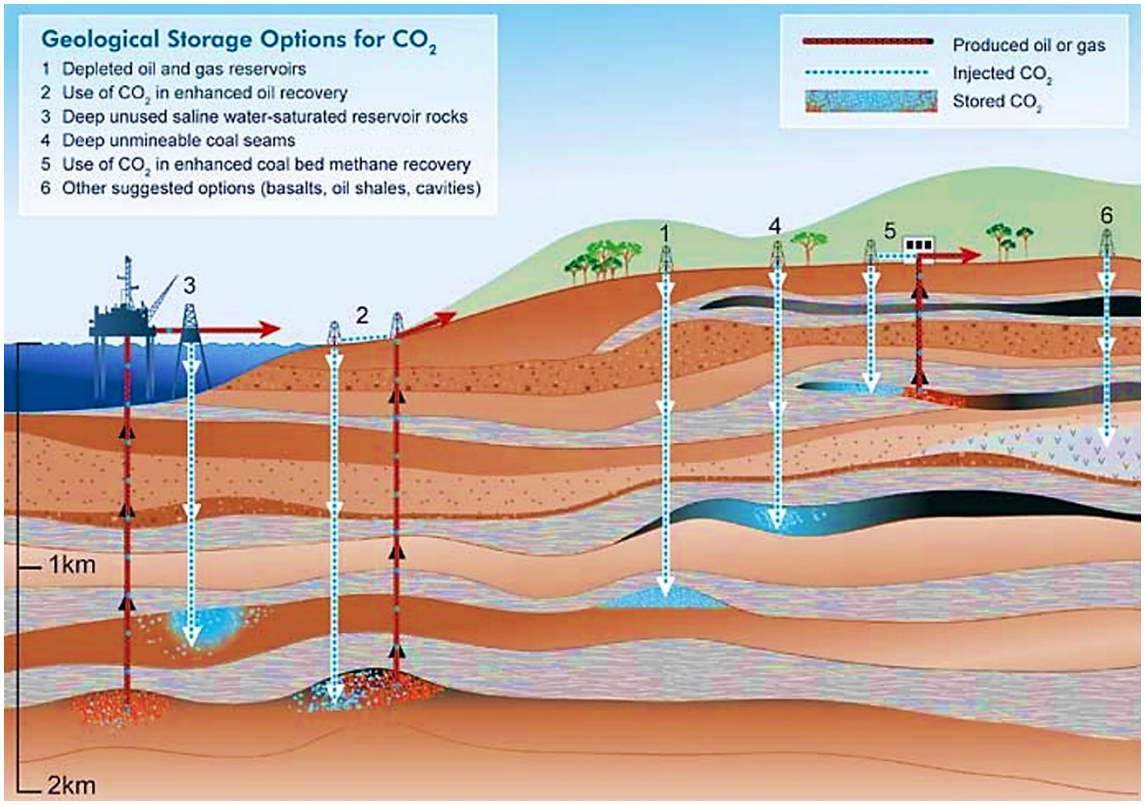


Figure 2.1 Options for storing CO_2 in deep underground geological formations (Source: IPCC, 2005).

The characterisation requirements differ substantially across these contexts. Depleted oil and gas reservoirs typically benefit from decades of production history and associated datasets, including well logs, pressure history, production and injection records, and calibrated geological models. These data constrain reservoir heterogeneity and provide direct evidence relevant to containment and well integrity (Worden et al., 2024). In contrast, saline aquifers often rely on more subsurface control, commonly regional seismic data and sparse well information, which increases uncertainty in storage capacity estimates and motivates conservative assumptions and more extensive pre-injection characterisation.

For the purposes of this thesis, the key distinction is not storage capacity per se, but how heterogeneity and initial conditions translate into multiphase flow behaviour and therefore into the constitutive relationships used for reservoir-scale prediction. In saline aquifers, injected CO_2 is typically buoyant relative to brine, so heterogeneity in permeability and capillary entry

pressure can control vertical migration, lateral spreading, and the development of internal plume structure, including stratified or laterally diverted flow where lower-permeability layers act as intra-reservoir barriers (IEAGHG, 2017). This behaviour is well illustrated at Sleipner, where thin internal layers influence upward migration and promote lateral spreading of the plume (IPCC, 2005).

In depleted gas fields, the in-place fluid is gas rather than brine, and the density contrast between CO_2 and the resident gas can reduce buoyant segregation effects compared with saline aquifers, depending on pressure and temperature. Consequently, heterogeneity often expresses as differences in sweep efficiency, compartment filling, and the accessibility of pore volume, rather than as purely buoyancy-driven vertical migration (Worden et al., 2024). In these settings, uncertainty can be dominated by connectivity across heterogeneity features and by the extent to which the injected CO_2 can access low-permeability volumes. Figure 2.2 illustrate the difference between CO_2 injection in these two geological settings.

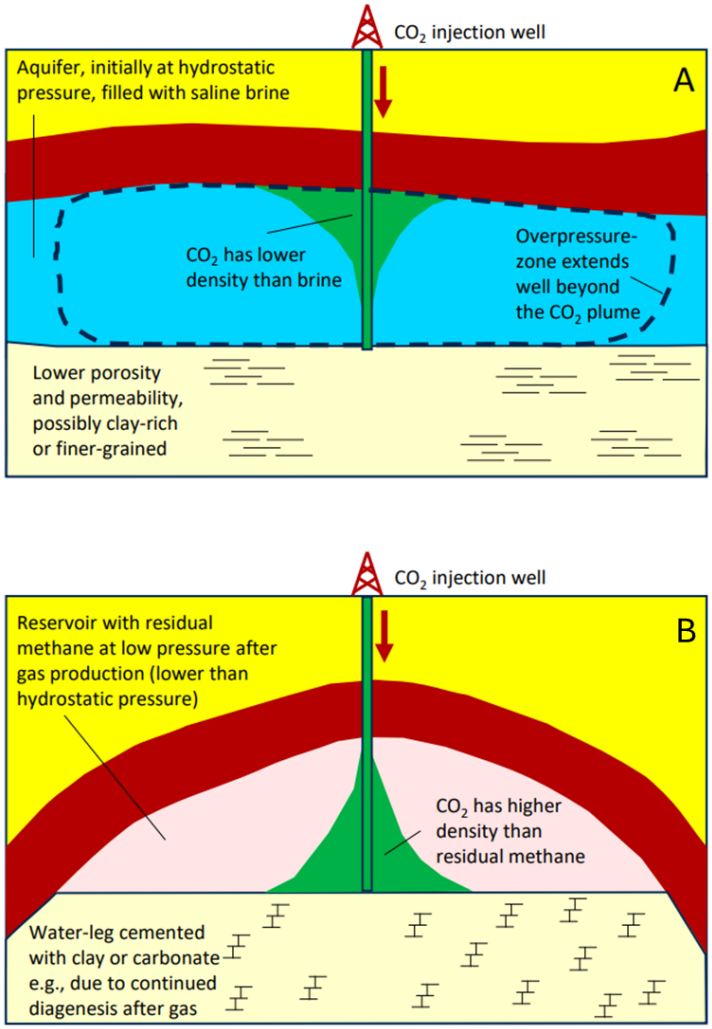


Figure 2.2 Schematic representation of A) saline aquifer and B) depleted gas field used for CO_2 storage (Source: Worden, 2024).

This distinction motivates a central theme of the thesis: even when bulk properties appear homogenous, heterogeneity in pore structure and capillary entry pressure can generate different saturation distributions during displacement, which in turn can modify the effective constitutive functions used in reservoir simulation. Moreover, trapping in saline aquifers is dominated by buoyancy-driven hydrodynamic trapping beneath structural and stratigraphic seals, with residual and dissolved CO_2 developing over time through interaction with heterogeneous flow paths (Snippe and Tucker, 2014). In contrast, in depleted gas fields, CO_2 displaces gas rather than imbibing into gas-filled pores and limited solubility trapping due to low residual water saturation, so heterogeneity primarily affects sweep efficiency and

compartment filling rather than capillary or dissolution processes (TNO, 2024). Saline aquifers therefore benefit from heterogeneity that disperses flow paths and increases CO_2-brine contact area, whereas depleted fields require good lateral connectivity to maximise volumetric sweep and avoid stranded reservoir compartments (Worden 2024; Snippe and Tucker, 2014). In a modelling study by (Snippe and Tucker, 2014), It was shown that the majority of the CO_2 remains mobile in the simulated depleted field, with small amounts of CO_2 dissolved in the oil leg and residual water (Figure 2.3).

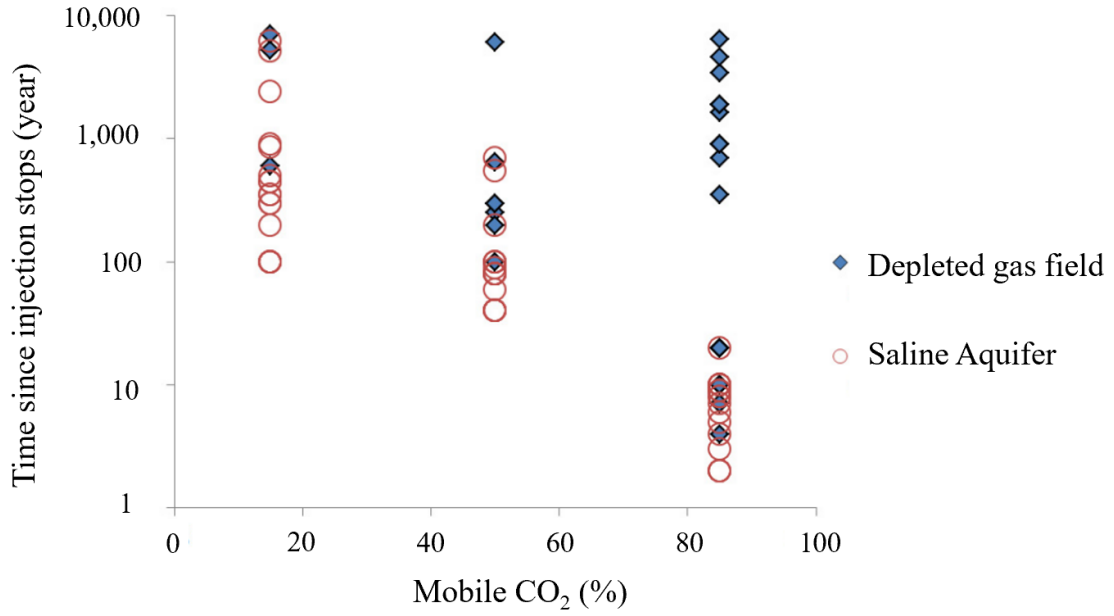


Figure 2.3 Time at which mobile gaseous CO_2 reaches selected modelling fractions (85%; 50%; 15%), 22 depleted gas fields models and 19 saline aquifer models were simulated, however, not every model reaches a selected percentage within the 10,000 year timeframe, (e.g. only 3 out of 22 depleted structurally closed models reach 15%) (Source: Snippe and Tucker, 2014).

However, in classical petroleum engineering, recovery efficiency (and, by implication, the inverse of trapping efficiency) is often framed as the product of three components (Equation 2.1):

Recovery efficiency = microscopic displacement efficiency × areal sweep efficiency × vertical sweep efficiency. (Equation 2.1)

Microscopic displacement efficiency is fundamentally a pore-scale concept, whereas areal and vertical sweep efficiencies reflect Darcy-scale behaviour and are usually treated at or above the grid-block scale in field-scale simulation. A key contribution from the CO_2 storage literature is the recognition that heterogeneity at length scales smaller than a simulation grid block can strongly influence trapping, plume migration, and related flow outcomes (Ni, et al. 2025).

Storage capacity is fundamentally constrained by two independent criteria, pressure constraints, and containment constraints. Critically, sweep efficiency has negligible impact on pressure buildup but exerts first-order control on plume migration and therefore on containment. Containment is directly sensitive to how efficiently the injected CO_2 utilises the available pore space: poor sweep efficiency results in a larger, more laterally extensive plume for a given injected volume, increasing the probability that the plume will reach a potential leak path, breach a structural boundary, or exit the permitted storage domain (Chadwick et al., 2019; Bickle et al., 2007).

This distinction is particularly relevant in heterogeneous formations, where preferential flow through high-permeability pathways can cause rapid lateral migration and poor volumetric sweep, even when total storage capacity appears adequate (Gasda et al., 2011).

2.2 Fluid Flow from pore-scale to continuum scale

2.2.1 Darcy's Law

Flow in porous media is usually described at the Darcy scale using Darcy's law (Equation 2.2). In its form, Darcy's law is a single-phase relationship, and it can be placed on a clear theoretical footing by rigorously deriving it through volume averaging of pore-scale Stokes equations over a representative elementary volume (REV) at scale of interest (Whitaker, 1986).

$$\mathbf{q} = -\frac{K}{\mu}(\Delta \mathrm{P} - \rho g) \qquad \text{(Equation 2.2)}$$

where q is Darcy velocity [m·s^{-1}], K is the absolute permeability [m^2], μ is the dynamic viscosity [Pa·s], ΔP is the pressure gradient, ρ the density [kg·m^{-3}] and g is the component of gravity in the direction of flow [m·s^{-2}].

For multiphase flow, the established continuum-scale approach is to adopt a two-phase (or multiphase) Darcy formulation (Equation 2.3). This framework is best understood as a phenomenological extension of single-phase Darcy's law, rather than a relationship derived from first principles with comparable rigour. As a consequence, the governing equations are not closed by the conservation laws alone and require additional constitutive relationships that must be specified from experiments or calibrated models. Consequently, the multiphase extension of Darcy's law is best understood as a phenomenological framework requiring experimentally determined constitutive relationships rather than a rigorously upscaled continuum theory. Moreover, for multiphase flow, this approach encounters fundamental difficulties: fluid–fluid interfaces and dynamic pore-scale displacement events prevent pressure and saturation fluctuations from converging to unique averaged values, making the existence of a true spatial REV problematic (Berg et al., 2025).

Assuming flow is unidirectional, linear, non-rate dependent, and involving incompressible phases and with negligible gravity and capillary forces. The equation is as follows:

$$\mathbf{q}_p = -\frac{K\, k_{rp}}{\mu_p}(\Delta \mathrm{P} - \rho_p g) \qquad \text{(Equation 2.3)}$$

where $\mathbf{q}_p$ is phase's Darcy velocity for the phase [m·s^{-1}], K is the absolute permeability [m^2], k_{rp} is the phase's relative permeability. μ_p is the phase's dynamic viscosity [Pa·s], ΔP is the

pressure gradient. ρ_p is the phase density [kg·m^{-3}] and g is the component of gravity in the direction of flow [m·s^{-2}].

In practice, the equation is satisfied by providing:

- Relative permeability functions, which describe the saturation-dependent reduction in each phase's effective mobility.
- Capillary pressure function of saturation relating the phase pressures.

Relative permeability and associated saturation-dependent relationships are usually inferred from laboratory measurements such as core-flood experiments, while capillary pressure may be measured directly from mercury intrusion tests or inferred and subsequently parameterised in forms suitable for reservoir-scale modelling.

A key limitation is that these constitutive functions are rarely simple. They often exhibit hysteresis and path dependence, and their behaviour can depend on additional variables beyond saturation alone, including wettability, pore structure, flow rate, flow history, interfacial tension, and heterogeneity (Krevor et al., 2015; Masalmeh et al., 2001; Jerauld, and Salter 1990)

2.2.2 Relative Permeability

Relative permeability strongly influences how fluids move in porous media, as a result, it has been the subject of extensive investigation over many decades (Equation 2.3). Historically, most measurements and interpretations assumed that the core samples used in experiments were homogeneous, and non-rate dependent. Consequently, early work concentrated on how reservoir conditions such as overburden stress, temperature, and fluid viscosity affect relative permeability (Welge, 1952; Johnson et al., 1959; Wyckoff et al., 1936; Leverett, 1939; Wilson, 1956).

Corey and Rathjens (1956) later demonstrated that rock heterogeneity can have a profound impact on relative permeability, showing a wide spread in measured permeabilities depending on the angle between the rock's bedding and the imposed flow direction. Because fluid–rock interactions vary on the millimetre scale, a single relative permeability curve averaged over the whole core cannot accurately capture or predict the detailed internal flow patterns. Their coreflood experiments also revealed that gas relative permeability decreases when flow is oriented perpendicular to bedding, leading them to conclude that explicit representation of rock heterogeneities is essential for reliable predictions of fluid flow. Boon and Benson (2021) show the effect of flow orientation and flow rate on relative permeability (Figure 2.4).

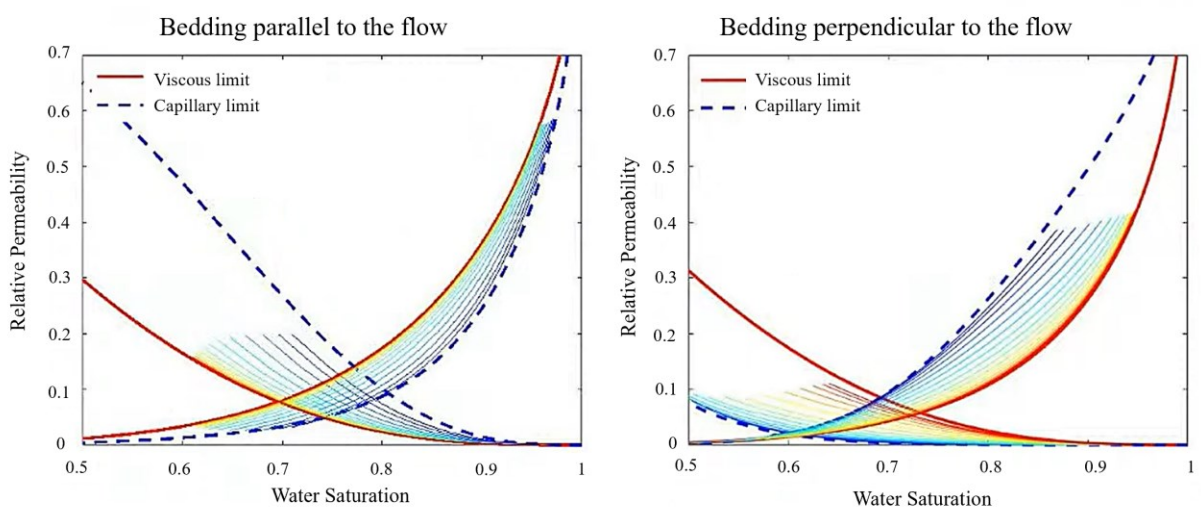


Figure 2.4 The impact of layers orientated a) parallel to the principal axis of flow on the relative permeabilities, b) perpendicular to the principal axis of flow on the relative permeabilities. (Modified from: Boon and Benson, 2021).

Subsequent research initially concentrated on spatial variations in wettability and their influence on multiphase flow. Fatt and Klikoff (1959) showed, using both experimental and numerical approaches, that capillary pressure and relative permeability depend on wettability and change with the amount of trapped fluid. Only later did attention shift to porosity–permeability heterogeneity, where studies found that moderately heterogeneous cores can

behave effectively homogeneously if the heterogeneities are well distributed (Kortekaas, 1985; Hove et al., 1990).

In contrast, the presence of large vugs produced strong rate dependence in waterflood responses, and even small heterogeneities embedded in an otherwise uniform system were shown to substantially modify fluid behaviour, for instance by changing the amount of residual trapped fluid. These works also highlighted that flow behaviour depends on the orientation of sedimentary structures within the core. Kortekaas (1985), for example, examined Festoon cross-bedding common in sandstone reservoirs. They reported that, at reservoir scale, displacement is more efficient when flow is directed perpendicular to these structures. Collectively, these studies established that rock heterogeneity is a central control on fluid behaviour, while also emphasising the difficulty of predicting its effects quantitatively.

2.2.3 Capillary Pressure

The second constitutive relationship required to be used in the multiphase flow Darcy's law (Equation 2.4) is capillary pressure. Capillary pressure, P_c, is defined as the pressure difference across an interface that separates two fluid phases in mechanical equilibrium, which simplifies to as the pressure difference between the less dense and more dense phases:

$$P_c \equiv P_\ell - P_h \qquad \text{(Equation 2.4)}$$

where, P_ℓ is the phase pressure of the less dense phase, and P_{h} is the phase pressure of the denser phase.

Capillary pressure quantifies how strongly a formation can hold water, and therefore it exerts a major influence on the initial distribution of fluid saturations within the rock (McPhee et al., 2015). It can be linked to rock and fluid properties via the Young–Laplace relationship:

$$P_c = \frac{2\sigma\cos\theta}{r} \quad \text{(Equation 2.5)}$$

where σ is the interfacial tension [N·m^{-1}], θ is the contact angle [°], and r is the pore radius [m]. In practice, capillary pressure depends on several factors, including pore size, permeability, fluid characteristics such as density and interfacial tension, and the nature of the pore surfaces, particularly their wettability and texture (Blunt et al., 2013; McPhee et al., 2015).

As research into the effects of heterogeneity on relative permeability progressed, it became clear that rock heterogeneity can also give rise to anisotropic capillary pressure behaviour and variations in the effective capillary pressure. The former refers to different regions within a single core sample exhibiting distinct capillary pressure characteristics, while the latter describes how the core-averaged effective capillary pressure changes with the heterogeneity structure. Dawe et al. (1992) conducted a comprehensive experimental investigation and observed that spatial variations in capillary pressure produce irregular displacement fronts that were detectable in X-ray CT images, a finding corroborated by Cuthiell et al. (1993). They concluded that a single $P_c - S_w$ relationship could not adequately represent the entire core.

Finally, with the recent advances in pore-scale experiments using synchrotron X-ray microtomography, four distinct flow regimes in multiphase systems are revealed depending on capillary number. Pore-scale capillary number is defined according to (Equation 2.6):

$$C_a = \frac{\mu.q}{\sigma} \quad \text{(Equation 2.6)}$$

where μ is the phase viscosity, q is the flow rate and σ is the interfacial tension. At low capillary numbers ($Ca < 10^{-6}$), representing the ratio of viscous to capillary forces, the pressure gradient remains proportional to flow rate with stable, well-defined flow pathways. At intermediate capillary numbers ($10^{-6} < Ca < 10^{-5}$), pressure fluctuations emerge while maintaining linear pressure-flow relationships. Above a critical capillary number ($Ca > 10^{-5}$), a nonlinear power-

law relationship develops with rapid pore-scale rearrangements and intermittent flow (Reynolds et al., 2017; Gao et al., 2020) and finally, capillary number ($Ca >>> 10^{-5}$) where it is a purely viscous regime.

These observations have led to empirical modifications of the multiphase Darcy law to account for high flow rate effects. Pore-scale modelling approaches, including lattice Boltzmann methods, volume-of-fluid techniques, and pore network models, enable direct simulation of multiphase flow by tracking fluid interfaces and capturing capillary-controlled displacement mechanisms (Blunt, 2017; Foroughi 2020).

2.3 Trapping Mechanisms in Geological CO_2 Storage

CO_2 storage security relies on four primary trapping mechanisms that operate across different spatial and temporal scales: structural/stratigraphic trapping, capillary/residual trapping, dissolution trapping, and mineral trapping (Figure 2.5) (Krevor et al., 2015). These mechanisms evolve dynamically throughout the injection and post-injection phases, with their relative importance shifting as the CO_2 plume migrates and interacts with formation fluids and minerals (Lu et al., 2025).

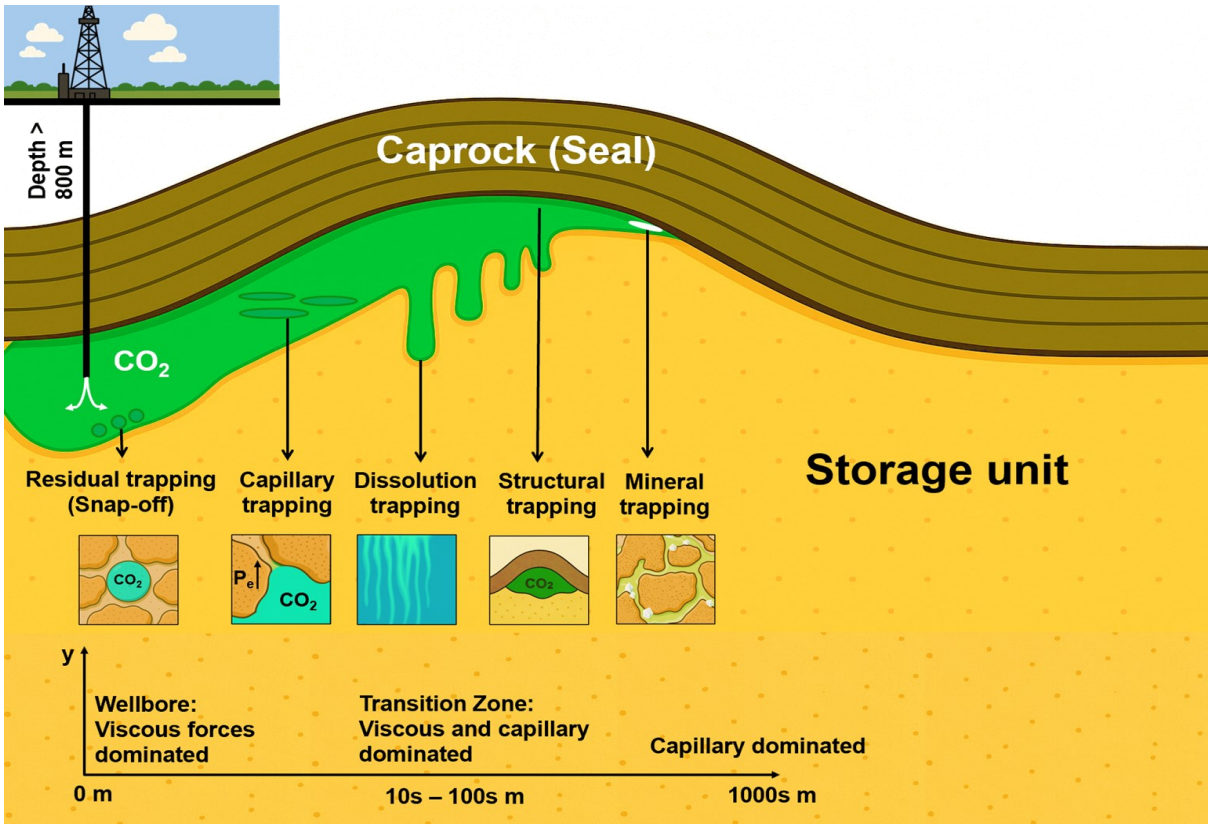


Figure 2.5 Schematic diagram of trapping mechanisms in field-scale CO_2 storage.

Structural and stratigraphic trapping provide the immediate containment mechanism during and immediately following injection, relying on buoyant CO_2 accumulating beneath low-permeability seals such as shale caprocks or cemented layers. Structural traps include anticlines, fault-bound closures, and dome structures that prevent upward migration of buoyant

CO_2 (Bachu, S. et al., 2007; IPCC, 2005). Simulation studies indicate that structural trapping typically dominates during injection, securing up to 86% of injected CO_2 in the early phase (Lu et al., 2025). However, as CO_2 migrates laterally and vertically away from injection points, the proportion of structurally trapped CO_2 decreases over time, with other mechanisms becoming progressively more important (Yang et al., 2017). Residual trapping occurs when CO_2 becomes immobilised as disconnected ganglia or bubbles within the pore space due to capillary forces exceeding buoyancy forces. Another mechanism is building up behind capillary barrier, where heterogeneity in entry pressure hold a pool of the non-wetting phase behind this region of heterogeneity (Krevor et al, 2011). Table 1.2 summarises recent contributions in CO_2 trapping mechanisms.

Table 2.3.1 Recent contributions in Trapping Mechanisms

Trapping Mechanism	**Author(S)**	**Contribution**
Structural (Caprock)	Chen et al. 2025	1) Synthesizes how caprocks seal (capillary vs. hydraulic) 2) identifies key controls and lithology rankings 3) proposes a framework to assess leakage risk under coupled hydro-mechanical effects.
Hydrodynamic (Structural Trap Dynamics)	Wang et al. 2022	1) Presents a full-cycle simulator (injection → migration → post-injection) 2) shows time-varying interplay among trapping modes: injection-period advection governs residual trapping, later convective dissolution weakens it 3) highlights the need to model buoyant structural trapping with time-dependent multiphase flow
Residual (Capillary)	Ni et al. 2021	1) Fast macroscopic percolation/upscaled pore-network model that reproduces post-imbibition residual CO_2 patterns (10–100× faster than full-physics) 2) shows mesoscale heterogeneity boosts trapping but plateaus when capillary barriers are leaky

Residual (Capillary)	Shanghvi et al. 2025	1) proposed ML-augmented pore-network model that predicts residual CO_2 trapping across diverse pore structures 2) speeds up capillary trapping capacity evaluation in heterogeneous reservoirs.
Solubility (Dissolution)	Lyu & Voskov 2023	1) advances two-phase continuum model with a capillary transition zone 2) shows capillary fringe advances convective mixing onset (>2×) and boosts steady-state dissolution flux (~2.5×)
Solubility (Dissolution)	De Paoli et al. 2025	1) 3-D high- Rayleigh simulations reveal a sustained constant-flux dissolution regime (~13% higher flux than 2-D) 2) yields a simple analytical uptake model
Mineral (Geochemical)	Matter et al. 2016	1) CarbFix field pilot shows injected CO_2 mineralizes to carbonates in basalt within ~2 years 2) monitoring/ reactive-transport modelling indicate >95% converted—validating mineral trapping and geochemical models.
Mineral (Geochemical)	Postma et al. 2022	1) Vertically integrated reactive-transport model that plume-averages across thickness to capture key basalt reactions 2) enables efficient field-scale forecasts of long-term CO_2 mineralization

In summary, the relative contribution of different trapping mechanisms throughout the storage period is site specific (Krishnamurthy, et al., 2022; Williams et al., 2013). Variations in rock properties, particularly permeability distributions, capillary entry pressures, and lithological contrasts, can alter migration velocities and plume geometry by orders of magnitude, with subtle changes in grain size contrasts alone capable of slowing migration speeds and increasing trapped volumes by significant amounts (Jackson and Krevor, 2020). The presence of low-permeability horizons and capillary barriers creates complex flow patterns that impede vertical buoyant migration, promoting lateral spreading and enhancing capillary heterogeneity trapping behind regions of high entry pressure (Harris et al., 2021). This spatial variability in geological

properties fundamentally influences the transition between trapping mechanisms over time, with heterogeneous reservoirs exhibiting distinctly different evolution of structural, residual, solubility, and mineral trapping compared to homogeneous systems (Williams et al., 2013). Consequently, accurate characterization of reservoir heterogeneity is essential for predicting storage efficiency and long-term containment security.

2.4 Impact of Pore-Scale (Small-Scale) Heterogeneity

Multiphase flow in porous media is a fundamental aspect of understanding CO_2 storage in the subsurface. Hence, the utilisation of core flooding and experimental imaging techniques has been pivotal element in understanding how CO_2 behaves in various rock types, offering valuable insights to inform simulation models (Georgiadis et al., 2013). Simulation models are informed by multiphase flow properties such as capillary pressure, relative permeability and residual trapping, all of which are contingent on fluid saturation, which in turn is significantly impacted by the structure of heterogeneity. Therefore, when the storage formation is heterogeneous, it introduces considerable intricacy into the analysis and modelling workflow.

2.4.1 The Effect of Heterogeneity on Saturation

The most significant early observation from core flooding experiments is that subcore-scale (Representative Elementary Volume (REV) at scale of interest) heterogeneity causes non-uniform CO_2 saturation distribution. Computed Tomography (CT) scanning on CO_2 core flood experiments has shown spatial variations in CO_2 saturation after the core flood has reached steady state (Krevor et al., 2011; Perrin and Benson, 2010; Shi et al., 2011). Numerical simulations of core flood experiments (Kong et al., 2015; Krause et al., 2011) have shown that a core with a homogeneous capillary pressure vs. saturation relationship tends to have a uniform saturation distribution after CO_2 flooding reaches steady state, even if permeability

and porosity fields are heterogeneous. However, when capillary heterogeneity is modelled in core flood simulations, the steady-state CO_2 saturation varies spatially and is more consistent with experimental observations from CT scans as shown in experimental studies from (Manoorkar et al., 2021; Darraj et al., 2024; Reynolds and Krevor, 2015) where they show that subcore-scale heterogeneity significantly influences multiphase flow during core flood, such as the unsteady-state core flood example shown in Figure 2.6 (Berg et al., 2013).

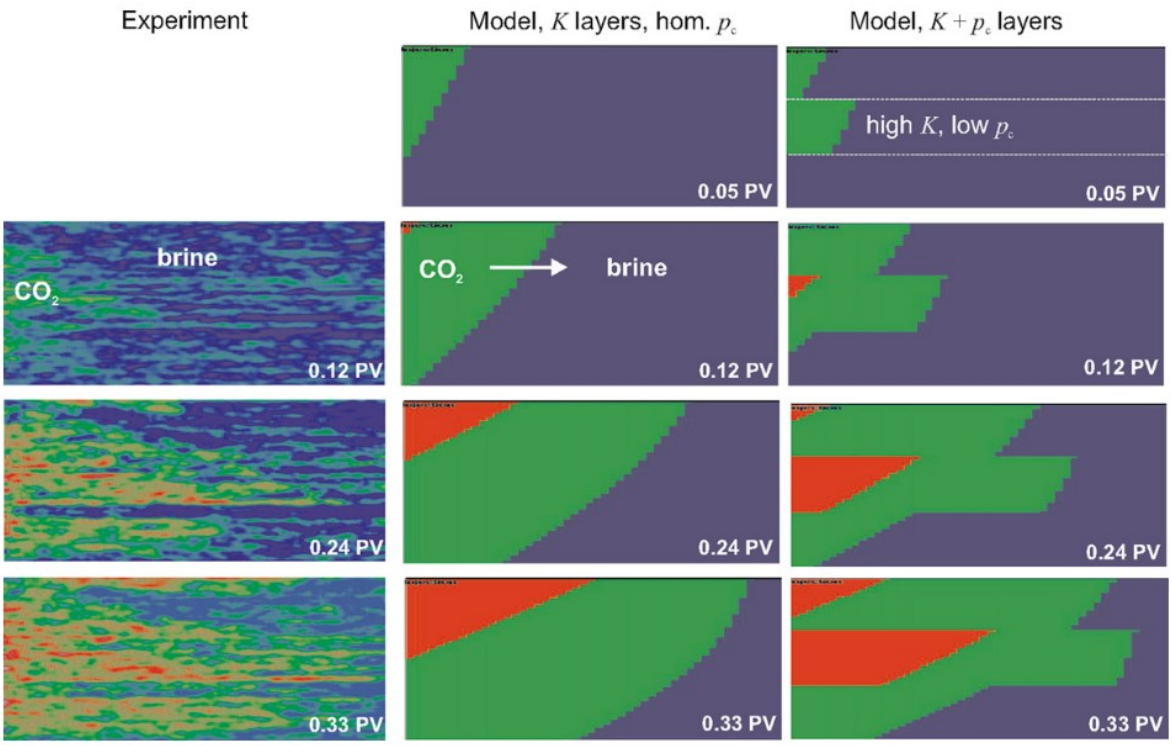


Figure 2.6 Comparing modeling results of CO_2 saturation front advancement in a core with (right) and without (middle) capillary pressure heterogeneity. The modeling results with heterogeneity added to capillary pressure (right) matches the experimental results (left) better. Figure taken from Berg et al. (2013).

2.4.2 The Effect of Heterogeneity on Relative Permeability

The non-uniform saturation distribution widely observed in experiments and simulations of core flood does not necessarily mean that REV-scale heterogeneities at scale of interest are important at larger scales. As argued by Li and Benson (2015), if such nonuniform saturation has no influence when averaged over a large scale, REV-scale heterogeneities are practically insignificant. Rock properties that determine the flow dynamics, such as relative permeability relationship, are almost always measured at the core scale, which is much larger than the REV. In other words, the laboratory-measured relative permeabilities are averaged properties (i.e., effective or upscaled properties) by nature. Therefore, whether the laboratory-measured relative permeability curves have already encapsulated all the effects of REV-scale capillary heterogeneities becomes the key question.

To answer this question, Li and Benson (2015) computed effective drainage relative permeability by conducting numerical simulations on a dm-scale 2D domain with random, REV-scale Gaussian heterogeneity. The way the effective relative permeability are computed mimics the core flood experimental process from which relative permeability are measured in the laboratory. The benefit of this "numerical" core flood is that the boundary condition can be set to eliminate capillary end effect, allowing multiple flow-rate conditions to be examined. Their results showed that when the core is homogeneous, the effective relative permeability is isotropic and not affected by flow rates. However, in the presence of heterogeneity, the effective relative permeability is flow-rate dependent and can be anisotropic (Figure 2.7). Specifically, the shape of the points fitting and the saturation endpoints (e.g., the critical CO_2 saturation) will vary depending on the flow rates and flow directions.

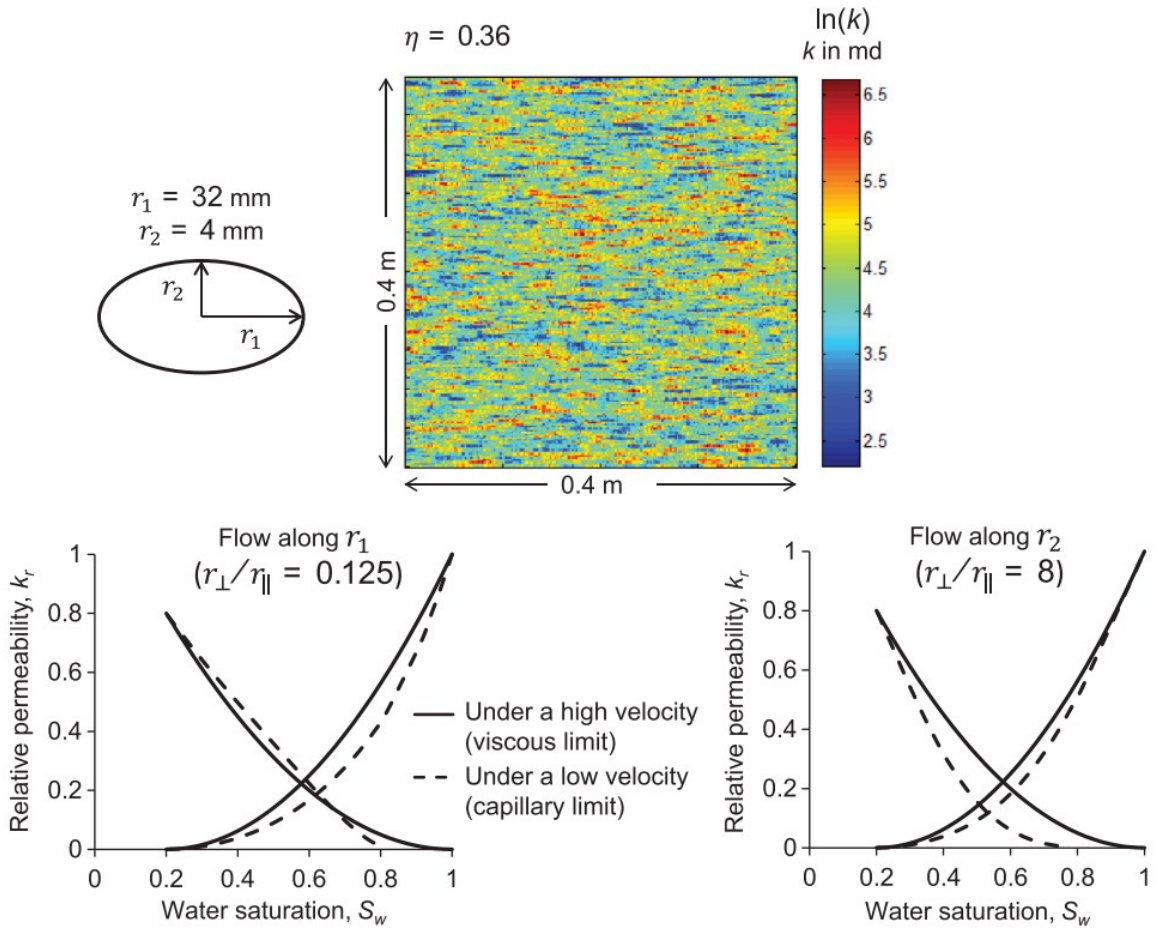


Figure 2.7 An example of anisotropic and flow-rate dependent effective (i.e., upscaled) relative permeability curve in the presence of small-scale capillary heterogeneity during drainage. Note that both the shape and the end point (i.e., critical CO_2 saturation) have changed as flow rate varies. r1 and r2 are correlation lengths of the media in different directions. Figure taken from Li and Benson (2015).

The significance of these observations is that, due to the presence of REV-scale heterogeneities, the viscous limit relative permeability measured from core flood experiments should not be directly used in modelling CO_2 migration under low flow rates. The other observation is that even at the REV scale (below which Darcy's Law no longer holds), small-scale heterogeneity can still affect large-scale CO_2 migration. Experiment and core flood simulation data has shown that even the relatively homogeneous part of Berea sandstones (which already have a lower degree of heterogeneity compared to many other sandstones) small-scale heterogeneities still affected the flow properties significantly (Krause et al., 2011; Perrin and Benson, 2010; Pini et al., 2012).

It is important to clarify that conventional scaling approaches which eliminate the capillary force term are not mathematically invalid; instead, they neglect the influence that local, capillary-driven saturation distributions exert on fluid mobility via the relative permeability function. Essentially, saturation is mapped directly to relative permeability without accounting for this effect, leading to underestimation or overestimation of relative permeability depending on flow orientation and the dominant flow regime. Consequently, the presence of heterogeneity at the small scale causes relative permeability to become anisotropic and dependent on the capillary number (Fadili and Ababou, 2004; Jackson et al., 2018; Li and Benson, 2015; Spurin et al., 2025; Virnovsky et al., 2004).

2.4.3 The Effect of Heterogeneity on Capillary Pressure

As previously discussed, heterogeneity can lead to uneven CO_2 saturation and plume migration. This effect is best represented by the heterogeneity in capillary pressure across different layers/regions of the reservoir: Regions of high capillary pressure may act as barriers, trapping CO_2 in localized areas, which can lead to CHT and enhance capillary trapping—a key mechanism for increasing long-term storage security. Conversely, areas with low capillary pressure might allow CO_2 to migrate more freely, potentially leading to leakage risks if the cap rock integrity is compromised.

Figure 2.8 shows the capillary pressure curves across the layers of a heterogeneous rock. With higher flow potential, there will be homogenous saturation across the layers, meaning that the viscous forces in the pressure equation need to be higher than the capillary pressure gradient to obtain invariant relative permeability. When the flow is driven by capillarity, the saturation will be heterogeneous, and the relative permeability will become sensitive. Hence, under capillary-

dominated flow regimes, multiphase flow properties such as relative permeability are strongly influenced by the presence of heterogeneity (Virnovsky et al., 2004).

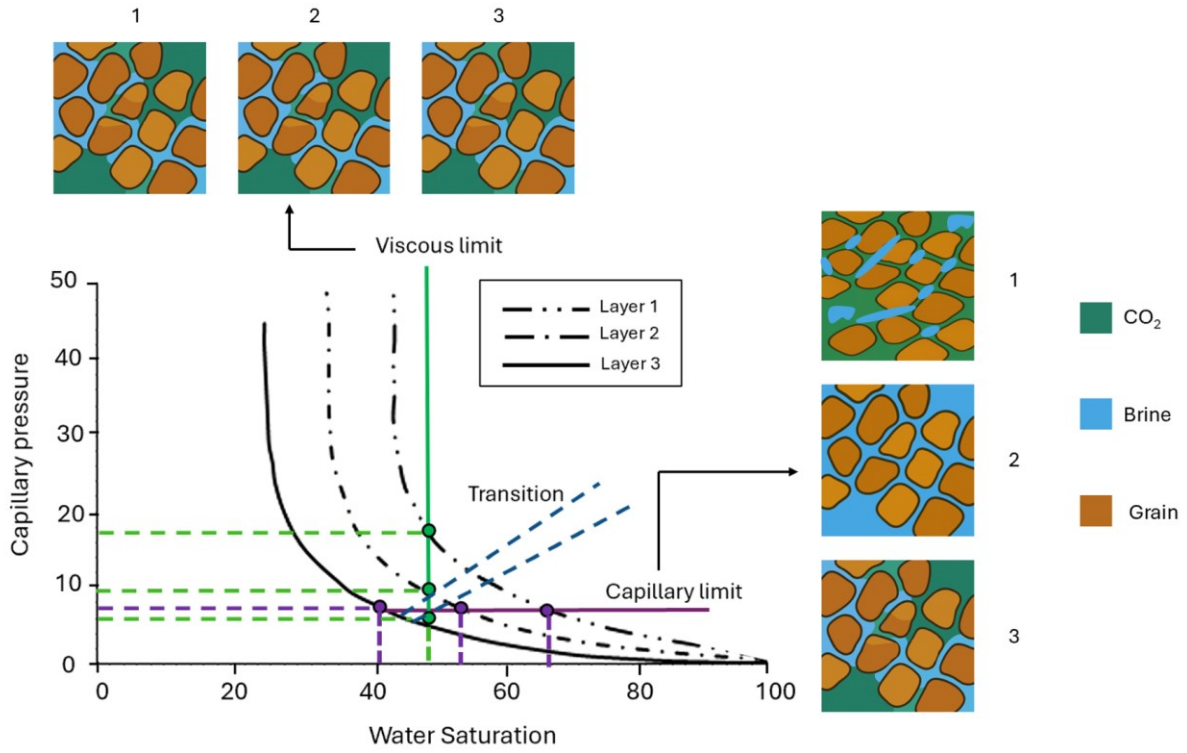


Figure 2.8 Illustration of flow through layered heterogeneous rock, showing the contrasting saturation distributions that arise under different flow regimes. Under capillary-dominated flow, saturation varies between layers because of differences in capillary entry pressure. Under viscous-dominated flow, saturation becomes more uniform across the layers. The schematic also shows representative capillary pressure curves and corresponding CO_2 saturation behaviour for viscous-dominated (green), capillary-dominated (purple), and transitional (blue) flow regimes. Modified from Reynolds and Krevor (2015).

2.4.4 The Effect of Heterogeneity on Trapping

In the context of waterflood for hydrocarbon production, capillary heterogeneity at small scales has a crucial role in influencing the migration and trapping behaviours of the nonwetting phase. Earlier studies by Corbett et al., (1992) simulated waterflooding a laminated sandstone core, and found that at high flow rates, oil trapping is the same for cross-lamination flow and along-lamination flow. But when flow rates are low and capillary-dominated flow regimes are achieved, a significant amount of oil is trapped in high-permeability layers upstream of low-permeability layers due to the capillary heterogeneity trapping mechanism. Therefore, cross-

lamination flow traps more oil than along-lamination flow. The same capillary heterogeneity trapping phenomenon after low-rate cross-lamination waterflooding has also been experimentally validated (Huang et al., 1995).

Moving to CO_2 storage, Krevor et al. (2011) published the first core flooding experimental study, which proved that capillary heterogeneity trapping can be significant compared to pore-scale residual trapping. Krevor et al. performed CO_2/water core flooding experiments on a Mt. Simon sandstone sample at reservoir conditions (Figure 2.9). The core contained a heterogeneity at the outlet end and was split in half to compare trapping behaviour between the homogeneous inlet section and the heterogeneous outlet section. Trapping was two to five times greater in the whole core than in the homogeneous portion alone, demonstrating that capillary heterogeneity significantly enhances post-imbibition CO_2 trapping.

Trapping is commonly characterised using empirically measured initial–residual saturation (IR) curves, which relate the nonwetting-phase saturation after drainage to the residual saturation remaining after imbibition. The Land model (Land, 1968) and linear trapping models are the simplest and most widely used in CO_2 storage studies, each condensing the trapping behaviour of a rock sample into a single trapping coefficient. In capillary-dominated flow regimes, residually trapped nonwetting fluids such as CO_2 tend to remain securely immobilised despite continued flow of the wetting phase, and under low flow rates these CO_2 trapping relationships appear largely insensitive to variations in temperature, pressure, and brine salinity (Niu et al., 2015).

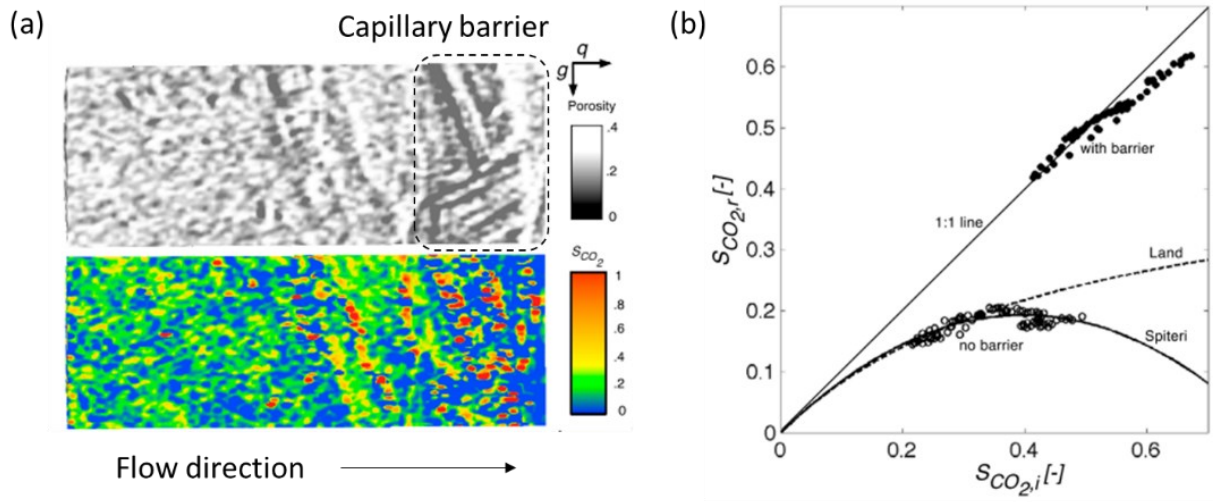


Figure 2.9 CO_2/water core flooding experimental results demonstrating a significant amount of CHT. (a) Porosity map and CO_2 saturation map (after 100% CO_2 drainage and 100% water imbibition) of the center slice of the core. (b) Initial-residual (IR) plot comparing the difference in capillary trapping with and without the cross-laminated capillary barrier at the end of the core. Figure taken from Krevor et al. (2011).

The Land trapping coefficient is highly sensitive to the heterogeneity structure of the rock, and can vary substantially within a single sample. Kim et al. (2021) showed that the Land parameter spans values from about 0.4 to 2 for layers with differing capillary properties within one core, and that capillary heterogeneity becomes more important as the initial CO_2 saturation increases. Because natural rocks are intrinsically heterogeneous, IR trapping relationships obtained from core-flood experiments reflect a combination of pore-scale residual trapping and capillary heterogeneity trapping, and it is experimentally challenging to disentangle these mechanisms. As a result, core-flood measurements typically report larger capillary trapping capacities in rocks with stronger heterogeneity (Ni et al., 2019), and numerical modelling is often required to separate the contributions of different trapping processes. Experiments on artificial, more uniform media such as homogeneous bead packs can also be used to isolate the purely pore-scale component of trapping (e.g. Kimbrel et al., 2015).

Scatter in IR data, commonly ascribed to experimental uncertainty, may in fact signal the extent of capillary heterogeneity trapping occurring in a given experiment (as seen in Chapter 4 of

this thesis). Krevor et al. (2015) supported this interpretation by comparing IR data for sandstones and carbonates, finding significantly larger scatter for carbonate rocks, consistent with their higher degree of heterogeneity. Reynolds et al. (2018) linked the wide variability in capillary trapping observed in Ormskirk sandstone to contrasts in capillary properties between otherwise homogeneous layers. Furthermore, Jackson et al. (2020) demonstrated that heterogeneity strongly influences connected nonwetting-phase saturations and thus the IR relationship; their numerical simulations reproduced residual saturations exceeding those predicted by pore-scale residual trapping alone, in line with experimental observations and providing additional evidence for the role of heterogeneity trapping.

2.5 Upscaling Continuum Scale Properties in Heterogenous Rock Samples

Local capillary heterogeneity can significantly alter the macroscopic behaviour of fluid flow through porous media. These alterations manifest in the multiphase flow continuum scale properties (also known as constitutive relationships) to be used to model fluid movement and trapping in the subsurface. Relative permeability and capillary pressure are such foundational constitutive relationships in reservoir simulation. Usually, these curves are derived from special core analysis (SCAL) of cm-scale samples representing only homogeneous rock types which can cause a significant misrepresentation of the plume migration, size, and shape when upscaled. Recognizing the inherent heterogeneity at the REV scale, upscaling procedures have been developed to translate multiphase physics across scales (Jackson and Krevor, 2020; Li and Benson, 2015; Pickup et al., 2000; Virnovsky et al., 2004).

Jackson et al. 2020 experimentally demonstrated that capillary heterogeneity trapping increases phase connectivity, illustrating the need to include heterogeneous fluid saturations in relative

permeability interpretations. This means that, in a heterogeneous reservoir, the relative permeability relationship is not uniform but can vary significantly from one location to another. This variation is a direct consequence of the different ways in which fluids distribute themselves across the heterogeneous pore structure. Simplified models that use a single set of relative permeability curves for the entire reservoir may fail to capture the complex flow dynamics induced by heterogeneity. Instead, advanced models must account for spatially varying relative permeability relationship, which are influenced by local rock properties and fluid saturations. Hence, SCAL measurements in different locations needed to have –as close as possible- a picture of how capillary heterogeneity is impacting the flow.

Upscaling in the presence of capillary heterogeneity can lead to anisotropic rate-dependent saturation functions (Boon and Benson, 2021; Li and Benson, 2015). Boon and Benson 2021 described the relative permeability and capillary pressure as a function of brine saturation, flow direction and flow rate. They showed that relative permeability and capillary pressure in homogeneous rock types are not flow-rate dependent, that the flow-rate dependent behaviour arises in laminated composite rocks. They also showed that, for flow parallel to the bedding layers, the relative permeability of the CO_2 phase increases with decreasing flow rate, while the water relative permeability decreases. The opposite was observed for flow perpendicular to the bedding layers. Consequently, capillary gradients can exist between the different rock types resulting in a capillary induced flux of water into the low permeable layer and CO_2 into the high permeable layer until the system reaches capillary equilibrium, leading to an increased amount of capillary heterogeneity trapping.

2.6 Pore-to-Core-to-Field Scale Transitions and Upscaling

Upscaling from pore-scale physics to field-scale reservoir simulation represents a fundamental challenge in predicting CO_2 storage performance, requiring integration of processes operating across many orders of magnitude in spatial scale. Effective upscaling must preserve essential physical behaviours while reducing computational complexity to enable practical reservoir-scale simulations (Ni et al., 2025; Rathmaier et al., 2024). The usual size ranges of rock variation that lead to differences in capillary behaviour are generally between tens of meters and less than a meter, depending on the rock type. Therefore, creating a large-scale model that effectively captures these variations at these sizes requires billions of grid blocks, making the task unfeasible. Even with today's advanced computing power, standard flow simulators would take a long time, from months to years, to properly simulate fluid movement over such a large grid.

Heterogeneity exists from the millimetre scale to the field scale, and at each scale it affects CO_2 plume migration and trapping with different magnitudes. Ni et al., 2025 propose a tiered system for modelling heterogeneity in field scale models. Heterogeneity is categorised into four classes and ranked based on their influence at the field scale:

- First-order effect (the most influential): heterogeneity between sand and large-scale flow baffles and barriers
- Second-order effect: heterogeneity in large-scale alternations of low- and high-quality sand facies.
- Third-order effect: heterogeneity in meter-scale laminations, cross-beddings, or low/high-permeability sand alternations that are finer than the grid resolution

- Fourth-order effect: heterogeneity that is smaller than the third-order effect, e.g., mm- to dm-scale heterogeneities.

The first- and second-order effects are influential during both the injection and post-injection periods.

The third- and fourth-order effects are most influential during the post-injection period. They can be overshadowed by the first- and second-order effects, but they could also be pervasive (e.g., thin laminations can occur everywhere in sand facies), leading to non-negligible cumulative influence. Since they are typically finer than the grid resolution in field-scale simulations, homogenisation or upscaling is required to preserve the fine-scale physics into effective properties of field-scale grid blocks. The properties to be upscaled include not only single-phase properties like porosity, permeability, and kv/kh, but also multiphase properties like relative-permeability and capillary-pressure curves. Among them, relative permeability upscaling is the most complicated. The upscaled relative-permeability curves can be flow-rate dependent and anisotropic as discussed in (Li and Benson, 2015; Virnovsky et al., 2004).

While usually first- and second-order effects of capillary heterogeneity in field-scale simulations are the most important ones; the risk of not including the more pervasive finer-scale heterogeneities that might have non-negligible cumulative influence in the post-injection period can be large.

2.7 Why Structural Heterogeneity Characterisation Alone is Insufficient

The characterisation of structural heterogeneity is typically organised into hierarchical scales such as lamina, lithofacies, and facies associations as shown in (Figure 1.1). Nordahl and Ringrose, 2008 provides a useful framework for single-phase flow, where the REV concept

enables effective upscaling based on spatial averaging of porosity and permeability. However, this spatial-only REV concept becomes questionable for multiphase flow, where dynamic length scales emerge from the interplay of capillary, viscous, and gravitational forces that are fundamentally independent of geological structure. For example, the capillary end-effect zone scales as (inverse of capillary number) rather than with any stratigraphic feature, and saturation front propagation is governed by the balance of viscous pressure gradients and capillary entry pressures rather than by bedding thickness alone. These dynamic length scales interact with structural heterogeneity in complex, nonlinear ways that cannot be predicted from porosity–permeability distributions alone. Consequently, effective multiphase flow properties must be determined experimentally on samples that span the relevant structural scales and under flow conditions that reproduce the appropriate balance of forces. This dual requirement—matching both structural and dynamic length scales—motivates the experimental approach adopted in Chapters 4–6, where samples are selected to represent increasing complexity and heterogeneity scales and flow regimes are controlled to remain within the capillary-dominated regime relevant to field-scale CO_2 storage.

Chapter Three Experimental Methodology and Image Processing

This chapter outlines the experimental workflow and coreflood apparatus used to generate the datasets analysed in this thesis.

3.1 Medical X-ray CT Imaging

In chapter 4, all experiments were conducted using a sample holder constructed from PEEK material. Each rock sample was wrapped in multiple layers of heat-shrink wrap to increase its diameter to the standard coreholdere diameter of 1.2 cm (from 1 cm), then enclosed within a flexible fluoropolymer (Viton) sleeve to ensure radial sealing. Before running the flow experiments, the samples were placed inside a Bruker SkyScan 1273 micro-CT scanner and imaged at a voxel size of 6 μm. After this, the core-holder was assembled for flow experiments and transferred to the medical CT apparatus shown in Figure 3.1. The micro-CT imaging was performed prior to the coreflooding experiments to resolve pore-scale structure for subsequent pore network model extraction, while medical CT scanning was employed during multiphase flow to capture time-resolved saturation distributions at the core scale.

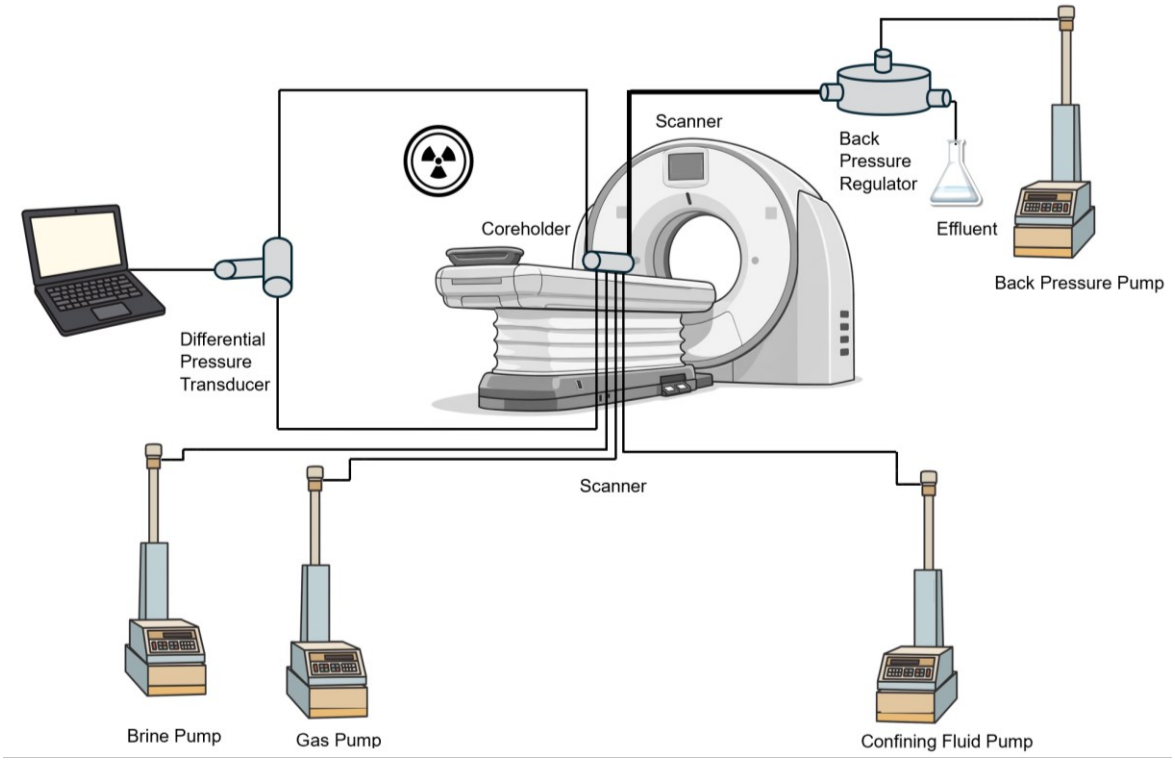


Figure 3.1 The experimental apparatus for the flow experiments with imaging using medical X-ray CT.

The experimental apparatus (Figure 3.1) was designed to reduce the effect of the boundary condition (also referred to as the capillary end effect). The capillary end effect is a well-documented artefact in steady-state and unsteady-state coreflooding experiments that arises from a capillary-pressure discontinuity at the outlet (and sometimes inlet) face of a core sample; because capillary pressure must be zero in the external tubing, a saturation gradient forms near the boundary, leading to anomalous accumulation of the wetting phase and non-uniform saturation profiles even under apparent steady-state flow (Huang and Honarpour, 1998; Gupta and Maloney, 2015; Goodarzian and Sorbie, 2023). Several experimental and analytical strategies have been developed to mitigate or correct for capillary end effect. On the experimental side, increasing core length, raising injection rates, and using higher fluid viscosities all reduce the fractional volume of the capillary end effect zone, although they cannot eliminate it entirely, and high rates may introduce secondary problems such as fines

migration or phase-behaviour changes (Gupta and Maloney, 2015). Analytical and numerical correction methods have therefore become standard practice: the "Intercept Method" employs multiple flow rates at each fractional-flow step and extrapolates pressure-drop and saturation data to infinite rate, yielding end-effect-free values without requiring in-situ saturation monitoring or prior capillary-pressure functions (Gupta and Maloney, 2015; Virnovsky et al., 1998). More recent approaches fit analytical or numerical steady-state models that explicitly incorporate the saturation gradient to the measured data, enabling robust correction even for low-rate tests in tight or reactive rock (Andersen et al., 2017).

However, previous experimental studies have either removed the affected region from analysis (Perrin and Benson, 2010; Pini and Benson, 2017), applied corrections during data processing (Archer and Wong, 1973), or added a porous plate or a second core downstream to stabilise the outlet conditions (Avraam and Payatakes, 1995).

In this study, the diameter of the outlet flow line was 1.587 mm (double the inlet line). This adjustment allowed the non-wetting phase to exit the core more freely to minimise saturation distortions near the outlet face. A dedicated validation experiment was performed on a Bentheimer sandstone sample (1.2 cm in diameter and 3 cm in length) to test for capillary end effects using the modified apparatus. The resulting observations were compared with the capillary end-effect behaviour reported for Bentheimer sandstone by Jackson et al. (2018). As shown in Figure 3.2, the resulting saturation profile shows no systematic boundary-driven accumulation near the inlet or outlet, indicating that capillary end effects were negligible for the conditions used and that the measured response is representative of the core-scale displacement.

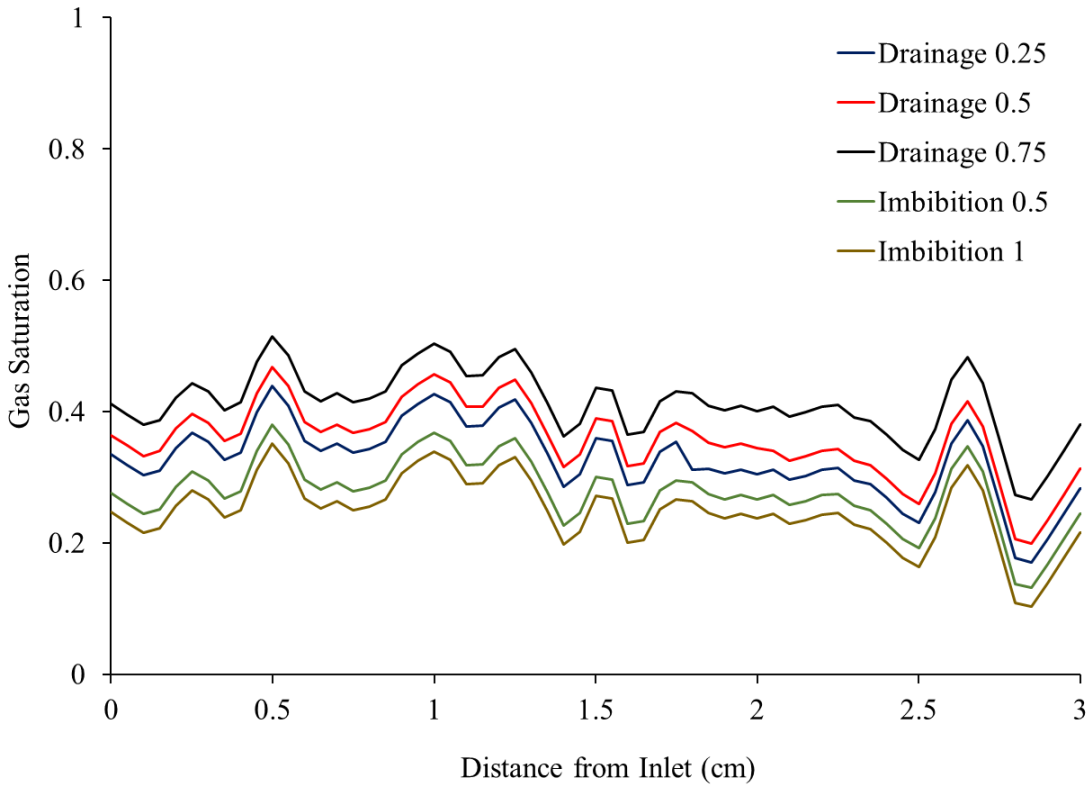


Figure 3.2 1D slice average saturation along Bentheimer sandstone sample for all fractional flows.

The rock sample was positioned horizontally within the core-holder, and the following steps were followed:

1. An initial confining pressure of 0.5 MPa was applied to secure the sample in place. A baseline dry scan of the sample was acquired.
2. Both pore pressure and confining pressure were increased simultaneously into 6 MPa and 6.5 MPa, respectively. The 0.5 MPa difference is to maintain effective radial sealing and prevent bypass flow along the core sleeve while avoiding any pore collapse from excessive confining pressure during the experiment. Nitrogen was injected at constant pressure until breakthrough was observed at the outlet, after which a nitrogen-saturated scan was acquired.

3. Nitrogen was displaced by flowing CO_2 through the dry core for approximately 30 minutes, ensuring full removal of the air from the sample. This step is done to avoid trapping bubbles of air and to ensure full brine saturation.
4. Brine was then injected to saturate the sample, and the absolute permeability was measured by using four different flow rates at steady-state single-phase flow.
5. A scan of the brine-saturated rock was then acquired for porosity and saturation referencing.
6. Sequential scans were acquired at varying fractional flows (the fraction of the flow rate of the aqueous phase to the total flow rate). After each injection step, fluid flow was maintained until steady-state conditions were confirmed, at which point CT imaging was performed.

Throughout the entire procedure, inlet and outlet pressures were continuously monitored using Keller pressure transducers. Fluid saturation and porosity were quantified using a medical X-ray CT scanner (Universal Systems HD-350) operating at 120 kV, 200 mA, and 1 s exposure time. Scans were acquired along the full core length at 0.5 mm slice thickness with a voxel size ($0.039 \times 0.039 \times 0.5$ mm³).

3.2 Medical-CT Image Processing

Porosity was calculated from CT images using air-filled and brine-saturated scans according to the following equation:

$$\phi = \frac{CT_{brine} - CT_{dry}}{I_{brine} - I_{air}} \quad (1)$$

where I and CT are the X-ray attenuation reported in Hounsfield units (HU). CT_{dry} and CT_{brine} are taken from the dry and brine-saturated images, respectively. I_{brine} = 500 and I_{air} = -1,000. These reference values are obtained by scanning two tubes, one filled with air and the other filled with brine, to determine the corresponding CT intensity values. At elevated pressures,

additional attenuation of the X-ray beam can cause a systematic shift in these values, leading to an uncertainty in the estimated porosity of approximately one part in 20 or 5% (Manoorkar et al., 2021).

Saturation in the rock samples was calculated at each fractional flow rate using the fractional flow scan. the following relation:

$$S_{N_2} = (1 - S_w) = \frac{CT_{flow} - CT_{brine}}{CT_{N_2} - CT_{brine}} \quad (2)$$

where CT_{flow} is the CT number of the core filled with both fluid phases, CT_{N_2} is the nitrogen scan, and CT_{brine} is the brine-saturated scan.

3D Medical CT volumes were processed in Python using a custom workflow (Spurin, 2025). The code uses the DICOM files produced by the medical-CT scanner. DICOM slices were read with pydicom and converted to floating-point arrays. To correct for small scan-to-scan misalignment and any apparent tilt of the core in the field of view, a slice-dependent centring correction was applied by linearly interpolating the core centre coordinates between inlet and outlet and masking the core cross-section with a circular region of interest. The resulting 3D stacks were optionally coarsened by block-averaging to reduce noise and computational time. Three-dimensional renderings of porosity and saturation fields were generated using an interactive voxel visualisation routine (voxel_map_3D, Matplotlib + ipywidgets) to support qualitative inspection of spatial structure and to generate figures.

3.3 Micro-CT Imaging

Chapters 5 and 6 apply the same core-flooding and CT-based analysis workflow introduced here in Chapter 3, so the experimental logic and data-processing steps are consistent across both datasets. The chapter-specific scanner settings and imaging parameters are reported within each chapter. The key difference is the experimental design chosen to match the heterogeneity

scale being interrogated: in Chapter 6, Edwards Brown dolomite, the study focuses on drainage followed by imbibition to isolate heterogeneity-driven trapping mechanisms, whereas in Chapter 5, Indiana limestone, the protocol is extended to multiple flow rates to quantify rate (capillary number) sensitivity of saturation structure and effective flow properties in a rock dominated by millimetre-scale heterogeneity.

The samples were encapsed in a transparent heat shrink wrap and a Viton sleeve, then inserted into a PEEK flow cell. Teledyne ISCO pumps were used for co-injection of the wetting and non-wetting phases. Pressure transducers (PD-33X, Keller) were installed at the inlet and outlet to measure differential pressure across the sample.

Figure 3.3 provides a schematic of the apparatus. The flow system was configured with six high-precision Teledyne ISCO pumps, enabling the control over fluid phase injection, application of confining pressure, and regulation of system pressure through a dedicated back pressure pump.

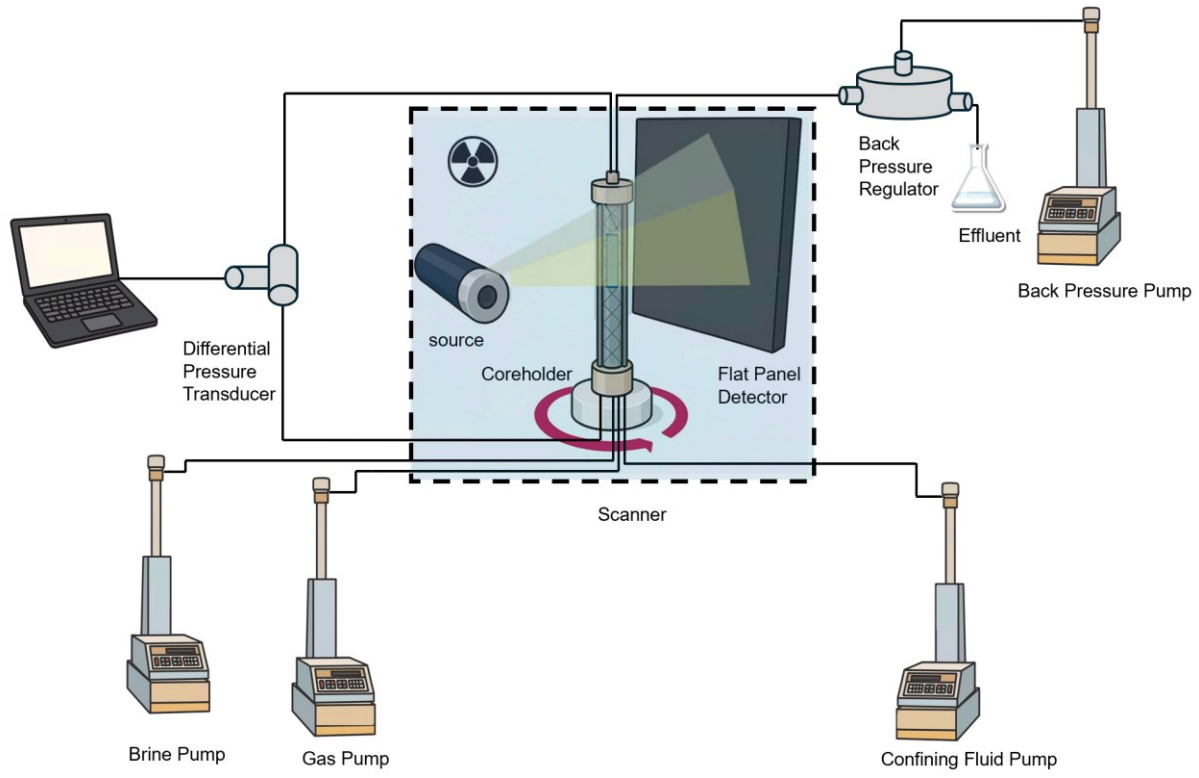


Figure 3.3 Micro-CT experimental apparatus.

3.4 Micro-CT Image Processing

Image processing for Chapters 5 and 6 was performed using commercial AVIZO software (ThermoFisher), with chapter-specific parameters (e.g., filtering, thresholds, and segmentation settings) reported in the relevant sections in each chapter. In both chapters, a pore-space mask was first generated to exclude the rock matrix and perform the subsequent analysis to the fluid-filled pore space. Within this masked pore domain, voxels were then classified as belonging to the wetting or non-wetting phase to quantify phase occupancy and saturation.

Because the samples are complex and heterogeneous where they exhibit spatially variable greyscale values, pore-space segmentation was not based on simple global thresholding. Instead, segmentation was performed using a watershed-based algorithm, in which the greyscale volume is treated as a topographic surface and local minima are interpreted as candidate pore centres. The watershed transform then partitions the pore space by "flooding" these minima and delineating boundaries along local intensity gradients, which is well suited to resolving complex, connected pore structures in multiphase imaging.

As an additional robustness check, the fully brine-saturated reference scan was subtracted from each flow scan, and the resulting saturation profile was compared to the profile obtained from the watershed segmentation method to confirm consistency and verify that the inferred phase distributions was not artefacts of reconstruction or segmentation.

3.5 Pore Network Extraction and Capillary Entry Pressure Mapping

A key component of the analysis workflow is the extraction of pore network models from micro-CT images. Pore network modelling provides a skeletal representation of the pore space, in which individual pores (void regions where a maximal inscribed sphere can fit) are

connected by throats (the narrowest constrictions between pores). This representation enables quantitative characterization of pore and throat size distributions, coordination number (the number of throats connected to each pore), and spatial organization of the pore space.

The pore network extraction is performed using the open-source PoreXtractor algorithm (Dong and Blunt, 2009; Raeini et al., 2017), which applies a maximal inscribed sphere method to the segmented dry-scan images. The algorithm identifies pore centres by finding the largest sphere that fits within the pore space at each location and then assigns each voxel to the nearest pore centre. Throats are identified as the local minima in the radius of the inscribed sphere along the pathways connecting adjacent pores. This partitioning yields a graph representation of the pore space, where nodes represent pores and edges represent throats, with associated geometrical properties (radius, volume, surface area) stored for each element.

From the extracted throat radii, local capillary entry pressures are estimated using the Young–Laplace equation (Equation 2.5). Assuming strongly water-wet conditions ($\theta \approx 0°$), this relationship directly links throat geometry to the capillary pressure required for less-dense phase invasion. Throats with smaller radii correspond to higher entry pressures, meaning that invasion into those regions requires greater driving pressure.

By mapping the estimated entry pressures back onto the three-dimensional pore space, we can visualize the spatial distribution of capillary heterogeneity within the sample. Regions with uniformly low entry pressures are expected to be invaded early during drainage and to exhibit relatively homogeneous saturation profiles. In contrast, regions with elevated or spatially variable entry pressures act as capillary barriers, restricting non-wetting phase advance and promoting preferential flow through alternative pathways. This spatial mapping provides a predictive framework for interpreting saturation distributions observed during multiphase flow experiments: high-saturation regions typically correspond to accessible, low-entry-pressure

zones, while low-saturation or uninvaded regions align with capillary barriers identified in the pore network.

It is important to note that this analysis is constrained by the imaging resolution. Pores and throats smaller than the voxel size (≈ 5–6 μm) are not explicitly resolved and therefore do not appear in the extracted network. In carbonate rocks with significant microporosity—such as Indiana limestone (Chapter 5) and Edwards Brown dolomite (Chapter 6)—this limitation can lead to underestimation of connectivity and overestimation of entry pressures, because unresolved micro-throats may provide persistent connections between larger pores (Carrillo et al., 2021). Consequently, the pore network models represent only the macropore structure, and conclusions about capillary entry pressures and displacement behaviour are valid primarily for the resolved pore space. The specifics of pore network analysis of each sample are discussed in chapters 4-6.

3.6 Rationale for Imaging Strategy and Resolution Selection

The central objective of this thesis is to characterise how heterogeneity at small-scale (sub-grid) scales controls multiphase flow properties. As discussed in Chapter 2, heterogeneity in geological formations is inherently multi-scale, spanning from pore-scale variations (micrometres) through bedding and diagenetic features (millimetres to centimetres) to facies architecture (metres to kilometres). Field-scale reservoir simulation grids typically operate at metre-to-decametre resolution, meaning that all finer-scale heterogeneity is effectively sub-grid and must be represented through upscaled or effective properties.

The experimental strategy adopted in this thesis targets heterogeneity at two complementary scales:

- core-scale saturation distributions that reveal how heterogeneity controls displacement patterns and trapping over centimetre-to-decimetre sample lengths, and
- pore-scale structure and connectivity that governs local capillary entry pressures and phase occupancy.

To resolve these scales simultaneously, two imaging modalities are employed:

1. Medical X-ray CT:

Used in Chapter 4 to capture saturation evolution during steady-state drainage and imbibition across 5 cm-long sandstone cores. Medical CT provides a large field of view with sufficient resolution (voxel size ≈ 39 μm in-plane, 0.5 mm slice thickness) to image the entire core while resolving millimetre-to-centimetre scale heterogeneity in porosity and saturation. This resolution is well suited to detecting cementation contrasts, porosity variations, and layered or barrier-type features that influence continuum-scale displacement behaviour. Critically, the spatial extent captured by medical CT allows one-dimensional saturation profiles to be

measured along the full core length, enabling direct identification of regions where heterogeneity restricts invasion, promotes bypass, or enhances trapping.

2. Micro-CT:

Used in Chapters 5 and 6 to resolve pore-scale structure and fluid configurations at voxel sizes of 4.9, 5.6 μm, respectively. This resolution captures individual pores, throats, and pore-body–throat connectivity, enabling extraction of pore networks and direct quantification of local capillary entry pressures capped at resolution limits. Micro-CT imaging is therefore essential for linking observed fluid interfaces and the underlying pore-scale mechanisms that govern displacement and trapping. The trade-off is a reduced field of view: typical micro-CT scans capture 1.2–6 cm sample lengths, which is sufficient to observe heterogeneity at the millimetre-to-centimetre scale but may under sample larger-scale variability.

An important distinction between the two imaging techniques is the segmentation reliability and its impact on derived flow properties. Medical CT images of fluid-saturated cores exhibit a uniform X-ray attenuation between scans. This reduces segmentation bias and enables robust quantification of phase saturations without the threshold-sensitivity issues that can bias the analysis. In contrast, micro-CT segmentation of multiphase systems, particularly in heterogeneous carbonates is more susceptible to greyscale overlap, partial volume effects, and beam-hardening artefacts, which can introduce segmentation-dependent errors in connectivity, saturation, and derived relative permeability (Schlüter et al., 2014; Garfi et al., 2020). Consequently, medical CT provides a more reliable basis for measuring core-averaged saturations used to calculate relative permeability, while micro-CT excels at resolving pore-scale structure and mechanisms despite its greater sensitivity to image processing choices.

Hence, the choice between medical CT and micro-CT is driven by the desired outcome in the context of heterogeneity scale being interrogated. In Chapter 4, where the focus is on within-

interval variability in less complex sandstone from closely spaced sampling depths, medical CT provides the segmentation reliability needed to confidently attribute differences in relative permeability to capillary heterogeneity. However, in Chapters 5 and 6, where millimetre-to-centimetre heterogeneity in carbonates governs local capillary contrasts and pore-scale trapping mechanisms, micro-CT resolution is required to understand these more complex systems. Together, these modalities enable a pore-to-core analysis that bridges the gap between mechanistic pore-scale observations and continuum-scale flow properties.

3.7 Methodological Limitations and Uncertainty

All experimental methods have an operating envelope, and in this work the most important constraint is the limits of the pumping system and core-holder. This defines which rock samples can be meaningfully characterised under the intended multiphase flow protocols.

A practical limitation of the experimental is imposed by the maximum operating pressure of the pump and core-holder system (10 MPa). For low-permeability ("tight") samples, achieving the target flow rates and establishing stable drainage–imbibition conditions can require differential pressures that approach or exceed this limit. In those cases, the experiment becomes pressure-limited rather than physics-limited: the required pressure gradient to drive throughflow cannot be applied safely, so meaningful multiphase displacement and saturation-profile acquisition are not possible.

This constraint is evident in the tighter samples considered in this thesis, including Sample 3 in Chapter 4, where limited the pressure drop from one phase flow reached 9.2 MPa leaving no room for achievable multiphase characterisation. A similar limitation was encountered in earlier set of experiments where two Silurian dolomite rock samples were trialled (Figure 3.4); the measured permeability was on the order of ~0.2 mD, implying that the pressure drop

required for the planned coreflood protocol would exceed the 10 MPa system limit. As a result, the full experimental sequence could not be conducted for those samples, and they were excluded.

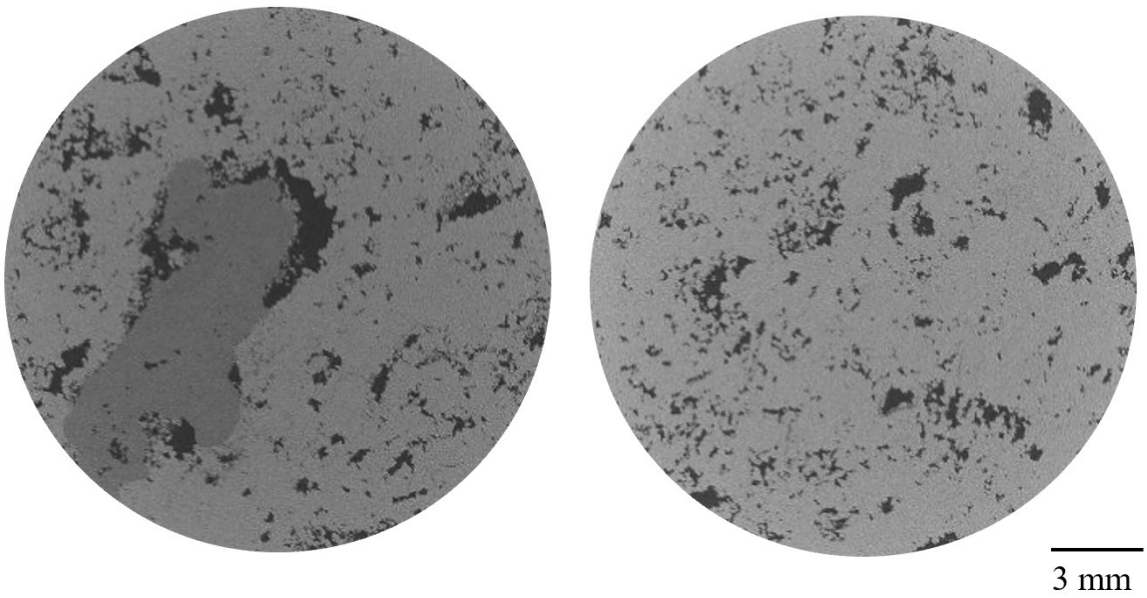


Figure 3.4 2D slice of 3D image of Silurian dolomite rock samples.

When it comes to uncertainties, a key limitation of the imaging analysis in Chapters 5 and 6 is that our interpretation is inherently constrained by voxel resolution: we can only segment and quantify pores and throats that are explicitly resolved in the scans. Sub-resolution porosity instead contributes indirectly through voxel-averaged greyscale values (partial-volume mixing), which is particularly relevant in carbonates with appreciable microporosity. In Chapter 5 (Indiana limestone), this is evident when comparing porosity inferred from medical-CT attenuation to porosity measured from the resolved micro-CT pore space, which implies that a non-trivial fraction of the total porosity resides in pores below the segmentation limit (Ketcham and Carlson, 2001; Flannery et al., 1987; Withers, 2007; Manoorkar et al., 2021). In Chapter 6 (Edwards Brown dolomite), pores and throats smaller than the voxel size (≈5.6 μm) are not represented in the segmented pore space, which can bias connectivity metrics and

capillary-threshold inferences because unresolved micro-throats may act as persistent connectors between larger pores (Carrillo et al., 2021).

A second, coupled uncertainty arises from phase segmentation. In both chapters, scans were co-registered to a reference state and intensity-normalised to reduce beam-hardening and scanner artefacts prior to segmentation (Raeini, Blunt and Bijeljic, 2017). Noise was reduced using a non-local means edge-preserving filter to improve phase boundary definition (Bhasuthkar et al., 2023), and a watershed-based segmentation approach was selected because simple global thresholding is often insufficient in heterogeneous, low-contrast datasets (Lindquist et al., 2000; Wildenschild and Sheppard, 2013; Andrew et al., 2014). Even with these controls, segmentation remains sensitive to greyscale overlap and histogram choices; published studies show that small misclassifications can produce substantial variation in physics-based outputs, including connectivity and inferred non-wetting saturation (Schluter et al., 2014; Garfi et al., 2020; Krygier et al., 2020), with resulting errors on the order of 10–20% in some cases and corresponding impacts on derived trapping and permeability metrics (Wang et al., 2021).

Chapter Four Heterogeneity Controls on Multiphase Flow Properties in a Reservoir Sandstone from CO_2 Storage Site

(Some of this material has been published in Darraj et al., 2025 (a)).

In this chapter, we address a fundamental question in reservoir characterisation for CO_2 storage: can core samples from the same stratigraphic interval with varying degrees of heterogeneity be treated as equivalent in reservoir simulation?

two steady-state experiments investigating the displacement behaviour, relative permeability and initial-residual trapped saturation for two sandstone samples.

Drainage and imbibition core flood experiments, with medical X-ray CT scanning, were performed to determine the effect of capillary heterogeneity at steady-state in two rock samples from a Dutch offshore CO_2 storage site.

The experiments were carried out on two heterogeneous sandstone samples (5 cm in length, 1 cm in diameter) to demonstrate that impact of heterogeneity on flow properties. The two samples were selected because, based on their bulk petrophysical properties and close stratigraphic spacing, they would typically be classified as a single rock type in reservoir-scale models. Differences in porosity and permeability of this magnitude are commonly treated as intra-facies variability, with identical relative permeability and capillary pressure functions assigned during model parameterisation.

The methodology used along with modifications to the experimental apparatus are outlined in Chapter 3. The sample show different displacement patterns, likely due to the different cementation patterns and heterogeneity in capillary pressure.

4.1 Introduction

As discussed in Chapter 2, among the mechanisms contributing to secure CO_2 storage, residual trapping has received significant attention and is routinely incorporated into reservoir-scale models (IPCC, 2005). In contrast, trapping and flow behaviour arising from spatial heterogeneity at scales below those typically resolved in continuum models remain less well constrained (Ni et al., 2025). Variations in pore structure, cementation, and permeability architecture can induce local capillary barriers and preferential flow paths, leading to nonuniform displacement and enhanced or diminished trapping depending on flow conditions. While such effects are conceptually recognised (Fadili and Ababou, 2004), their quantitative impact on multiphase flow parameters is difficult to isolate and parameterise, particularly because they emerge from interactions across multiple length scales (Jackson and Krevor 2020; Krevor et al., 2015). This gap contributes to uncertainty in upscaling laboratory measurements to reservoir-scale predictions. As seen from Trevisan, et al., 2017; Dai et al., 2016; Krevor et al., 2015; Ni et al., 2025; Spurin et al., 2025; Zhang et al., 2025, An et al., 2023; and Wenck et al., 2025) capillary heterogeneity has strong impact on trapping outcomes by reshaping the relationship between initial and post-imbibition gas saturation. Moreover, capillary barriers promote redistribution and barrier-controlled immobilisation during imbibition, leading to spatially variable immobilised saturations that cannot be inferred from homogeneous-core residual trapping alone. In this context, scatter in initial–residual (IR) trapping relationships, commonly ascribed to experimental uncertainty, may instead provide a diagnostic of the strength and spatial organisation of capillary heterogeneity and the resulting heterogeneity-driven immobilisation (Ni et. al, 2019; Ni et al., 2025). This behaviour is evident from its systematic departure above the trapping relationship observed in homogeneous sandstones.

Experimental investigations provide a direct means of probing the influence of rock heterogeneity on multiphase flow processes. In particular, core flooding experiments combined with X-ray computed tomography (CT) imaging allow spatially resolved measurements of fluid saturations during drainage and imbibition. These methods enable direct observation of displacement patterns, bypassed regions, and trapped phases that cannot be inferred reliably from bulk pressure and production data alone. Imaging-based experiments are especially valuable for assessing the role of capillary forces in heterogeneous rocks, where local variations can dominate flow behaviour even under nominally steady-state conditions (Perrin and Benson, 2010; Herring et al., 2013).

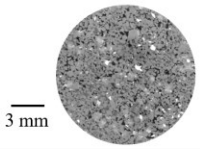
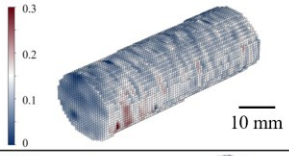
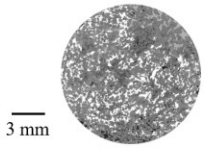
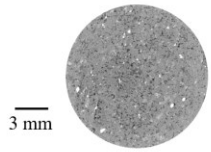
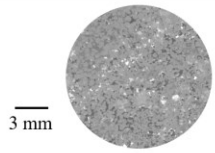
In this study, we examine how small-scale heterogeneity influences multiphase flow through steady-state flow experiments conducted on two sandstone samples obtained directly from an offshore CO_2 storage reservoir, extracted from depths separated by approximately 2 cm and exhibiting different degrees of cementation. The use of field-derived reservoir samples provides a realistic basis for assessing the practical significance of heterogeneity-driven effects. A micro X-ray CT scan is taken and the pore network is extracted from the scan to quantify spatial variations in capillary entry pressure, providing a link between pore-scale structure and continuum-scale flow behaviour. Subsequent multiphase nitrogen–brine experiments, imaged using medical X-ray CT during drainage and imbibition, are used to visualise saturation distributions and to evaluate displacement patterns and trapping behaviour in both samples.

4.2 Materials and Methods

4.2.1 Rocks

Four samples were received but only two samples were tested. Table 4.1 summarises the outcome of each experimental attempt and includes images of the corresponding samples.

Table 4.2.1 Photographs, 3D Medical CT porosity and 2D Micro CT dry image of the centre slice of all rock samples.

Sample	Outcome	Micro CT	Medical CT	Rock Sample
1	Successful			
2	Successful			
3	Unsuccessful (Low Permeability)			
4	Unsuccessful (sample broke)		--	

The two tested cylindrical sandstone samples measured approximately 1 cm in diameter and 5 cm in length. They were extracted from the same reservoir interval within a CO_2 storage site offshore the Netherlands. This reservoir can be described as a quartz-rich feldspathic sandstone with minor calcite/dolomite cement, minor amounts of swelling clay, with volumetric fractions of approximately 6- 8%, and patchy quartz overgrowths, deposited in a Triassic fluvial environment that facilitated high original porosity and only moderate cementation. This is consistent with the geological features observed in the CT images, with both samples exhibiting moderate cementation and Sample 2 containing naturally occurring barite (showing as very bright spots as seen in Table 4.1).

From the experimental procedure discussed in Chapter 3, Sample 1 had an average porosity of 19% and an absolute permeability of approximately 100 mD, while Sample 2 had an average porosity of 15% and a permeability of approximately 85 mD. Despite their close stratigraphic

proximity, medical CT-derived porosity shows clear differences in cementation distribution and heterogeneity patterns between the two samples (Figure 4.1).

The two samples were selected from closely spaced intervals within the same stratigraphic unit and do not cross a recognised non-conformity or major depositional boundary. Both samples correspond to the same depositional facies, characterised by fine-grained textures with laterally continuous bedding and no evidence of abrupt facies transitions at the sampling scale. Based on their bulk petrophysical properties and stratigraphic context, such samples would typically be grouped as a single rock type in reservoir-scale models. Differences in porosity and permeability of this magnitude are commonly treated as intra-facies variability, with identical relative permeability and capillary pressure functions assigned during model parameterisation (Aliakbardoust and Rahimpour-Bonab, 2013; Aslannezhad et al., 2024). However, the CT images reveal coherent heterogeneity patterns that are not captured by average petrophysical properties alone. For such barrier-type and layered heterogeneities, previous work has shown that even modest levels of heterogeneity can exceed the cut-off beyond which flow behaviour and continuum scale parameters are significantly affected, despite similar bulk porosity and permeability (Maas et al., 2019). This pairing therefore enables a controlled investigation of how small-scale heterogeneity influences continuum-scale multiphase flow and trapping behaviour.

It is important to point out that the heterogeneity observed in these samples is predominantly oriented perpendicular to the primary flow direction imposed during the core flooding experiments. While the experimental configuration represents horizontal displacement, the orientation of such heterogeneity relative to injection and migration pathways in the field is also relevant (Ide et al., 2007). In particular, heterogeneities of this type are expected to play a dominant role during the post-injection phase, when buoyancy-driven vertical migration and

subsequent imbibition of formation brine govern CO_2 redistribution and trapping (Hesse et al. 2008; Krishnamurthy et al., 2022). Under these conditions, capillary barriers-oriented transverse to vertical flow can strongly influence gas immobilisation and local accumulation (Pini and Benson, 2013; Krevor et al., 2012).

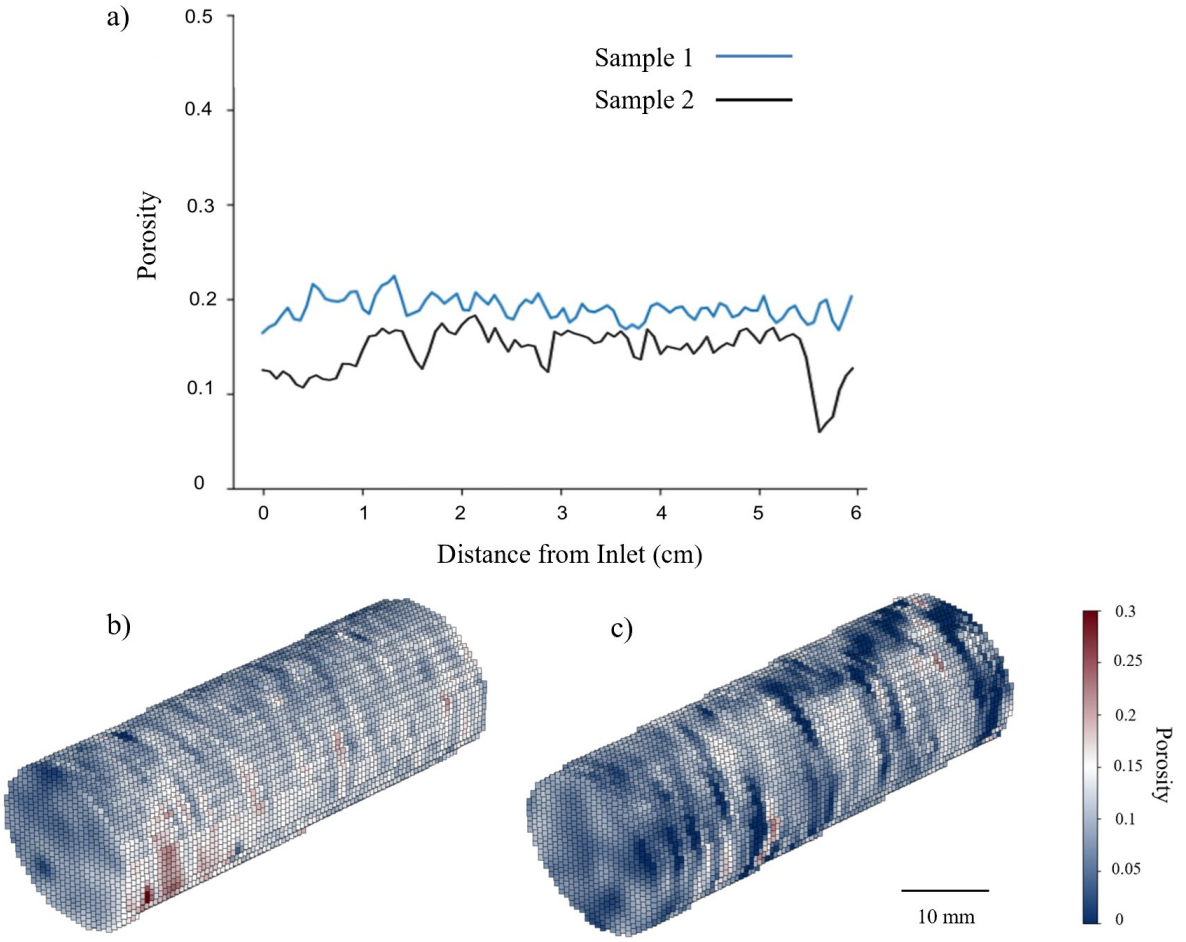


Figure 4.1 Porosity profiles along the length of the two sandstone samples used in this study, derived from medical X-ray CT imaging. (a) One-dimensional porosity profiles along the core length, obtained by averaging porosity over cross-sectional slices and plotted as a function of distance from the inlet. (b) Three-dimensional renderings illustrate the spatial distribution of porosity of Sample 1. (c) Three-dimensional renderings illustrate the spatial distribution of porosity of Sample 2.

4.2.2 Fluids, Interfacial Tension and Viscosity

Two immiscible fluid phases were used in this study, consisting of a gas–water system with nitrogen as the non-wetting phase and brine as the wetting phase. A standard brine was formulated to avoid clay swelling, using a salinity of 21 wt% NaCl (4.5 mol/kg). This

composition was maintained consistently across all experiments to ensure comparability of the measured flow behaviour.

Nitrogen was used as a proxy for CO_2 to investigate multiphase flow under immiscible conditions while avoiding complications arising from CO_2 dissolution, chemical reactivity, and pressure-dependent phase behaviour. Under the experimental pressure and temperature (6 MPa, 22 °C) conditions, nitrogen and CO_2 exhibit viscosities and densities of the same order of magnitude, such that the relative contributions of viscous and capillary forces governing displacement and trapping are comparable (Wildenschild et al., 2011; Reynolds et al, 2015). Consequently, the resulting saturation distributions and residual trapping behaviour are expected to be controlled primarily by pore structure and capillary heterogeneity rather than by fluid-specific mass transfer processes (Berg et al., 2013). Moreover, the substantially lower solubility of nitrogen in brine further minimises dissolution-driven alterations to saturation. The physical properties of the fluids used in this study, including viscosity and interfacial tension with water, are summarised in Table 4.2.

Table 4.2.2 The properties of the non-wetting and the wetting phases used in this work (NIST Chemistry Webbook, 2018).

Fluid	Viscosity, μ (Pa.s)	Interfacial tension with water, σ (N/m)
Nitrogen	1.9×10^{-5}	64×10^{-3}
Brine	1.44×10^{-5}	-

Table 4.3 summarises the physical properties of the core samples, including dimensions, average porosity, absolute permeability, and fractional flows used. The full experimental methodology is described in Chapter 3.

Table 4.2.3 Properties of the rock samples used in the study and associated experimental conditions.

	Sample 1	Sample 2
Diameter, D (m)	0.01	0.01
Length, L (m)	0.05	0.05
Porosity, ϕ	0.19	0.15
Permeability, K (mD)	100	85
Pressure, P (MPa)	6	6
Temperature, T (°C)	21	21
Flow rate, Q (mL/min)	0.1	0.1
Pore-scale capillary number, $C_a = \frac{\nu\mu}{\gamma}$	10^{-6}	10^{-6}
Fractional flows (for drainage and imbibition), f_w	0.9, 0.5, 0.3, 0.1, 0	0.9, 0.75, 0.5, 0.3, 0.1, 0

4.2.3 Pore Network Modelling

As discussed in Chapter 3, to quantify pore-scale capillary structure and assess internal heterogeneity, a pore network model was extracted from the micro-CT segmented dry-scan images using the open-source algorithm PoreXtractor (Dong and Blunt, 2009; Raeini et al., 2017; Foroughi et al., 2020). Based on the extracted throat radii, capillary entry pressures were estimated across the sample using the Young–Laplace equation (Equation 2.5), assuming a constant interfacial tension and perfect wetting conditions. These spatially distributed entry pressures were used to evaluate variations in capillary structure along the sample length and to identify zones of heterogeneity that may influence fluid displacement behaviour.

4.3 Results and Discussion

4.3.1 Saturation along the samples after drainage and imbibition

One-dimensional CT-derived saturation profiles (axial saturation versus length) provide a compact diagnostic of heterogeneity by revealing spatial variations in saturation along the core. During drainage they primarily reflect invasion and sweep, highlighting barriers and preferential pathways, whereas during imbibition they capture remobilisation, redistribution and immobilisation, and therefore constrain how heterogeneity controls trapping and post-injection saturation evolution. Core heterogeneity causes strong saturation gradients along the length (Rücker et al., 2021). Midtlyng and Stensen (2000) found that a layered sandstone yielded nearly uniform saturation under steady flow, but a very steep gradient at the outlet after waterflooding. Likewise, Kong et al. (2014) reported that in a CO_2–brine flood even small porosity/permeability variations produced large axial CO_2-saturation differences.

Figure 4.2 shows the one-dimensional saturation profiles measured by X-ray CT during drainage and imbibition for Sample 1. During drainage (Figure 4.2a), gas saturation increases gradually across the sample as the gas fractional flow is raised, with no sharp transitions or localised features that would indicate restricted displacement. The profiles display a smooth saturation gradient from inlet to outlet, consistent with a relatively homogeneous pore structure and a lack of strong capillary barriers at the core scale. These one-dimensional CT profiles therefore provide a direct view of the displacement behaviour, highlighting capillary-dominated flow and making the effects of heterogeneity and imposed fractional flow conditions readily observable.

During imbibition (Figure 4.2b), water successfully displaces the gas phase across the core, with decreasing gas saturation observed as fractional flow of water increases. The profiles are

consistent with capillary-controlled displacement, and residual gas is largely retained in a uniform pattern. However, a noticeable reduction in gas saturation at the inlet region is observed across all imbibition steps. This trend is consistent with previous reports by Gao et al. (2021), Gao et al. (2023), and Spurin et al. (2025) and likely reflects a local inlet effect arising from gas–brine mass transfer and/or heterogeneity-driven saturation redistribution. In our experiments, the injected brine was not pre-equilibrated with nitrogen. Under these conditions, injection of large brine volumes (approximately 20 pore volumes per step) can maintain a concentration gradient and promote local dissolution near the inlet, particularly where residence time and interfacial area are elevated. At the same time, small-scale heterogeneity can promote local capillary-driven redistribution during imbibition, which may further suppress inlet saturations relative to the core average. Importantly, prior work indicates that inlet-associated saturation reductions can persist even when the gas–brine system is pre-equilibrated, implying that this behaviour is not solely an artefact of using under-saturated brine but can be an inherent feature of gas–brine imbibition under these conditions (Gao et al., 2021; Gao et al., 2023). We therefore treat the inlet-region reduction as potentially influenced by combined dissolution and heterogeneity-driven redistribution, and exclude the affected region from trapping interpretations where appropriate. At the experimental conditions, the equilibrium solubility of N_2 in brine corresponds to approximately 9.3×10^{-6} mol (≈ 0.26 mg) dissolved within the pore volume of the core. Another potential explanation is the one introduced by Clennell et al. (2020), who attribute early inlet-region gas saturation reduction to an inlet-controlled spontaneous imbibition effect, where capillary pressure drives local brine invasion that suppresses gas saturation ahead of the core-average imbibition front rather than via bulk dissolution. This hypothesis can be tested directly within the numerical framework by running transient two-phase simulations and tracking the evolution of saturation profiles at fixed boundary conditions, thereby assessing whether capillary-pressure-driven spontaneous

imbibition at the inlet, relative to viscous retardation governed by relative permeability, reproduces the observed time-dependent inlet depletion.

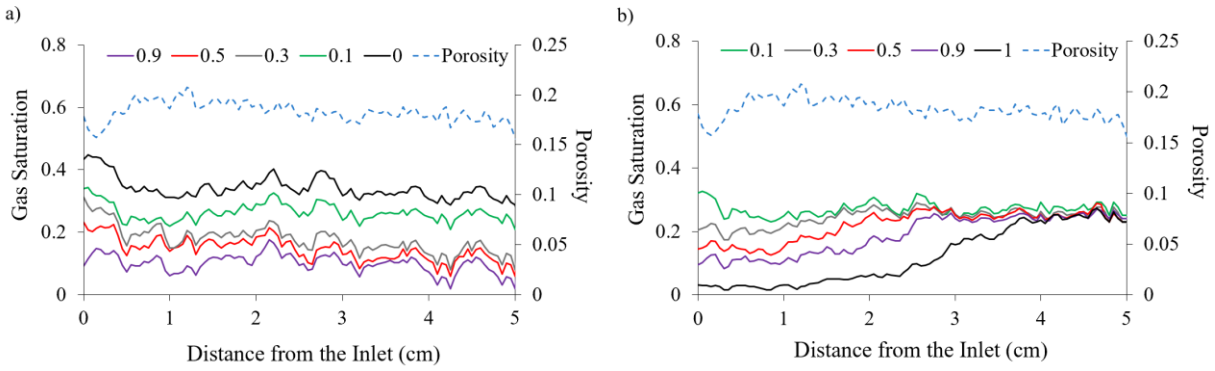


Figure 4.2 1D slice average saturation along Sample 1 after drainage (a) and imbibition (b) for all fractional flows.

The reduction in gas saturation from the end of drainage to the first imbibition step suggests that the gas phase remained well connected and therefore readily displaced at the onset of brine injection. At higher brine fractional flows in imbibition, changes become confined mainly to the inlet half of the core, whereas the downstream region shows little further response. This indicates that the remaining gas had largely reached a residual, disconnected configuration, so increasing brine fractional flow produced only limited additional displacement. The stronger inlet response is consistent with local capillary-driven imbibition and possible dissolution effects near the inlet, while the stable downstream profile reflects the establishment of residual trapping rather than capillary end effects.

The final water saturation achieved in these experiments ($S_{N_2} \approx 0.35$) is substantially higher than would be expected at connate water saturation. In clean sandstones, connate water saturation is typically $S_{wc} \lesssim 0.1$(Buckles, 1965; Viksund et al., 1998; Abba et al., 2018), corresponding to gas saturations $S_{N_2} \gtrsim 0.9$. Reaching such low water saturations cannot generally be expected in core flooding experiments involving gas–brine systems, owing to the unfavorable mobility ratio (Krevor et al., 2012), and the associated displacement limitations as

described by Buckley–Leverett theory (Berg and Ott, 2012; Owusu et al., 2014). As a result, the accessible saturation range in these experiments is constrained well before connate water conditions are approached (Bull et al., 2011; Levine et al., 2011).

In contrast, porous-plate experiments (Avraam , 1995) allow capillary pressure to be controlled more directly and over a much wider range, enabling approach to true connate water saturation under near-equilibrium conditions. The saturation ultimately attained in the field, however, depends on scale and flow regime. While viscous forces increase with length scale, the fundamental constraint imposed by unfavourable mobility remains. Simple Buckley–Leverett estimates therefore provide a useful framework for assessing how closely the experimental saturation range approaches field-relevant conditions and for placing laboratory observations in the context of expected subsurface behaviour.

Figure 4.3 shows the saturation profiles for Sample 2 during the experiment. During drainage (Figure 4.3a), while gas saturation increases with fractional flow as expected, a marked heterogeneity in response is evident. In particular, saturation changes occur primarily in the upstream half of the core. The downstream half of the core shows little change in gas saturation across all drainage steps, indicating limited penetration of the non-wetting phase. Near the outlet, there is an abrupt increase in the gas saturation, this is consistent with a sharp drop in porosity and the presence of a highly cemented zone. This creates a buildup of gas just upstream of this region. These observations suggest the presence of a localised heterogeneity or capillary barrier near the centre of the sample that limits further gas invasion. This interpretation is examined in more detail using micro-CT images, which are presented in a later section of this chapter. The cemented region near the outlet appears to enhance local pore occupancy behind the barrier and may contribute to greater gas trapping.

In Sample 2, the downstream half of the core maintains a relatively stable gas saturation level across all drainage stages, indicating limited invasion by the non-wetting phase. Towards the end of the core there is a region that is largely cemented (a sudden drop in the porosity profile towards the end), hence we see a large increase the non-wetting phase saturation due to the build of the gas behind this cemented region. This strongly suggests the presence of a heterogeneity or capillary barrier in the midsection of the sample, impeding gas penetration beyond this region while the cementation towards the outlet of the core helps to access the pore space just behind this region and potentially increase the amount of trapped gas.

During imbibition (Figure 4.3b), the residual gas saturation remains highest in the downstream region of the core, which aligns with the region previously unaffected during drainage. This suggests that gas retained behind the capillary barrier remains largely inaccessible to imbibing water. The persistence of saturation in the same region across both drainage and imbibition indicates ineffective sweep in this region due to the heterogeneity.

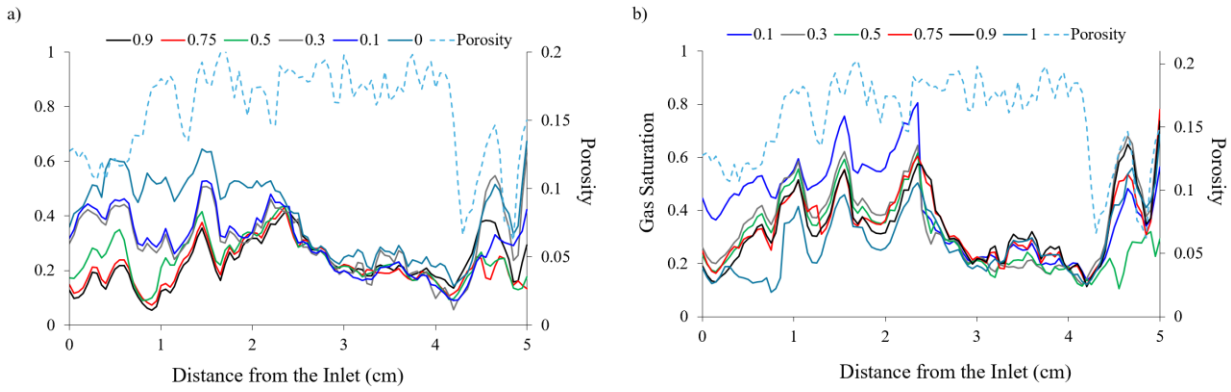


Figure 4.3 1D slice average saturation along Sample 2 after drainage (a), and imbibition (b) for all fractional flows.

The differences in saturation evolution between Samples 1 and 2 illustrate the critical role of small-scale heterogeneity in governing multiphase flow behaviour. This is highlighted in the 3D saturation maps obtained from medical CT imaging (Figures 4.4 and 4.5). These contrasting behaviours are important for understanding CO_2 invasion and trapping in heterogeneous

formations. Sample 1, with its more uniform displacement front, mimics a favourable condition for efficient CO_2 storage, where capillary forces allow for deep invasion and uniform sweep. Sample 2, by contrast, demonstrates how capillary barriers—arising from local mineralogical or structural contrasts—can restrict CO_2 movement, confining it to smaller portions of the rock volume and leading to irregular saturation profiles. Such behaviour, if unaccounted for, could result in underutilisation of storage capacity or misrepresentation of residual trapping efficiency in larger-scale simulations.

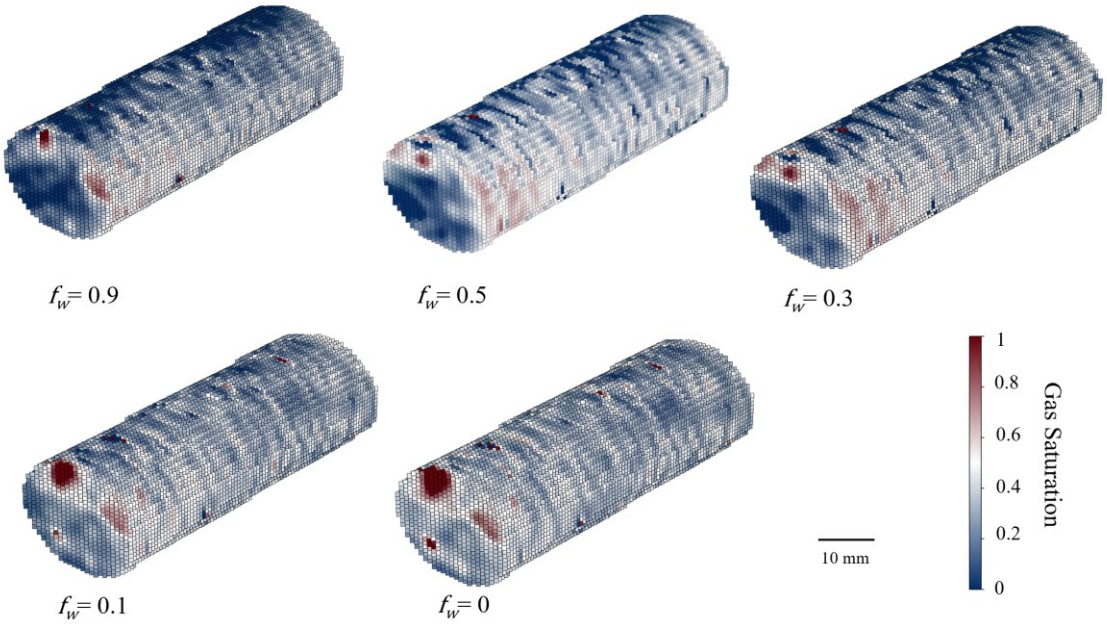


Figure 4.4 3D saturation profile of Sample 1 for all drainage fractional flow steps.

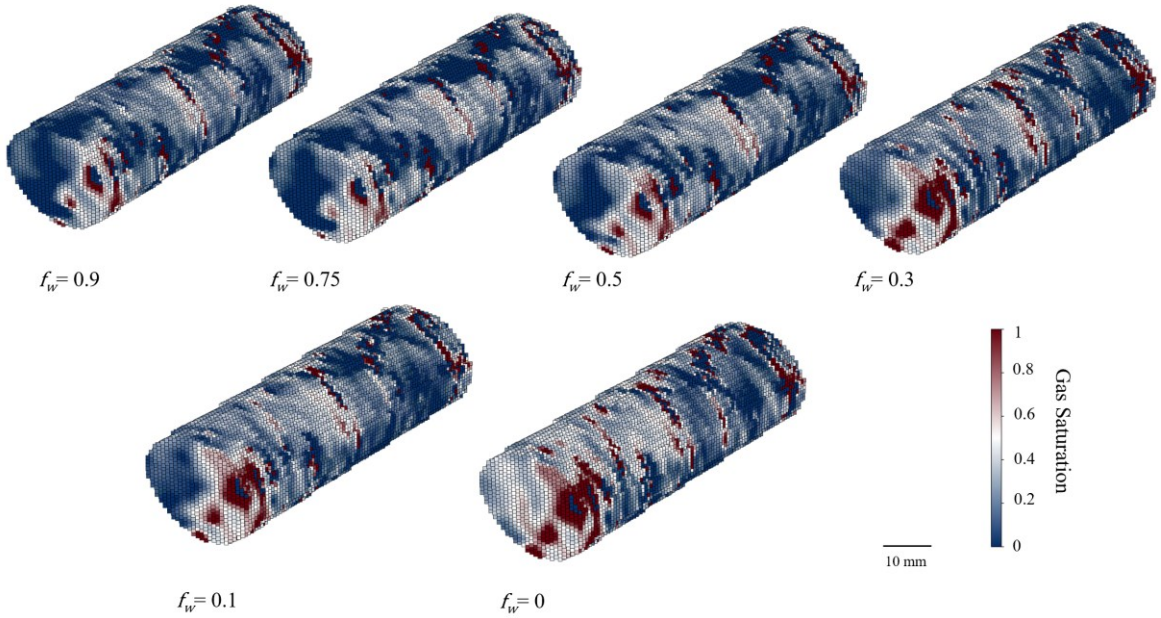


Figure 4.5 3D saturation profile of Sample 2 for all drainage fractional flow steps.

4.3.2 Pore network modelling and local heterogeneity

The pore networks for Samples 1 and 2 were extracted directly from the dry-scan 3D micro-CT image (Figure 4.6) (voxel size ≈6 µm). From the resulting throat size distributions and using the Young–Laplace equation (Equation 2.5), capillary entry pressures were calculated separately for the first and second halves of each sample, providing spatial estimates of the pressure required for non-wetting phase invasion (limited by the image resolution). This analysis helps identify variations in displacement behaviour between the two samples.

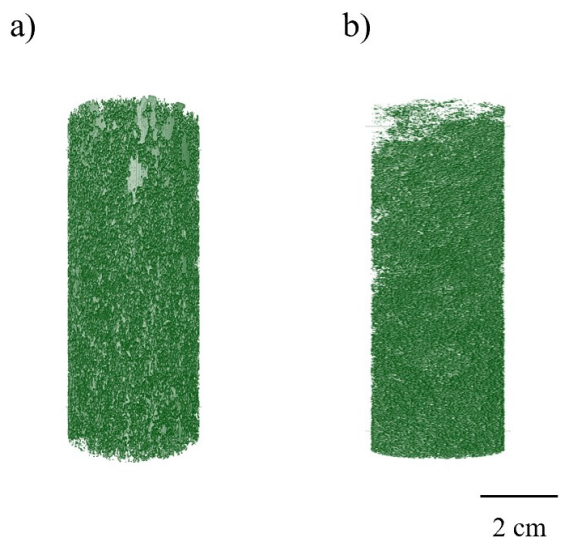


Figure 4.6 3D rendering of the micro-CT porosity for a) Sample 1,and b) Sample 2.

For Sample 1, the capillary pressures from the two halves closely match, showing that the change in entry pressure is negligible. The wetting phase fills the smaller pores, while the non-wetting phase moves through the larger ones following the percolation theory. Because the throat sizes are fairly uniform, this results in a single, clear capillary pressure–saturation relationship (Figure 4.7a).

Sample 2's predictions from network modelling shows two distinct capillary pressures (Figure 4.7b), indicating heterogeneity in its pore structure. One curve reaches lower pore saturation than the other, consistent with two pore populations. Together with the evidence from the saturation profiles, we infer that Sample 2 is comprised of two regions with two different throat sizes and capillary pressure. During drainage, gas preferentially invades the more accessible pores first (given by the lower capillary pressure), but only at higher pressure does it intrude less accessible ones. As the pressure of the non-wetting phase increases with higher fractional flow rates, gas begins to occupy more of the upstream pore space. However, it does not reach a high enough pressure to invade further into the downstream region, where pores have higher entry pressures due to reduced throat size and stronger capillary forces. This indicates that the

downstream pores remain largely inaccessible under the applied conditions, limiting gas advance and contributing to uneven saturation distribution.

In the pore network model, invasion proceeds until the applied capillary pressure equals the entry pressure of the smallest pores that are explicitly resolved in the micro-CT image, beyond which further invasion cannot be constrained by the image data and unresolved pores remain water-filled (Blunt et al., 2002). The effective resolution limit of the micro-CT scan (≈ 6 μm voxel size) therefore imposes an upper bound on the capillary pressures that can be directly assessed. Using the Young–Laplace relation, this resolution corresponds to a maximum resolvable capillary entry pressure on the order of 0.05–0.1 MPa for the fluid system considered.

Although the pore network model can formally extrapolate invasion to higher capillary pressures, such extrapolation reflects assumed pore-size distributions below the imaging resolution rather than directly observed pore geometry. As a result, capillary pressures exceeding this resolution-limited cutoff cannot be interpreted quantitatively, and pores requiring higher entry pressures are effectively treated as permanently water-filled within the resolved network. This limitation should be considered when interpreting the upper range of

capillary pressures and associated saturation behaviour derived from the micro-CT–based pore network model.

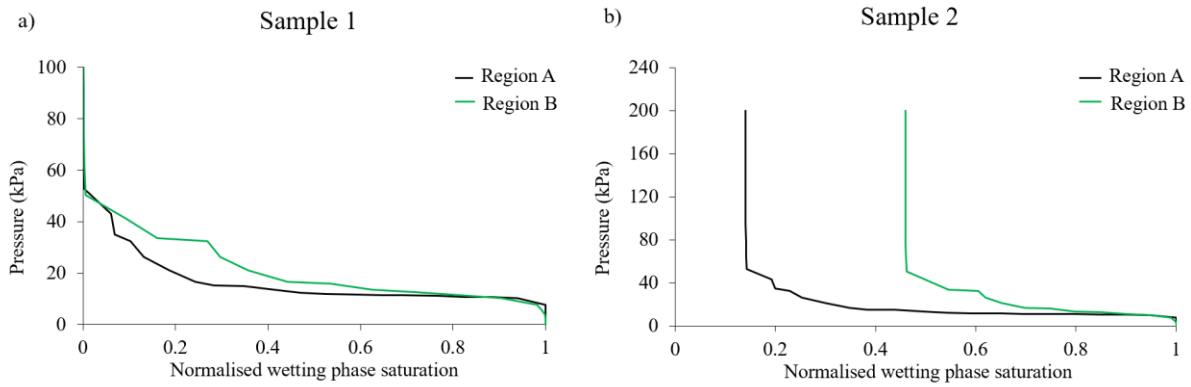


Figure 4.7 Capillary pressure as a function of saturation in (a) Sample 1 and (b) Sample 2, derived from pore network modelling. In each panel, region A corresponds to the upstream half of the core and region B to the downstream half.

As mentioned before, any pore smaller than the roughly 6 µm voxel dimension will not be resolved. Thus, pores smaller than this voxel size would require higher capillary pressure to drain; since they are below the CT voxel size they are simply omitted from the network. In practice this "capillary cutoff" means that the curve abruptly ends at the minimum resolvable pore size, and any experimental capillary pressure above that cutoff is due to sub-resolution porosity. For example, published data for similar sandstones show mercury intrusion up to MPa pressures (submicron pores) that are not seen in the CT-derived network (Tanino and Blunt, 2012; Carrillo et al., 2022).

In summary, the network model findings mirror the core flood observations. Sample 1's saturation was homogeneous across the rock sample consistent with one capillary pressure curve. While Sample 2 exhibited two distinct capillary pressures, corresponding to different displacement events, hence, more heterogenous saturation.

4.3.3 Trapping efficiency

To obtain the trapping efficiency, slice-averaged initial gas saturation plotted against residual gas saturation, calculated averaged for each slice of the image along the length of the sample from X-ray CT–derived saturation profiles (Land, 1968; Suekane et al., 2013; Dance et al., 2016; Mohanty 1987; Stegemeier 1977; Lake 1989). For sample 1, all points fall below the 1:1 line (residual < initial). This behaviour reflects classic pore-scale snap-off trapping: as brine invades, narrow throats pinch off the gas bubbles and leave smaller residual ganglia, (Figure 4.8a) shows the trapping efficiency of the sample alongside homogeneous Bentheimer sandstone, providing a reference for assessing deviations from homogeneous behaviour. The circled cluster of data points at very low saturations represents an anomalous response that may arise from several factors that are discussed earlier. It is important to note that, to accurately quantify the trapping efficiency, regions affected by dissolution/other factors must be excluded from the analysis, as the trapping in these regions is a result of another trapping mechanism and not related to capillary trapping.

Figure 4.8b highlights one of the most consequential outcomes of this study: capillary heterogeneity can yield markedly higher immobilised gas saturations than would be inferred from a classical pore-scale trapping relationship (Krevor et al., 2011; Ni et al., 2019; Kim et al., 2021), with local differences on the order of tens of percent and, in some regions, approaching a factor of two relative to the homogeneous reference behaviour. This result raises an important terminology point. Under the classical special core analysis (SCAL) definition, residual non-wetting saturation is the saturation remaining immobile after imbibition within a locally swept pore network, and by this definition saturations that plot above a Land-type trapping curve are not interpreted as residual trapping. A conventional counterargument is that such ‘above-residual’ saturations can arise from boundary-condition artefacts (for example,

capillary end effects near a core outlet) and therefore do not extrapolate to the field. Here, however, the effect is not associated with the external outlet boundary but with internally generated capillary barriers and connected heterogeneity within the core. These barriers create internal capillary discontinuities that promote redistribution and accumulation of gas during imbibition, producing persistent immobilised saturations that are controlled by the same capillary entry-pressure contrasts that govern reservoir-scale migration and post-injection imbibition (Saadatpoor et al., 2010). We therefore interpret the points above the 1:1 line in Fig. 10b as evidence of heterogeneity-driven, barrier-controlled immobilisation that is distinct from classical pore-scale residual trapping, yet relevant to reservoir-scale trapping because it arises from internal capillary architecture rather than laboratory boundary conditions.

The contrast between the two samples has important implications for CO_2 storage. Sample 1 yielded predictable residual trapping but relatively limited immobilisation while sample 2, by comparison, can immobilise substantially more CO_2. Capillary heterogeneity trapping can pin extra gas beyond the normal residual amount an also complicate sweep efficiency and plume spread (Krevor et al., 2011; Li and Benson, 2015). In practice, this means that samples like Sample 2 – with small-scale heterogeneities– can store additional CO_2 (some voxels end up with higher saturation than they began with) because displaced CO_2 is captured by capillary barriers. Such findings underline that reservoir heterogeneity tends to boost capillary trapping and long-term storage security. However, they also warn that simulations must account for these dynamic phase redistributions (and exclude artifacts) to accurately predict CO_2 fate in storage reservoirs.

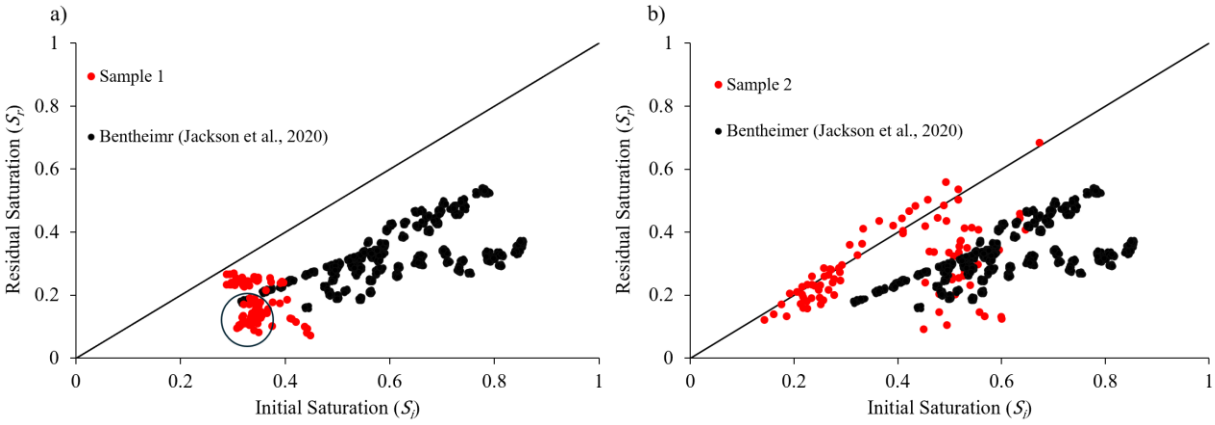


Figure 4.8 Slice average initial saturation versus residual saturation along the samples' length (red) in comparison with homogenous Bentheimer sandstone (black). a) Sample 1. b) Sample 2. For Sample 2, some points lie above the production line because they represent slice-averaged values.

4.3.4 Relative permeability

In a uniform-pore medium, the relative permeabilities for drainage and imbibition tend to be smooth and similar to each other, apart from the effect of capillary trapping. As water saturation increases, the water-phase permeability rises and the non-wetting phase permeability falls. Hysteresis between drainage (decreasing S_w) and imbibition (increasing S_w) is primarily due to wettability and trapping effects, but in a homogeneous pore network these effects are modest.

In this study, relative permeability functions for both samples (Figure 10), derived from pressure measurements obtained during the experiment (Equation 2.3) and saturation distributions quantified from images, lower gas mobility across the saturation range, with the effect being most pronounced during imbibition. This brings our attention to a key limitation in the interpretation of the measured relative permeabilities is the restricted range of mobile saturations accessible in gas–brine core flooding experiments, which arises from the large viscosity contrast between the two phases. For such unfavourable mobility ratios, displacement is inherently limited by the development of sharp saturation fronts, as described by Buckley–Leverett theory. Consequently, only a subset of the full saturation range can be sampled experimentally under steady-flow conditions, even when multiple pore volumes are injected.

For Sample 1 (panel a), the relative permeability to the gas phase remains low even at low brine saturations, suggesting significant connectivity loss of the gas phase upon brine reintroduction. During drainage, the permeability increases only modestly as the brine saturation drops, indicating that gas flow remains limited even during primary invasion, likely due to the dominance of smaller pore throats or poor connectivity within the gas-filled pathways.

In Sample 2 (panel b), a similar suppression of gas relative permeability is observed, although both drainage and imbibition curves exhibit a slightly broader spread. The highest gas permeability remains below 0.25, suggesting that heterogeneities within the pore structure impede gas-phase connectivity. Notably, the difference between the drainage and imbibition results is narrower in Sample 2, implying less pronounced hysteresis compared to Sample 1. This behaviour is consistent with the increased heterogeneity and potential capillary barriers observed in previous saturation profile and capillary pressure analyses.

Overall, these low relative permeability values for both samples reinforce the significance of pore-scale trapping and poor gas-phase connectivity, particularly under imbibition. These observations are in agreement with findings from pore-scale modelling and imaging studies that highlight the impact of wettability, pore throat constrictions, and rock heterogeneity on phase mobility (Nasir et al., 2025).

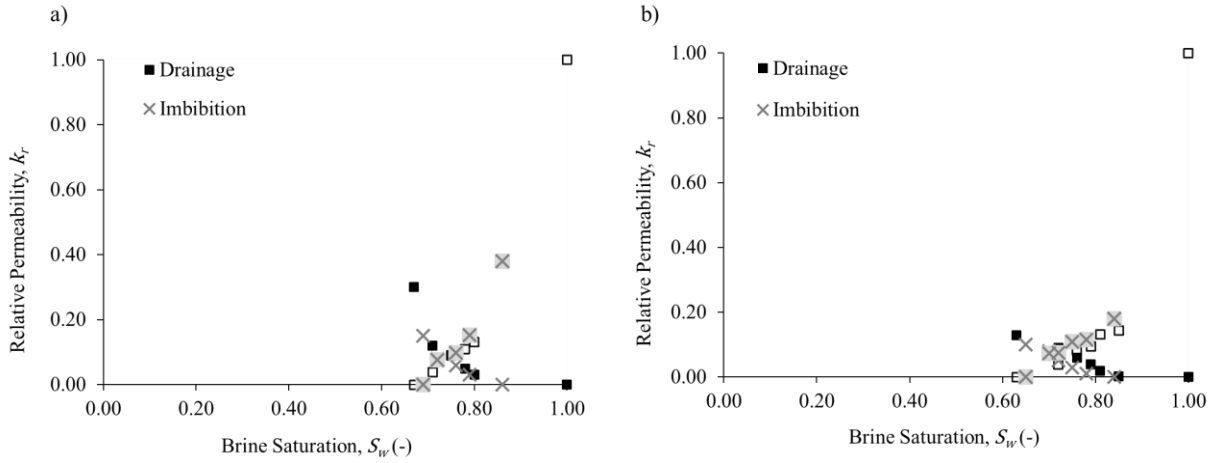


Figure 4.9 Relative permeabilities showing drainage and imbibition cycles for wetting and non-wetting phases a) Sample 1, b) Sample 2.

4.4 Conclusions

Significant effort is routinely invested in characterising multiphase flow properties for geological CO_2 storage, with the implicit assumption that core-scale measurements obtained from a limited number of samples are representative of larger reservoir intervals. This study suggests that these assumptions may not be valid in the presence of small-scale heterogeneity. Two sandstone samples extracted from the same reservoir interval and separated by approximately 2 cm exhibit markedly different saturation evolution and trapping behaviour under otherwise identical experimental conditions. Despite belonging to the same depositional facies and exhibiting similar bulk porosity and permeability, the samples display contrasting responses during both drainage and imbibition, indicating that equivalence in multiphase flow behaviour cannot be assumed even within a single facies.

In conventional reservoir simulation workflows, samples such as those studied here would typically be grouped into a single rock type and assigned identical saturation functions and trapping relationships. Our results indicate that this practice can lead to substantial misrepresentation of capillary CO_2 trapping at cm scale, which at larger scales may lead to inaccurate CO_2 plume evolution predictions. The more homogeneous sample exhibits uniform

saturation profiles and classical residual trapping behaviour, whereas the more heterogeneous sample develops strong saturation gradients, incomplete non-wetting phase invasion, and enhanced trapping associated with capillary barriers. These differences arise directly from small-scale heterogeneity that is not captured by average petrophysical properties.

The trapping analysis further demonstrates that capillary heterogeneity can fundamentally alter the relationship between initial and residual gas saturation. In the heterogeneous sample, local increases in gas saturation during imbibition occur as displaced gas accumulates behind capillary barriers, resulting in residual saturations exceeding initial values in parts of the core. This behaviour is absent in the more homogeneous sample and cannot be predicted using conventional trapping models that assume uniform displacement and pore-scale snap-off alone. Failure to account for this behaviour would lead to incorrect estimates of immobilised CO_2 and misleading assessments of storage security.

Overall, these findings highlight that small-scale heterogeneity, even over centimetre-scale vertical separations, introduces significant uncertainty in saturation distributions and residual trapping behaviour. When such variability is treated as intra-facies noise and homogenised in reservoir models, it can propagate into uncertainty in predictions of plume migration, sweep efficiency, and storage capacity at the field scale. This underscores the need to account for heterogeneity-driven capillary effects when upscaling laboratory measurements, not as deterministic controls, but as sources of uncertainty that should be represented in field-scale simulations.

We will now develop this study by performing an integrated imaging, flow and analysis of the multiphase properties of a heterogeneous carbonate sample in the subsequent chapter. Specifically, we study a sample with a wide range of pore size and investigate the effect of flow rate.

Chapter Five Millimetre-Scale Heterogeneity in Carbonates: Indiana Limestone

(This material has been published in Darraj et al., (2026))

Building on Chapter 4's demonstration that centimetre-scale heterogeneity in theoretically less complex sandstone produces non-representative flow behaviour within a single reservoir interval, this chapter systematically isolates how heterogeneity on mm-scale in more complex carbonate rock manifest with changes with flow rate.

We focus on how spatial variability in porosity and entry pressure, resolved at the millimetre scale, affects saturation distribution, phase connectivity, and relative permeability under capillary-dominated flow conditions. Steady-state nitrogen–brine experiments combined with micro-CT imaging are used to examine how heterogeneity is expressed across the sample and how this expression changes with flow rate. The chapter explores the extent to which viscous forces can partially overcome capillary barriers, and how this transition influences the interpretation of laboratory-derived flow properties in heterogeneous carbonate rocks.

5.1 Introduction

Among the potential geological storage formations for CO_2, carbonate rocks represent particularly promising candidates due to their widespread global distribution and storage capacity. Sedimentary basins composed of carbonate rocks offer potential for thousands of gigatonnes of carbon dioxide storage (Tang et al., 2024; Bradshaw et al., 2012). However, storage is complicated by their intrinsic heterogeneity, which spans a range of spatial scales. This complexity directly influence capillary pressure, permeability, and CO_2 migration and trapping (Manoorkar et al., 2021; Bradshaw et al., 2012). Moreover, their heterogeneity makes it difficult to characterise multiphase flow properties leading to challenges in upscaling and

prediction, as discussed in Chapter 2 (Manoorkar et al., 2021; Benson & Cole, 2008; Fischer et al., 2010; Krevor et al., 2012).

As discussed in Chater 2 and demonstrated in Chapter 4, local heterogeneity affects relative permeability and trapping. This effect is particularly relevant in carbonate formations and other complex lithologies, where capillary heterogeneity can substantially alter storage behaviour in comparison with more homogeneous systems. Experimental and numerical investigations further suggest that these effects are inadequately captured by conventional upscaled models, thereby emphasising the need for refined approaches that incorporate the capillary number dependence of relative permeability and capillary pressure functions (Fadili et al., 2004; Nordbotten & Celia, 2006; Shao et al., 2022; Shao et al., 2023).

In this study, we address these uncertainties by conducting steady-state core flooding experiments on Indiana limestone, a model carbonate with pronounced millimetre-scale heterogeneity. Using micro-CT imaging, we directly observe how variations in flow rate and capillary number affect fluid saturation, distribution, and trapping at the pore-scale and how it compares to core-scale experiments from previous studies. Our results provide insights into the mechanisms by which capillary heterogeneity governs CO_2 saturation and distribution. This can inform the development of improved models for heterogeneous reservoirs.

5.2 Methods and Materials

The apparatus and detailed description of the experimental apparatus and protocol were provided in Chapter 3. Here we briefly review the experiments and provide additional details where they were not previously covered. We conducted steady-state drainage and imbibition experiments at different flow rates to observe how flow rate influences the non-wetting phase saturation and distribution. Through micro-CT imaging, image segmentation and pore network

analysis, we captured detailed fluid configurations, quantified changes in pore occupancy, and evaluated the impact of heterogeneity on relative permeability and trapping.

5.2.1 Rock and Fluids

A cylindrical Indiana limestone sample, 12 mm in diameter and 45 mm in length, was used in this experiment. Indiana limestone is a calcite-cemented grainstone, primarily composed of calcite (~97.07%) with minor amounts of magnesium carbonate (~1.2%) (El-Maghraby & Blunt, 2012; Alanazi et al., 2023). The rock fabric is highly heterogeneous, featuring fossil fragments and oolites, and exhibits heterogeneity on the millimetre scale (Manoorkar et al., 2021). Its pores range from intergranular macropores to intragranular micropores , but heterogeneity above the sub-centimetre scale is minimal (Alanazi et al., 2023). This makes Indiana limestone an ideal benchmark carbonate as it captures the key capillary contrasts of stratified media while remaining amenable to pore-scale imaging and modelling (Freire-Gormaly et al., 2016; Alanazi et al., 2023).

To illustrate the complexity, and broad pore and throat size distribution of Indiana limestone, Figure 5.1 presents a micro-CT (4.9 μm) voxel size of the rock alongside the measured mercury intrusion capillary pressure (MICP) . The micro-CT image highlights the millimetre-scale heterogeneity and varation in resolved pore sizes (>5 μm), while the MICP results demonstrate a range of entry pressures across the sample, reflecting heterogeneity in throat sizes. Together, these observations support the argument that Indiana limestone possesses multiscale structural heterogeneity.

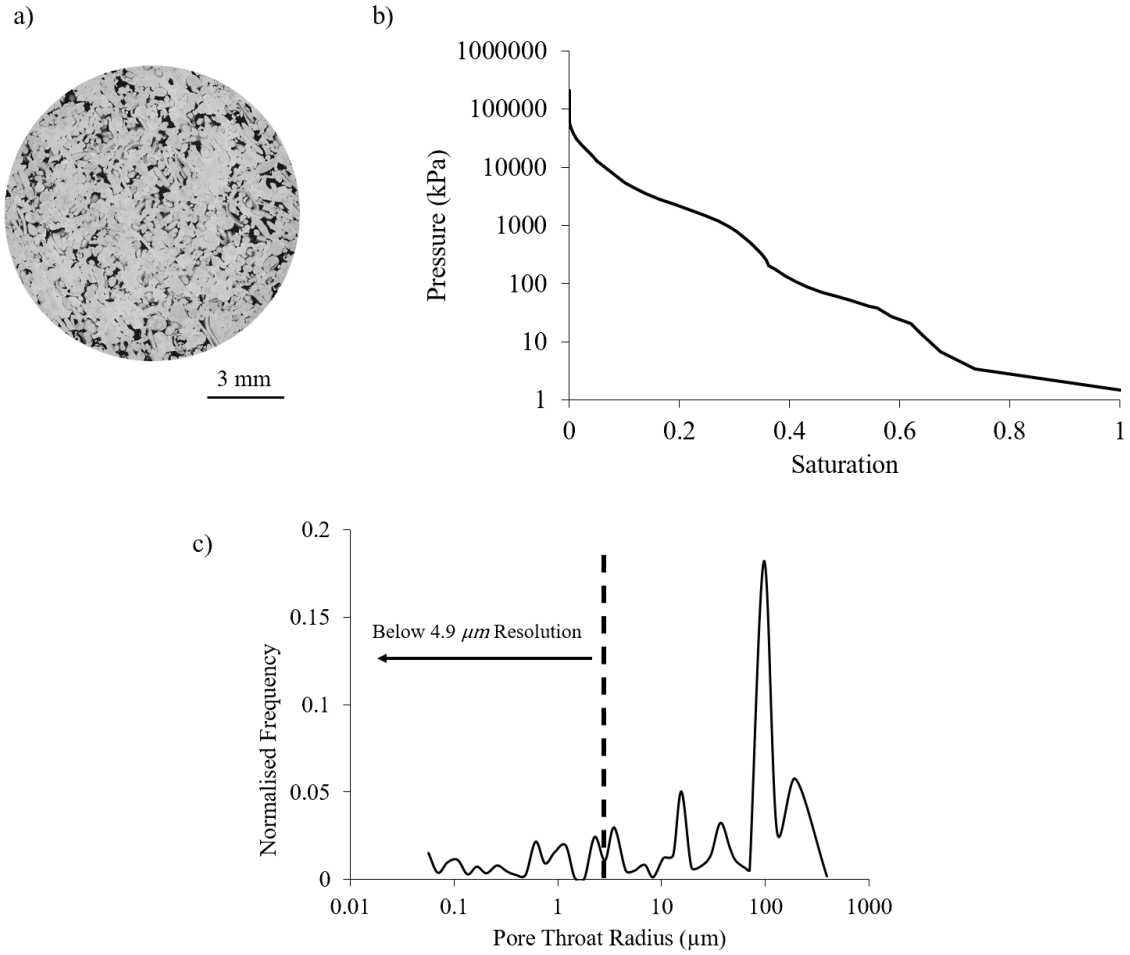


Figure 5.1 (a) Two-dimensional cross- section (xy direction) of three-dimensional micro-CT image: grey is grain, black is pores. (b) MICP-derived capillary pressure indicating multiple entry pressures throughout the sample. (c) Mercury intrusion capillary pressure data that has been converted to show the distribution of pore-throat radius, normalized such that the maximum value is 1. Throats of radius below the voxel size of the image (4.9 μm) cannot be resolved.

After drilling, the sample was dried in a vacuum oven at 80°C for 72 hours to remove residual moisture. The fluids used were nitrogen gas, as an analogue to CO_2, as previously justified in Chapter 4, and a brine solution. The brine was composed of deionized water doped with 30 wt.% potassium iodide (KI), corresponding to a concentration of 2.85 mol/kg, to enhance X-ray contrast during imaging. The brine viscosity was 0.822 mPa.s (Gao et al., 2017). At the experimental conditions of 6 MPa pressure and 21–22°C temperature, nitrogen is in a supercritical-like state. The interfacial tension between nitrogen and brine was measured at

69.3 mN/m (NIST Chemistry Webbook, 2018). The absolute permeability of the sample was measured at 60 ± 2 mD.

5.2.2 Experimental Methodology

Imaging was performed using a Thermo Fisher Heliscan micro-CT X-ray scanner. Scans were acquired at a voltage of 95 keV, a tube current of 65 mA, and an exposure time of 1.2 seconds over 3,240 projections, resulting in a voxel size of 4.9 µm. Fluid injection was conducted using a high-pressure, ambient-temperature closed-loop apparatus (as shown in chapter 3). Steady-state nitrogen–brine drainage and imbibition experiments were carried out at two total flow rates: 0.1 ml/min and 0.2 ml/min. The corresponding capillary numbers (C_a) were calculated according to (Equation 2.6).

The capillary numbers were C_a=0.5×10^{-8} (for 0.1 ml/min) and C_a =1.0×10^{-7} (for 0.2 ml/min). Both values are within the capillary-dominated regime and remain well below the critical capillary number associated with viscous fingering. Prior studies, such as Blunt et al. (2002), have shown that at low capillary numbers, displacement is governed by intermittent Haines jumps and pore-filling events, rather than continuous mobilization of the non-wetting phase. Thus, flow remains in the capillary regime where non-linear effects are minimal (Blunt et al., 2002).

The experimental appratus and general workflow is mentioned in Chapter 3. However, the workflow for each flow rate was as follows:

- A confining pressure of 2 MPa above the pore pressure was applied to compress the Viton sleeve and prevent fluid bypass.
- A dry scan of the sample (air-filled) was acquired.
- The sample was flooded with gaseous CO_2 at 1 MPa to displace residual air.

- Full brine saturation was achieved and the pore pressure was increased to 6 MPa.
- Absolute permeability was measured under brine flow conditions.
- A scan was taken with full brine saturation.
- Nitrogen and brine were co-injected at decreasing brine fractional flows (f_w = 0.85, 0.5, 0.3, 0.1, 0) for drainage, acquiring scans at each steady-state. Steady-state was defined as the condition when the pressure drop across the core stabilised for a minimum of 2 hours.
- Subsequent co-injection followed increasing brine fractional flows for imbibition. At 0.1 ml/min, fractional flows of f_w = 0.1, 0.3, 0.5, 0.85, and 1 were used; at 0.2 ml/min, imbibition was performed at f_w = 1 only (one step imbibition). Scans were, again, acquired during steady-state.

Manoorkar et al. (2021) conducted experiments on an Indiana limestone sample using a medical X-ray CT scanner, with a diameter of 4 cm and a length of 15 cm. Scans were acquired at 1 mm thickness across the full length, with a nominal in-plane voxel size of 170 µm. It is important to note that CT scanners do not directly measure porosity, but instead capture X-ray attenuation coefficients, typically scaled to water-air references using Hounsfield units. Porosity is inferred by calibrating the CT attenuation data against known reference materials or fluid saturations, allowing for an indirect estimation of pore volume (Ketcham & Carlson, 2001; Flannery et al., 1987; Withers, 2007). Although the medical CT have lower voxel size compared to micro-CT scanners, they remain sensitive to density contrasts at the millimetre to sub-millimetre scale. Micropores, while not individually resolvable, influence the effective grey level of each voxel, contributing to the measurement of total porosity.

Using this approach, the porosity estimated from the medical CT scans was approximately 17%, which is consistent with the total porosity reported from measurements by Alanzi et al.

(2023). In contrast, porosity measured from the micro-CT images, based on the resolved pore space alone, was 11%. (Figure 5.2) This discrepancy indicates that about 35% of the total porosity resides within sub-resolution microporosity.

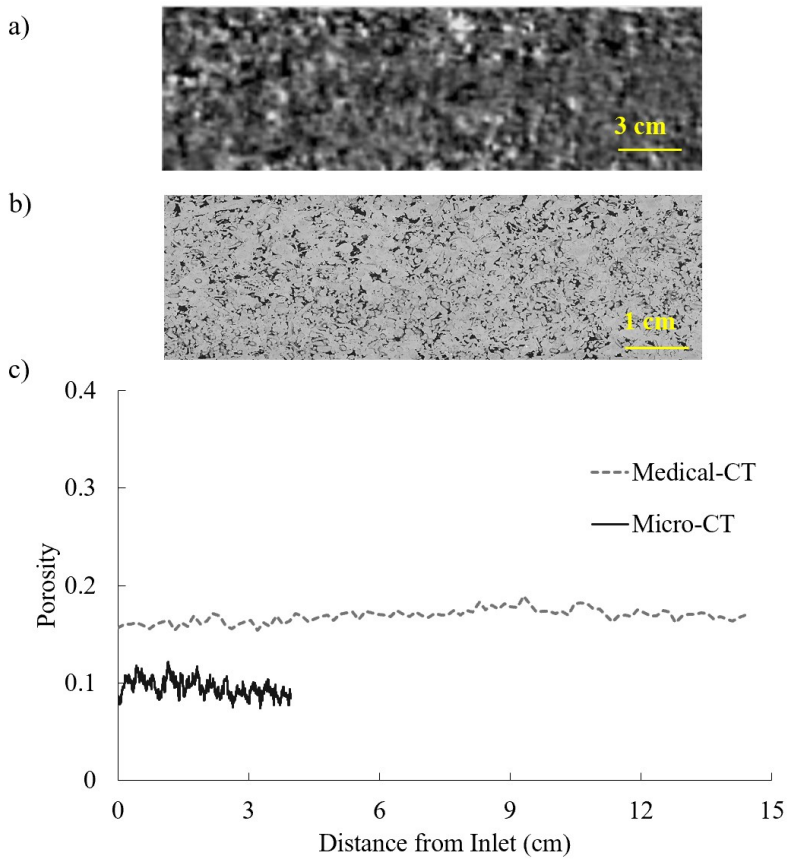


Figure 5.2 (a, b) Two-dimensional cross-sections from the medical CT scan (top, a) and the micro-CT scan (bottom, b). In medical CT, higher intensity corresponds to higher reconstructed X-ray attenuation (higher apparent density), whereas in micro-CT the grey scale primarily reflects phase contrast used to delineate pore space and solid matrix (pores appear as low-intensity voxels, grains as high-intensity voxels). (c) One-dimensional porosity profiles along the flow direction, computed by averaging the slice-wise porosity over each transverse cross-section for each imaging technique.

5.2.3 Image Segmentation

After acquisition, all images were first registered to the dry scan to ensure accurate spatial alignment across different flow conditions. Grey values corresponding to the rock matrix and fluid phases were normalized to account for any beam hardening and scanner-related artifacts, thereby improving the consistency of phase identification (Raeini, Blunt and Bijeljic, 2017).

To reduce noise while preserving sharp phase boundaries, a non-local means edge-preserving filter was applied prior to segmentation (Bhasuthkar et al., 2023). This step enhances the clarity of interfaces between the solid, brine, and gas phases, improving the reliability of the subsequent pore-scale analysis.

The segmentation of the pore space was performed using a watershed-based algorithm, which is particularly effective in complex heterogeneous rocks where simple thresholding is insufficient. In this method, the greyscale images were treated as topographic surfaces, where the local minima represent potential pore centres. The watershed transform was then applied to partition the pore space by simulating the flooding of these minima, delineating the fluid phases based on the local gradients. This approach has been widely adopted in digital rock analysis and multiphase flow imaging due to its ability to resolve connected pore structures and phase boundaries in complex, heterogenous, low-contrast or noisy datasets (Lindquist et al., 2000; Wildenschild & Sheppard, 2013; Andrew et al., 2014). An example of the segmentation outcome is shown in Figure 5.3, highlighting the steps taken to identify the brine and gas phases.

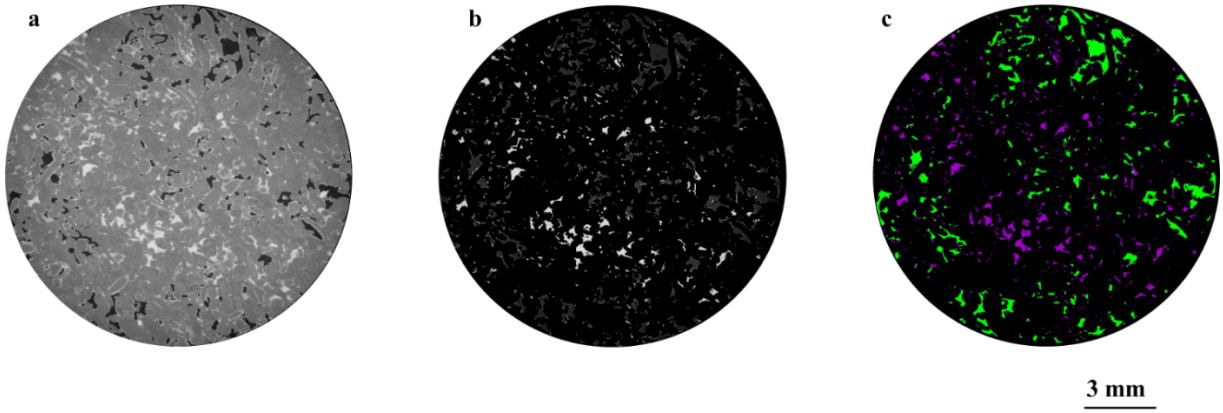


Figure 5.3 Two-dimensional cross-sections (xy direction) of three-dimensional micro-CT images of the middle slice at 0 brine fractional flow (gas injection). (a) Raw image where grey is grain, black is gas, and white is brine, (b) masked image, where black is the masked grain, dark grey is gas, and white is brine, and (c) segmented image, where green is gas and purple is brine.

Uncertainties in image segmentation arise from multiple sources and can significantly influence the accuracy of pore-scale characterisation. These include greyscale ambiguity at fluid–solid and fluid–fluid interfaces, partial volume effects near phase boundaries, and beam hardening artifacts that can introduce spatial intensity variations. While the application of a non-local means edge-preserving filter mitigates high-frequency noise and improves phase delineation, threshold-based segmentation remains sensitive to user-defined parameters and the inherent overlap in intensity distributions of brine and gas. To minimise bias, all scans were co-registered to the dry reference scan and normalised prior to segmentation. Nevertheless, segmentation errors may propagate into derived quantities such as fluid saturation, pore occupancy, and throat size distributions. Based on prior validation studies using synthetic and benchmark datasets (e.g., Raeini et al., 2017; Wildenschild & Sheppard, 2013), we estimate the segmentation-induced uncertainty in fluid-phase volume fractions to be within ±5%. While this does not fundamentally alter the observed flow trends, it introduces bounds on the quantitative interpretation of local saturation and capillary entry pressure measurements.

5.2.4 Characterisation of Heterogeneity

As discussed in Chapter 3, pore network extraction was performed using the PoreXtractor tool (Raeini et al. 2017) applied to the segmented air-filled (dry) scan sample.

Each voxel within the pore space was assigned to a specific pore region based on the maximal ball algorithm, enabling precise identification of pore sizes and connectivity patterns between pores and throats. It is important to note that this extraction method only works on the resolvable pores limited by the micro-CT voxel size; sub-resolution porosity remains undetected and is therefore excluded from the network model. From the average throat size, and using the Young-Laplace equation (Equation 2.5), the average entry pressure was calculated.

Moreover, fluid phase occupancy was determined by overlaying the extracted pore network onto the segmented flow images. For each pore and throat, the dominant fluid phase was identified as the phase occupying more than 50% of the local volume (Foroughi et al. 2020; Foroughi et al. 2021).

This analysis was conducted on six selected sub-volumes (Figure 5.8b), chosen to represent regions exhibiting distinct non-wetting phase saturation behaviour. The objective was to investigate the underlying factors controlling fluid invasion, particularly focusing on structural heterogeneity in pores and throats as well as capillary entry pressure variations.

5.3 Results and Discussion

5.3.1 Saturation Profile

To evaluate the influence of heterogeneity on fluid distribution, we conducted drainage experiments at two distinct flow rates corresponding to different capillary numbers. By

comparing the resulting one-dimensional saturation profiles, we assessed how heterogeneity within the rock controls fluid displacement and distribution under varying forces balance. At lower flow rates, the profiles exhibit distinct peaks and troughs, which are indicative of spatial variations in capillary pressure (Figure 5.4). These features reflect the presence of capillary heterogeneity, where the invasion of the non-wetting phase is tightly controlled by local pore and throat geometry.

As the flow rate increases, these features become less pronounced, and the saturation profile becomes more uniform across the sample. This smoothing of the saturation distribution suggests that increased viscous forces enable the non-wetting phase to bypass local capillary barriers, accessing a broader fraction of the pore space. This behaviour is consistent with observations reported by Reynolds and Krevor (2015), who noted that higher flow rates suppress the manifestation of capillary-driven heterogeneity.

Although the degree of heterogeneity appears reduced at higher flow rates, the spatial locations of the major saturation features remain correlated between the two flow conditions. This implies that the structural heterogeneity continues to influence displacement patterns even under increased viscous control. Flow rate thus provides a means to investigate how heterogeneity governs the fluid distribution.

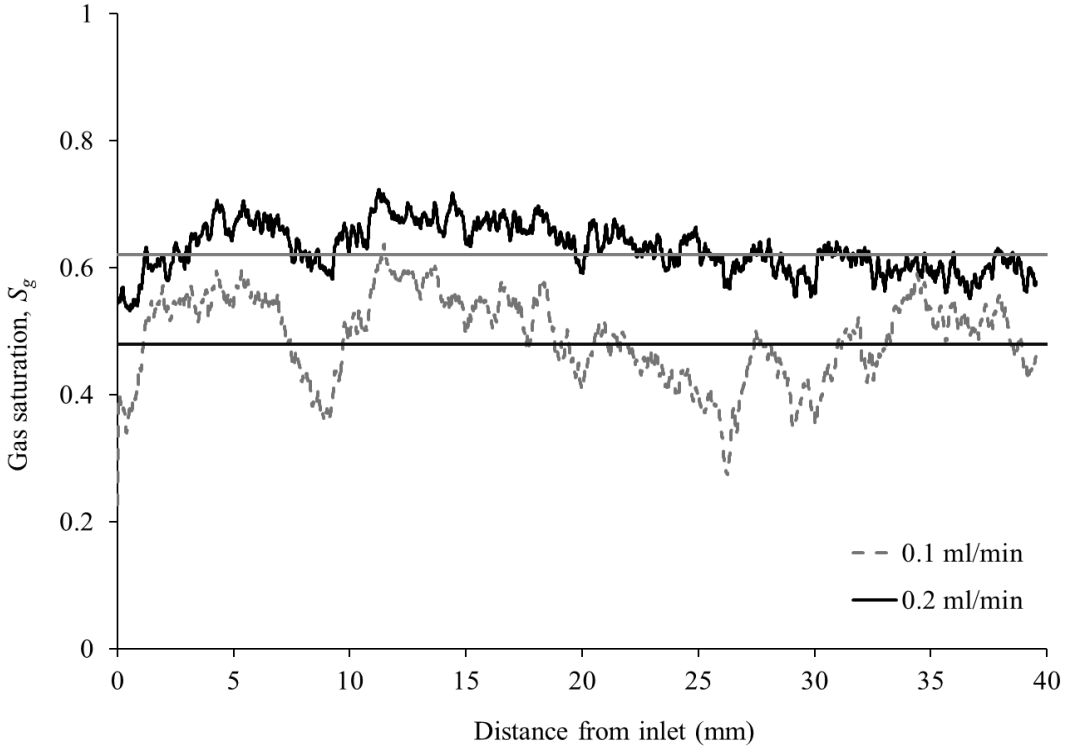


Figure 5.4 One-dimensional slice averaged gas saturation profile in the flow direction at the end of drainage (brine fractional flow of 0). Lines represent the average saturation value across the sample for both flow rates.

Saturation maps (Figure 5.5) provide further evidence that the observed homogenisation in fluid distribution and its correlation with spatial variations in the porosity profile. Regions with lower porosity, remained largely uninvaded at lower flow rates. However, as the flow rate increased, these same regions progressively became saturated, indicating an increased control of viscous forces even in a capillary-dominated flow regime.

At low flow rates, displacement is confined to the most accessible pore pathways, as the non-wetting phase is unable to overcome local capillary entry pressures. In contrast, at higher flow rates, the increased viscous pressure drop enables the non-wetting phase to invade previously inaccessible regions, including those with lower porosity. The strong spatial correlation between the porosity and saturation profiles suggests that the structure of the pore network exerts a dominant influence on displacement dynamics, particularly under capillary-dominated conditions.

Although this trend is clearly observable in the Indiana limestone sample, the magnitude and expression of such transitions are expected to vary across different lithologies, depending on their pore size distributions and capillary pressure characteristics. This interpretation aligns with the findings of Rücker et al. (2020), who demonstrated that pore access thresholds shift under different flow regimes, reflecting the interplay between pore structure and force balance.

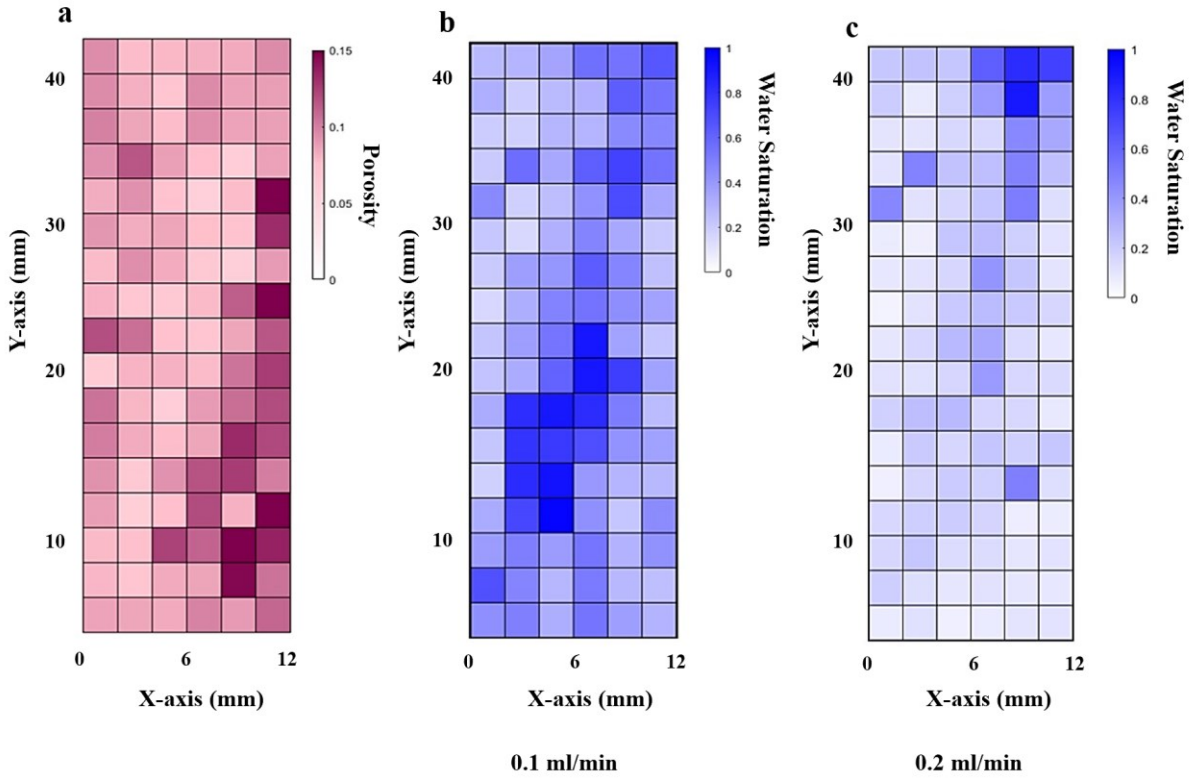


Figure 5.5 (a) Two-dimensional voxel-by-voxel porosity of the middle slice. (b) Two-dimensional voxel-by-voxel saturation maps for end of drainage (fw =0) at (q= 0.1ml/min) (c) Two-dimensional voxel-by-voxel saturation maps for end of drainage (fw =0) at (q= 0.1ml/min). The fine-scale saturation field was upscaled in MATLAB by spatially averaging voxel-scale saturation over larger computational blocks, yielding the coarsened saturation map shown.

5.3.2 Relative Permeability and Trapping

The relative permeability plotted as a function of the average saturation over the whole sample reveal a clear dependence on flow rate and underlying heterogeneity (Figure 5.6). The difference in flow rate resulted in a shift in the relative permeability upwards and to the right (higher wetting phase, brine, saturation) as flow rate decreased.

For the non-wetting phase, for example, at a relative permeability of 0.1, gas saturations were lower (higher brine saturation) at the lower flow rate. In this regime, gas flow is restricted to specific preferential pathways or channels. These channels correspond to high-permeability regions, while much of the surrounding pore space remains uninvaded. At the higher flow rate, achieving the same effective permeability still requires gas flow through these main channels. However, due to the increased pressure drop, the gas also extends into lower-permeability regions. Although these additional areas are invaded, they contribute very little to the overall flow. The effective transport remains dominated by the original high-permeability channels. This behaviour accounts for the observed shift in the relative permeability with increasing flow rate.

The wetting phase displays an opposite trend. At the higher flow rate, the same effective permeability is observed at a higher brine saturation. This reflects the tendency of the wetting phase to remain in the smaller pores under elevated flow conditions, thereby occupying a greater fraction of the pore volume. In contrast, at the lower flow rate, the corresponding relative permeability is achieved at a lower brine saturation. Under these capillary-dominated conditions, brine flows through narrow, well-connected channels, which often requires partial occupancy of intermediate-sized pores to maintain continuity. As a result, a higher relative permeability is achieved at a lower saturation compared to the high flow rate case.

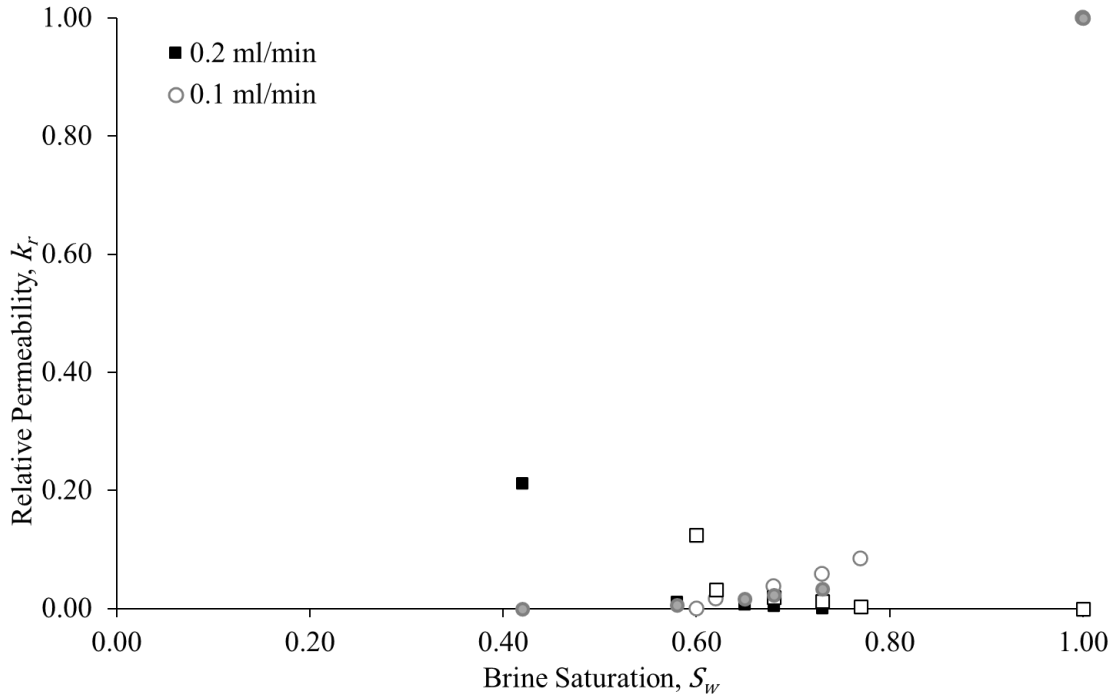


Figure 5.6 Relative permeability measured during drainage; black is 0.2 ml/min and grey 0.1 ml/min.

Residual trapping was assessed by comparing the initial and residual gas saturations at both flow rates obtained from 1D slice average, as described in Chapter 4 (Figure 5.7). For the high flow rate (0.2 ml/min), the initial gas saturation was 0.62 and the residual saturation was 0.47. At the low flow rate (0.1 ml/min), those values were 0.49 and 0.34, respectively.

At the lower flow rate, the non-wetting phase tended to remain trapped in distinct layers aligned with the direction of flow, something we typically associate with capillary-dominated displacement. These layers suggest that capillary entry pressures restricted the gas to particular regions, preventing it from spreading more widely through the rock.

At the higher flow rate, this layered pattern largely disappeared. The higher viscous forces allowed the gas to push through more of the pore space, including areas that were previously inaccessible at low flow. Despite this difference in distribution, we did not observe a major change in trapping efficiency between the two flow rates. A key reason for the limited change

in trapping efficiency is the orientation of the heterogeneity. Because the heterogeneity is aligned parallel to the flow direction, the non-wetting phase encounters fewer abrupt capillary barriers that would otherwise restrict its movement and enhance trapping. If the heterogeneity were oriented perpendicular to flow, the gas would be more frequently forced to cross contrasting pore structures, likely leading to greater local trapping and a more significant difference in efficiency between the two flow regimes. So, although more gas was trapped at the higher flow rate, it is mostly due to the higher initial saturation rather than a significant change in trapping efficiency.

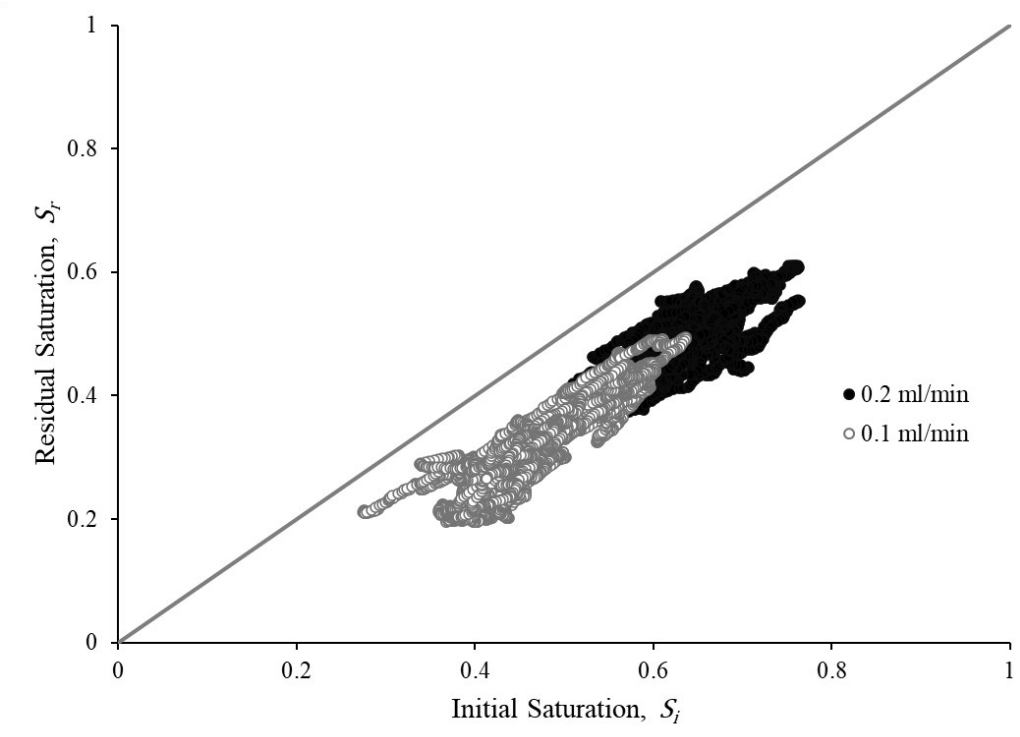


Figure 5.7 Amount of residual trapping as a function of the initial saturation, black is 0.2 ml/min and grey is 0.1 ml/min.

5.3.3 Pore Network and Pore Occupancy

To better understand continuum-scale flow behaviour through the lens of pore-scale mechanisms, we examined six representative sub-volumes within the rock sample, as shown in Figure 5.8b. These sub-volumes were selected based on clear differences in gas saturation

between the two flow rates. Regions 1, 2, and 3 correspond to areas where the non-wetting phase showed limited invasion at the lower flow rate, suggesting the presence of higher capillary entry pressures. In contrast, 4, 5, and 6 marked regions represent zones where gas invaded readily under both flow conditions, indicating lower entry pressures.

The analysis showed a consistent trend across the sub-volumes. Areas that remained uninvaded at the lower flow rate generally had smaller throats, which are associated with higher capillary thresholds. These local conditions restricted gas entry when capillary forces were dominant. On the other hand, regions that were invaded even at low flow rates had visibly larger throats, reflecting lower entry pressures that facilitated easier displacement by the non-wetting phase (Figure 5.8a).

These local differences in throat geometry help explain the spatial variability in gas saturation observed across the sample. They also demonstrate how capillary heterogeneity, driven by small-scale structural variation, directly controls the accessibility of the pore space under different flow regimes.

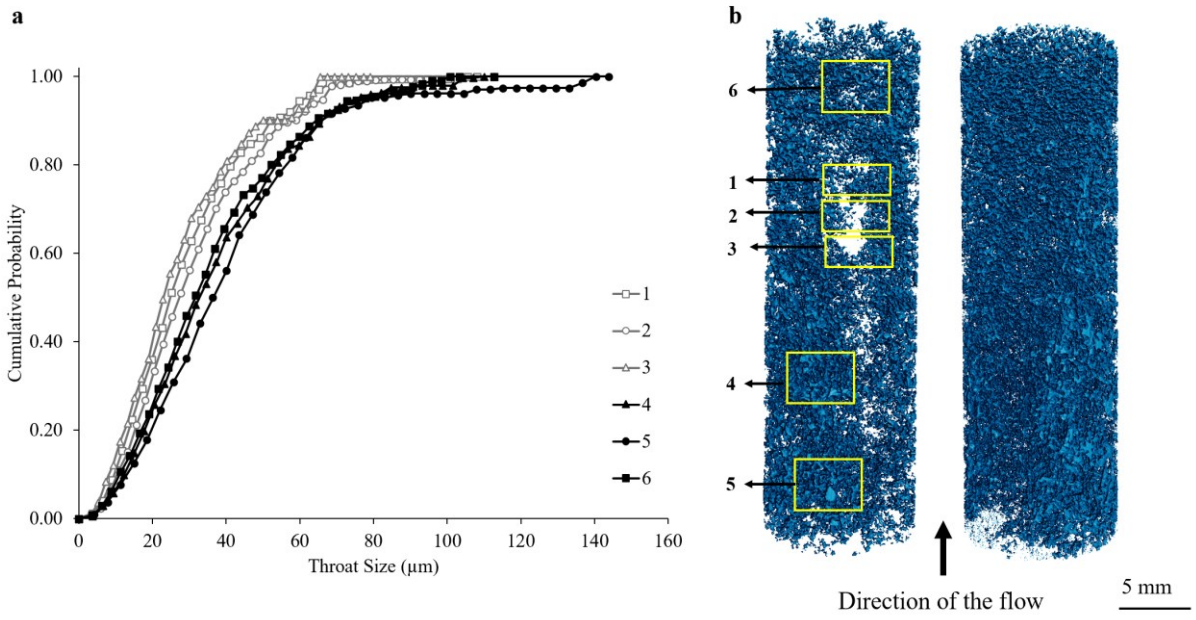


Figure 5.8 (a) Throat size distribution (radius) of six sub-volumes across the sample. (b) Three-dimensional segmented gas phase at end of drainage (fw=0) for both flowrates. The boxes show the location of the sub-volumes taken.

Furthermore, pore occupancy analysis across these sub-volumes revealed distinct differences based on capillary number. In regions with low capillary entry pressures, the non-wetting phase was able to invade effectively at both low and high flow rates, resulting in minimal differences in occupancy between the two cases. In contrast, sub-volumes characterised by higher capillary entry pressures exhibited a pronounced change: at the lower flow rate, the gas phase was largely excluded, while at the higher flow rate, the increased viscous forces allowed it to overcome capillary thresholds and occupy a significantly larger fraction of the pore space (Figure 5.9).

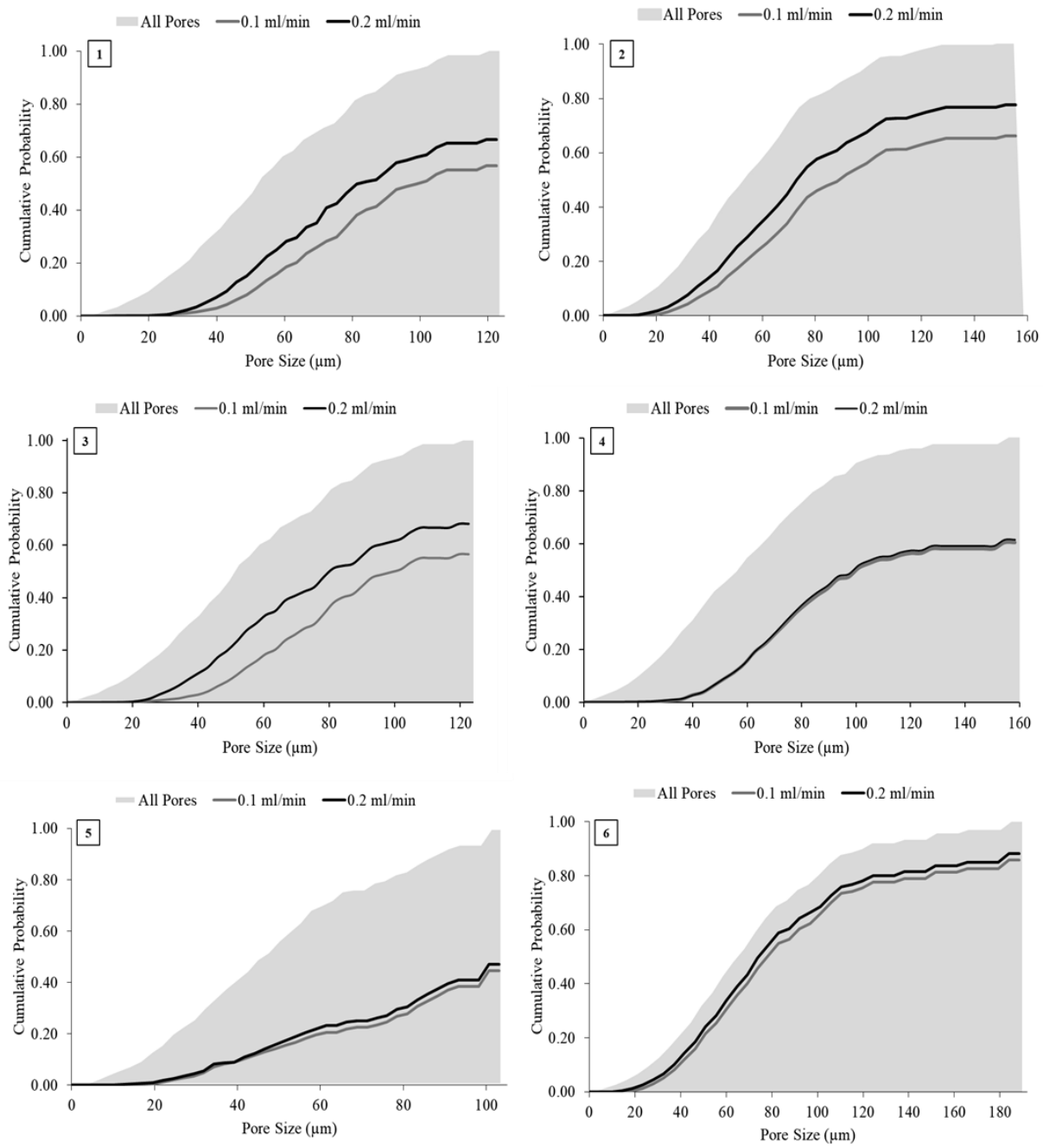


Figure 5.9 Pore occupancy for the six sub-volumes analysed. Panels (1-3) corresponds to regions with low high capillary entry pressures, while panels (4-6) represent regions with low capillary pressures.

These observations demonstrate that even a modest increase in capillary number, specifically, a doubling in this case, can significantly alter the spatial distribution of the non-wetting phase. Importantly, this shift is not uniform across the rock but is strongly influenced by local pore-scale heterogeneity. In Figure 5.10, we present estimated capillary pressure–saturation

relationships for each of the six sub-volumes. These estimates are based on average pore throat diameters obtained from pore network modelling, applying the Young–Laplace equation (Equation 2.5). As expected from the throat size distributions shown in Figure 5.8a, the results show clear differences in capillary pressure characteristics between the different regions.

These findings suggest that at higher flow rates, the increased viscous pressure drop allows the non-wetting phase to mobilise into smaller pore spaces that remain inaccessible under capillary-dominated conditions. This behaviour is particularly relevant in stratified or compositionally layered rocks, where heterogeneity can give rise to uneven phase distribution, restricted sweep, and preferential flow pathways.

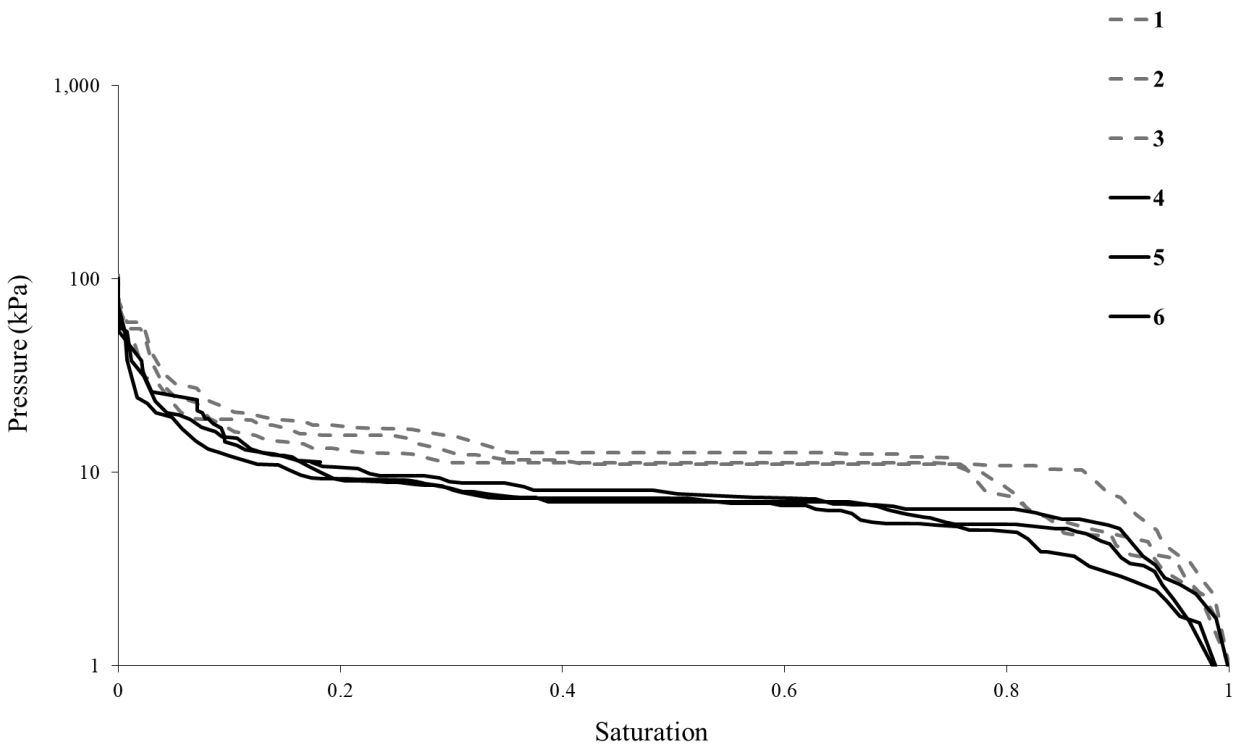


Figure 5.10 Estimated capillary entry pressures for the six sub-volumes, calculated using average pore throat diameters obtained from pore network modelling and the Young–Laplace equation.

Key flow and structural properties derived from pore network modelling of the six sub-volumes are summarised in Table 1. The estimated capillary entry pressures in the different regions varied by nearly a factor of two. Notably, at the higher flow rate, the higher-capillary pressure

region was invaded at a differential pressure that also increased by approximately the same factor. While we do not suggest a direct or linear relationship between capillary entry pressure and viscous pressure drop, the similarity in their relative magnitudes is noteworthy.

Table 5.3.1 Summary of pore network model–derived porosity, absolute permeability, and average capillary entry pressure for each of the six analysed subvolumes highlighted in figure 5.8b.

Subvolume	∅ (%)	K (mD)	P_e (kPa)
1	8	67	13
2	7	68	12.5
3	7	52	14
4	13	137	7.7
5	12	200	8
6	15	337	6.7

5.4 Conclusions

This study demonstrates that pore-scale heterogeneity exerts a fundamental control on the flow-rate dependence of fluid distribution in porous media. Through micro-CT imaging and pore network modelling of Indiana limestone, we show that even modest changes in capillary number can produce markedly different patterns of non-wetting phase occupancy. These differences arise from local variations in capillary entry pressure, governed by throat geometry, which determine phase accessibility under a given flow regime.

As flow rate increases and viscous forces begin to play a greater role (even within a capillary-dominated regime), the non-wetting phase gains access to smaller and previously uninvaded pores. This leads to a more homogeneous saturation profile and a systematic shift in the shape

and position of the relative permeability curves. However, despite this increased pore accessibility, the relative permeability of the non-wetting phase decreases due to greater interfacial contact and increased flow tortuosity, emphasising the trade-off between spatial distribution and mobility.

Digital rock analysis proved critical in this work, offering a predictive understanding of capillary pressure characteristics based solely on pore structure. The ability to estimate local displacement thresholds without performing full core flood experiments highlights the value of this approach in pre-screening rock types and informing experimental design. Nonetheless, uncertainties remain due to sub-resolution porosity, particularly in microporous domains, which may lead to under- or overestimation of accessible pore space and flow behaviour.

Importantly, the structure and findings of this study align with trends increasingly recognised in both empirical investigations and machine-assisted literature reviews, which converge on capillary heterogeneity as a high-impact control on CO_2 storage performance. This reinforces the relevance of our analysis and situates it within the broader evolution of data-driven approaches to multiphase flow modelling.

Our findings strengthen the mechanistic link between pore-scale structure, capillary heterogeneity, and continuum-scale flow properties. This connection is crucial for advancing upscaling frameworks, particularly those developed by Jackson and Krevor (2020) and An et al. (2023), which incorporate rate-dependent flow functions into field-scale simulation. Together, these approaches point toward a more robust and physically grounded methodology for deriving relative permeability functions that are sensitive to both heterogeneity and flow regime—an essential requirement for reliable forecasting of CO_2 storage performance in complex and heterogeneous geological formations.

We will now continue our investigation of the role of small-scale heterogeneity by performing a pore-to-core analysis of multiphase flow in another heterogeneous carbonate, namely Edwards dolomite, in the next chapter.

Chapter Six Centimetre-Scale to Decimetre-Scale Heterogeneity in Carbonates: Edwards Brown Dolomite

(This material has been published in Darraj et al., 2025 (b))

This chapter extends the analysis to larger complexity and larger scale of heterogeneity to address the mechanistic question of: how do spatially organised capillary barriers at centimetre-to-decimetre scales control saturation and trapping, and to what extent does immobilisation arise from heterogeneity-driven accumulation rather than classical pore-scale snap-off alone? We investigate how low-connectivity regions act as partial capillary barriers, restricting non-wetting phase invasion and promoting immobilisation upstream. By focusing on larger-scale heterogeneity than that considered in Chapter 5, this chapter highlights how increasing heterogeneity scale leads to qualitatively different trapping behaviour and challenges conventional interpretations of residual trapping based solely on pore-scale mechanisms.

6.1 Introduction

In this work, we present a pore-scale experimental investigation of multiphase flow in Edwards Brown rock sample to elucidate how small-scale heterogeneity has an influence on CO_2 trapping and saturation profiles (Saadatpoor et al., 2010; Krishnamurthy et al., 2022; Behzadi et al., 2011; Gershenzon et al., 2017; Jackson and Krevor, 2020; Ershadnia et al., 2021; Krevor et al, 2015; Spurin et al., 2025; Darraj et al., 2024; and Tavassoli et al., 2021). The rationale for selecting Edwards Brown dolomite lies in its highly complex pore structure, which makes it an effective analogue for heterogeneous carbonate reservoirs. The rock exhibits multi-scale porosity, combining microporous dolomite crystals with larger vugs and moldic pores, which together produce a broad distribution of pore throat sizes and capillary entry pressures. Unlike

many layered carbonates, Edwards Brown displays spatially isotropic heterogeneity, where low-permeability patches and vug-rich zones are distributed irregularly throughout the matrix rather than forming distinct stratification (Wenck et al., 2021; Manoorkar et al., 2021). This heterogeneous arrangement amplifies capillary contrasts and enhances the likelihood of local barriers and snap-off, providing an ideal system for investigating pore-scale trapping mechanisms. The sample size (12 mm in diameter and 60 mm in length) is large enough to capture continuum-scale properties, while still being small enough to resolve pore-scale phenomena. This includes direct observation of fluid–fluid interfaces, connectivity of the pore network, and the displacement mechanisms that control trapping.

Carbonate rock samples present an important case study, as they host approximately 60% of the world's oil reserves making them prime candidates for CO_2 storage (Seyyedi, et al., 2020). Moreover, compared to sandstones, carbonate rocks exhibit a diverse array of pore and throat types and sizes. This inherent complexity leads to unique fluid flow and trapping behaviour (Lucia, 1995; Bultreys et al., 2016; Manoorkar et al., 2021). Some carbonate formations have been reported to contain significant microporosity, contributing as much as 10–60% of the total porosity (Baechle et al., 2008; Gharieb et al., 2024). In such heterogeneous carbonate rocks, the non-wetting phase may preferentially invade the more accessible macropores, leaving large volumes of brine-saturated microporosity untouched or leading to the isolation of CO_2 in disconnected pore regions and higher trapping efficiency (Krevor et al., 2015; Al-Menhali and Krevor, 2016).

We utilise X-ray imaging with a 5.6 μm voxel size is combined with core flooding experiments to directly observe fluid displacement patterns under capillary-dominated flow conditions. By quantitatively linking spatial variations in pore structure to local fluid occupancy and residual non-wetting phase trapping, we bridge the gap between pore-scale processes and continuum-

scale implications. The findings provide insight into how heterogeneity in carbonates can lead to different trapping efficiencies within the same sample. These observations apply to Edwards Brown carbonate and similar rocks exhibiting the same scale and nature of heterogeneity.

6.2 Materials and Methods

6.2.1 Rock Sample and Fluids

The experimental methods are described in detail in Chapter 3. Here additional information is provided, specific to this set of experiments. The rock used in this study is Edwards Brown dolomite, quarried from an Upper Cretaceous carbonate formation in Texas, USA. It is a dolomitised limestone with pronounced diagenetic heterogeneity. Mineralogical analysis indicates that dolomite is the dominant phase, with minor calcite and trace quartz impurities (Lai et al., 2015).

Measured on a cylindrical sample 3.8 cm in diameter and 15 cm long the total porosity of the Edwards Brown dolomite sample was measured at approximately 26% using a medical CT scanner (using dry scan-wet scan correlation) (Manoorkar et al., 2021). Reported mercury injection capillary pressure results for Edwards Brown indicate a throat radius range of approximately 0.1 to 20 µm and a mean of 10.5 µm (Kurotori et al., 2020).

We analysed a cylindrical rock plug (12 mm in diameter and 60 mm in length). The plug's porosity is ~22% as determined by 5.6 µm voxel size X-ray imaging considering only resolvable pores (Figure 6.1), and its permeability to brine at ambient temperature and pressure was measured to be approximately 110 ±10 mD.

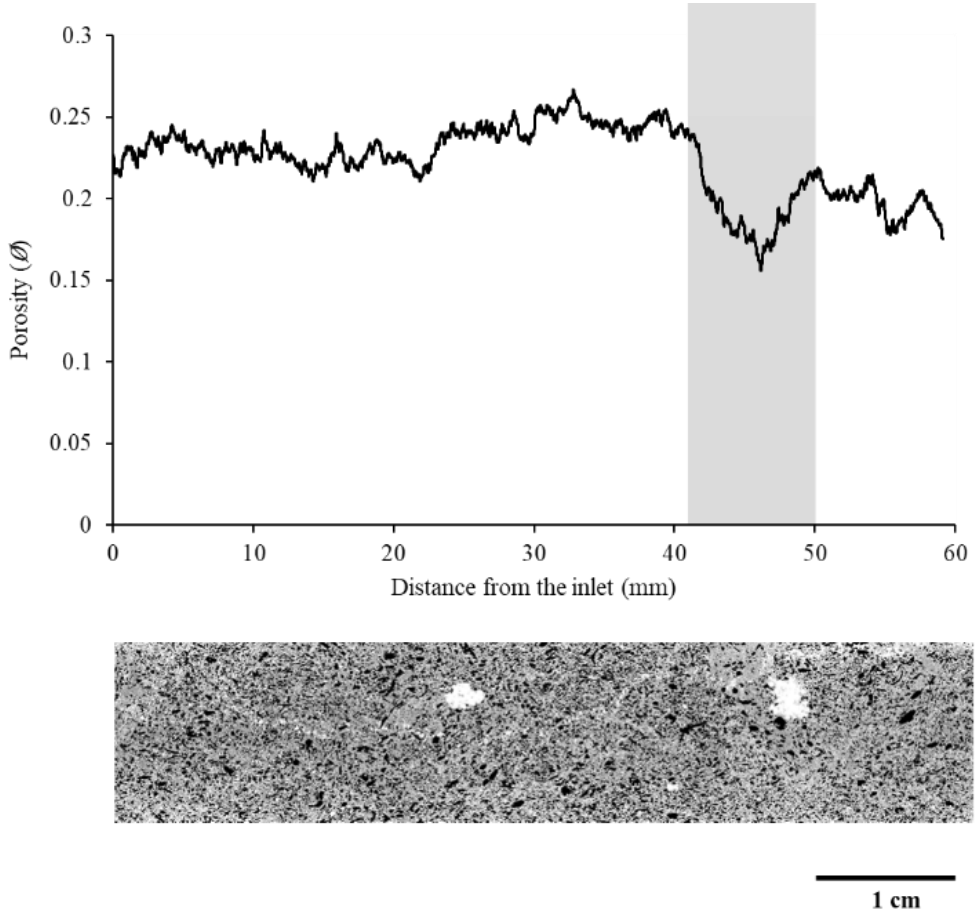


Figure 6.1 The top panel is a one-dimensional porosity profile along the sample's length (averaged over cross-sectional slices) indicating the low porosity region with the shading. The bottom image shows the middle slice of a representative two-dimensional cross-section of a 3D micro-CT image through a region of interest (grey is the rock matrix, black is the pore space, and white is mineral).

The sample was oven-dried under vacuum at 80 °C for 72 hours prior to the experiment. Two fluid phases were used in the flooding experiments: an aqueous brine as the wetting phase and an oil (decane) as the non-wetting phase. The brine was a KI (potassium iodide) solution (30 wt% KI, ~2.58 mol/kg), chosen to provide X-ray contrast with the non-wetting phase (Lin et al., 2021). The density of the brine was measured to be 1,263 ± 2 kg/m^3 and the viscosity was 0.822 ± 0.013 mPa s at experimental conditions (Gao, et al., 2017), the salinity of the KI brine is 2.4 molar, which is greater than that of seawater at 0.6 molar, but in the same range of highly saline carbonate reservoirs where brine molarity can range from 2 to 3 molar (Meekangwal et al., 2018; Gholanlo et al., 2016; Iampen et al., 2000). Decane (n-decane, $C_{10}H_{22}$) was selected as an analogue for CO_2: n-decane is frequently used as a proxy for supercritical CO_2 due to its

similar capillary displacement characteristics and convenient experimental handling (Andrew et al., 2014; Berg et al., 2013). The decane–brine interfacial tension (IFT) was 47 ± 2 mN/m (NIST Chemistry WebBook), is on the same order of magnitude as supercritical CO_2–brine systems, which is typically 20–35 mN/m at reservoir conditions (Chalbaud, et al., 2009). Moreover, as long as the capillary number (Equation 2.6) remains well below 10^{-5}, the system is in the capillary-dominated regime, and macroscopic properties such as relative permeability and residual non-wetting phase saturation are insensitive to the absolute value of interfacial tension (Lake, 1989; Blunt 2017). Around 1000 m depth, supercritical CO_2 begins to mimic two key properties of a light hydrocarbon (like decane): a density on the order of 600 – 700 kg/m^3 and interfacial tension ~47 mN/m. By 1500–2000 m, CO_2's density essentially equals that of decane. However, CO_2's viscosity remains an order-of-magnitude lower than decane's at all depths (NIST Chemistry WebBook).

Furthermore, decane remains liquid at atmospheric conditions and is chemically inert with brine, enabling straightforward laboratory handling and X-ray imaging without specialized high-pressure equipment (Singh et al., 2017). Using decane allows a controlled, capillary-dominated multiphase displacement experiments under room temperature conditions, while still capturing physics relevant to CO_2 injection in brine-filled rock. The n-decane/brine system is employed here as a controlled analogue to explore capillary-dominated flow behaviour. While it does not replicate the exact physical properties of CO_2, the flow remains within the same dimensionless regime where displacement mechanisms are governed by pore geometry and wettability rather than absolute fluid properties.

6.2.2 Experimental Methodology

The sample holder was of a (PEEK) material, with the rock wrapped in a flexible fluoropolymer (Viton) sleeve. This assembly was placed inside a Zeiss Xradia 510 Versa X-ray micro-CT scanner for in situ imaging.

All core-flooding and imaging experiments were conducted at room temperature (22 ± 1 °C) and atmospheric pressure (1 bar; 0.1 MPa). However, the Edwards Brown Dolomite represents a shallow to mid-depth carbonate reservoir, where typical in situ conditions are on the order of 50–80 °C and 10–15 MPa. These values are provided for reference only, as the present experiments were designed to examine capillary-dominated displacement mechanisms under controlled laboratory conditions. During imaging, a constant confining pressure of 3.5 MPa (applied with deionized water around the Viton sleeve) was maintained to emulate an in situ overburden stress and to prevent any bypass flow along the sample walls. The pore pressure inside the sample was maintained at 0.3 MPa at the outlet (backpressure). Micro-CT scans were acquired at various stages of the flow experiment to visualize the internal distribution of fluids. Each scan was performed at an X-ray energy of 75 kV and power of 6.5 W. A large field-of-view detector was used to capture the entire sample cross-section at a voxel size of 5.6 µm. For each static scan, 3200 projection images were collected over 360° rotation, which, after reconstruction (using Zeiss Reconstruction software with appropriate centre-shift and beam-hardening corrections), yielded a three-dimensional image of the X-ray attenuation within the sample.

The voxel size (~5.6 µm) is sufficient to resolve the macropores and larger pore throats in the dolomite, though the finest microporosity remains below this detection limit (Figure 6.2).

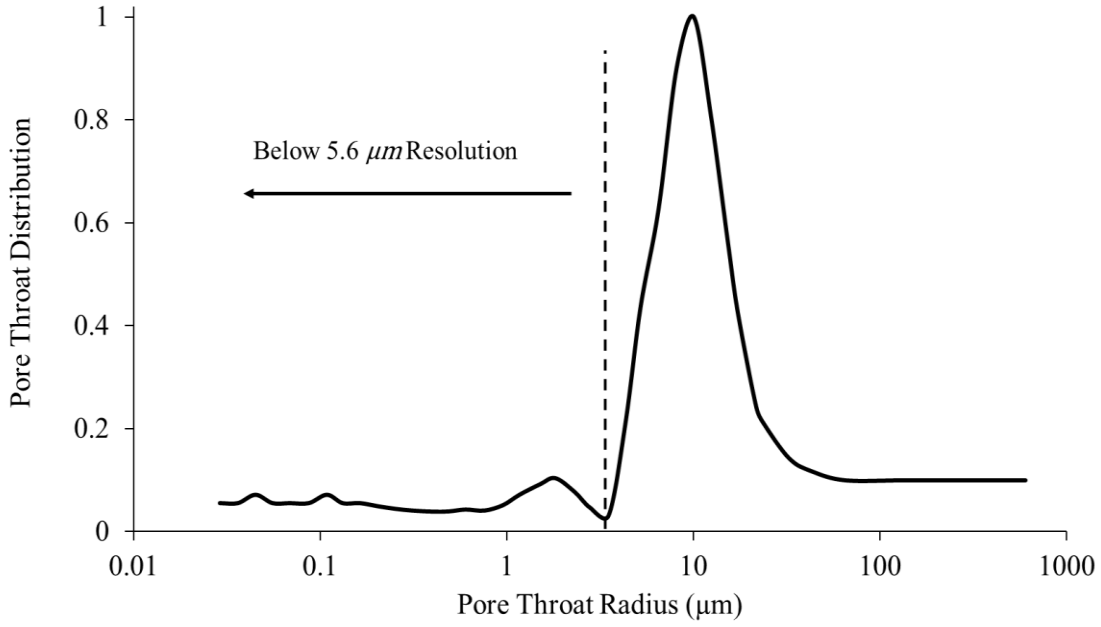


Figure 6.2 Mercury intrusion capillary pressure data that has been converted to show the distribution of pore-throat radius, normalized such that the maximum value is 1. Throats of radius below the voxel size of the image (5.6 μm) cannot be resolved.

The reconstructed grey-scale images distinguish solid mineral matrix (high attenuation), brine (moderate attenuation due to KI content), and decane (low attenuation, similar to air) by their X-ray absorption contrast (Figure 6.3b). The multiphase flow experiment consisted of a sequence of steps designed to initially saturate the sample with CO_2 to purge the air, then establish a brine-saturated condition, and finally perform controlled drainage and imbibition cycles while imaging at steady-state conditions.

The overall procedure was as follows:

1. Initialisation: The dry sample was assembled in the core holder and placed inside the scanner. A net confining pressure of 3.2 MPa was applied around the sleeve and left for 3 hours with close monitoring of the confining pump. This step ensured the sample was isolated from the confining fluid and there is no flow bypass along the sleeve-rock interface once fluids were introduced. The dry scan was taken.

2. CO_2 Saturation: Gaseous CO_2 was injected into the sample at a pore pressure of ~1 MPa for 30 minutes displacing air, which here acts as an initial pore-filling gas.
3. Brine Saturation: Brine was injected into the sample at a constant flowrate of 1 mL/min displacing the CO_2 gas. This brine flooding continued until the sample was fully saturated with brine. During this and all other subsequent stages, the pressure difference across the sample was measured. During this step, the absolute permeability of the rock was measured by varying the flowrate and recording the pressure differential, then using Darcy's law and pressure correction. The brine filled scan was taken.
4. Drainage (CO_2 analogue injection): After establishing a brine-saturated state, we initiated a drainage sequence. Using the dual pump system, decane and brine were co-injected at a fixed total flow rate of 0.1 mL/min, while gradually increasing the fractional flow of decane. We conducted a series of steady-state fractional flow steps with brine fractional flows of f_w = 0.9, 0.75, 0.5, 0.25, 0.05, 0 (100% decane). Each step was maintained until pressure equilibrium was reached, indicating steady state, and then a 3D micro-CT scan was taken. The capillary number during these flows was ($C_a = \mu \cdot q/\sigma \approx 2.6\times10^{-7}$, using the decane viscosity and brine–decane IFT), ensuring that the displacement was capillary-dominated and representative of immiscible flow regimes in the subsurface. By the end of the drainage cycle (100% decane injection), the sample's pore space had a high saturation of decane, with brine remaining only in the most difficult-to-invade pores.
5. Imbibition (brine re-injection): Next, an imbibition sequence was performed to simulate the post-injection brine encroachment and investigate trapping. We gradually increased the brine fraction in co-injection steps reversing the sequence: brine fractional flows f_w = 0.05, 0.25, 0.5, 0.75, 0.9, and finally 1.0 (for 100% brine). Again, each fractional flow condition was held until steady-state was achieved before imaging. After the final

imbibition step (100% brine), the sample was left with a certain amount of residual decane trapped in the pore space, analogous to residually trapped CO_2 after a water flush or plume migration. Micro-CT scans were taken at the end of each fractional flow step in the imbibition cycle.

At each imaged steady state (both during drainage and imbibition), the three-dimensional distribution of brine and decane inside the pore space was mapped from the micro-CT images. This stepwise variation in fractional flow was designed to probe the effect of pore-scale heterogeneity on saturation evolution under capillary-dominated conditions. Since the displacement mechanisms are path-dependent in such regimes, each steady-state image captures the cumulative impact of injection history on non-wetting phase configuration. To reach the residual and irreducible saturations, injection was carried out for about six hours (approximately 24 pore volumes) prior to scanning to ensure steady-state conditions are reached. Image processing steps (described below) were applied to segment the grey-scale images into binary phases (brine and decane) and to quantify local saturations, connected pathways, and trapping metrics.

6.2.3 Image Processing and Analysis

As described in the previous chapters, all reconstructed micro-CT images were processed and analysed using Thermo Fisher's (Avizo) software. Initially, due to the 30% overlap between consecutive scans, images were registered to each other, followed by cropping to remove cone-beam artifacts. Subsequently, intensity normalisation was performed across all sections to ensure consistent grey value distributions. Following these adjustments, the individual images were merged to reconstruct the complete sample. This procedure was repeated with all scans, registered and reassembled to the dry scan, providing a consistent reference for comparison across different saturation states. To reduce noise while preserving structural details, a non-

local means filter was applied. Watershed segmentation was then implemented (Figure 6.3), and subtraction of the flow scans from the brine-saturated images was performed. The resulting non-wetting phase saturations were quantitatively compared, confirming the robustness and accuracy of the segmentation approach. Phase saturation was quantified by calculating the volume fraction of each segmented phase relative to the total pore space.

While watershed is a robust segmentation method, it is important to acknowledge that subtle changes in the grey-scale histogram limits can impact connectivity analysis. It has been shown that choices in segmentation methodology can cause substantial variation in physics-based outputs (Schluter et al., 2014; Garfi et al., 2020; Krygier et al., 2020). Numerically, this implies that even small misclassifications may induce errors in phase connectivity and non-wetting saturations on the order of 10–20 %. These uncertainties can lead to under- or over-estimation of residual trapping, saturation, connectivity, and permeability (Wang et al., 2021). Moreover, it is important to note that our observations are inherently limited to the resolvable pores. Any porosity below ~5.6 μm (the voxel size limit) cannot be explicitly imaged. Carrillo et al., (2021) showed that sub-resolution porosity can alter predictions of residual saturations by as much as

20% and relative permeability by a factor of up to 3, because unresolved porosity can act as persistent connectors between larger pores

.

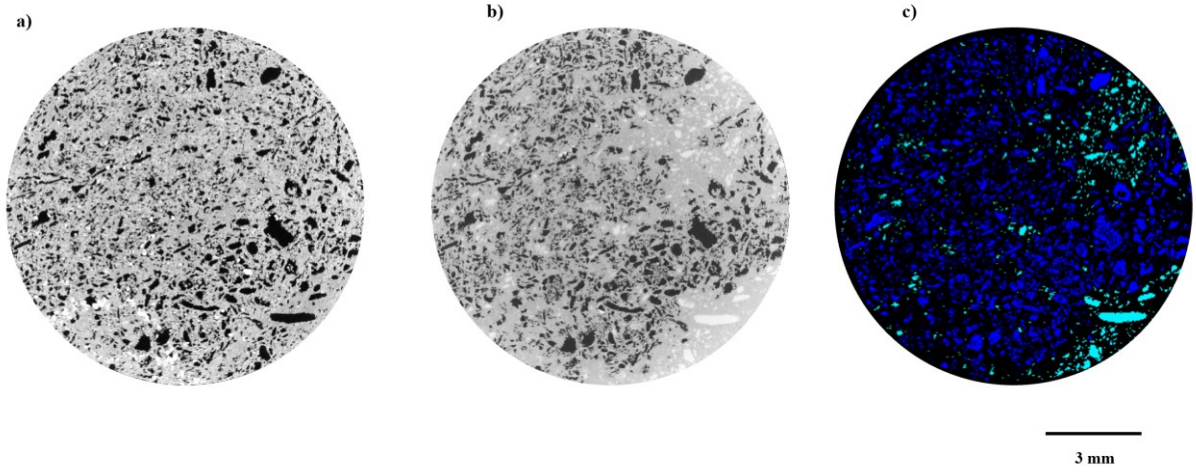


Figure 6.3 Two-dimensional cross-sections of a 3D micro-CT images at the end of drainage (f_w =0): (a) dry scan, rock in grey and pores in black; (b) filtered flow scan, showing rock in grey, decane in black, and brine in white; (c) segmented image, with rock represented in black, decane in blue, and brine in green.

As mentioned Chapter 3, to analyse the pore-scale displacement mechanisms, we performed a pore network extraction on the segmented pore space of the rock using the open-source algorithm PoreXtractor (Raeini et al., 2017) to extract a skeletal network of pores and throats from the dry scan. The output of this analysis is a graph representation of the pore space, providing metrics such as pore size distribution, throat size distribution, and coordination number (the number of throats connected to each pore). We note that this network represents only the macro-porosity of the sample (pores and throats with radius larger than ~5.6 μm), any regions below that scale are not included and effectively treated as part of the solid matrix in this analysis. As a result, our network might under-represent the total porosity, permeability, and coordination number since sub-resolution pores and throats that could connect into the network were excluded.

As described in Chapter 5, the extracted pore network as a template, we then mapped the time-resolved fluid occupancy onto it. For each pore and throat identified in the network, we determined whether it was filled with decane or brine at the end of drainage and at the end of imbibition. This was done by overlaying the pore-network on the segmented fluid images from those time steps. A pore was classified as containing the non-wetting phase (decane) if more than 50% of its voxels were labelled as decane in the image, a threshold criterion based on previous pore-by-pore analyses (Foroughi et al., 2021). This approach avoids misclassifying pores that have only a thin film of brine or a minor presence of decane: it distinguishes pores that are predominantly filled with the non-wetting phase from those predominantly water filled. Similarly, throats were labelled by the majority phase present. Moreover, an estimation of the capillary entry pressures for some regions of rock were estimated using average throat diameters derived from pore network modelling and applying the Young–Laplace equation (Equation 2.5).

Finally, volume, surface area, count of distinct ganglia, and connectivity were derived from the images. This offers insights on how the non-wetting phase connectivity progressed.

6.3 Results and Discussion

6.3.1 Fluid Saturation Profiles and Phase Distribution

The saturation of brine and decane in the macro pores was quantified after each injection step. The fluid saturations were measured on segmented images of the whole sample both drainage (Figure 6.4a) and imbibition (Figure 6.4b). The non-wetting phase saturation profile increases systematically across the sample with rising non-wetting phase fractional flow. However, a local minimum in non-wetting saturation persists between 45 mm and 48 mm across all fractional-flow conditions (Figure 6.4 a&b). Unlike other minor valleys that shift or diminish

with changing fractional flow, this feature remains fixed in both position and amplitude, indicating that the non-wetting phase did not invade this region at any stage.

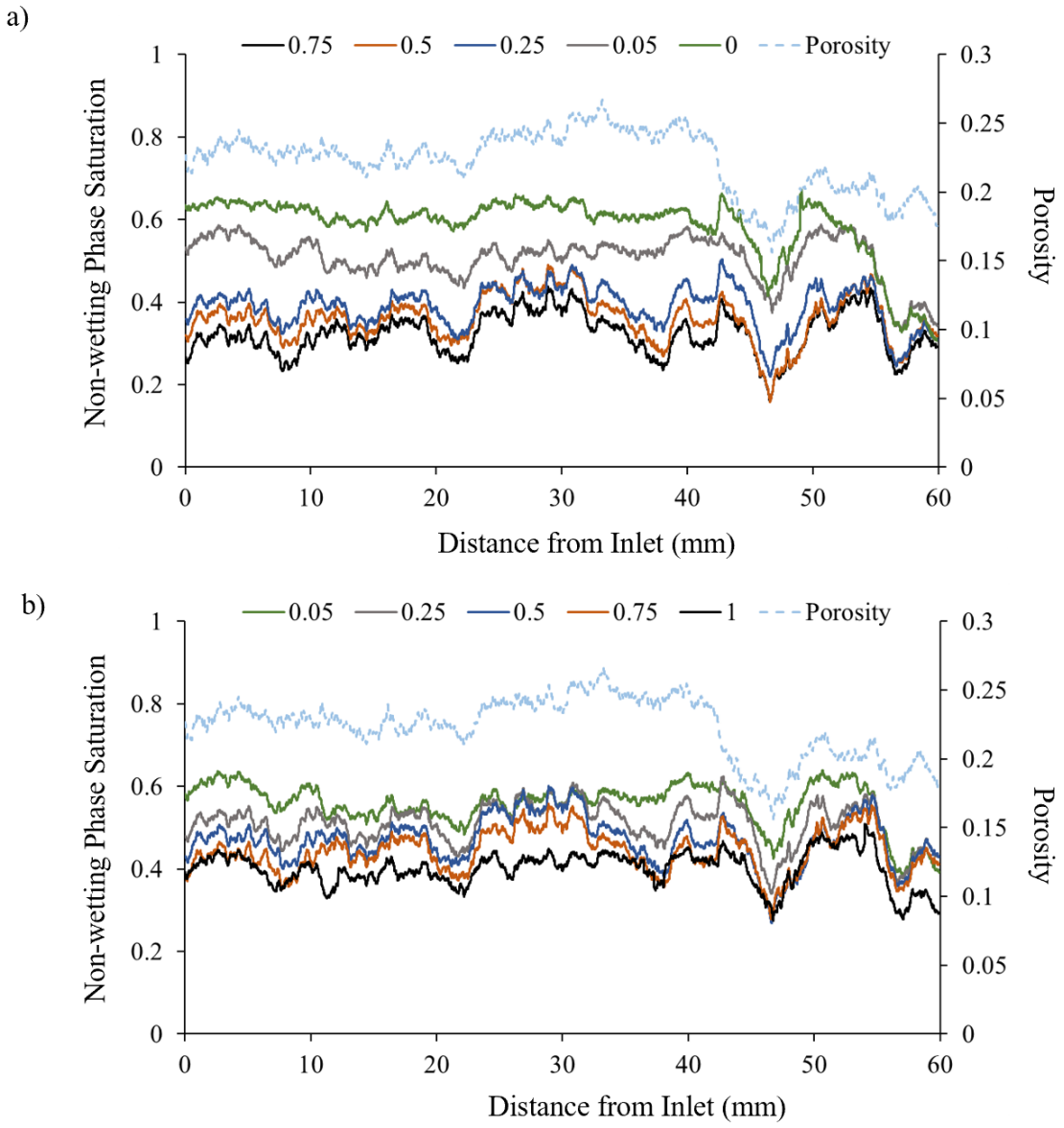


Figure 6.4 a) 1D saturation profiles across the length of the sample during drainage (the legend indicates the imposed brine fractional flow). b) 1D saturation profiles across the length of the sample during imbibition (the legend indicates the imposed brine fractional flow).

Table 6.3.1 Average non-wetting phase saturation during the experiment.

Brine fractional flow (f_w)	**Cycle**	**Average non-wetting phase saturation**
0.75	Drainage	0.32
0.5	Drainage	0.38
0.25	Drainage	0.43
0.05	Drainage	0.50
0	Drainage	0.55
0.05	Imbibition	0.54
0.25	Imbibition	0.50
0.5	Imbibition	0.47
0.75	Imbibition	0.44
1	Imbibition	0.41

A notable observation is that partial barrier region remains brine-saturated throughout the experiment and not invaded by the non-wetting phase even under 100% decane injection at the end of drainage. As shown in Figure 6.5, the tight downstream interval retains brine in both drainage (Figure 6.5a) and imbibition (Figure 6.5b) and demonstrates that decane could not enter those pores at any stage. This implies that the local capillary entry pressure in this zone exceeded the driving capillary pressure applied during the experiment. According to capillary pressure theory, smaller or poorly connected throats require higher threshold pressures (described by the Young–Laplace equation) for non-wetting phase invasion. Because this threshold was not reached, the pores remained brine-filled from start to finish, acting as a capillary barrier that blocked non-wetting advance and redirected flow along alternative pathways. This aligns with the findings of Pak et al. (2015) where they showed that relatively

large pores connected by numerous small throats can act as capillary barriers, preventing invasion of the non-wetting phase and promoting local trapping.

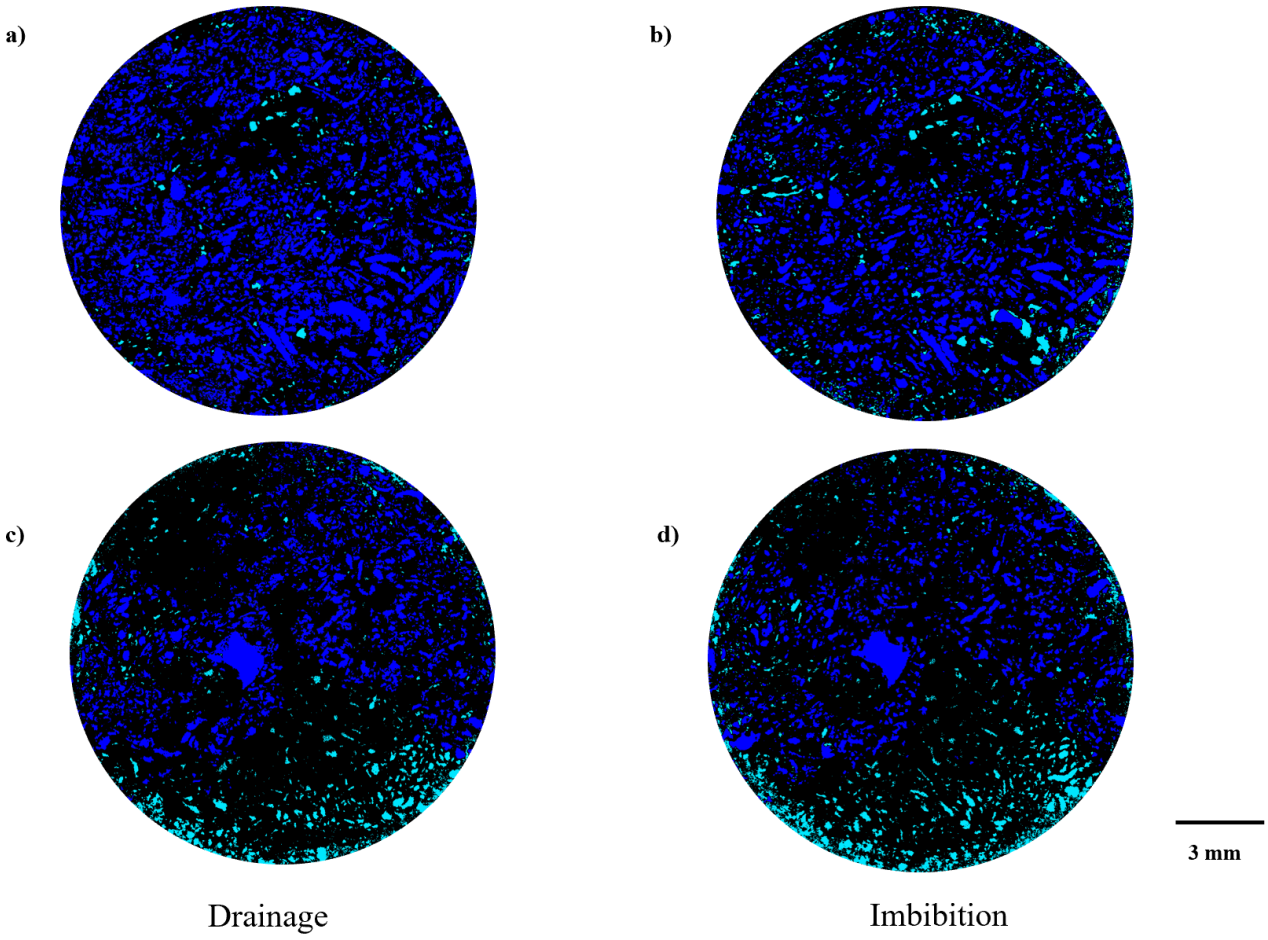


Figure 6.5 Representative 2D cross-sections segmented images extracted from 3D micro-CT images at the end of drainage (f_w =0) and imbibition (f_w =1), captured from two distinct regions of the sample. Panels (a) and (b) correspond to a higher-porosity zone, while panels (c) and (d) are taken from a lower-porosity region, illustrating spatial variability in fluid distribution as a function of local porosity (black is grain, green is brine, and blue is decane).

Figure 6.6 provides a voxel-by-voxel view of sample where porosity and saturation are averaged in a 2 mm cube. The dry scan (Figure 6.6a) shows the spital distribution of the porosity profile, highlighting regions of higher and lower porosity. During drainage (Figure 6.6b), the non-wetting phase progressively fills the accessible pore space, accumulating at higher saturation upstream of the low-porosity zone, while the barrier region itself remains at

low saturation. Moreover, at the end of imbibition (Figure 6.6c) at full brine injection shows that while displacement occurs, a high residual saturation is clearly visible, confirming the combined roles of residual trapping and heterogeneity-driven capillary barriers in controlling fluid distribution.

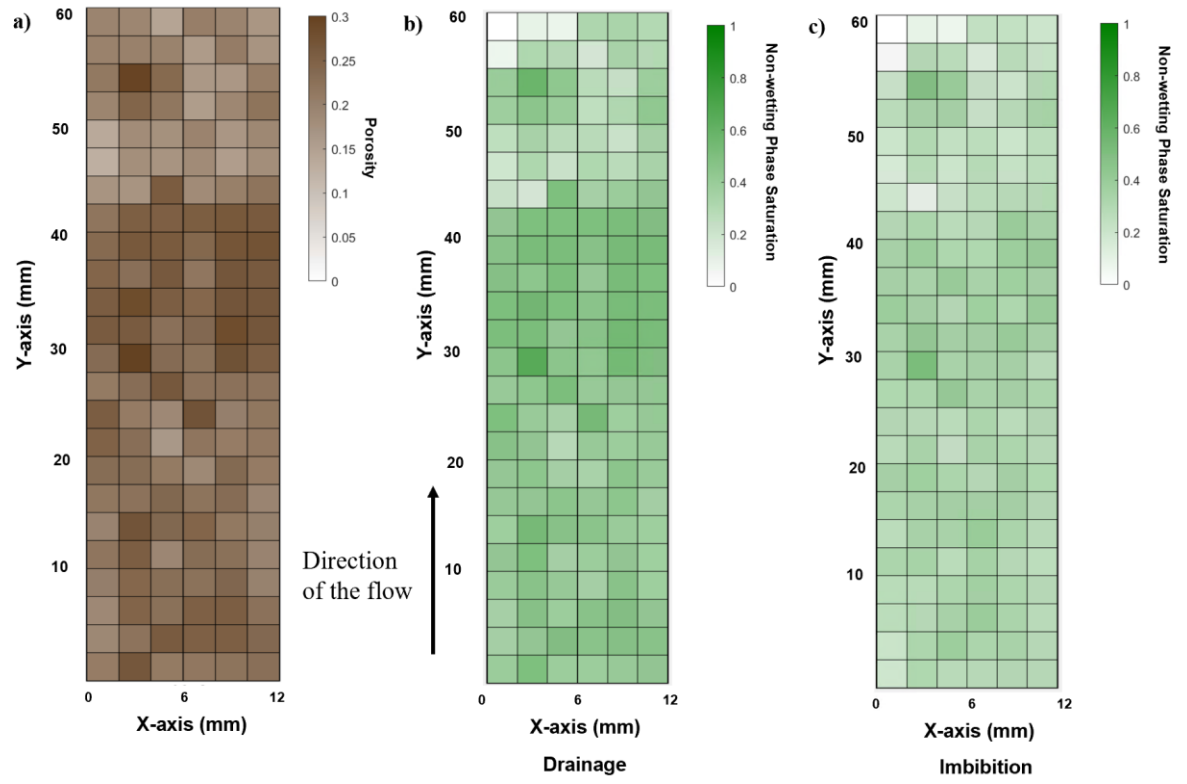


Figure 6.6 A voxel-by-voxel (coarse-grained) saturation distribution for the middle slice, obtained from the segmented micro-CT image. The fine-scale saturation field was upscaled in MATLAB by spatially averaging voxel-scale saturation over larger computational blocks, yielding the coarsened saturation map shown. (a) dry scan, illustrating pore space distribution (porosity); (b) drainage, showing non-wetting phase (oil) saturation at a water fractional flow (fw= 0); and (c) imbibition, displaying oil saturation at water fractional flow (fw= 1).

6.3.2 Relative Permeability

Relative permeability measurements directly connect the pore-scale trapping mechanisms observed with their manifestation at the continuum scale. The hysteresis in relative permeability represents the macroscopic response to pore-scale processes such as snap-off, disconnection, and capillary barrier formation, demonstrating how internal heterogeneity governs both localised trapping and overall flow behaviour.

The relative permeabilities obtained from drainage and imbibition cycles (Figure 6.7) showed pronounced hysteresis in the non-wetting phase, alongside smaller hysteresis in the wetting phase, as typically expected in strongly water-wet porous media (Krevor et al., 2011). At the end of imbibition, the non-wetting phase relative permeability shifts to the left (lower wetting phase saturation), indicating a reduction in relative permeability consistent with significant phase immobilisation and enhanced residual trapping. The endpoint saturations further confirmed this interpretation, exhibiting a high residual non-wetting phase saturation. These findings align closely with those reported in Chapters 4 and 5, and by Manoorkar et al. (2021) who demonstrated an increased residual trapping in Edwards dolomite with initial and residual saturations of 28% and 20%, respectively. They also concluded that that the flow behaviour is strongly controlled by the heterogeneity across multiple flow rates.

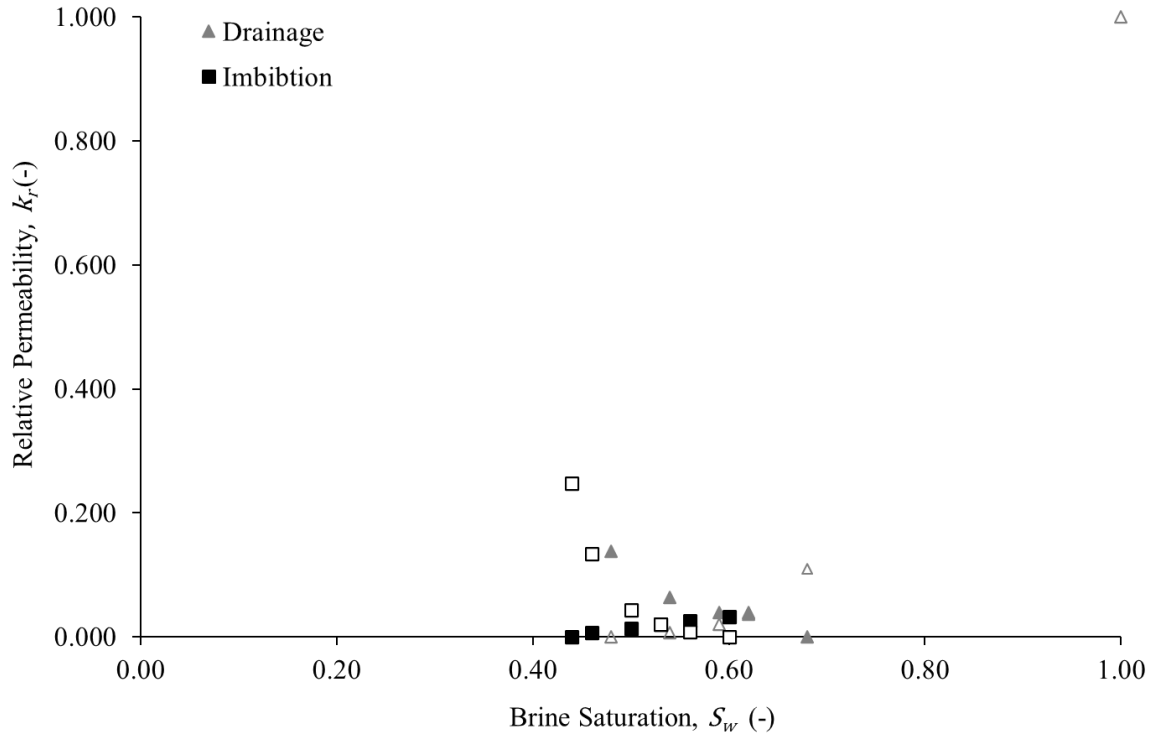


Figure 6.7 Relative permeabilities showing drainage and imbibition cycles for wetting and non-wetting phases.

6.3.3 Trapping Behaviour

One of the primary objectives in geological CO_2 storage is to maximise the extent of residual trapping namely, the amount of injected CO_2 that becomes immobilised as disconnected ganglia once brine reoccupies the pore space (Doughty et al., 2004; Pentland et al., 2017; Huang et al., 1995; Li et al., 2012; Ni et al., 2019). We assessed trapping efficiency by comparing the slice average non-wetting phase saturation along the sample at the end of drainage and imbibition. Across the full sample, a large proportion of the non-wetting phase introduced during drainage remained in place as isolated residual clusters following brine reinjection. Overall, the rock exhibited high volume of trapped non-wetting phase saturations with initial saturation of 55% and residual saturation of 41%.

Furthermore, a spatial variation in trapping efficiency was observed when comparing the bulk rock to regions adjacent to the partial capillary barrier (Figure 6.8). As in Chapters 4 and 5 the sliced-averaged residual saturation is plotted as a function of the sliced-average initial saturation. The barrier region exhibited a particularly high degree of trapping, with data points approaching the 1:1 line indicating that nearly all the non-wetting phase initially present remained immobilised after imbibition. The slightly higher residual saturation immediately downstream of the barrier is attributed to the accumulation of disconnected non-wetting ganglia trapped against the barrier and retained during imbibition. The subsequent decrease in saturation towards the outlet reflects a capillary end effect, where reduced entry pressure at the open boundary facilitates enhanced brine invasion. This behaviour is consistent with restricted phase accessibility due to finer pore structures and higher entry pressures in the barrier zone, leading to enhanced capillary trapping or build up behind the partial barrier.

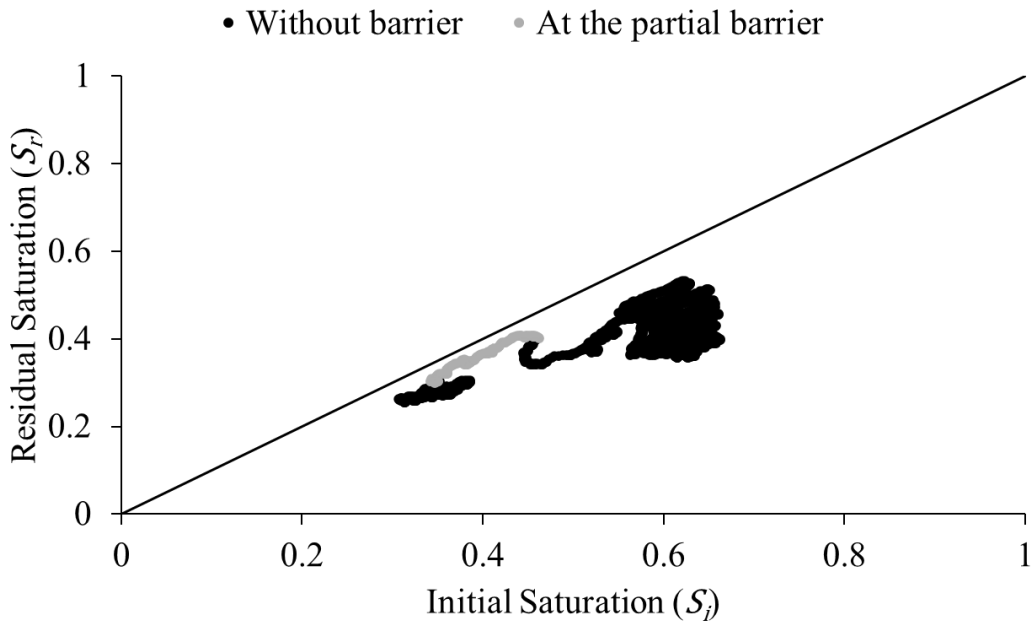


Figure 6.8 Slice average initial saturation versus residual saturation along the sample (grey is at the partial capillary barrier and black is the rest of the sample).

To further investigate the spatial characteristics of residual trapping, a ganglia analysis was conducted. After segmentation, each disconnected cluster of the non-wetting phase was uniquely labelled, allowing for quantitative analysis of ganglia count and spatial distribution, as shown in Figure 6.9. At the end of drainage, the pore space was dominated by a single large, connected non-wetting phase ganglion extending longitudinally, consistent with piston-like invasion behaviour. However, in the vicinity of the partial barrier region, we observed a higher count of disconnected ganglia relative to other regions, which is not consistent with piston-like invasion. These observations indicate that the barrier region triggered early fragmentation of the invading phase, most likely due to locally elevated capillary entry pressures and limited pore connectivity. Roof snap-off could also account for such fragmentation, as it can generate either temporary or permanent isolation of the non-wetting phase depending on local geometry and pressure conditions (Roof, 1970; Herring et al., 2013; Blunt, 2017; Holtzman et al., 2015). However, because no reconnection or coalescence of the phase was observed and given the strong correlation with the low-porosity barrier, the evidence points more convincingly to

capillary thresholding and connectivity constraints rather than Roof snap-off as the dominant mechanism.

Following imbibition, the single large ganglion had broken down into numerous smaller ganglia distributed more uniformly throughout the sample. This increase in ganglia count reflects the onset of the snap-off trapping mechanism during brine re-invasion (Pickell et al., 1966; Herring et al., 2013). Notably, after imbibition in the barrier region, the ganglia count remains almost similar to that of the drainage.

These observations support the findings from the trend of residual saturation as a function of initial saturation, Figure 6.8, that the barrier region acts to retain the non-wetting phase behind it, promoting early disconnection and enhancing the overall trapping efficiency. Hence, residual trapping in this sample arises from two distinct mechanisms: pore-scale snap-off and build-up of the non-wetting phase behind the capillary barrier.

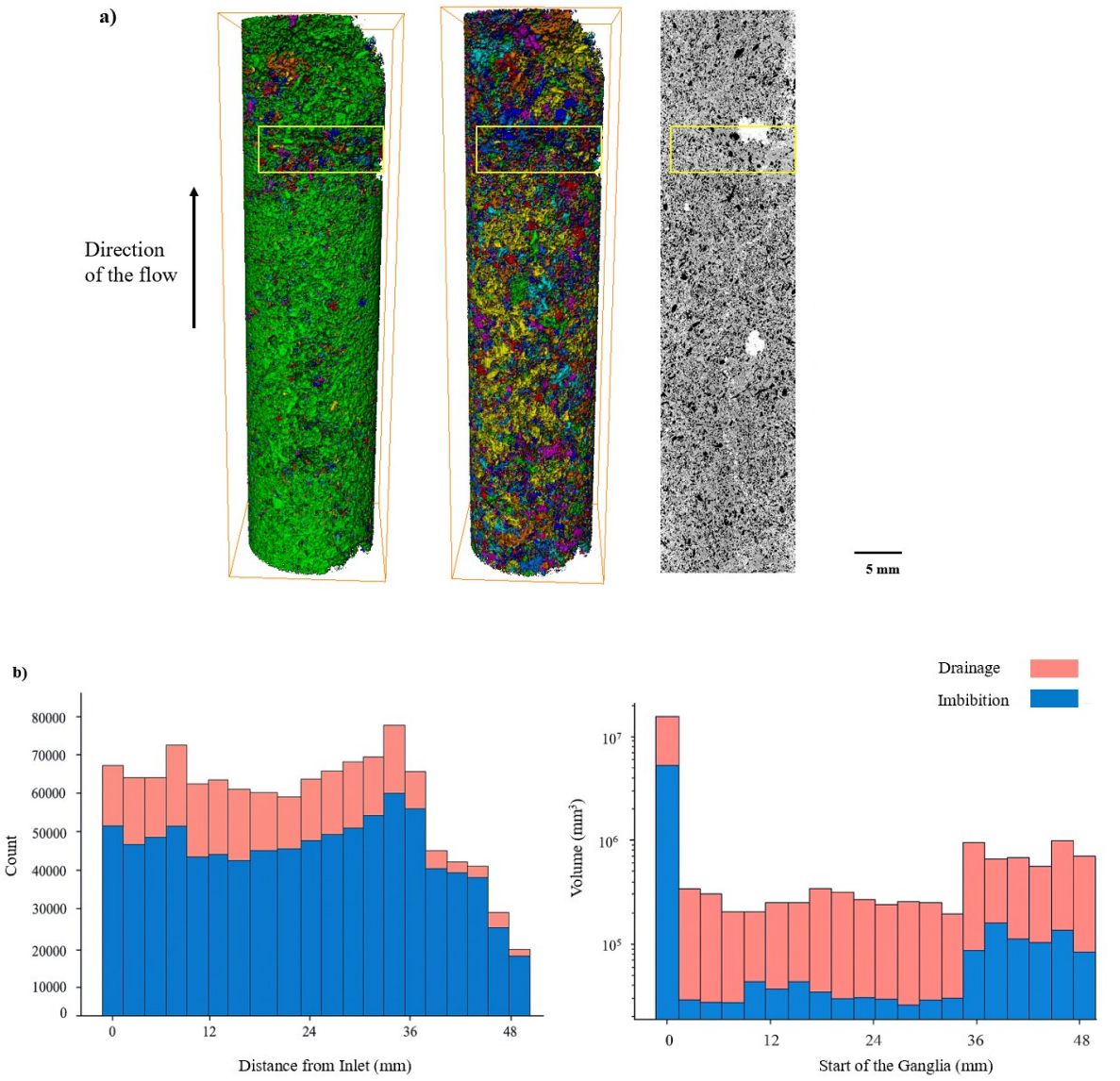


Figure 6.9 Ganglia analysis of the non-wetting phase across the sample. (a) 3D rendered volumes showing ganglia distribution at the end of drainage and imbibition. At the end of drainage, a single large, connected ganglion (green) spans the sample, with smaller disconnected clusters appearing primarily near the barrier region. Following imbibition, the phase becomes fragmented into numerous smaller ganglia, as indicated by the multicoloured blobs. (b) On the left is the ganglia count across the sample at the end of drainage and imbibition, highlighting an increase in the number of disconnected clusters away from the barrier region and retention of ganglia count around the barrier region after brine re-invasion (drainage count is the subtraction of the y-axis value and imbibition). On the right is the distribution of ganglia volumes along the sample axis at the end of drainage and imbibition, illustrating the breakdown of the large ganglia at the end of drainage to smaller ones after imbibition. (drainage volume is the total shown on y-axis).

6.3.4 Pore Network Occupancy and Connectivity

The pore network modelling and occupancy analysis (Foroughi et al., 2020; Foroughi et al., 2021) was performed on the sub-volumes of equal size across the length of the sample (Figure

6.10a). The sub-volumes are selected at the barrier region and away from the barrier to be able to make a direct comparison of the connectivity and displacement patterns. The resolved throat size distribution within the barrier region exhibits narrower throats compared to the upstream region away from the barrier zone (Figure 6.10b).

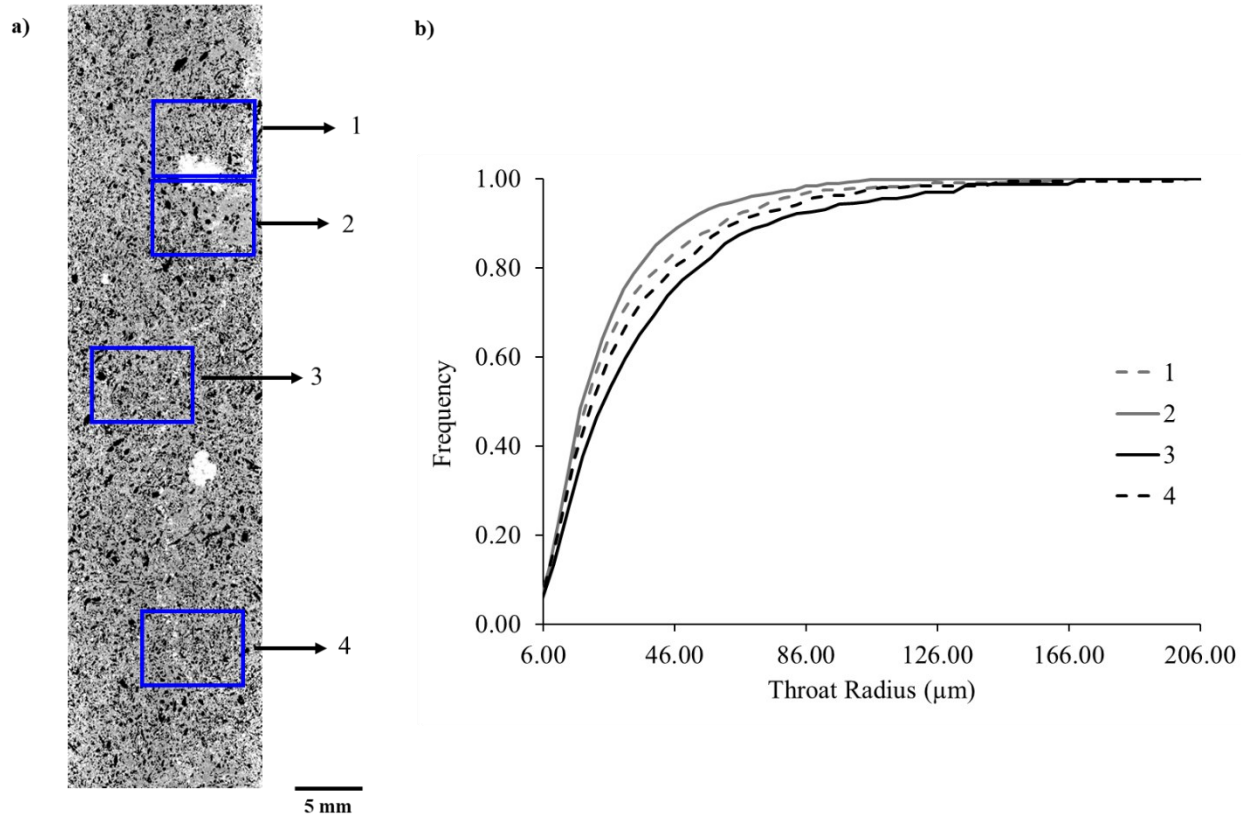


Figure 6.10 a) Spatial distribution of selected sub-volumes across the sample, used for detailed analysis. 1 and 2 denotes the barrier zone characterised by reduced porosity and distinct flow behaviour; 3 and 4 corresponds to a higher porosity zone located away from the heterogeneity barrier. b) throat-size distribution of sub-volumes 1, 2, 3 and 4.

The detailed pore-by-pore occupancy analysis during drainage and imbibition provides direct link between the entry capillary pressure (controlled by throat radius), (equation 2.5) to displacement behaviour. Figure 6.11 illustrates the evolution of the non-wetting phase occupancy in the selected sub-volumes both in pores and throats, respectively. During drainage and subsequent imbibition, the barrier regions (1 and 2) exhibit minimal changes saturation between the two flow stages in pores, while in throats we only see the changes in the smaller

throats indicating limited fluid displacement and a high degree of residual non-wetting phase retention. This minor apparent changes in occupancy occur near the barrier boundaries where slightly larger throats are connected to smaller pore clusters or where the imaging resolution approaches the voxel limit. These do not represent full invasion but rather marginal redistribution within the partially resolved pore space. In contrast, the sub-volumes located away from the barrier (3 and 4) display more pronounced changes in phase occupancy, with larger displacement during imbibition. This contrast shows the influence of local heterogeneity and connectivity on phase displacement and trapping efficiency.

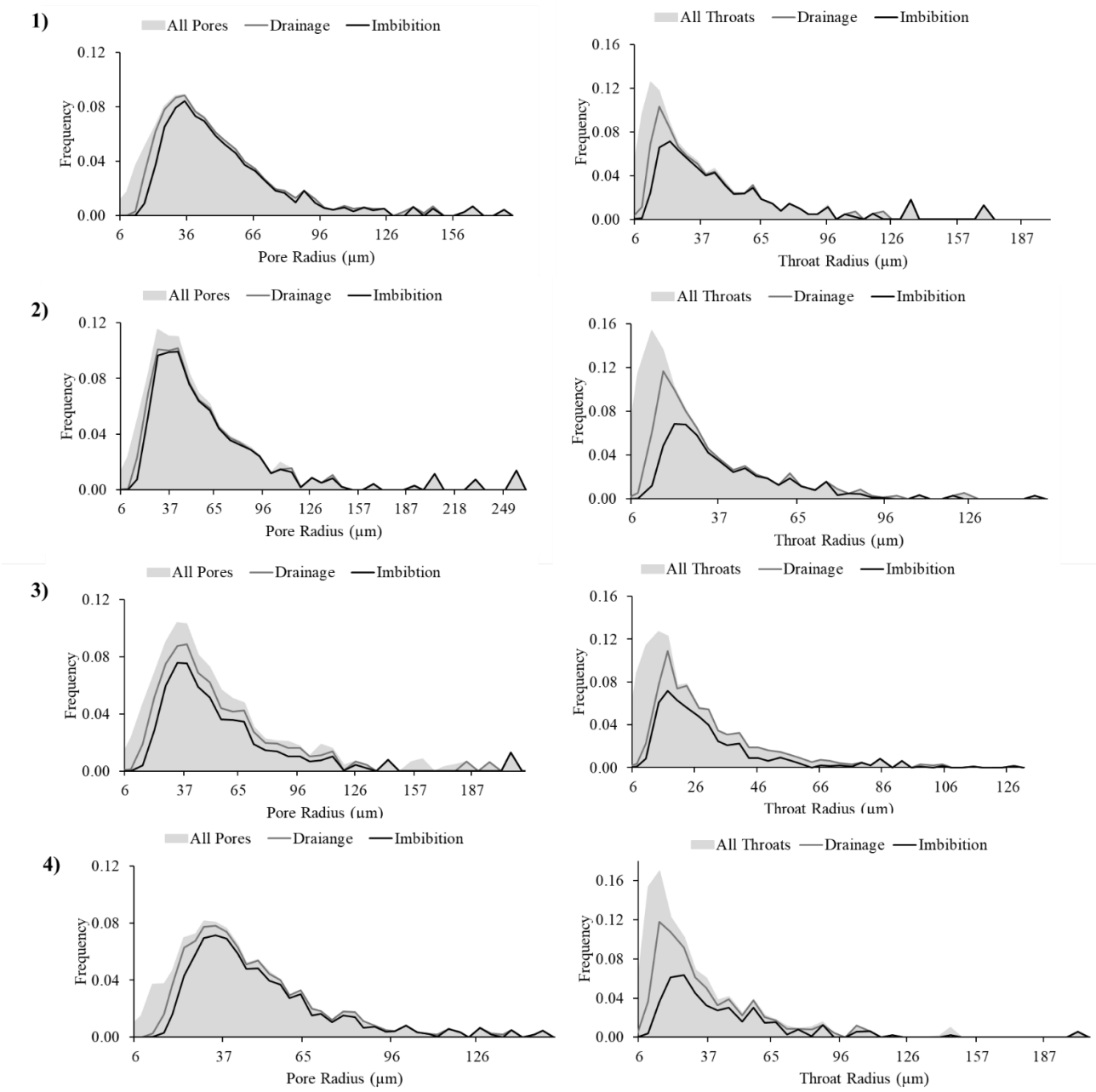


Figure 6.11 Pore and throat occupancy analysis comparing barrier and non-barrier regions. Panels 1, 2, 3, and 4 correspond to sub-volumes 1, 2, 3, and 4, respectively shown in Figure 6.10.

Two key pore-network metrics are the coordination number and the pore–throat aspect ratio. The coordination number, defined as the number of throats connected to a given pore (Blunt, 2017), quantifies network connectivity and directly impacts simulated flow behaviour and saturation patterns (Valvatne et al., 2004). In well-sorted, high-permeability sandstones such as Bentheimer or Berea, the mean coordination number is typically 4–6, reflecting a highly

interconnected structure (Dong et al., 2020; McCaskill et al., 2024). By contrast, the Edwards Brown dolomite exhibits a lower connectivity, with a mean coordination number of approximately 2; over 30% of the resolved pore bodies are connected by only two or fewer throats (Figure 6.12a). However, it is important to acknowledge the uncertainty introduced by imaging voxel size; sub-resolution throats may provide connections that are not visible in the images. However, no evidence of non-wetting invasion into such unresolved features was observed during the experiment. If the viscous pressure gradients during the experiment had been sufficient to overcome entry pressure of those, the non-wetting phase could have been seen in the "isolated" pores. Since this was not the case, it implies that those connections did not activate, and these pores remain occupied by brine.

The second metric and the more important one, is aspect ratio, defined as the ratio of pore radius to the average radius of its connecting throats (Blunt, 2017). A higher aspect ratio indicates large pores connected by narrower throats, a geometry that strongly favours snap-off during imbibition. In the Edwards Brown dolomite, the barrier region shows higher aspect ratios compared to the other regions, implying an increased likelihood of snap-off and enhanced residual trapping.

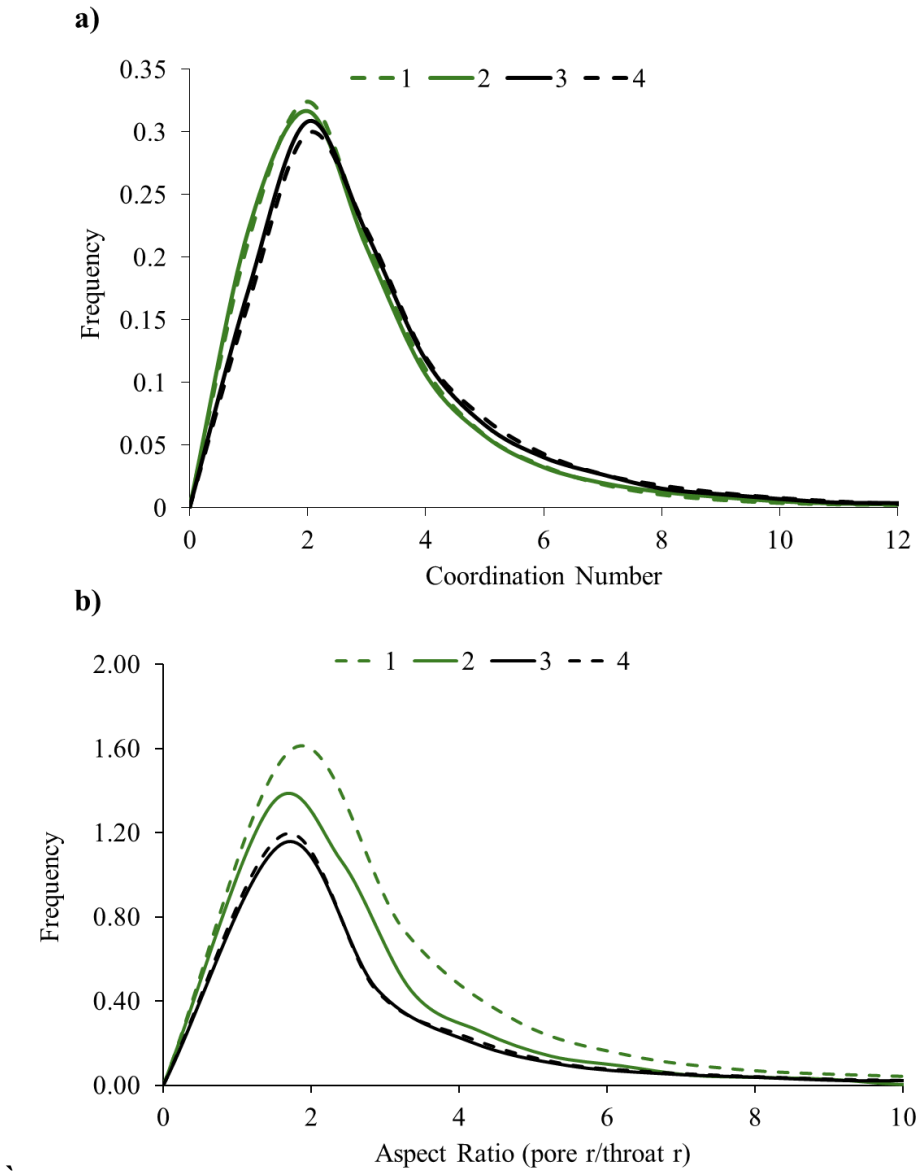


Figure 6.12 a) Distribution of coordination number and b) aspect ratio. These distributions are evaluated for the four sub-volumes shown in Figure 6.10.

6.3.5 Entry Capillary Pressure

The Young–Laplace equation (Equation 2.5) provides a quantitative basis for estimating capillary entry pressures as a function of pore throat diameter, interfacial tension, and contact angle. For our water–decane system with an interfacial tension of approximately 47 mN/m, a throat diameter of 5 μm corresponds to an entry pressure near 0.02 MPa, comfortably within

our imposed flow conditions. In contrast, throats in the 0.6 µm range would require entry pressures exceeding 0.3 MPa and remained sealed with brine during our experiment.

Upon analysing the average throat sizes and applying the Young–Laplace equation to the four sub-volumes, we observed that the barrier region exhibits higher capillary entry pressures than the areas away from it as shown in Figure 6.13.

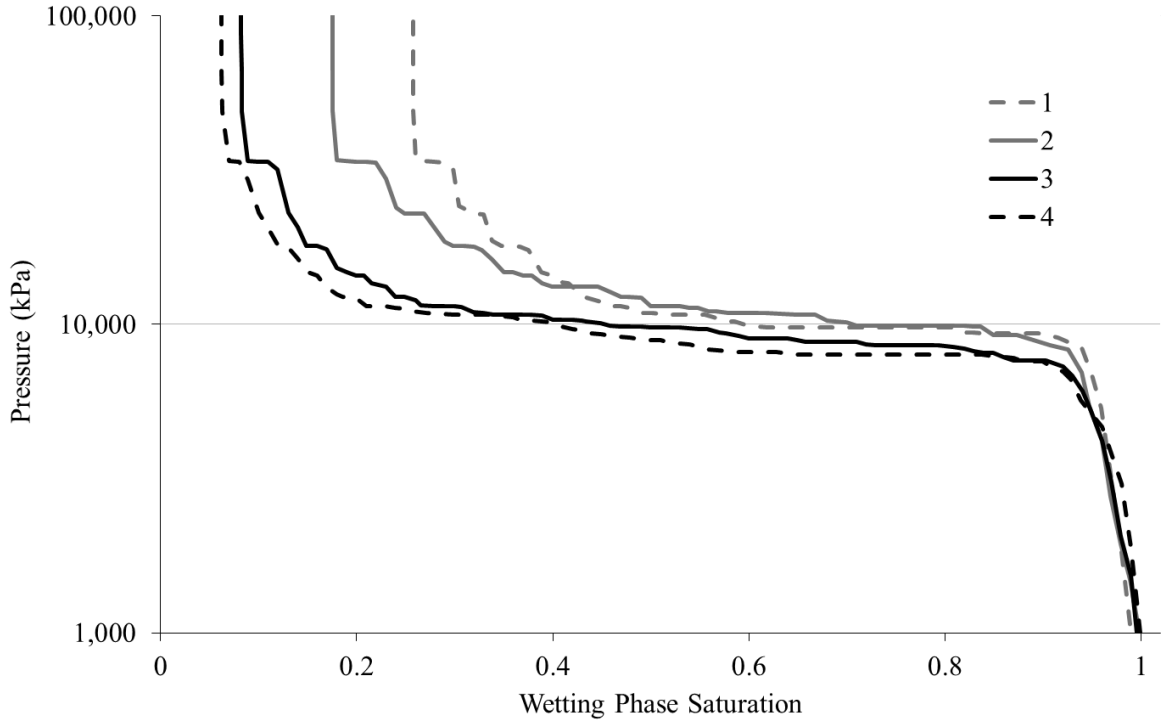


Figure 6.13 Entry capillary pressure in the barrier region and away from the barrier. The four sub-volumes shown in Figure 6.10 are analysed.

As mentioned earlier, the four sub-volumes analysed are equal in size and image voxel size. Under such conditions, it is expected to have comparable number of resolved pores and throats across the selected regions. The extracted networks show that the resolved pore radii range from approximately 6 to 60 µm and throat radii from ~5.6 to 27 µm across the four sub-volumes (Table 6.2). Throats smaller than one voxel in radius (≈ 5.6 µm) are below the detection threshold and thus not explicitly represented in the analysis. In the barrier sub-volumes, the number of identified pore bodies and connecting throats was nearly halved relative to the

regions away from the barrier (Table 6.2). This suggests that a substantial portion of the pore space in the barrier falls below the voxel size threshold of our imaging. As a result, the calculated capillary entry pressures in this region are likely underestimated, since unresolved pores and throats smaller than the voxel size would require even higher entry pressures to be invaded. Therefore, the true capillary threshold in the barrier is expected to be higher than what is inferred from the resolved structure.

This interpretation is reinforced by the absolute permeability measurements from the pore network, Table 6.2, shows that the barrier region exhibits values nearly an order of magnitude lower than those measured in the higher-porosity zones. Taken together, these observations indicate the presence of a smaller, more resistive pore structure within the barrier and highlights the critical role of local pore structure in controlling phase accessibility and flow.

The analysis shows that enhanced trapping is controlled by a combination of factors, with capillary entry pressure, coordination number, and pore–throat aspect ratio playing the most significant roles. Elevated entry pressures limit invasion across the barrier, coordination number shows a limited connectivity, and high aspect ratios favour snap-off during imbibition, together producing the persistent immobilisation observed in this sample.

One of the main observations is that a digital rock workflow provides a practical way to evaluate these mechanisms directly from micro-CT images. Regions of reduced porosity can be mapped as potential barriers, and pore-network analysis offers further diagnostics. Aspect ratios highlight where snap-off is likely to occur, coordination number gives an indication on connectivity, while capillary pressure functions capture threshold behaviour and the extent of capillary trapping. Taken together, these metrics describe the two complementary components of the trapping process—snap-off, governed by geometry and connectivity, and capillary thresholding, governed by entry pressure contrasts. Flow experiments remain valuable for

confirmation, particularly in clarifying the role of sub-resolution porosity, since displacement patterns provide evidence of whether hidden connections contribute to fluid migration or remain inactive.

Table 6.3.2 Summary of the pore network analysis for the four sub-volumes (barrier region and away from the barrier).

Sub-volume	Porosity (%)	Permeability (mD)	Number of Pores (10^3)	Number of Throats (10^3)	Pore radius range (µm)	Throat radius range (µm)	Average Entry Pressure (kPa)
Barrier (1)	17	12	41	40	6 – 42	5.6 – 18	12
Barrier (2)	19	13	45	42	7 – 45	5.6 – 19	11
Away from barrier (3)	24	103	68	76	8 – 58	6 – 25	9
Away from barrier (4)	25	112	70	80	9 – 60	6 – 27	9

6.4 Implications for larger scale flow

The central uncertainty in extrapolating from pore-scale observations is how connectivity within the imaged domain continues into larger volumes beyond the micro-CT sample. A single centimetre-scale plug captures only a fraction of the connectivity architecture that governs plume migration in the reservoir. Whether the barriers and low-connectivity zones observed at the pore scale persist, merge, or average out at larger scales remains an open question, but their impact must be considered when linking pore-scale metrics to reservoir-scale parameters.

A second consideration is the difference in pressure regimes between laboratory and field conditions. In the core-flood experiments presented here, the viscous pressure drop across the

6-cm plug is relatively small, meaning that invasion is dominated by capillary thresholds and limited to the most accessible pathways. In the field, however, a plume migrating over tens to hundreds of metres will experience larger viscous pressure gradients and gravity–capillary interactions that can overcome additional entry pressures. This raises the possibility that more pores may be invaded under reservoir conditions than are accessed in the laboratory. Manoorkar et al. (2021) provide supporting evidence, showing that increasing viscous forces by an order of magnitude accessed additional pore space and modestly shifted initial saturations from 28% to 33%. Importantly, while this effect demonstrates that field-scale forces can mobilise some additional pore space, the overall trapping efficiency remained high, confirming that heterogeneity-driven barriers continue to exert a strong influence even under more favourable displacement conditions.

Together, these observations suggest that pore-scale diagnostics such as coordination number, aspect ratio, and capillary entry pressure provide a lower-bound estimate of trapping potential. Field conditions may mobilise some otherwise isolated pores, but the persistence of barriers and snap-off geometries means that heterogeneity-driven trapping remains a controlling factor at reservoir scale.

In summary, upscaling pore-scale heterogeneity into continuum-scale models requires translating geometric and topological features into effective constitutive parameters. The metrics derived here (coordination number, pore–throat aspect ratio, and entry pressure can be embedded in models to represent local variations in connectivity. For example, locally elevated capillary entry pressures associated with barrier zones can be represented as subgrid-scale contrasts in the entry-pressure field, which in turn govern plume fingering and trapping at the Darcy scale. Similarly, coordination number and aspect ratio statistics can be used to define

effective residual saturation functions or trapping coefficients that vary spatially according to heterogeneity intensity.

Beyond parameterisation, these observations also motivate stochastic or multiscale modelling approaches, in which pore-scale heterogeneity is explicitly sampled to inform the statistical structure of continuum models. Such approaches have already been applied to sandstones with layered heterogeneity, but comparable efforts for carbonate systems remain limited (Wang et al., 2022).

6.5 Conclusions

This study examined the influence of pore-scale heterogeneity on multiphase flow behaviour and trapping mechanisms in an Edwards Brown dolomite sample under capillary-dominated conditions representative of the capillary limit relevant to geological CO_2 storage. Using micro-CT imaging we directly visualised fluid configurations during drainage and imbibition, capturing the effects of local pore structure on saturation distribution, fluid accessibility, and residual trapping.

The sample exhibited substantial heterogeneity both in the overall structure and in the upstream region the acts as a partial capillary barrier. This region resisted invasion by the non-wetting phase during drainage, even at high fractional flow, leading to accumulation of the non-wetting phase upstream. Moreover, the mean coordination number of roughly two indicates limited pore connectivity, which restricts fluid mobility, while the high pore–throat aspect ratios in the barrier region further promote early snap-off during imbibition. Together, these factors explain the residual trapping observed in the system (initial saturation 55%, residual saturation 41%), which arises from a combination of pore-scale snap-off and accumulation of the non-wetting phase behind the capillary barrier.

These findings stress the relevance of recognising and incorporating pore-scale heterogeneity in the design and modelling of CO_2 storage operations. While such heterogeneity can enhance trapping and contribute to long-term containment, it can also limit accessible pore volume and skew estimates of plume migration if not properly accounted for. Conventional models that treat carbonate formations as homogenous media risk oversimplifying this complexity, potentially underestimating both residual trapping and flow diversion. As seen from this rock, the increased trapping observed in the barrier region is best explained as a combined effect of multiple factors. In this setting, pores are either not invaded or invaded but quickly disconnected as the non-wetting phase is pinched off, a behaviour that is captured by the elevated pore–throat aspect ratios measured in the barrier. This implies that predictive models cannot rely solely on a Darcy-scale description, since a standard drainage capillary pressure alone does not capture the enhanced trapping. Instead, pore-scale diagnostics such as aspect ratio and coordination number are needed to explain and predict the observed immobilisation.

Methodologically, this study demonstrates the power of combining pore-scale imaging with dynamic displacement experiments to investigate the effect of heterogeneity on fluid flow in complex porous media. At the same time, the work highlights current limitations in segmentation and voxel size constraints, which introduce uncertainty into network-based metrics such as coordination number. Continued advances in image processing and multi-scale characterisation are needed to resolve these ambiguities and support more accurate pore-to-field scale translation.

The use of n-decane as an analogue for CO_2 under ambient conditions likely results in higher apparent residual saturations than would be observed with supercritical CO_2 at reservoir pressure and temperature. This arises from the higher interfacial tension and higher viscosity of n-decane relative to CO_2, which suppress viscous instabilities and enhance capillary

immobilisation. Consequently, while the absolute saturation values reported here should not be interpreted as direct quantitative predictions for CO_2, the displacement and trapping mechanisms we observe are representative of those that occur under capillary-dominated flow in heterogeneous formations.

At the same time, our results provide a mechanistic foundation for upscaling. The pore-scale observations of barrier-induced trapping and limited connectivity can be translated into continuum models through parameters such as effective capillary entry pressure distributions, aspect ratio–controlled snap-off functions, and local trapping coefficients. These findings highlight that heterogeneity exerts a first-order control on plume migration and immobilisation efficiency that must be explicitly incorporated into large-scale simulations of CO_2 storage in carbonates. This study demonstrates how internal heterogeneity governs the structure and persistence of residual trapping and provides direct pore-scale evidence of its controlling influence on subsurface flow and storage security.

Overall, the results contribute to a more nuanced understanding of how fine-scale rock features impact CO_2 storage performance. By explicitly accounting for internal barriers, and limited connectivity, future reservoir models can better reflect the physical realities of carbonate systems. This will enable more robust predictions of plume behaviour, more informed risk assessments, and ultimately, more secure long-term carbon storage

Chapter Seven Conclusions and Future Work

7.1 Thesis Summary

The primary objective of this thesis is to determine how pore-scale heterogeneity manifest in larger-scale affecting continuum scale properties, with direct relevance to geological CO_2 storage. Although the work is motivated by carbon storage applications, the findings also apply more broadly to multiphase transport in heterogeneous porous media, where spatial contrasts in capillary entry pressure and connectivity can reorganise invasion pathways and modify effective flow behaviour.

As established in Chapter 1 and 2, reservoir simulators operate on discretised grids with typical cell dimensions of metres to tens of metres, far coarser than the small-scale heterogeneities presents and consequently, on which relative permeability and capillary pressure functions are measured. The central practical challenge is therefore to assign effective saturation functions to each grid block that reliably represent the integrated multiphase flow response of heterogeneous rock volumes, despite the fact that much of this heterogeneity remains unresolved at the grid scale.

Chapter 2 reviews the physical basis of multiphase flow and trapping in geological CO_2 storage, with emphasis on how constitutive relationships, particularly relative permeability, and capillary pressure, are measured and then transferred into continuum-scale models. The chapter highlights the central limitation addressed in this thesis, namely that heterogeneity at pore to centimetre scales is frequently homogenised in practice, despite its capacity to generate spatially structured saturation fields and non-representative trapping responses.

Chapter 3 describes the experimental and analysis framework used throughout the thesis. It presents the steady-state drainage and imbibition core flood protocols, the medical X-ray CT

workflow used to quantify core-scale saturation profiles during flow, and the micro-CT based structural characterisation and pore-network diagnostics used to interpret heterogeneity in terms of entry-pressure contrasts and connectivity. Methodological uncertainties, including imaging voxel size limits and segmentation sensitivity, are documented to support a defensible interpretation of derived flow properties.

Chapter 4 applies this framework to reservoir sandstone samples from a potential storage-site to test whether centimetre-scale variability within a single reservoir interval can lead to distinct saturation evolution and trapping outcomes. The results demonstrate that even closely spaced samples can exhibit markedly different saturation profiles and trapping curves under comparable experimental conditions, implying that assuming within-interval representativity can introduce material error when parameterising reservoir simulations for CO_2 storage.

Chapter 5 investigates Indiana limestone to isolate the role of millimetre-scale heterogeneity in carbonates. By combining core flood-derived saturation profiles with pore-scale structural analysis, the chapter shows that spatial organisation of entry-pressure contrasts can produce layered or preferential displacement and that modest changes in flow conditions within a capillary-dominated regime can redistribute the non-wetting phase between heterogeneity domains. These effects translate into measurable shifts in effective relative permeability and residual trapping behaviour.

Chapter 6 extends the analysis to Edwards Brown dolomite, where heterogeneity is more pronounced and organised over larger length scales. The chapter demonstrates how low-connectivity regions and elevated entry pressures act as partial barriers that restructure saturation pathways and enhance heterogeneity-mediated trapping. Together with Chapter 5, these carbonate case studies show that heterogeneity length scale and organisation relative to

flow direction are decisive in determining whether heterogeneity is averaged out or becomes a first-order control on continuum-scale multiphase properties.

Collectively, the thesis provides a coherent experimental basis for linking heterogeneity-controlled saturation structure to effective relative permeability and trapping behaviour in real reservoir and carbonate rocks. The results imply a practical implication for CO_2 storage modelling: laboratory-derived constitutive functions should be treated as conditional on heterogeneity and scale, and their transfer to field-scale simulations should explicitly incorporate uncertainty associated with within-interval variability and heterogeneity-driven flow organisation.

Table 7-1: Comparative summary of the samples, heterogeneity characteristics, and principal findings across Chapters 4 to 6

Sample	**Dominant heterogeneity**	**Main saturation behaviour**	**Relative permeability / trapping response**	**Main implication**
Reservoir Sandstone (1)	Centimetre-scale cemented regions in an alternating pattern.	Saturation profile is relatively uniform across the core; pore-network analysis is consistent with essentially one capillary pressure response	Shows classical residual trapping, with residual saturation remaining below initial saturation, consistent with pore-scale snap-off	Provides the closest thing to a "representative" response, but only in contrast to Sample 2, showing that even apparently similar samples cannot automatically be treated as equivalent
Reservoir Sandstone (2)	Centimetre-scale capillary heterogeneity associated with	Develops strong saturation gradients and incomplete non-wetting	Trapping is strongly enhanced by barrier-controlled immobilisation; some	Demonstrates that within-interval representativity can fail, even for samples that would normally be

	different cementation distribution and internal capillary barriers	invasion; pore-network analysis indicates two distinct capillary pressure responses	regions plot above the classical 1:1 initial-residual expectation, indicating heterogeneity-driven redistribution rather than simple snap-off alone	grouped into one rock type in reservoir simulation
Indiana limestone	Millimetre-scale heterogeneity, with local capillary entry pressures varying by nearly a factor of two across sub-volumes	At lower flow rate, displacement is layered / preferential and more strongly correlated with local porosity and entry pressure; at higher flow rate, the saturation profile becomes more uniform as viscous forces partially overcome local capillary barriers	Relative permeability is flow-rate dependent; curves shift with flow rate. At higher flow, the non-wetting phase accesses more pore space, yet its relative permeability decreases because transport remains dominated by preferential pathways. Trapping efficiency changes only modestly between the two flow rates	Shows that even within the capillary-dominated regime, effective flow properties are non-unique and flow-rate dependent when heterogeneity controls accessibility of the pore space
Edwards Brown dolomite	Centimetre- to decimetre-scale heterogeneity, with a low-connectivity	During drainage, the non-wetting phase accumulates upstream of the	Pronounced hysteresis and high residual saturation are observed, with initial saturation	Demonstrates that when heterogeneity becomes spatially organised over larger scales, trapping

	partial capillary barrier. Barrier sub-volumes have lower porosity and permeability and higher entry pressure than regions away from the barrier	barrier, while the barrier itself remains poorly invaded; during imbibition, high residual saturation persists	55% and residual saturation 41%. Trapping arises from a combination of restricted accessibility, limited connectivity, and snap-off, not from classical pore-scale residual trapping alone	becomes barrier-controlled and connectivity-limited, requiring continuum models to include heterogeneity-informed capillary thresholds and trapping descriptors

Viewed together, Chapters 4 to 6 show a consistent progression in the role of heterogeneity. Chapter 4 demonstrates that even centimetre-scale variability within a single sandstone interval can invalidate the assumption of representative constitutive behaviour. Chapter 5 then shows that, in carbonates, millimetre-scale entry-pressure contrasts produce flow-rate-dependent saturation structure and relative permeability, even when the system remains capillary dominated. Chapter 6 extends this further by showing that larger and more spatially organised heterogeneity can create partial capillary barriers, so that trapping is governed not only by pore-scale snap-off but also by barrier-controlled accumulation and limited connectivity. The combined implication is that continuum-scale flow functions are conditional on heterogeneity scale, organisation, and flow regime, rather than being intrinsic properties transferable across samples or scales.

7.2 Thesis Contributions

This thesis establishes, using experiments on complex carbonate rocks and reservoir rocks that pore-scale heterogeneity can dominate the continuum-scale multiphase flow properties that underpin predictions of CO_2 storage. The work departs from the common assumption that a

small number of "representative" samples can provide transferable constitutive functions for an entire reservoir interval and instead demonstrates that spatial variation of entry-pressure contrasts and connectivity can restructure saturation pathways and immobilisation, even when bulk porosity and permeability are close.

The principal contributions are summarised as follows:

1. The combination of medical X-ray CT for core-scale saturation profiling and micro-CT for pore-scale structural analysis has been established in prior studies, primarily on well-characterised model rocks such as Bentheimer sandstone. However, this thesis demonstrates this workflow is applicable on actual reservoir core samples from a potential CO_2 storage site (Chapter 4). This validation is significant because reservoir core samples often present practical challenges absent in model rocks.

   By relying on medical CT to quantify core-scale saturation distributions during flow, the workflow provides a robust basis for estimating relative permeability while avoiding the segmentation sensitivity that can dominate quantitative analysis when phase occupancy is derived directly from multiphase micro-CT. Micro-CT is instead used where it is strongest, to characterise pore architecture and extract network-scale descriptors, allowing the saturation structures observed in medical CT to be linked to pore-scale controls on invasion pathways and trapping.

2. Demonstration that millimetre-scale entry-pressure can generate layered displacement in carbonate rocks. Chapter 5 uses Indiana limestone as a controlled carbonate case to demonstrate that millimetre-scale heterogeneity expressed through multiple capillary thresholds can organise drainage into stratified or preferential pathways, producing layered saturation structure that persists into imbibition and affects residual trapping.

Under capillary-dominated conditions, modest changes in flow rate (and therefore capillary number) can redistribute the non-wetting phase between heterogeneity domains, effectively activating or deactivating pore regions that are accessible only once local entry thresholds are exceeded. This redistribution produces measurable shifts in effective relative permeability behaviour and alters the relationship between initial saturation and residual trapping, even though the flow regime remains below the threshold where viscous forces exceed capillarity.

3. Identification of barrier-controlled saturation build-up and immobilisation in a more strongly heterogeneous carbonate.

The analysis is extended where heterogeneity occurs over larger length scales and includes regions of reduced connectivity and elevated entry thresholds. As seen in Chapter 6, the effective trapped saturation can be strongly influenced by barrier-like regions that impede invasion and promote upstream accumulation.

This proves that, spatially oriented low-connectivity zones act as partial barriers, diverting flow and generating persistent saturation contrasts, with implications for both the spatial distribution of trapped non-wetting phase and the interpretation of "residual trapping" inferred from bulk measurements. In such systems, the effective trapped saturation is not solely a function of pore-scale snap-off and ganglion dynamics, it can be amplified by barrier-controlled saturation build-up at heterogeneity transitions.

4. Quantification of how heterogeneity orientation and length scale relative to flow direction controls continuum responses.

Across the reservoir sandstone and carbonate chapters, the thesis shows that heterogeneity is not only about "how much variation exists", but also about how it is arranged relative to the imposed flow direction and how its characteristic length scale compares with the sample length

and diameter. When capillary pressure contrasts are arranged such that flow repeatedly encounters transitions transverse to the dominant flow direction, saturation can become structured (layered or channelised), and the effective constitutive response can depart from what would be expected from bulk petrophysical averages.

The contribution is not the statement that heterogeneity matters, which is well known, but a coherent, evidence-based demonstration that orientation and length scale determine whether heterogeneity remains "averaged out" or becomes a first-order control on saturation and trapping. This provides a principled basis for deciding when upscaled single-curve parameterisations are defensible and when spatially varying constitutive descriptions, or at minimum uncertainty-aware ensembles, are required.

7.3 Recommendations for Future Research

The results presented in Chapters 4–6 demonstrate that pore-scale heterogeneity has an impact on continuum scale properties. Building on these findings, the following recommendations identify directions to strengthen representativity, extend applicability to storage conditions, and improve transfer of laboratory-derived multiphase flow functions to field-scale models.

7.3.1 Representativity and sampling across centimetre-scale reservoir variability

Future work should adopt structured sampling strategies that quantify within-interval variability, for example through closely spaced sister plugs, systematic core description aligned with sampling depth, and statistical characterisation of property distributions. The objective is to define how many plugs are required to bound the plausible range of relative permeability and trapping behaviour for a given reservoir unit, and how that variability should be mapped into simulation rock types and grid-block properties.

The reservoir samples demonstrated in Chapter (4) shows that closely spaced samples from a single reservoir interval can exhibit distinct saturation functions and trapping behaviour, challenging the assumption that one or two core plugs adequately represent an entire facies or rock type. However, the reality of reservoir characterisation is constrained by sample availability and cost: routine core analysis (RCAL) is typically performed at one-foot (≈30 cm) intervals to measure porosity and single-phase permeability, while special core analysis (SCAL) for relative permeability is conducted on far fewer samples due to time and expense (often only 1–3 plugs per facies or key interval). The practical challenge is therefore to estimate the plausible range of multiphase flow properties—including within-interval variability—when direct SCAL measurements are sparse and most characterisation data consist of RCAL properties and whole-core imaging. Hence, future work should develop approaches to infer constitutive function variability from more readily available data.

7.3.2 Protocol limitations

Future experimental work should expand the accessible parameter space by using higher-pressure-rated core holders and pumping systems, enabling stable operation on tighter rocks and over a broader range of flow conditions.

This would allow injection rates to be varied systematically, with clear separation between capillary-dominated and more viscous-dominated regimes, and with direct quantification of rate dependence in both saturation profiles and trapping metrics.

7.3.3 Improved segmentation, uncertainty quantification, and reproducibility

Image-derived saturation fields are the foundation for the constitutive functions and interpretations developed in this thesis. Future work should formalise uncertainty

quantification across the entire image-to-property pipeline, including scanner calibration, filtering choices, segmentation parameters, and connectivity definitions. This can be supported by: (i) sensitivity analyses that propagate segmentation uncertainty into flow-property uncertainty; (ii) benchmark datasets with repeated scans and controlled perturbations; and (iii) machine-learning-assisted segmentation or hybrid physics-informed workflows that improve robustness across heterogeneous carbonates.

7.3.4 Dissolution in equilibrated fluids and its interaction with residual trapping

Chapters 4-6 prioritise controlled interpretation of heterogeneity-driven displacement and trapping using proxy fluid systems in which dissolution is either negligible or not the dominant process. In field settings, however, CO_2 dissolution into brine can contribute materially to long-term immobilisation and can also modify local fluid properties, including density and interfacial tension, thereby coupling to capillary processes and residual trapping. (Fu et al., 2015)

Future work should quantify how dissolution alters the heterogeneity-controlled saturation structures observed in this thesis. A practical next step is to repeat selected core floods with CO_2–brine systems at representative pressure and temperature, explicitly comparing cases with (i) pre-equilibrated CO_2 and brine and (ii) non-equilibrated fluids. Even under nominal pre-equilibration, dissolution can persist due to concentration gradients, pressure and temperature transients, and mixing, and these effects can be assessed through coupled mass balance, time-lapse CT density changes, and post-test fluid sampling. In parallel, modelling studies should examine the competing roles of diffusion and density-driven convection in promoting dissolution, and how these processes interact with capillary heterogeneity at core and larger scales. (Fruton et al., 2023)

7.3.5 Pressure fluctuations and pore-scale invasion events

A recurring feature of multiphase displacement in porous media is that macroscopic flow can be composed of intermittent pore-scale invasion events, including rapid interface jumps as the non-wetting phase breaks through pore throats into larger pore bodies (often termed Haines jumps). These events are associated with transient drops in capillary pressure and can reorganise local fluid configurations, influencing subsequent invasion pathways and trapping outcomes. (Berg et al., 2013; Armstrong et al., 2015; Moura et al., 2020)

Future work should exploit pressure data more fully by acquiring differential pressure at higher temporal voxel size during drainage and imbibition steps and by analysing these signals in both the time and frequency domains. Synchronising high-frequency pressure measurements with time-lapse imaging would allow pore-scale events, capillary-barrier breakthroughs, and snap-off sequences to be linked directly to macroscopic changes in saturation profiles and effective permeability. Complementary diagnostics, such as acoustic emissions, offer an additional pathway to connect abrupt invasion events to measurable signatures at larger scales. (Moebius et al., 2012).

7.3.6 Coupling pore-scale structure to continuum descriptions

A central implication of this thesis is that continuum-scale saturation functions can be non-representative when heterogeneity introduces distinct capillary domains and connectivity structures within what would otherwise be treated as a single rock type. While the experimental chapters provide mechanistic explanations grounded in pore-scale structure and imaging, the remaining challenge is to translate those observations into modelling workflows that improve field-scale prediction without requiring pore-scale resolution.

Future work should develop an explicit small-scale -to-field translation framework with three components. First, define a reduced set of heterogeneity descriptors that can be estimated from core-scale imaging and core analysis, for example spatial statistics of entry pressure and connectivity derived from pore-network representations. Second, establish mappings between those descriptors and ensembles of constitutive functions (relative permeability, capillary pressure, and initial–residual trapping curves) under specified flow regimes. Third, implement those ensembles in reservoir simulation as uncertainty-aware parameterisations through spatially varying constitutive parameters and upscaling the capillary pressure on a grid-by-grid basis.

BIBLIOGRAPHY

Abba, M.K., Abbas, A.J. and Nasr, G.G. (2018) 'Experimental investigation on the impact of connate water salinity on dispersion coefficient in consolidated cores', Journal of Natural Gas Science and Engineering, 60, pp. 190-201. https://doi.org/10.1016/j.jngse.2018.10.007

Akbarabadi, M., Piri, M., 2013. Relative permeability hysteresis and capillary trapping characteristics of supercritical CO_2/brine systems: An experimental study at reservoir conditions. Advances in Water Resources 52, 190–206. https://doi.org/10.1016/j.advwatres.2012.06.014

Aljaberi, F., Belhaj, H., Foroughi, S., Al-Kobaisi, M. and Blunt, M. (2025) Spatially distributed wettability characterization in porous media. arXiv. https://doi.org/10.48550/arXiv.2507.01617

Aliakbardoust, E. and Rahimpour-Bonab, H. (2013) 'Integration of rock typing methods for carbonate reservoir characterization', Journal of Geophysics and Engineering, 10(5), p. 055004. Available at: https://doi.org/10.1088/1742-2132/10/5/055004

Al-Kharusi, A. S., & Blunt, M. J. (2007). Network extraction from sandstone and carbonate pore space images, Journal of Petroleum Science and Engineering. https://doi.org/10.1016/j.petrol.2006.09.003

Al-Menhali, A. S., and Krevor, S. 2016. Capillary trapping of CO_2 in oil reservoirs, observations in a mixed-wet limestone. Environmental Science & Technology 50, 2727–2734. https://doi.org/10.1021/acs.est.5b05925

Alanazi, A., Baban, A., Ali, A., Keshavarz, A., Iglauer, S., Hoteit, H., Residual trapping of CO_2, N_2, and a CO_2-N_2 mixture in Indiana limestone using robust NMR coreflooding: Implications for CO_2 geological storage, Fuel,2023. https://doi.org/10.1016/j.fuel.2023.129221

Andersen, P.Ø., Zhou, Y., 2020. Steady state relative permeability experiments with capillary end effects: Analytical solutions including derivation of the intercept method. Journal of Petroleum Science and Engineering 192, 107249. https://doi.org/10.1016/j.petrol.2020.107249

Aslannezhad, M., Sayyafzadeh, M., Tang, D., Iglauer, S., Keshavarz, A., You, Z., n.d. Upscaling Relative Permeability and Capillary Pressure from Digital Core Analysis in Otway Formation: Considering the Order and Size Effects of Facies. https://doi.org/10.2139/ssrn.4703754

Aslannezhad, M., Tang, D., Bason, D., Gomez, L., Iglauer, S., Keshavarz, A., 2025. Digital Core Analysis and Pore Network Modeling of CO_2 Flow and Trapping in the Otway Basin. Energy Fuels 39, 15369–15385. https://doi.org/10.1021/acs.energyfuels.5c02672

An, S., Wenck, N., Manoorkar, S., Berg, S., Taberner, C., Pini, R. and Krevor, S. (2023). Inverse modeling of core flood experiments for predictive models of sandstone and carbonate rocks. Water Resources Research, 59, e2023WR035526. https://doi.org/10.1029/2023WR035526

Andrew, M., Bijeljic, B. & Blunt, M.J., 2014. Pore-scale contact angle measurements at reservoir conditions using X-ray microtomography. Advances in Water Resources, 68, pp.24, https://doi.org/10.1016/j.advwatres.2014.02.014

Archer, J.S. and Wong, S. (1973). Use of a Reservoir Simulator To Interpret Laboratory Waterflood Data. SPE Journal, 13, pp. 343–347. https://doi.org/10.2118/3551-PA

Avraam, D.G. and Payatakes, A.C. (1995). Flow regimes and relative permeabilities during steady-state two-phase flow in porous media. Journal of Fluid Mechanics, 293, pp. 207–236. https://doi.org/10.1017/S0022112095001698

Bachu, S., Bonijoly, D., Bradshaw, J., Burruss, R., Holloway, S., Christensen, N.P., Mathiassen, O.M., 2007. CO_2 storage capacity estimation: Methodology and gaps. International Journal of Greenhouse Gas Control 1, 430–443. https://doi.org/10.1016/S1750-5836(07)00086-2

Baechle, G., Colpaert, A., Eberli, G., Weger, R., n.d. 2008. Effects of microporosity on sonic velocity in carbonate rocks. The leading edge 27, 1012–1018. https://www.researchgate.net/profile/Gregor-Eberli/publication/238439276_Effects_of_microporosity_on_sonic_velocity_in_carbonate_rocks/links/55994d2508ae21086d259819/Effects-of-microporosity-on-sonic-velocity-in-carbonate-rocks.pdf

Behzadi, H., Alvarado, V., Mallick, S., 2011. CO_2 saturation, distribution and seismic response in two-dimensional permeability model. Environ Sci Technol 45, 9435–9441. https://doi.org/10.1021/es201969a

Benson, S.M. and Cole, D.R. (2008) 'CO_2 sequestration in deep sedimentary formations', Elements, 4(5), pp. 325–331. https://doi.org/10.2113/gselements.4.5.325

Bentham, M., Kirby, Mg., 2005. CO_2 Storage in Saline Aquifers. Oil & Gas Science and Technology - Revue d'IFP Energies nouvelles 60, 559–567. https://doi.org/10.2516/ogst:2005038

Berg, S., Ott, H., Klapp, S.A., Schwing, A., Neiteler, R., Brussee, N., Makurat, A., Leu, L., Enzmann, F., Schwarz, J.O. & Kersten, M., 2013. Real-time 3D imaging of Haines jumps in porous media flow. Proceedings of the National Academy of Sciences, 110(10), pp.3755–3759. https://doi.org/10.1073/pnas.1221373110

Berg, S., Oedai, S., Ott, H. Displacement and Mass Transfer Between Saturated and Unsaturated CO_2-Brine Systems in Sandstone International Journal of Greenhouse Gas Control 12, 478-492, (2013). https://doi.org/10.1016/j.ijggc.2011.04.005

Berg, S. and Ott, H. (2012). Stability of CO_2–brine immiscible displacement. International Journal of Greenhouse Gas Control, 11, pp. 188-203. doi: 10.1016/j.ijggc.2012.07.001. https://doi.org/10.1016/j.ijggc.2012.07.001

Berg, S., Armstrong, R.T., Rücker, M., Hansen, A., Kjelstrup, S., Bedeaux, D., n.d. From Interface Dynamics to Darcy Scale Description of Multiphase Flow in Porous Media. (Pre-print) https://doi.org/10.48550/arXiv.2510.19582

Bhasuthkar, P., Kumar, J.D. and Nagpal, T. (2023) 'Efficient edge preserving image denoising using non-local algorithms', 2023 5th International Conference on Advances in Computing, Communication Control and Networking, pp. 246–250. https://doi.org/10.1109/ICAC3N60023.2023.10541597

Bickle, M., Chadwick, A., Huppert, H. E., Hallworth, M., & Lyle, S. (2007). Modelling carbon dioxide accumulation at Sleipner: Implications for underground carbon storage. Earth and Planetary Science Letters, 255(1-2), 164 176. https://doi.org/10.1016/j.epsl.2006.12.013

Blunt, M. J. (2017). Multiphase flow in permeable media: A pore-scale perspective. Cambridge University Press. 10.1017/9781316145098

Blunt, M. J., Bijeljic, B., Dong, H., Gharbi, O., Iglauer, S., Mostaghimi, P., Paluszny, A., and Pentland, C. (2013). Pore-scale imaging and modelling. Advances in Water Resources, 51:197–216. https://doi.org/10.1016/j.advwatres.2012.03.003

Blunt, M.J., Jackson, M.D., Piri, M. and Valvatne, P.H. (2002). Detailed physics, predictive capabilities and macroscopic consequences for pore-network models of multiphase flow. Advances in Water Resources, 25(8–12), pp. 1069–1089. https://doi.org/10.1016/S0309-1708(02)00049-

Boon, M. and Benson, S.M. (2021) 'A physics-based model to predict the impact of horizontal lamination on CO_2 plume migration', Advances in Water Resources, 150, 103889. DOI: https://doi.org/10.1016/j.advwatres.2021.103889

Bradshaw, J., Bachu, S., Bonijoly, D., Burruss, R., Holloway, S., Christensen, N.P. and Mathiassen, O.M. (2012) 'CO_2 storage capacity estimation: Issues and development of standards', International Journal of Greenhouse Gas Control, 4(2), pp. 523–531. DOI: https://doi.org/10.1016/j.ijggc.2010.11.003

Buckles, R.S. (1965) 'Correlating and averaging connate water saturation data', Journal of Canadian Petroleum Technology, 4(2), pp. 42-52. doi: https://doi.org/10.2118/65-01-07

Bui M, Adjiman CS, Bardow A, Anthony EJ, Boston A, Brown S, Fennel PS, Fuss S, Galindo A, Hackett LA, Hallett JP, Herzog HJ, Jackson G, Kemper J, Krevor S, Maitland GC, Matuszewski M, Metcalfe IS, Petit C, Puxty SA, Reimer J, Reiner DM, Rubin ES, Scott SA, Shah N, Smit B, Martin Trusler JP, Weble P, Wilcox J, Mac Dowell N. Carbon capture and storage (CCS): the way forward. Energy, Environ. Sci. 2018;11:1062–176. https://doi.org/10.1039/c7ee02342a

Bull, Ø., Ringen, J.K., Self, C., Heifer, K.J., Kvamme, B. and Bodvarsson, G.S. (2011). The quest for the true residual gas saturation. In: International Symposium of the Society of Core Analysts, Austin, Texas, USA, 18-21 September 2011. Available at: https://jgmaas.com/SCA/2011/SCA2011-03.pdf

Bultreys, T., De Boever, W., & Cnudde, V. (2016). Imaging and image-based fluid transport modeling at the pore scale in geological materials: A practical introduction to the current state-of-the-art. Earth-Science Reviews, 155, 93–128. https://doi.org/10.1016/j.earscirev.2016.02.001

Carrillo, F.J., Soulaine, C. and Bourg, I.C. (2022). The impact of sub-resolution porosity on numerical simulations of multiphase flow. Advances in Water Resources, 161, 104094. https://doi.org/10.1016/j.advwatres.2021.104094

Chadwick, R. A., Noy, D. J., & Holloway, S. (2009). Flow processes and pressure evolution in aquifers during the injection of supercritical CO_2 as a greenhouse gas mitigation measure. Petroleum Geoscience, 18(1), 59-73 https://doi.org/10.1144/1354-079309-793

Chalbaud, C., Robin, M., Lombard, J.M., Martin, F., Egermann, P., & Bertin, H. (2009). Interfacial tension measurements and wettability evaluation for geological CO_2 storage. Advances in Water Resources, 32(1), 98–109. https://doi.org/10.1016/j.advwatres.2008.10.012

Chen, B., Li, Q., & Tan, Y. (2025). Caprock sealing for geologic CO_2 storage: Research advances, challenges and prospects. Journal of Rock Mechanics and Geotechnical Engineering, S1674775525001350. https://doi.org/10.1016/j.jrmge.2025.02.006

Clennell, M.B., White, C., Giwelli, A., Myers, M., Esteban, L., Cullingford, M., Richardson, W., Ward, G., Waugh, M., Cole, S., Hunt, A. and Bright, P. (2020) Improved method for complete gas–brine

imbibition relative permeability curves. E3S Web of Conferences, 146, 03003. https://doi.org/10.1051/e3sconf/202014603003

Corbett, P.W.M., Ringrose, P.S., Jensen, J.L., Sorbie, K.S., 1992. Laminated Clastic Reservoirs: The Interplay of Capillary Pressure and Sedimentary Architecture, in: SPE Annual Technical Conference and Exhibition. Society of Petroleum Engineers, pp. 365–376. https://doi.org/10.2118/24699-MS

Cuthiell, D., Sedgwick, G., Kissel, G., and Woolley, J. (1993). Steam Corefloods With Concurrent X-Ray Ct Imaging. Journal of Canadian Petroleum Technology, 32(03). 10.2118/93-03-03

Dai, Z. et al. (2016). CO_2 accounting and risk analysis for CO_2 sequestration at enhanced oil recovery sites. Environmental Science & Technology, 50, pp. 7546–7554. https://doi.org/10.1021/acs.est.6b01744

Dance, T. and Paterson, L. (2016). Observations of carbon dioxide saturation distribution and residual trapping using core analysis and repeat pulsed-neutron logging at the CO2CRC Otway site. International Journal of Greenhouse Gas Control, 47, pp. 210–220. https://doi.org/10.1016/j.ijggc.2016.01.042

Darraj, N., Bender, G., Carbon Neutral Energy Intensive Industries, UNECE, Geneva, Switzerland, 2022. https://unece.org/sustainable-energy/cleaner-electricity-systems/carbon-neutral-energy-intensive-industris

Darraj, N., Manoorkar, S., Spurin, C., Foroughi, S., Saleh, M., Berg, S., Blunt, M.J. and Krevor, S. (2025). Heterogeneity Driven Trapping at the Pore-Network Scale in Edwards Brown Dolomite. Energy & Fuels. https://doi.org/10.1021/acs.energyfuels.5c04544

Darraj, N., Spurin, C., Manoorkar, S., Berg, S., Blunt, M. J., Pini, R., Cunsolo, V., & Krevor, S. (2024). Pore-scale dynamics in carbonate reservoirs: The influence of heterogeneity on CO_2 storage in Indiana Limestone. Proceedings of GHGT-17 (17th International Conference on Greenhouse Gas Control Technologies), Oct 20–24, 2024. http://dx.doi.org/10.2139/ssrn.5069647

Dawe, R. A., Wheat, M. R., and Bidner, M. S. (1992). Experimental investigation of capillary pressure effects on immiscible displacement in lensed and layered porous media. Transport in Porous Media, 7:83 – 101. https://doi.org/10.1007/BF00617318

De Paoli, M., Zonta, F., Enzenberger, L., Coliban, E., & Pirozzoli, S. (2025). Simulation and Modeling of Convective Mixing of Carbon Dioxide in Geological Formations. Geophysical Research Letters, 52(7), e2025GL114804. https://doi.org/10.1029/2025GL114804

Dong, H. and Blunt, M.J. (2009). Pore-network extraction from micro-computerized-tomography images. Physical Review E, 80(3), 036307. https://doi.org/10.1103/PhysRevE.80.036307

Doughty, C., Pruess, K., 2004. Modeling supercritical carbon dioxide injection in heterogeneous porous media. Vadose Zone J. 3, 837–847.

Drax (2025). Geological Storage of CO_2. Available at: https://www.drax.com/wp-content/uploads/2025/06/DR1907-5_Geological-Storage-of-CO2_GB_V002.pdf (Accessed: 22 January 2026).

Elizarev, M., Wenck, N., Krevor, S., Muggeridge, A. (2024). Upscaling Algorithm to Preserve Effects of Small-Scale Capillary Heterogeneity: Field-Scale Studies on CO_2 Storage Sites. Proceedings of the

17th Greenhouse Gas Control Technologies Conference (GHGT-17) 20-24 October 2024, http://dx.doi.org/10.2139/ssrn.5068897

Ershadnia, R., Hajirezaie, S., Amooie, A., Wallace, C.D., Gershenzon, N.I., Hosseini, S.A., Sturmer, D.M., Ritzi, R.W., Soltanian, M.R., 2021. CO_2 geological sequestration in multiscale heterogeneous aquifers: Effects of heterogeneity, connectivity, impurity, and hysteresis. Adv Water Resour 151, 103895. https://doi.org/10.1016/j.advwatres.2021.103895

Fadili, A., Ababou, R., Dual homogenization of immiscible steady two-phase flow in random porous media, Water Resources Research 40, W01513, 2004. DOI: http://doi.org/10.1029/2003WR002465

Fatt, I. and Klikoff, W. A. (1959). E↵ect of Fractional Wettability on Multiphase Flow Through Porous Media. Journal of Petroleum Technology, 11(10):71–76. https://doi.org/10.2118/1275-G

Fischer, U. and Paterson, L. (2010) 'Pore geometry in Indiana limestone', Journal of Petroleum Science and Engineering, 7(3), pp. 221–229. DOI: http://doi.org/10.1016/0920-4105(92)90007-W

Fitch, P. J., Lovell, M. A., Davies, S. J., Pritchard, T., and Harvey, P. K. (2015). An integrated and quantitative approach to petrophysical heterogeneity. Marine and Petroleum Geology, 63:82–96. http://dx.doi.org/10.1016/j.marpetgeo.2015.02.014

Flannery, B.P., Deckman, H.W., Roberge, W.G. and D'Amico, K.L. (1987) 'Three-dimensional X-ray microtomography', Science, 237(4821), pp.1439–1444. DOI: http://doi.org/10.1126/science.237.4821.1439

Foroughi, S., Bijeljic, B. and Blunt, M.J., 2021. Pore-by-pore modelling, validation and prediction of waterflooding in oil-wet rocks using dynamic synchrotron data. Transport in Porous Media, 138(2), pp.285-308. https://doi.org/10.1007/s11242-021-01609-y

Foroughi, S., Bijeljic, B., Lin, Q., Raeini, A.Q. and Blunt, M.J. (2020). Pore-by-pore modeling, analysis, and prediction of multiphase flow. Water Resources Research. https://doi.org/10.1029/2020WR027343

Freire-Gormaly, M., Ellis, J., MacLean, H., Bazylak, A., Pore Structure Characterization of Indiana Limestone and Pink Dolomite from Pore Network Reconstructions, Oil Gas Sci. Technol. – Rev. IFP Energies nouvelles, 2016, DOI: https://doi.org/10.2516/ogst/2015004

Gao, Y., Georgiadis, A., Brussee, N., Coorn, A., van der Linde, H., Dietderich, J., Alpak, F.O., Eriksen, D., Mooijer-van den Heuvel, M., Appel, M., Sorop, T., Wilson, O.B. and Berg, S. (2021). Capillarity and phase-mobility of a hydrocarbon gas–liquid system. Oil & Gas Science and Technology, 76, 25. https://doi.org/10.2516/ogst/2021025

Gao, Y., Lin, Q., Bijeljic, B. and Blunt, M.J. (2020) 'Pore-scale dynamics and the multiphase Darcy law', Physical Review Fluids, 5(1), 013801. https://doi.org/10.1103/PhysRevFluids.5.013801

Gao, Y., Lin, Q., Bijeljic, B., & Blunt, M. J.(2017). X-ray microtomography of intermittency in multiphase flow at steady state using a differential imaging method. Water Resources Research, 53, 10,274–10,292. https://doi.org/10.1002/2017wr021736

Gao, Y., Sorop, T., Brussee, N., van der Linde, H., Coorn, A. and Berg, S. (2023). Advanced Digital-SCAL Measurements of Gas Trapped in Sandstone. Petrophysics, 64(03), pp. 368–383. https://doi.org/10.30632/PJV64N3-2023a4

Garfi, G., John, C.M., Berg, S. et al. The Sensitivity of Estimates of Multiphase Fluid and Solid Properties of Porous Rocks to Image Processing. Transp Porous Med 131, 985–1005 (2020). https://doi.org/10.1007/s11242-019-01374-z

Gasda, S. E., Nordbotten, J. M., & Celia, M. A. (2011). Vertically averaged approaches for CO_2 migration with solubility trapping. Water Resources Research, 47(5), W05528. https://doi.org/10.1029/2010WR009075

Gershenzon, N.I., Ritzi, R.W., Dominic, D.F., Mehnert, E., Okwen, R.T., Patterson, C., 2017. CO_2 trapping in reservoirs with fluvial architecture: Sensitivity to heterogeneity in permeability and constitutive relationship parameters for different rock types. J Pet Sci Eng 155, 89–99. https://doi.org/10.1016/j.petrol.2016.09.008

Georgiadis, A., Berg, S., Makurat, A., Maitland, G., Ott, H., 2013. Pore-scale micro-computed-tomography imaging: Nonwetting-phase cluster-size distribution during drainage and imbibition. Phys. Rev. E 88, 033002. https://doi.org/10.1103/PhysRevE.88.033002

Gharieb, A., Gabry, M., Algarhy, A., Elsawy, M., Darraj, N., Adel, S., Taha, M., and Abdelrafae H. "Revealing Insights in Evaluating Tight Carbonate Reservoirs: Significant Discoveries via Statistical Modelling. An In-Depth Analysis Using Integrated Machine Learning Strategies." Paper presented at the GOTECH, Dubai, UAE, May 2024. https://doi.org/10.2118/219199-MS

Gholanlo, H., Amirpour, M., Ahmadi, S., (2016). Estimation of water saturation by using radial based function artificial neural network in carbonate reservoir: A case study in Sarvak formation, Petroleum, Volume 2, Issue 2, https://doi.org/10.1016/j.petlm.2016.04.002.

Goodarzian, S. and Sorbie, K.S. (2025). Numerical and semi-analytical modelling of the capillary end effect for porous media of any wettability state. Capillarity, 14(3), pp. 82–99. https://doi.org/10.46690/capi.2025.03.03

Gozalpour, F., Ren, S.R. and Tohidi, B., 2005. CO_2 enhanced oil recovery and storage in oil reservoir. Oil & gas science and technology, 60(3), 537-546. https://doi.org/10.2516/ogst:2005036

Gupta, R. and Maloney, D. (2015) 'Applications of the Intercept Method to correct steady-state relative permeability for capillary end-effects', paper SCA2015-001, presented at the International Symposium of the Society of Core Analysts, St. John's, Newfoundland and Labrador, Canada, 16–21 August. https://www.jgmaas.com/SCA/2015/SCA2015-001.pdf

Ni, H., Møyner, O., Kurtev, K., S M., Quantifying CO_2 capillary heterogeneity trapping through macroscopic percolation simulation, Advances in Water Resources, Volume 155, 2021,103990,ISSN 0309-1708, https://doi.org/10.1016/j.advwatres.2021.103990

Harris, C., Jackson, S.J., Benham, G.P., Krevor, S. and Muggeridge, A.H. (2021). The impact of heterogeneity on the capillary trapping of CO_2 in the Captain Sandstone. International Journal of Greenhouse Gas Control, 112, 103511. https://doi.org/10.1016/j.ijggc.2021.103511

Hassanizadeh, S.M. and Gray, W.G. (1993) ‘Thermodynamic basis of capillary pressure in porous media’, Water Resources Research, 29(10), pp. 3389–3405. DOI: https://doi.org/10.1029/93WR01495

Herring, A.L., Harper, E.J., Andersson, L., Sheppard, A.P. & Wildenschild, D. (2013) ‘Effect of fluid topology on residual non-wetting phase trapping: Implications for geologic CO_2 sequestration’, Advances in Water Resources, http://dx.doi.org/10.1016/j.advwatres.2013.09.015

Hesse, M.A., Orr, F.M. and Tchelepi, H.A. (2008). Gravity currents with residual trapping. Journal of Fluid Mechanics, 611, pp. 35–60. https://doi.org/10.1017/S002211200800219X

Holloway, S. (2005) 'Underground sequestration of carbon dioxide—a viable greenhouse gas mitigation option', Energy, 30(11-12), pp. 2318-2333. https://doi.org/10.1016/j.energy.2003.10.023

Holtzman, R. & Segre, E. (2015). Wettability stabilizes fluid invasion into porous media via nonlocal, cooperative pore filling. Physical Review Letters. https://link.aps.org/doi/10.1103/PhysRevLett.115.164501

Hove, A. O., Nilsen, V., and Jorgen, L. (1990). Visualization of Xanthan flood behaviour in core samples by means of X-ray tomography. SPE Reservoir Engineering, 5:475 – 480. https://doi.org/10.2118/17342-PA

Huang, D.D. and Honarpour, M.M. (1998). Capillary end effects in coreflood calculations. Journal of Petroleum Science and Engineering, 19, pp. 103–117. https://doi.org/10.1016/S0920-4105(97)00040-5

Huang, Yaduo, Ringrose, P. S., and K. S. Sorbie. "Capillary Trapping Mechanisms in Water-Wet Laminated Rocks." SPE Res Eng 10 (1995): 287–292. doi: https://doi.org/10.2118/28942-PA

Iampen H., Rostron, B., (2000). Hydrogeochemistry of pre-Mississippian brines, Williston Basin, Canada–USA, Journal of Geochemical Exploration, doi:10.1016/s0375-6742(00)00007-8

Ide, S.T., Jessen, K. and Orr, F.M. (2007). Storage of CO_2 in saline aquifers: Effects of gravity, viscous, and capillary forces on trapping. International Journal of Greenhouse Gas Control, 1(4), pp. 481–491. https://doi.org/10.1016/S1750-5836(07)00091-6

IEAGHG, "Case Studies of CO_2 Storage in Depleted Oil and Gas Fields", 2017-01, January 2017.

Intergovernmental Panel on Climate Change (IPCC) (2014) Climate Change 2014: Synthesis Report. Geneva: IPCC.

IPCC (2005) Carbon Dioxide Capture and Storage. IPCC Special Report. Cambridge: Cambridge University Press.

IPCC (2022) Climate Change 2022: Mitigation of Climate Change. Contribution of Working Group III to the Sixth Assessment Report of the Intergovernmental Panel on Climate Change. Cambridge: Cambridge University Press.

International Energy Agency (IEA) (2021) CCUS in Clean Energy Transitions. Paris: IEA.

Jackson, S.J. and Krevor, S. (2020) 'Small-scale capillary heterogeneity linked to rapid plume migration during CO_2 storage', Geophysical Research Letters, 47(18), e2020GL088616. DOI: https://doi.org/10.1029/2020GL088616

Jackson, S. J., Agada, S., Reynolds, C. A., & Krevor, S. (2018). Characterising drainage multiphase flow in heterogeneous sandstones. Water Resources Research, 54, 3139–3161. https://doi.org/10.1029/2017WR022282

Jerauld, G. R., and S. J. Salter, Effect of pore-structure on hysteresis in relative permeability and capillary pressure: Pore-level modeling, Transport in Porous Media, 5, 103-151, 1990. https://doi.org/10.1007/BF00144600

Johnson, E., Bossler, D., and Bossler, V. N. (1959). Calculation of Relative Permeability from Displacement Experiments. Transactions of the AIME, 216(01):370–372. https://doi.org/10.2118/1023-G

Juanes, R., Spiteri, E.J., Orr, F.M. Jr. & Blunt, M.J. (2006) 'Impact of relative permeability hysteresis on geological CO_2 storage', Water Resources Research, 42(12), W12418. https://doi.org/10.1029/2005WR004806

Ketcham, R.A. and Carlson, W.D. (2001) 'Acquisition, optimization and interpretation of X-ray computed tomographic imagery: Applications to the geosciences', Computers & Geosciences, 27(4), pp.381–400. DOI: https://doi.org/10.1016/S0098-3004(00)00116-3

Kong, X., Delshad, M., Wheeler, M.F., 2015. History matching heterogeneous coreflood of CO_2/brine by use of compositional reservoir simulator and geostatistical approach. SPE Journal 20, 267–276. https://doi.org/10.2118/163625-pa

Kortekaas, T. F. (1985). Water/Oil Displacement Characteristics in Crossbedded Reservoir Zones. Society of Petroleum Engineers journal, 25(6):917–926. https://doi.org/10.2118/12112-PA

Kim, K., Kim, M. and Oh, J. (2021). Core-scale investigation of the effect of heterogeneity on the dynamics of residual and dissolution trapping of carbon dioxide. Journal of Hydrology, 596, 126109. https://doi.org/10.1016/j.jhydrol.2021.126109

Kimbrel, E.H., Herring, A.L., Armstrong, R.T., Lunati, I., Bay, B.K., Wildenschild, D., 2015. Experimental characterization of nonwetting phase trapping and implications for geologic CO_2 sequestration. International Journal of Greenhouse Gas Control 42, 1–15. https://doi.org/10.1016/j.ijggc.2015.07.011

Krause, M., Perrin, J. and Benson, S.M. (2011) 'Modeling permeability distributions in a sandstone core for history matching coreflood experiments', SPE Journal, 16(4), pp. 768–777. DOI: https://doi.org/10.2118/126340-PA

Krevor, S., Blunt, M.J., Benson, S.M., Pentland, C.H., Reynolds, C., Al-Menhali, A., Niu, B., 2015. Capillary trapping for geologic carbon dioxide storage - From pore scale physics to field scale implications. International Journal of Greenhouse Gas Control 40, 221–237. https://doi.org/10.1016/j.ijggc.2015.04.006

Krevor, S., Pini, R., Zuo, L. and Benson, S.M. (2012) 'Relative permeability and trapping of CO_2 and water in sandstone rocks at reservoir conditions', Water Resources Research, 48(2), W02532. DOI: https://doi.org/10.1029/2011WR010859

Krevor, S.C.M., Pini, R., Li, B. & Benson, S.M. (2011) Capillary heterogeneity trapping of CO_2 in a sandstone rock at reservoir conditions. Geophysical Research Letters, https://doi.org/10.1029/2011GL048239

Krishnamurthy, P.G., DiCarlo, D.A. and Meckel, T. (2022). Geologic heterogeneity controls on trapping and migration of CO_2. Geophysical Research Letters, 49(16), e2022GL099104. https://doi.org/10.1029/2022GL099104

Krishnamurthy, P.G., Meckel, T.A. and DiCarlo, D. (2019) 'Mimicking geologic depositional fabrics for multiphase flow experiments', Water Resources Research, 55(11), pp. 9623–9638. DOI: https://doi.org/10.1029/2019WR025664

Krygier, M.C., LaBonte, T., Martinez, C. et al. Quantifying the unknown impact of segmentation uncertainty on image-based simulations. Nat Commun 12, 5414 (2021). https://doi.org/10.1038/s41467-021-25493-8

Kuo, C.W. and Benson, S.M. (2013) 'Analytical study of effects of flow rate, capillarity and gravity on CO_2/brine multiphase-flow system in horizontal corefloods', SPE Journal, 18(4), pp. 708–720. DOI: https://doi.org/10.2118/150301-PA

Kurotori, T., Zahasky, C., Benson, S. M., & Pini, R. (2020). Description of chemical transport in laboratory rock cores using the continuous random walk formalism. https://doi.org/10.1029/2020WR027511

Lai, P., Moulton, K., & Krevor, S. (2015). Pore-scale heterogeneity in the mineral distribution and reactive surface area of porous rocks, Chemical Geology, Volume 411, Pages 260-273, https://doi.org/10.1016/j.chemgeo.2015.07.010

Lake, L.W. (1989). Enhanced Oil Recovery. Prentice Hall, Englewood Cliffs, NJ.

Lake, L.W., Johns, R.T., Rossen, W.R. and Pope, G.A. (2014). Fundamentals of Enhanced Oil Recovery. Richardson, TX: Society of Petroleum Engineers. https://doi.org/10.2118/9781613993286

Land, C. (1968). Calculation of imbibition relative permeability for two- and three-phase flow from rock properties. SPE Journal, 8, pp. 149–156. https://doi.org/10.2118/1942-PA

Leverett, M. C. (1939). Flow of oil-water mixtures through unconsolidated sands. Transactions of the AIME, 132(01):149–171. https://doi.org/10.2118/939149-G

Levine, J.S., Matter, J.M., Goldberg, D., Cook, A. and Lackner, K.S. (2011). Two-phase brine-CO_2 flow experiments in synthetic and natural media. Energy Procedia, 4, pp. 4347-4353. https://doi.org/10.1016/j.egypro.2011.02.386

Li, B. and Benson, S.M. (2015). Influence of small-scale heterogeneity on upward CO_2 plume migration. Advances in Water Resources, 83, pp. 389–404. http://dx.doi.org/10.1016/j.advwatres.2015.07.010

Li, X., Akbarabadi, M., Karpyn, Z. T., Piri, M., Bazilevskaya., E., 2012. An experimental study of CO_2 trapping due to capillary retention in saline aquifers. Geofluids. https://doi.org/10.1111/gfl.12127

Lin, Q., Bijeljic, B., Berg, S., Pini, R., Blunt, M.J. & Krevor, S., 2021. Minimal surfaces in porous media: Pore-scale imaging of multiphase flow in three dimensions. Physical Review E, 103(6), 063103. https://doi.org/10.1103/PhysRevE.99.063105

Lindquist, W.B., Venkatarangan, A., Dunsmuir, J. and Wong, T.F., 2000. Pore and throat size distributions measured from synchrotron X-ray tomographic images of Fontainebleau sandstones. Journal of Geophysical Research: Solid Earth, 105(B9), pp.21509–21527. https://doi.org/10.1029/2000JB900208

Lu, J., Wu, N., Lv, Y. et al. Long distance migration assisted structural trapping during CO_2 storage in offshore basin. Sci Rep 15, 45249 (2025). https://doi.org/10.1038/s41598-025-28680-5

Lucia, F. J. (1995). Rock-fabric/petrophysical classification of carbonate pore space for reservoir characterization. AAPG Bulletin, 79(9), 1275–1300. https://doi.org/10.1306/7834D4A4-1721-11D7-8645000102C1865D

Maas, J.G., Springer, N. and Hebing, A. (2019). Defining a sample heterogeneity cut-off value to obtain representative SCAL measurements. Proceedings of the Society of Core Analysts, SCA2019-024. https://jgmaas.com/SCA/2019/SCA2019-024.pdf

McPhee, C., Reed, J., and Zubizarreta, I. (2015). Core Analysis: A Best Practice Guide, volume 64.

Manoorkar, S., Jackson, S.J. and Krevor, S. (2021) 'Observations of the impacts of millimeter- to centimeter-scale heterogeneities on relative permeability and trapping in carbonate rocks', Water Resources Research, 57(12), e2020WR028597. DOI: https://doi.org/10.1029/2020WR028597

Matter, J. M., Stute, M., Snæbjörnsdottir, S. Ó., Oelkers, E. H., Gislason, S. R., Aradottir, E. S., Sigfusson, B., Gunnarsson, I., Sigurdardottir, H., Gunnlaugsson, E., Axelsson, G., Alfredsson, H. A., Wolff-Boenisch, D., Mesfin, K., Taya, D. F. D. L. R., Hall, J., Dideriksen, K., & Broecker, W. S. (2016). Rapid carbon mineralization for permanent disposal of anthropogenic carbon dioxide emissions. Science, 352(6291), 1312–1314. https://doi.org/10.1126/science.aad8132

Masalmeh, S.K.: "Experimental Measurements of Capillary Pressure and Relative Permeability Hysteresis" SCA 2001-23 presented at the SCA 2001 conference, Edinburgh, September (2001)

McCaskill, B., Gong, Y., Qin, Z. et al. Pore-to-Core Upscaling of Two-Phase Flow in Mixed-Wet Porous Media: Part I—Seamless Pore-Network Extraction. Transp Porous Med 151, 2529–2560 (2024). https://doi.org/10.1007/s11242-024-02126-4

Meckel T.A., Bryant, S.L. Buoyancy-driven Flow in Heterogeneous Materials, Energy Procedia, Volume 63, 2014, P 5495-5502, https://doi.org/10.1016/j.egypro.2014.11.582

Meekangwal, S., and Srisuriyachai, F., 2018. Effects of Formation Brine Compositions on Effectiveness of Low Salinity Brine Injection in Carbonate Reservoir. https://doi.org/10.1051/matecconf/201817104002

Midtlyng, S.H. and Stensen, J.Å. (2000). Improved flooding experiments in heterogeneous rocks using in-situ saturations from X-ray CT measurements. https://www.jgmaas.com/SCA/2000/SCA2000-40.pdf

Michael, K., Golab, A., Shulakova, V., Ennis-King, J., Allinson, G., Sharma, S., Aiken, T., 2010. Geological storage of CO_2 in saline aquifers—A review of the experience from existing storage operations. International Journal of Greenhouse Gas Control 4, 659–667. https://doi.org/10.1016/j.ijggc.2009.12.011

Moctezuma-Berthier, A., Vizika, O. and Adler, P.M. (2002). Macroscopic conductivity of vugular porous media. Transport in Porous Media, 49, pp. 313–332. https://doi.org/10.1023/A:1016297220013

Mohanty, K.K., Davis, H.T. and Scriven, L.E. (1987). Physics of oil entrapment in water-wet rock. SPE Reservoir Engineering, 2(1), pp. 113–128. https://doi.org/10.2118/9406-PA

Ni, H., Boon, M., Garing, C., Benson, S.M., 2019. Predicting CO_2 residual trapping ability based on experimental petrophysical properties for different sandstone types. International Journal of Greenhouse Gas Control 86, 158–176. https://doi.org/10.1016/j.ijggc.2019.04.024

Ni, H., Li, B., Darraj, N., Ren, B., Harris, C., Krishnamurthy, P.G., Bukar, I., Berg, S., Snippe, J., Ringrose, P., Meckel, T.A., Krevor, S. and Benson, S. (2025). The impact of capillary heterogeneity on

CO_2 flow and trapping across scales. Earth-Science Reviews, 270, 105257. https://doi.org/10.1016/j.earscirev.2025.105257

Ni, H., Meckel, T.A., 2021. Characterizing the Effect of Capillary Heterogeneity on Multiphase Flow Pulsation in an Intermediate-Scale Beadpack Experiment Using Time Series Clustering and Frequency Analysis. Water Resour. Res. 57, 1–17. https://doi.org/10.1029/2021WR030876

Ni, H., Bakhshian, S., Meckel, T.A., 2023. Effects of grain size and small-scale bedform architecture on CO_2 saturation from buoyancy-driven flow. Sci. Rep. 13, 2474. https://doi.org/10.1038/s41598-023-29360-y

Ni, H., Benson, S.M., 2020. Using Unsupervised Machine Learning to Characterize Capillary Flow and Residual Trapping. Water Resour. Res. 56. https://doi.org/10.1029/2020WR027473

NIST Chemistry Webbook (2018). https://webbook.nist.gov/chemistry/

Nordbotten, J. M., & Celia, M. A. (2006). Similarity solutions for fluid injection into confined aquifers. Journal of Fluid Mechanics, 561, 307-327. https://doi.org/10.1017/S0022112006000802

Nordahl, K., Ringrose, P.S. Identifying the Representative Elementary Volume for Permeability in Heterolithic Deposits Using Numerical Rock Models. Math Geosci 40, 753–771 (2008). https://doi.org/10.1007/s11004-008-9182-4

Owusu, P.A., Nagre, R.D. and Tagbor, T.A. (2014). Buckley-Leverett displacement theory for heterogeneous porous media. Petroleum & Coal, 56(3), pp. 268-278. Petroleum & Coal

Pak, T., Butler, IB., Geiger, S., Van Dijke, MIJ., Sorbie, KS. Droplet fragmentation: 3D imaging of a previously unidentified pore-scale process during multiphase flow in porous media Proceedings of the National Academy of Sciences 2015. doi: https://doi.org/10.1073/pnas.1420202112

Pentland, C.H., El-Maghraby, R. & Blunt, M.J., 2011. Measurements of the capillary trapping of super-critical carbon dioxide in Berea sandstone. Geophysical Research Letters, 38(6), L06401. https://doi.org/10.1029/2011GL046683

Perrin, J.C. and Benson, S.M. (2010) 'An experimental study on the influence of sub-core scale heterogeneities on CO_2 distribution in reservoir rocks', Transport in Porous Media, 82(1), pp. 93–109. DOI: https://doi.org/10.1007/s11242-009-9426-x

Pickell, J.J., Swanson, B.F., and W.B. Hickman. "Application of Air-Mercury and Oil-Air Capillary Pressure Data In the Study of Pore Structure and Fluid Distribution." SPE J. 6 (1966): 55–61. https://doi.org/10.2118/1227-pa

Pickup, G., Ringrose, P.S., Sharif, A., 2000. Steady-State Upscaling: From Lamina-Scale to Full-Field Model. SPE J. 5, 208–217. https://doi.org/10.2118/62811-PA

Pini, R. and Benson, S.M. (2013). Simultaneous determination of capillary pressure and relative permeability curves. Water Resources Research, 49(6), pp. 3516–3530. https://doi.org/10.1002/wrcr.20274

Pini, R. Krevor, S. and Benson, S.M. (2012). Capillary pressure and heterogeneity for the CO_2/water system in sandstone rocks at reservoir conditions. Advances in Water Resources. https://doi.org/10.1016/j.advwatres.2011.12.007

Pruess, K. and Garcia, J. (2002) 'Multiphase flow dynamics during CO_2 disposal into saline aquifers', Environmental Geology, 42(2–3), pp. 282–295. DOI: https://doi.org/10.1007/s00254-001-0496-3

Postma, T. J. W., Bandilla, K. W., Peters, C. A., & Celia, M. A. (2022). Field-Scale Modeling of CO_2 Mineral Trapping in Reactive Rocks: A Vertically Integrated Approach. Water Resources Research, 58(1), e2021WR030626. https://doi.org/10.1029/2021WR030626

Raeini, A. Q., Bijeljic, B. & Blunt, M. J. (2017) Generalized network modelling: Network extraction as a coarse-scale discretization of the void space of porous media. Physical Review E. 96 (1), 013312. https://doi.org/10.1103/PhysRevE.97.023308

Raeini, A.Q., Imperial College London (2023) Pore Occupancy Analysis Toolbox. GitHub repository. Available at: https://github.com/ImperialCollegeLondon/poreOccupancyAnalysis

Rathmaier, D.; Naim, F.; William, A.C.; Chakraborty, D.; Conwell, C.; Imhof, M.; Holmes, G.M.; Zerpa, L.E. A Reservoir Modeling Study for the Evaluation of CO_2 Storage Upscaling at the Decatur Site in the Eastern Illinois Basin. Energies 2024, 17, 1212. https://doi.org/10.3390/en17051212

Ren, B., (2018). Local capillary trapping in carbon sequestration: Parametric study and implications for leakage assessment, International Journal of Greenhouse Gas Control, https://doi.org/10.1016/j.ijggc.2018.08.001

Reynolds, C.A., Blunt, M.J. and Krevor, S. (2018). Multiphase flow characteristics of heterogeneous rocks. Water Resources Research, 54, pp. 729–745. https://doi.org/10.1002/2017WR021651

Reynolds, C.A., Krevor, S., 2015. Characterizing flow behavior for gas injection: Relative permeability of CO_2 -brine and N2 -water in heterogeneous rocks. Water Resour Res 51, 9464–9489. https://doi.org/10.1002/2015WR018046

Reynolds, C.A., Menke, H, Andrew, M., Blunt, M.J. & S. Krevor, (2017). Dynamic fluid connectivity during steady-state multiphase flow in a sandstone, Proc. Natl. Acad. Sci. U.S.A. 114 (31) 8187-8192, https://doi.org/10.1073/pnas.1702834114.

Ringrose, P. (2020) How to Store CO_2 Underground: Insights from Early-Mover CCS Projects. Cham: Springer. DOI: https://doi.org/10.1007/978-3-030-42099-4

Roof, J.G.. "Snap-Off of Oil Droplets in Water-Wet Pores." SPE J. 10 (1970): 85–90. doi: https://doi.org/10.2118/2504-PA

Rücker, M., Berg, S., Armstrong, R.T., Georgiadis, A., Ott, H. and Spurin, C. (2020) 'The effect of capillary pressure on two-phase flow in complex porous media', Journal of Colloid and Interface Science, 562, pp.159–169. DOI: https://doi.org/10.1016/j.jcis.2019.12.026

Rücker, M., Georgiadis, A., Armstrong, R.T., Ott, H., Brussee, N., van der Linde, H., Simon, L., Enzmann, F., Kersten, M. and Berg, S. (2021). Origin of non-thermal fluctuations in multiphase flow. Frontiers in Water, 3, 45. https://doi.org/10.3389/frwa.2021.671399

Ruprecht, C., Pini, R., Falta, R., Benson, S., Murdoch, L., 2014. Hysteretic trapping and relative permeability of CO_2 in sandstone at reservoir conditions. International Journal of Greenhouse Gas Control 27, 15–27. https://doi.org/10.1016/j.ijggc.2014.05.003

Saadatpoor, E., Bryant, S.L. & Sepehrnoori, K. New Trapping Mechanism in Carbon Sequestration. Transp Porous Med 82, 3–17 (2010). https://doi.org/10.1007/s11242-009-9446-6

Schluter, S., A. Sheppard, K. Brown, and D. Wildenschild (2014), Image processing of multiphase images obtained via X-ray microtomography: A review, Water Resour. Res., 50, 3615–3639, https://doi.org/10.1002/2014WR015256https://doi.org/10.1002/2014WR015256

Seyyedi, M., Mahmud, H.K.B., Verrall, M. et al. Pore Structure Changes Occur During CO_2 Injection into Carbonate Reservoirs. Sci Rep 10, 3624 (2020). https://doi.org/10.1038/s41598-020-60247-4

Shao, J., Benson, S.M. and Myhrer, K. (2023) 'Capillary number-dependent relative permeability and capillary pressure models for heterogeneous CO_2 storage formations', International Journal of Greenhouse Gas Control, 126, 103913. DOI: https://doi.org/10.1016/j.ijggc.2023.103913

Shao, J., Wilkinson, D., Wang, Y., Benson, S.M. and Myhrer, K. (2022) 'Capillary heterogeneity control on CO_2 trapping: Characterization and upscaling', International Journal of Greenhouse Gas Control, 119, 103699. DOI: https://doi.org/10.1016/j.ijggc.2022.103699

Shanghvi, E. R., Meng, Q., Abelly, E. N., & Mkono, C. N. (2025). A data-driven prediction of residual carbon dioxide under different porous media structures. Gas Science and Engineering, 138, 205602. https://doi.org/10.1016/j.jgsce.2025.205602

Shi, J.-Q., Xue, Z., Durucan, S., 2011. Supercritical CO_2 core flooding and imbibition in Tako sandstone—Influence of sub-core scale heterogeneity. International Journal of Greenhouse Gas Control 5, 75–87. https://doi.org/10.1016/j.ijggc.2010.07.003

Singh, K., Menke, H., Andrew, M. et al. Dynamics of snap-off and pore-filling events during two-phase fluid flow in permeable media. Sci Rep 7, 5192 (2017). https://doi.org/10.1038/s41598-017-05204-4

Snippe, J., Tucker, O., 2014. CO_2 Fate Comparison for Depleted Gas Field and Dipping Saline Aquifer. Energy Procedia 63, 5586–5601. https://doi.org/10.1016/j.egypro.2014.11.592

Spurin, C., Callas, C., Darraj, N., Rücker, M. and Benson, S. (2025). Importance and challenges of multi-scale heterogeneity. InterPore Journal, 2(1), IPJ260225. DOI: https://doi.org/10.69631/ipj.v2i1nr76

Spurin, C., Callas, C., Kurotori, T., Tchelepi, H.A. and Benson, S.M. (2025). Sensitivity of trapping efficiency and relative permeability. arXiv. https://arxiv.org/abs/2505.09044

Spurin, C., Roberts, G. G., O'Malley, C. P. B., Kurotori, T., Krevor, S., Blunt, M. J., & Tchelepi, H. (2023). Pore-scale fluid dynamics resolved in pressure fluctuations at the Darcy scale. Geophysical Research Letters,50, e2023GL104473. https://doi.org/10.1029/2023GL104473

Spurin, C., Medical CT Image Processing for Flow in Porous Rocks, 2025. https://github.com/cspurin/medical_ct_processing

Stegemeier, G.L. (1977). Mechanisms of entrapment and mobilization of oil in porous media. https://doi.org/10.1016/B978-0-12-641750-0.50007-4

Suekane, T. and Nguyen, H.T. (2013). Relation between initial and residual gas saturations. Journal of Fluid Science and Technology, 8(3), pp. 322–336. https://doi.org/10.2118/84038-MS

Tang J., Zhang Z., Xie J., et al., (2024). Re-evaluation of CO_2 storage capacity of depleted fractured-vuggy carbonate reservoir. The Innovation Energy 1(2): 100019. https://doi.org/10.59717/j.xinn-energy.2024.100019

Tanino, Y. and Blunt, M.J. (2012). Capillary trapping dependence on pore structure. Water Resources Research, 48(8), 8525. https://doi.org/10.1029/2011WR011712

TNO (2024) CO_2 storage capacity in depleted gas fields offshore the Netherlands. TNO Report 2025 R10114. Available at: https://publications.tno.nl/publication/34644091/N1lkCowc/TNO-2025-R10114.pdf (Accessed: 21 January 2026).

Tavassoli, S., Krishnamurthy, P., Beckham, E., Meckel, T., Sepehrnoori, K., 2021. Carbon dioxide storage in deltaic saline aquifers: Invasion percolation and compositional simulation. SPE Reservoir Evaluation and Engineering 24, 462–474. 10.2118/196723-PA

Trevisan, L., Illangasekare, T.H. and Meckel, T.A. (2017). Modelling plume behavior through a heterogeneous sand pack. Geomechanics, Geophysics, Geo-energy, Geo-resources, 3, pp. 327–337. 10.1007/s40948-017-0055-5

Valvatne, P. H., and M. J. Blunt (2004), Predictive pore-scale modeling of two-phase flow in mixed wet media, WaterResour. Res., 40, 10.1029/2003WR002627

Vinegar, H.J. and Wellington, S.L. (1987). Tomographic imaging of three-phase flow experiments. Review of Scientific Instruments, 58(1), pp. 96–107. 10.1063/1.1139522

Virnovsky, G. A., Vatne, K. O., SkjaeveLand, S. M., & Lohne, A. (1998). Implementation of Multirate Technique to Measure Relative Permeabilities Accounting. https://doi.org/https://doi.org/10.2118/49321-MS

Viksund, B.G., Morrow, N.R., Ma, S., Wang, W. and Graue, A. (1998) 'Initial water saturation and oil recovery from chalk and sandstone by spontaneous imbibition', in Proceedings of the International Symposium of the Society of Core Analysts, The Hague, Netherlands, 14-16 September, pp. 1-12. https://www.jgmaas.com/SCA/1998/SCA1998-14.pdf

Wang, S., Ruspini, L. C., Øren, P.-E.,Van Offenwert, S., & Bultreys, T.(2022). Anchoring multi-scale modelsto micron-scale imaging of multiphaseflow in rocks. Water Resources Research,58, https://doi.org/10.1029/2021WR030870

Wang, Y.D., Shabaninejad, M., Armstrong, R.T. & Mostaghimi, P., 2021. Deep neural networks for improving physical accuracy of 2D and 3D multi-mineral segmentation of rock micro-CT images, Applied Soft Computing, Volume 104,

Wang, Y., Vuik, C., & Hajibeygi, H. (2022). CO_2 Storage in deep saline aquifers: Impacts of fractures on hydrodynamic trapping. International Journal of Greenhouse Gas Control, 113, 103552. https://doi.org/10.1016/j.ijggc.2021.103552

Wyckoff, R.D., Botset, H.G., and M. Muskat. "The Mechanics of Porous Flow Applied to Water-flooding Problems." Trans. 103 (1933): 219–249. doi: https://doi.org/10.2118/933219-G

Welge, H. J. (1952). A Simplified Method for Computing Oil Recovery by Gas or Water Drive. Journal of Petroleum Technology, 4:370 – 372. https://doi.org/10.2118/124-G

Wellington, S.I. and Vinegar, H.J. (1987). X-ray computerized tomography. Journal of Petroleum Technology, 39(8), pp. 885–898. https://doi.org/10.2118/16983-PA

Wenck, N., Jackson, S. J., Manoorkar, S., Muggeridge, A., & Krevor, S.(2021). Simulating core floods in heterogeneous sandstone and carbonate rocks. Water Resources Research, https://doi.org/10.1029/2021WR030581

Wenck, N., Muggeridge, A., Jackson, S., An, S. and Krevor, S. (2025). Impact of capillary heterogeneity on CO_2 plume migration. Geoenergy, 2024–2029. https://doi.org/10.1144/geoenergy2024-029

Whitaker, S. Flow in porous media I: A theoretical derivation of Darcy's law. *Transp Porous Med* **1**, 3–25 (1986). https://doi.org/10.1007/BF01036523

Wildenschild, D. and Sheppard, A.P., 2013. X-ray imaging and analysis techniques for quantifying pore-scale structure and processes in subsurface porous medium systems. Advances in Water Resources, 51, pp.217–246. https://doi.org/10.1016/j.advwatres.2012.07.018

Wildenschild, D., Armstrong, R.T., Herring, A.L., Young, I.M. and Carey, J.W. (2011). Exploring capillary trapping efficiency. Energy Procedia, 4, pp. 4945–4952. https://doi.org/10.1016/j.egypro.2011.02.464

Withers, P.J. (2007) 'X-ray nanotomography', Materials Today, 10(12), pp.26–34. DOI: https://doi.org/10.1016/S1369-7021(07)70304-X

Williams, J.D.O., Bentham, M., Jin, M., Pickup, G., Mackay, E., Gammer, D., Green, A., 2013. The Effect of Geological Structure and Heterogeneity on CO_2 Storage in Simple 4-way Dip Structures; a Modeling Study from the UK Southern North Sea. Energy Procedia 37, 3980–3988. https://doi.org/10.1016/j.egypro.2013.06.297

Wilson, J. W. (1956). Determination of relative permeability under simulated reservoir conditions. AIChE Journal, 2(1):94–100. https://doi.org/10.1002/aic.690020120

Worden, R.H. Carbon Dioxide Capture and Storage (CCS) in Saline Aquifers versus Depleted Gas Fields. Geosciences 2024, 14, 146. https://doi.org/10.3390/geosciences14060146

Zhang, Q., Geiger, S., Storms, J.E.A., Voskov, D.V., Jackson, M.D., Hampson, G.J., Jacquemyn, C. and Martinius, A.W. (2025). Capillary pinning in sedimentary rocks for CO_2 storage. International Journal of Greenhouse Gas Control, 144, 104385. 10.1016/j.ijggc.2025.104385

Zuo, L. and Benson, S.M. (2014) 'Process-dependent residual trapping of CO_2 in sandstone', Geophysical Research Letters, 41(8), pp. 2820–2826. DOI: https://doi.org/10.1002/2014GL059653.

Appendix A

(Supporting Chapter 4)

A.1. Low Permeability Sample (Sample 3)

An initial experimental attempt was conducted on Sample SK-02-1H; however, due to its low permeability (0.9 mD) and porosity ~9% (figure A.1) single-phase flow across the core resulted in a differential pressure of approximately 9.2 MPa. This value approached the operational limit of the core holder (10 MPa), rendering further testing infeasible. Despite this constraint, two drainage–imbibition cycles were successfully completed (Figure A.2).

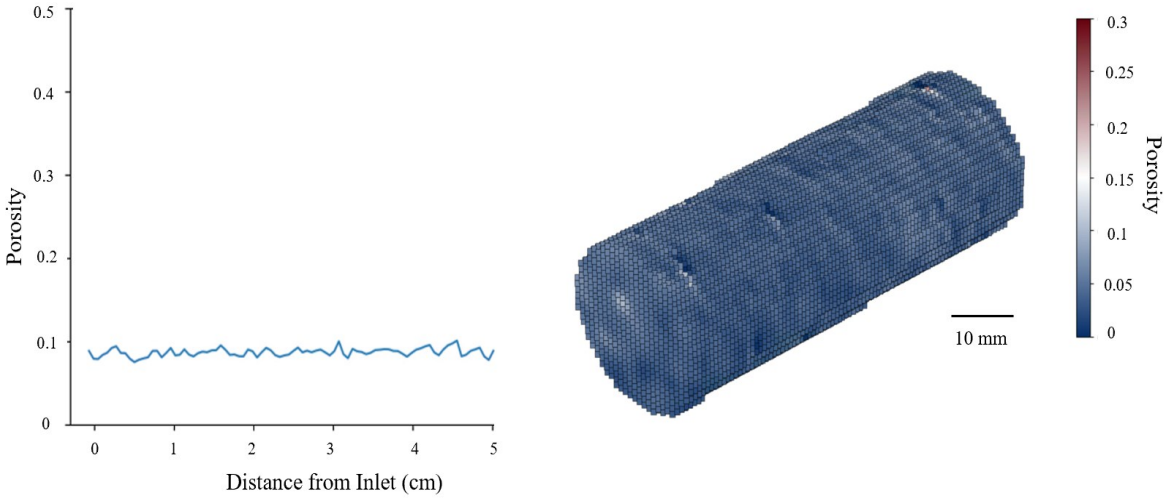


Figure A. 1 1D and 3D porosity profile of Sample 3.

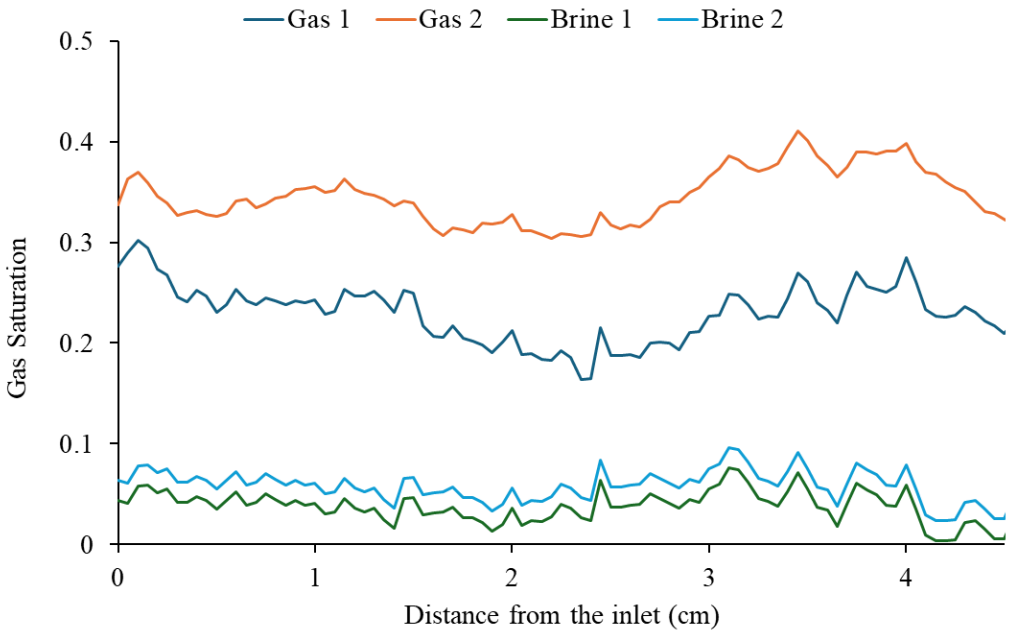


Figure A. 2 1D saturation profile for Sample 3.

Investigation of the three-dimensional gas saturation distributions shows a complex heterogeneity structure that varies both parallel and perpendicular to the primary flow direction. The saturation patterns indicate the presence of multi-directional cementation features that act as impediments to non-wetting phase migration. In particular, vertically oriented cemented streaks intersect the flow path locally, while more laterally extensive cemented regions span significant portions of the core length. These combined heterogeneity components result in spatially non-uniform gas invasion and retention, demonstrating that flow behaviour is controlled by a hierarchy of cementation features operating at different orientations and length scales rather than by a single dominant heterogeneity direction.

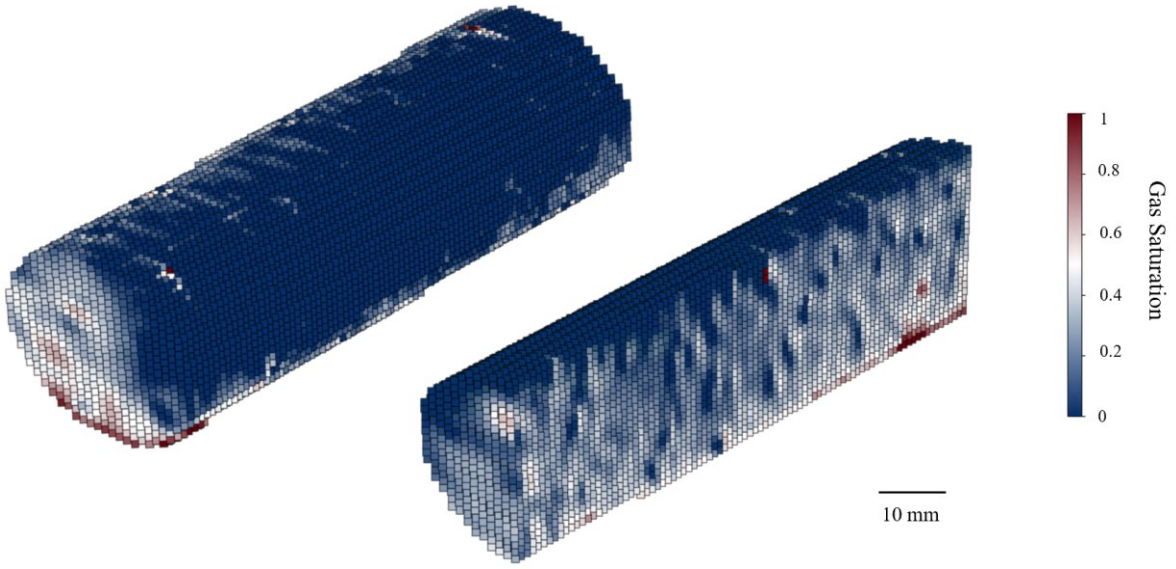


Figure A. 3 3D gas saturation distributions obtained from medical X-ray CT imaging during multiphase flow for Sample 3. The rendering highlights complex heterogeneity expressed both parallel and perpendicular to the primary flow direction.

After performing the 2 cycles of drainage and imbibition, the preliminary results indicated a slight increase in residual trapping with successive cycles, suggesting progressive entrapment mechanisms may be enhanced under repeated flow reversal conditions (Figure A.4).

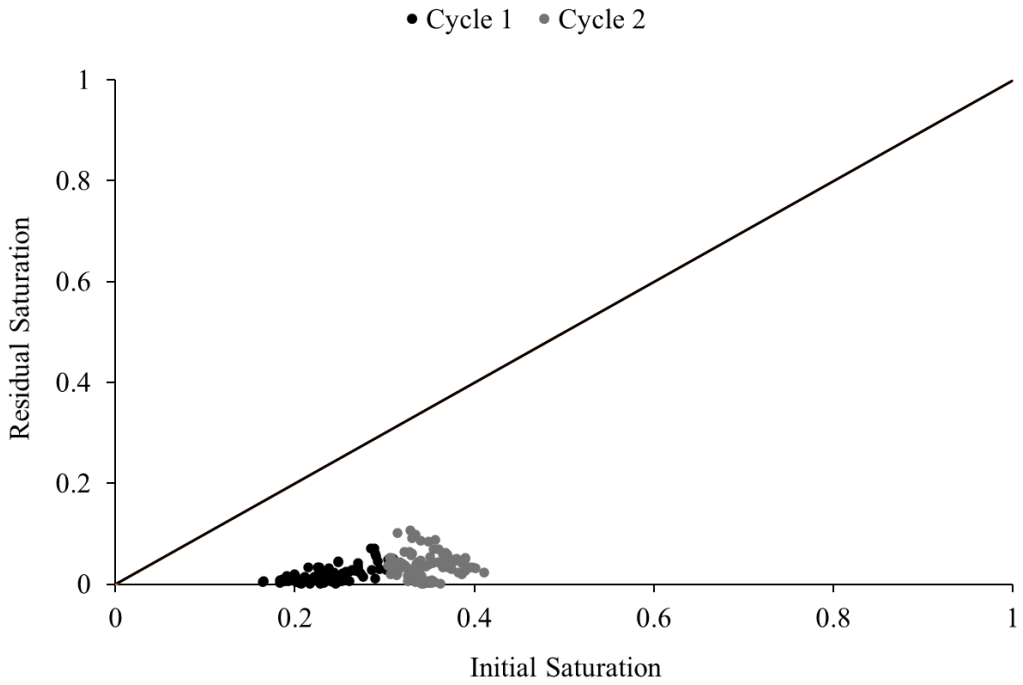


Figure A. 4 Trapping efficiency showing a slight increase in trapping with cyclic injection for Sample 3.

A.2. Viscous limit relative permeability

A repeat drainage experiment was conducted on Sample 1 at a flow rate increased by one order of magnitude (1 mL min^{-1}). Despite only a modest reduction in average porosity of approximately 2%, the saturation distribution changed distinctly compared to the original experiment. This change was accompanied by a measurable reduction in absolute permeability from approximately 100 mD to 90 mD. The three-dimensional gas saturation profile also

differed substantially, indicating a change of flow pathways and phase distribution within the sample (Figure A.5).

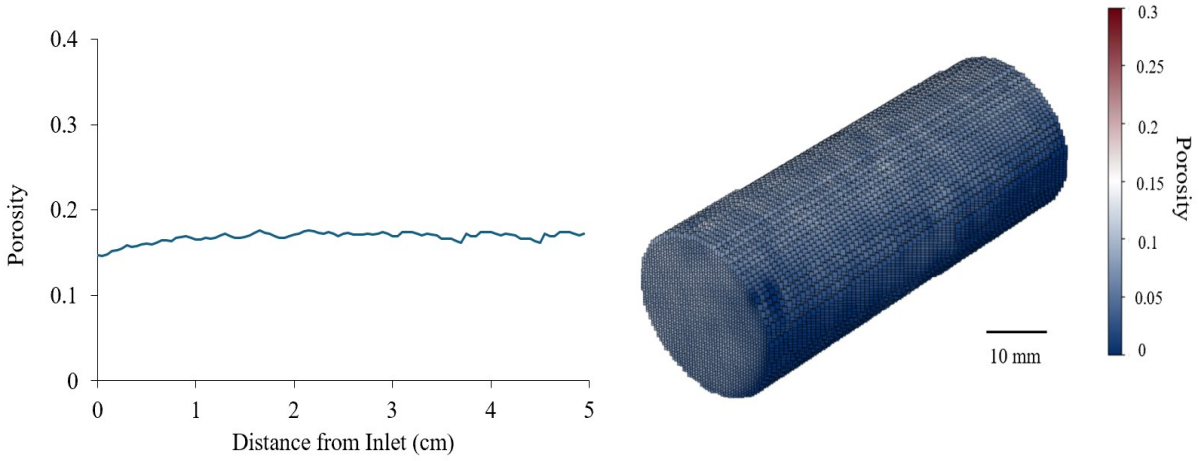


Figure A. 5 1-D and 3-D porosity profiles for Sample 1 after the first set of experiments.

These observations suggest that even small changes in bulk properties can correspond to significant changes in effective heterogeneity and multiphase flow behaviour. The altered saturation patterns imply that local cementation features or weakly consolidated regions may have been mobilised or reconfigured under the higher flow rate, leading to a different internal connectivity and flow, saturation profiles are shown in Figure A.6. As a result, the sample exhibits a distinct heterogeneity signature despite originating from the same core. The repeated drainage experiment yielded a lower non-wetting phase relative permeability than the first experiment. This is counterintuitive: however, this behaviour is consistent either with a reorganisation of flow pathways induced by heterogeneity activation under the higher flow rate, leading to reduced gas-phase connectivity, or with preferential gas bypassing through a limited number of high-permeability channels that do not contribute effectively to bulk flow across the core (Figures A.7 and A.8). Figure A.9 shows the pressure evolution in the experiment.

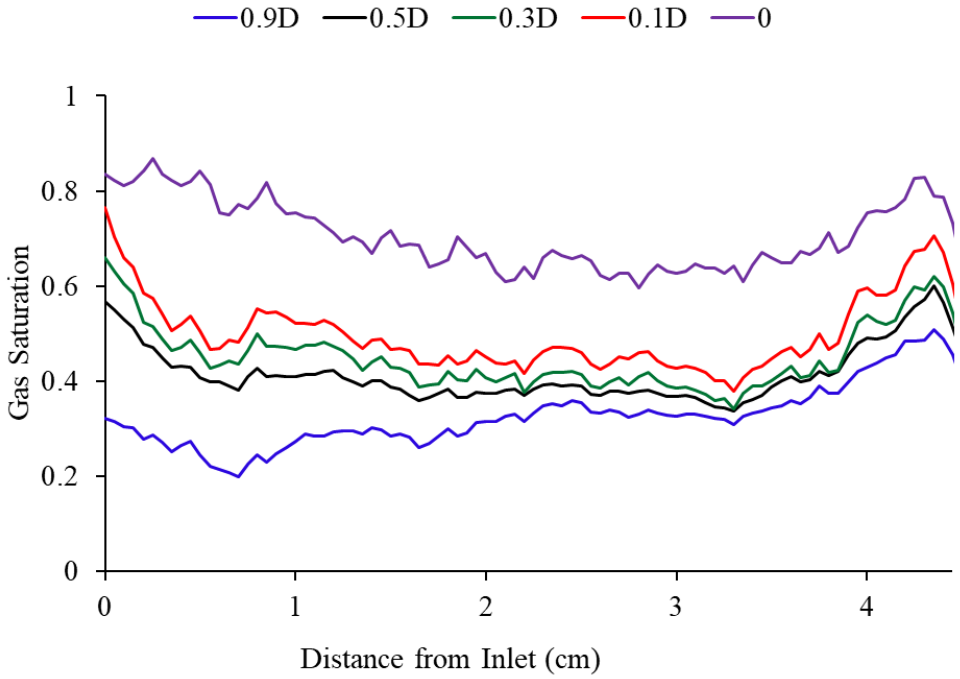


Figure A. 6 1-D saturation profile for Sample 1 (2nd experiment).

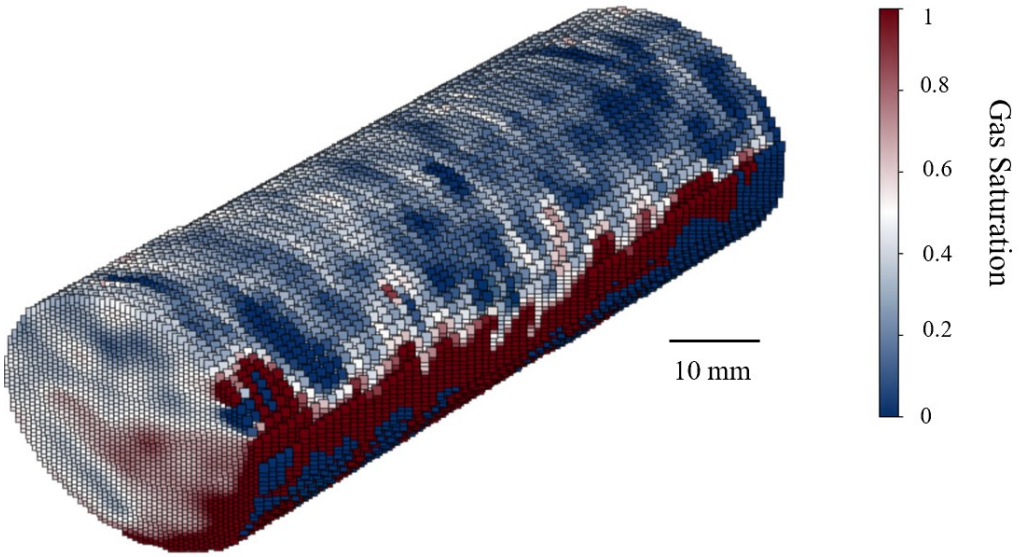


Figure A. 7 3D saturation profile at the end of drainage of Sample 1 (2nd experiment).

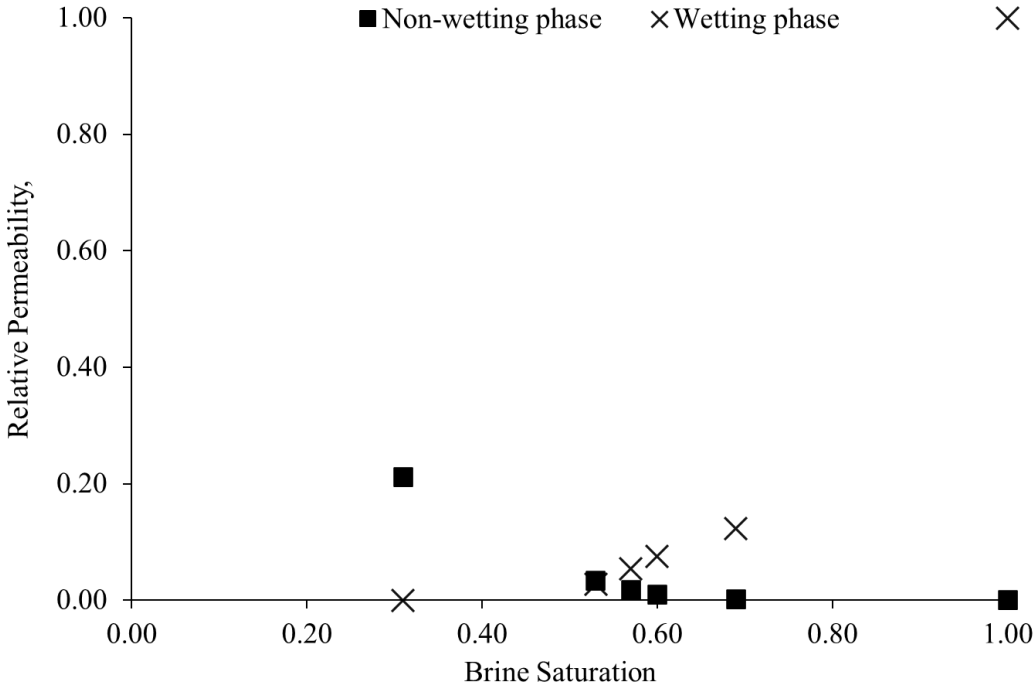


Figure A. 8 Drainage relative permeability of Sample 1 (2nd experiment).

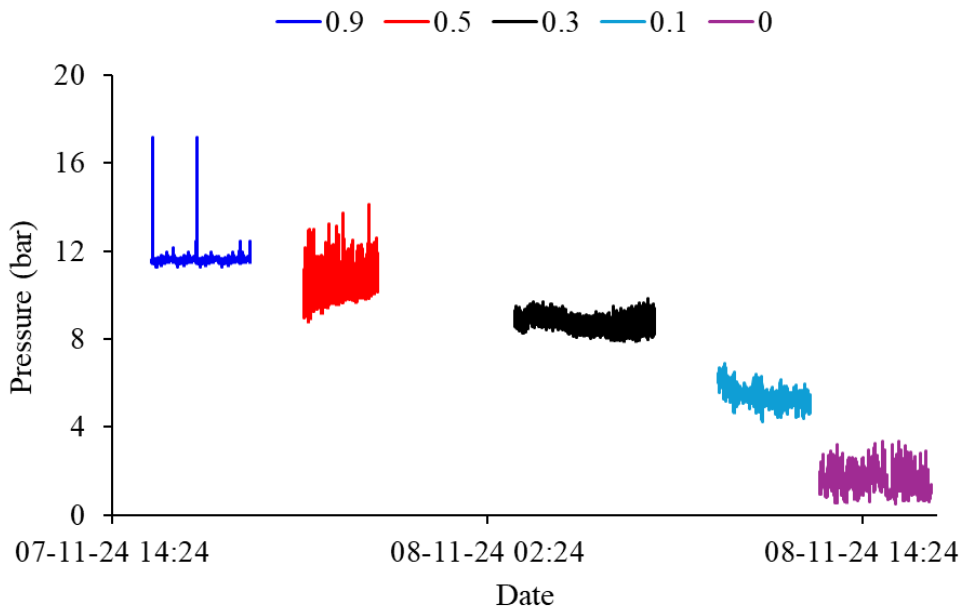


Figure A. 9 Pressure-time series for Sample 1 (2nd experiment).

This finding highlights two important aspects. First, it reinforces the strong sensitivity of multiphase flow properties to small-scale heterogeneity, which can be activated differently under varying flow conditions. Second, it illustrates the inherent difficulty in achieving strict experimental repeatability in multiphase core flooding experiments, particularly when working

with fragile reservoir samples. Even when changes in porosity and permeability appear minor, the internal structure controlling multiphase flow may evolve sufficiently to produce qualitatively different saturation and trapping behaviour.

A.3. Tabulated relative permeability values

Table A- 1 Tabulated relative permeability data for drainage in Sample 1.

f_w	S_w	k_{N_2}	k_w	ΔP (kPa)
0.9	0.8	0.007	0.13	63
0.5	0.78	0.05	0.11	55
0.3	0.75	0.09	0.09	42
0.1	0.71	0.12	0.04	20
0	0.67	0.22	0.03	15

Table A- 2 Tabulated relative permeability data for imbibition in Sample 1.

f_w	S_w	k_{N_2}	k_w	ΔP (kPa)
0.1	0.69	0.15	0.009	21
0.3	0.72	0.08	0.08	28
0.5	0.76	0.06	0.1	33
0.1	0.79	0.02	0.15	36

Table A- 3 Tabulated relative permeability data for drainage in Sample 2.

f_w	S_w	k_{N_2}	k_w	ΔP (kPa)
0.9	0.85	0.03	0.15	120
0.75	0.81	0.02	0.12	100
0.5	0.79	0.04	0.09	65
0.3	0.76	0.051	0.08	43

0.1	0.72	0.09	0.04	33
0	0.63	0.13	0.004	20

Table A- 4 Tabulated relative permeability data for imbibition in Sample 2.

f_w	S_w	k_{N_2}	k_w	ΔP (bar)
0.1	0.65	0.1	0.003	0.25
0.3	0.7	0.08	0.07	0.41
0.5	0.72	0.05	0.11	0.6
0.75	0.75	0.03	0.12	1.2
0.9	0.78	0.01	0.18	1.32

A.4. Pressure data

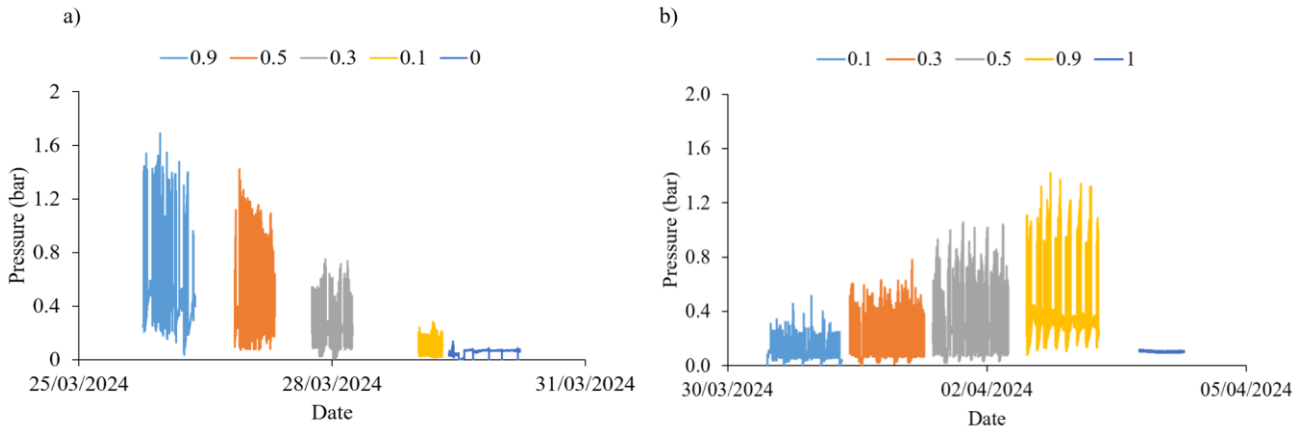


Figure A. 10 Pressure time series for Sample 1 during (a) drainage and (b) imbibition.

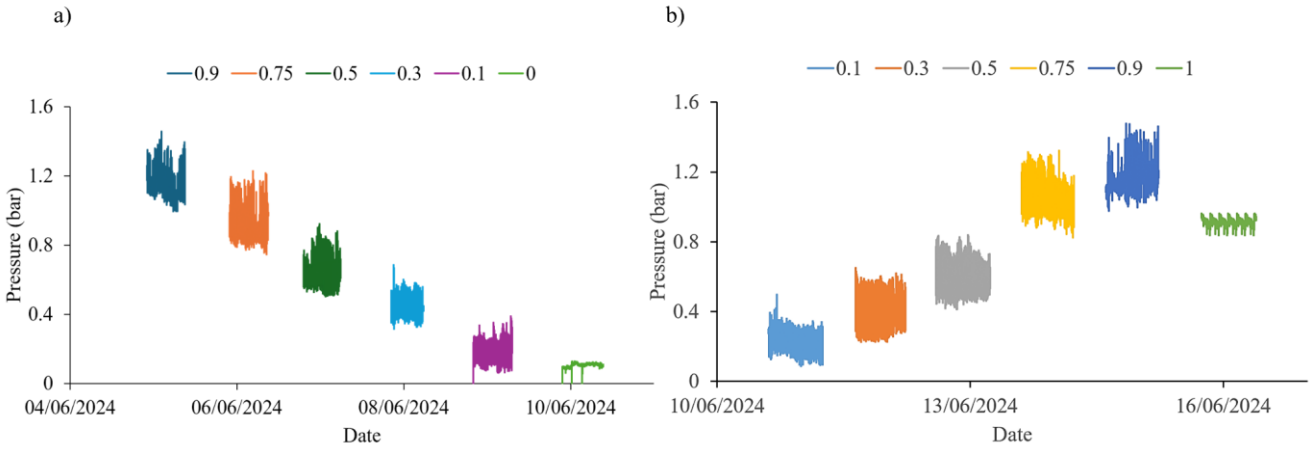


Figure A. 11 Pressure time series for Sample 2 during (a) drainage and (b) imbibition.

A.5. 3D saturation profiles during imbibition

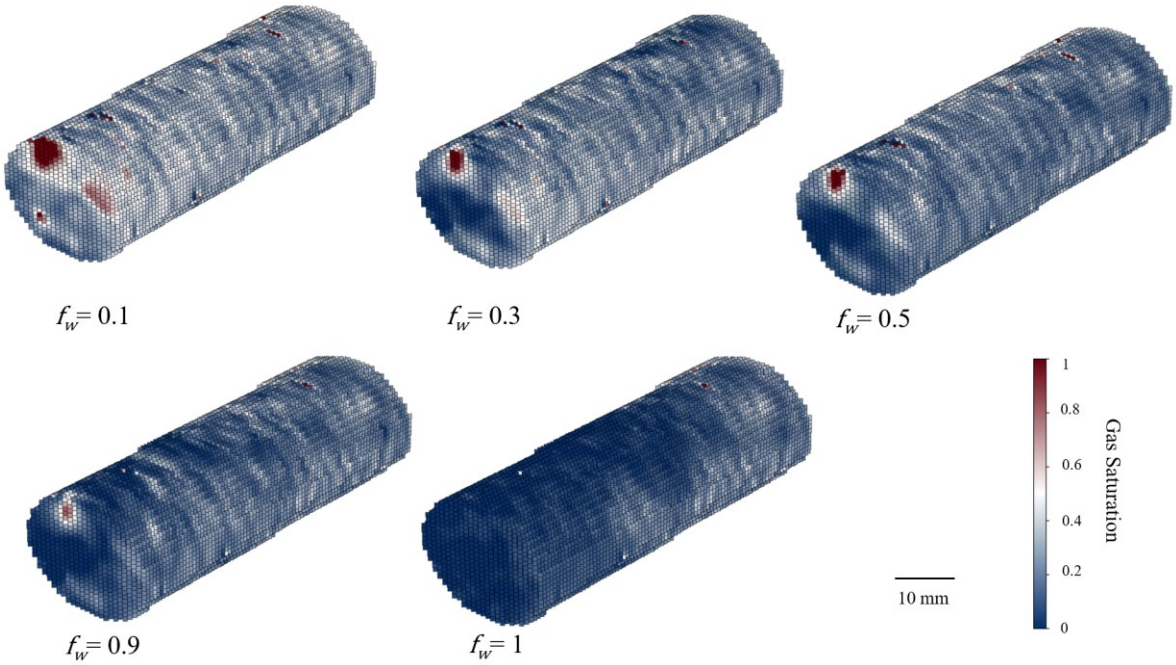


Figure A. 12 3D saturation profile for Sample 1 imbibition fractional flow steps.

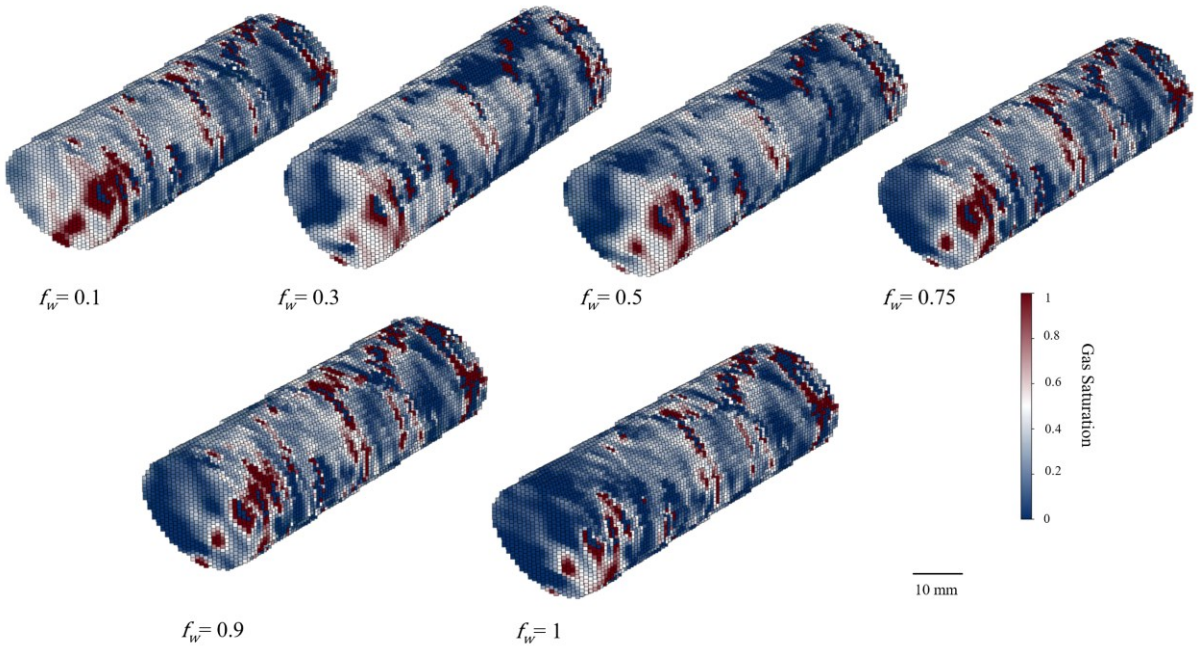


Figure A. 13 3D saturation profile for Sample 2 imbibition fractional flow steps.

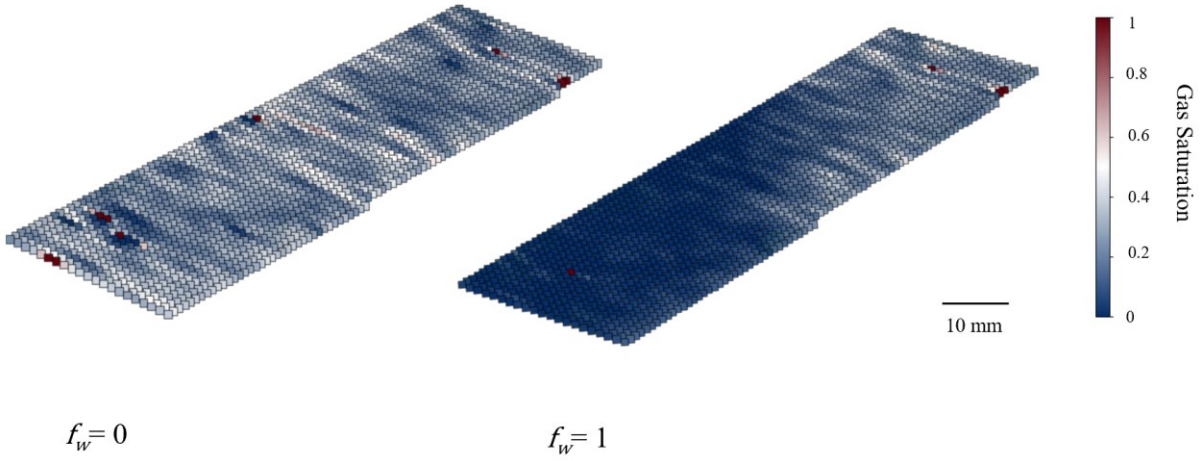


Figure A. 14 Two-dimensional saturation maps of the central horizontal slice in Sample 1 at the end of drainage and imbibition.

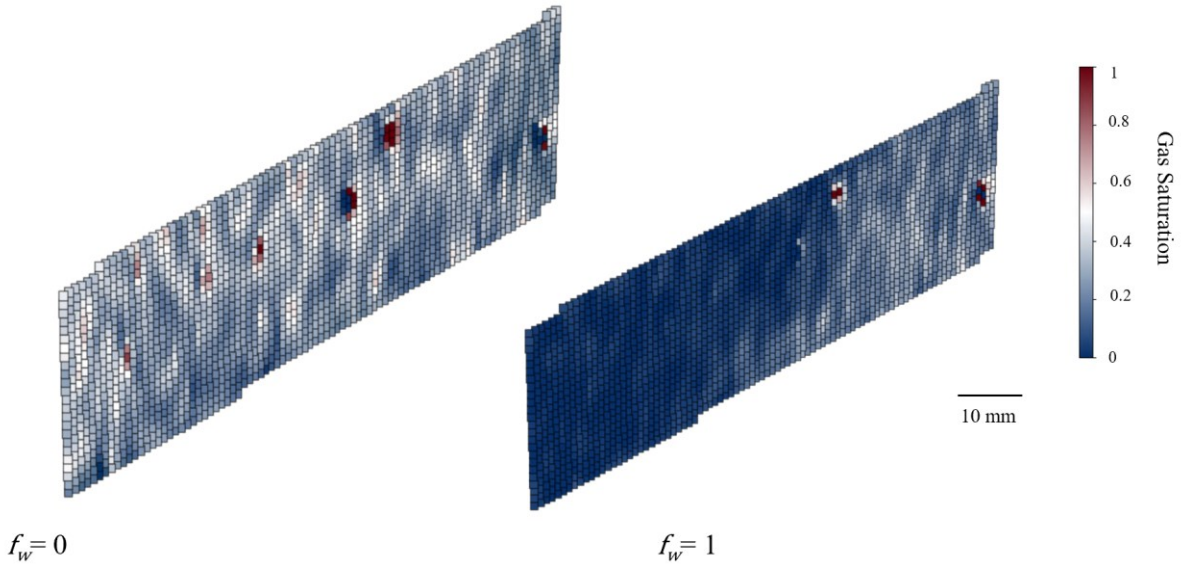


Figure A. 15 Two-dimensional saturation maps of the central vertical slice in Sample 1 at the end of drainage and imbibition.

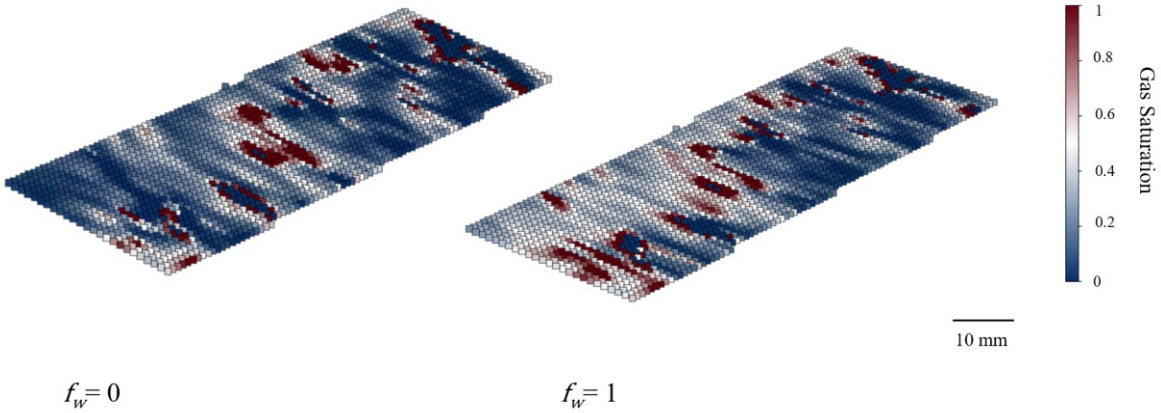


Figure A. 16 Two-dimensional saturation maps of the central horizontal slice in Sample 2 at the end of drainage and imbibition.

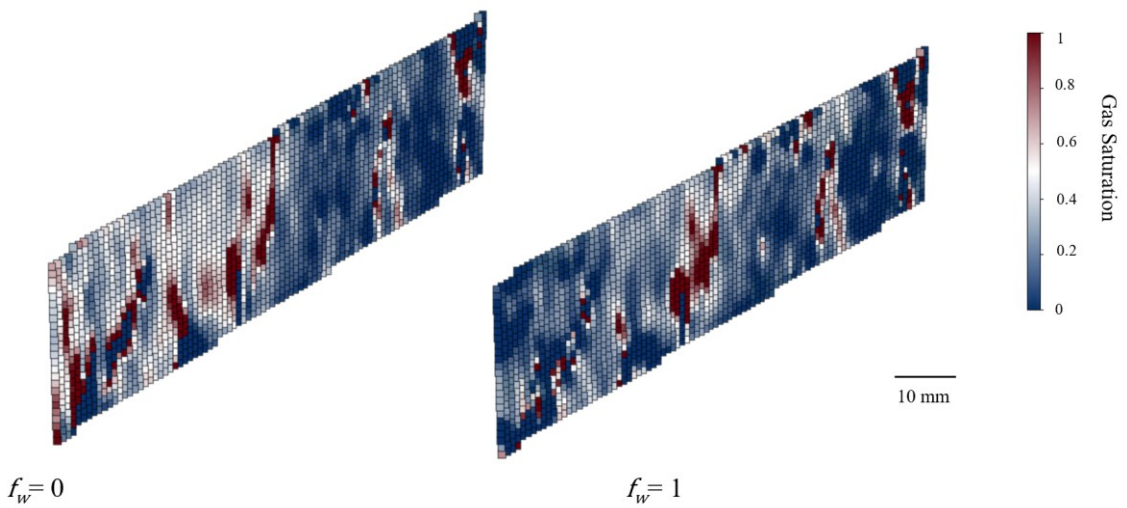


Figure A. 17 Two-dimensional saturation maps of the central vertical slice in Sample 2 at the end of drainage and imbibition.

Appendix B: Supporting Chapter 5

(Supporting Chapter 5)

This analysis compares the three-dimensional connectivity of two distinct regions within the rock, one characterised by a high capillary entry pressure and the other by a lower entry pressure, under both low and high flow-rate conditions in order to assess how flow regime influences saturation and trapping.

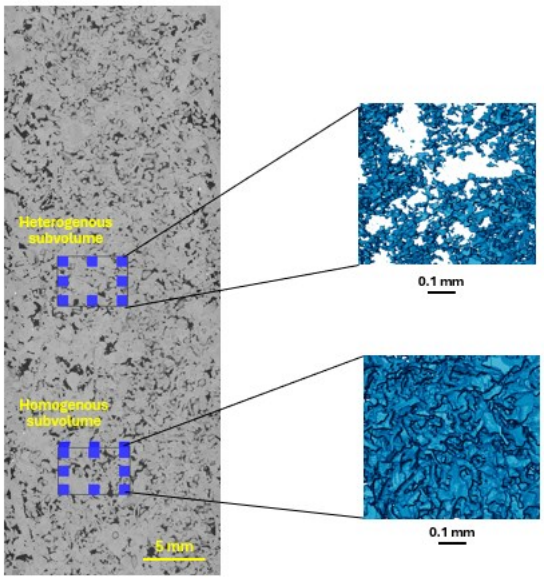


Figure B. 1 The two sub-volumes selected.

B.1. Saturation Profile

Initially, the two regions were saturated with brine; at flow rates of 0.1 mL/min and 0.2 mL/min, we examined how gas displaced the brine and occupied the pore space at the end of the drainage (100% gas flow). In the high entry pressure region (Figure B.2a), significant variation in gas saturation was observed. In contrast, the homogeneous region displayed minimal variation in gas saturation, as shown in (Figure B.2b).

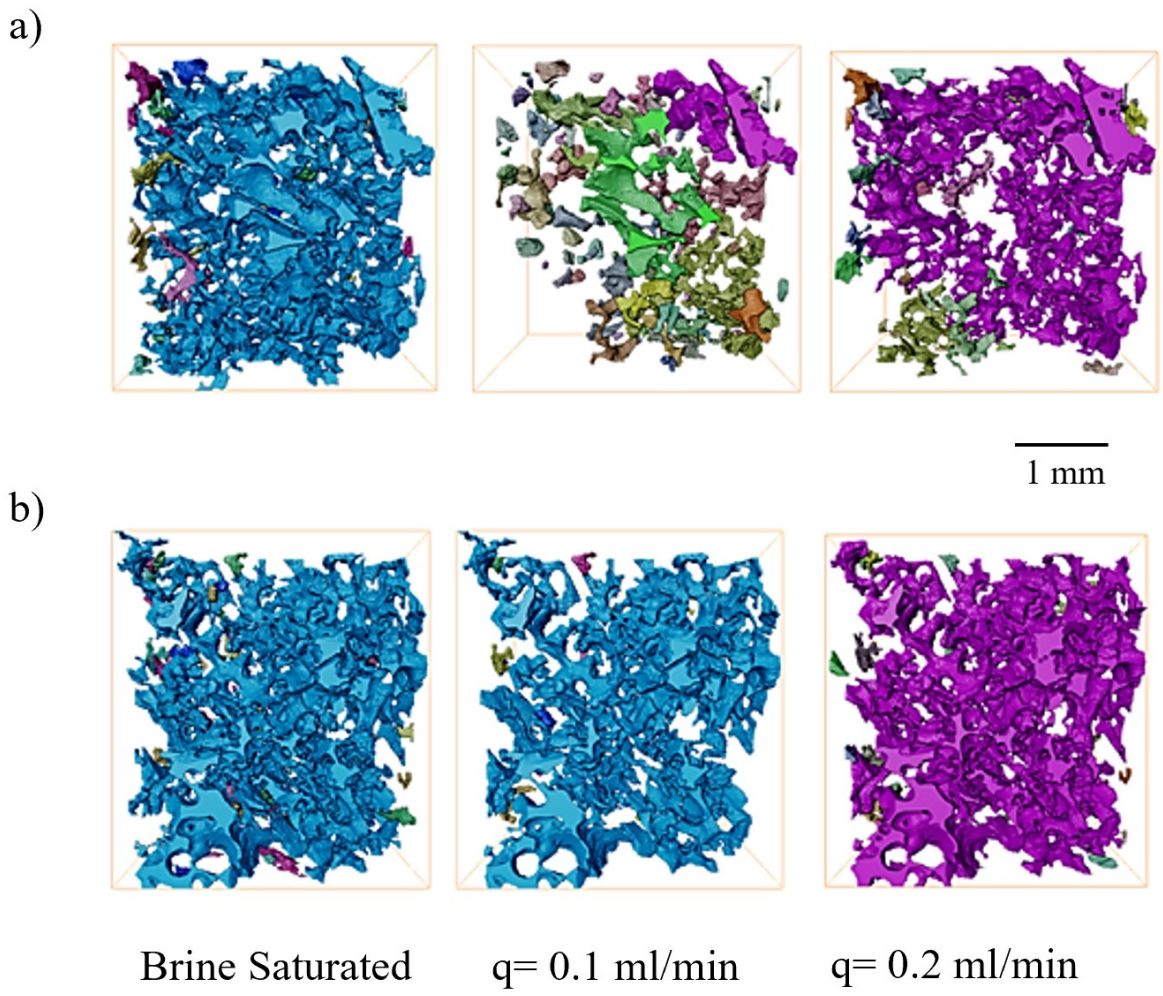


Figure B. 2 (a) High entry pressure region sub-volume. All pores image is the segmented brine phase when the rock was completely filled with brine. The 0.1 ml/min and 0.2 ml/min are the segmented gas phase at these two total flow rates, respectively. (b)Low entry pressure region sub-volume. All pores image is the segmented brine phase when the rock was completely filled with brine. The 0.1 ml/min and 0.2 ml/min are the segmented gas phase at these two total flow rates, respectively.

B.2. Trapping

We find that trapping is more pronounced in the high entry pressure region compared to the low entry pressure region. However, the trapping efficiency is not higher by a significant amount, it is likely a result of higher initial saturation. Figures B.3 and B.4 show the gas phase distribution at the end of imbibition and drainage for both flow rates in both regions. We also show that, by the end of imbibition, the gas phase is more connected in the low entry pressure region compared to the high entry pressure region.

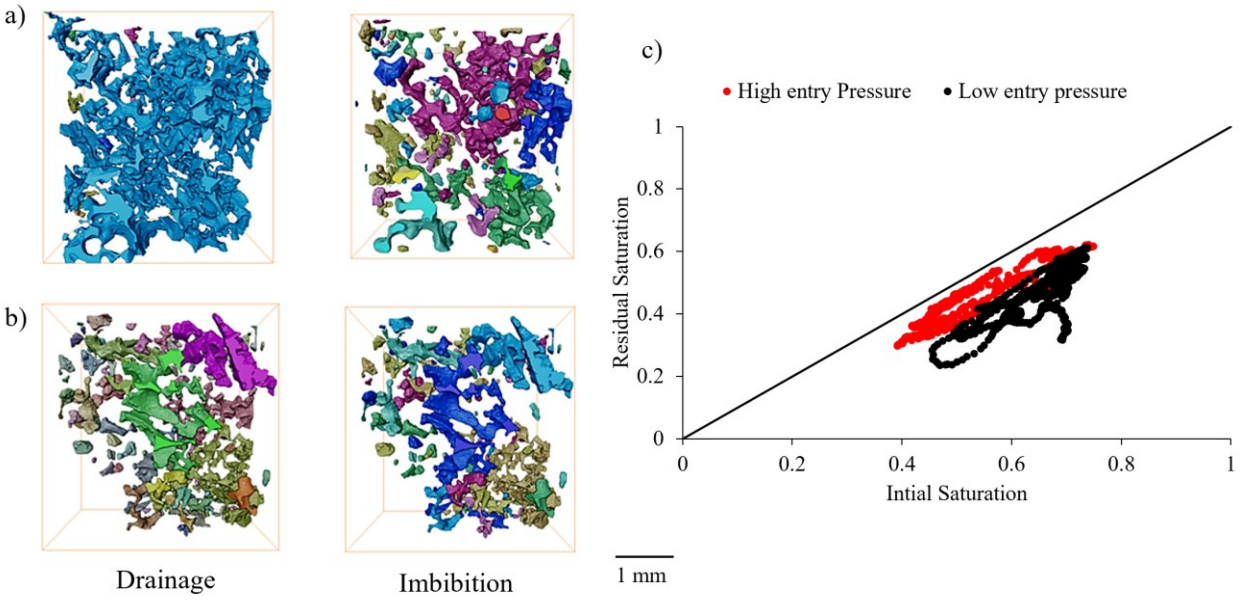


Figure B. 3 Low flow rate (Q=0.1 ml/min). (a) Segmented gas phase at the end of drainage and imbibition in the low entry pressure region. (b) Segmented gas phase at the end of drainage and imbibition in the high entry pressure region. (c) Residual versus initial saturation for low entry pressure (black) and high entry pressure (red) regions.

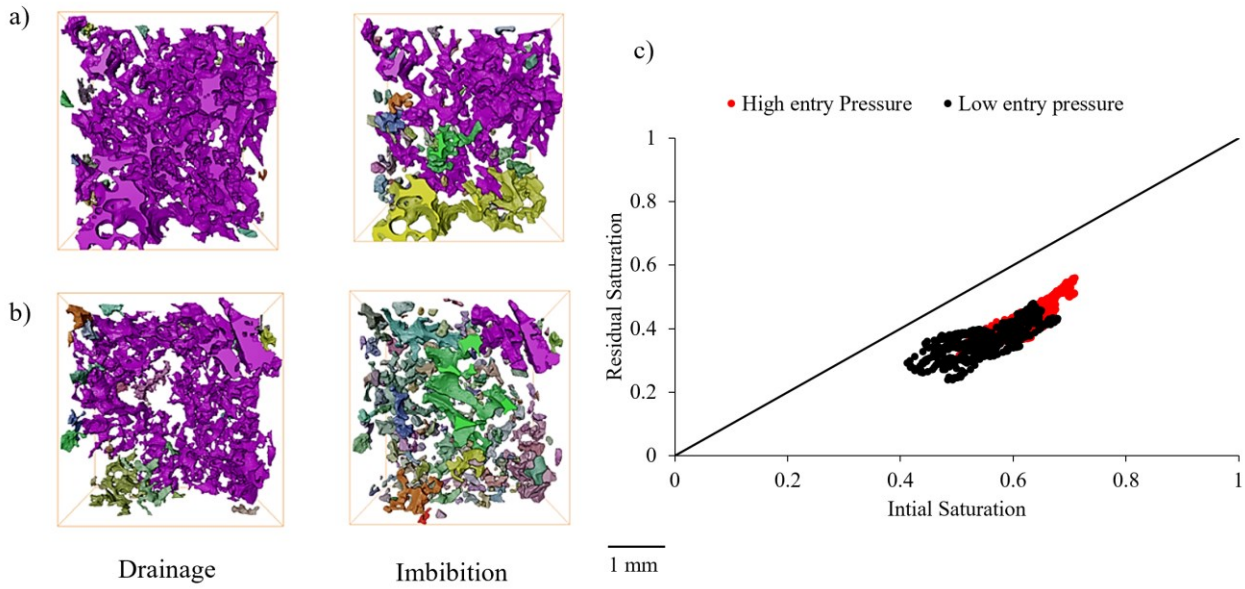


Figure B. 4 High flow rate (Q=0.2 ml/min). (a) Segmented gas phase at the end of drainage and imbibition in the low entry pressure region. (b) Segmented gas phase at the end of drainage and imbibition in the high entry pressure region. (c) Residual versus initial saturation for low entry pressure (black) and high entry pressure (red) regions.

B.3. Ganglia Analysis

While examining individual sub-volumes provides valuable insights into the contribution of the heterogeneity in the overall trapping. It is essential to assess the fluid connectivity and pathways across the entire sample. We assessed the number and size of disconnected ganglia throughout the sample and found that at higher flow rates, where the initial saturation was higher, there was a greater number of ganglia, though they were smaller in size. In both flow rate cases, the non-wetting phase was completely disconnected, with lower residual saturation observed at the lower flow rate as shown in Figure B.5. Figure B.5 (b) and compares the size and number of the disconnected ganglia at both flow rates. At a higher flow rate there are more, and larger, disconnected ganglia.

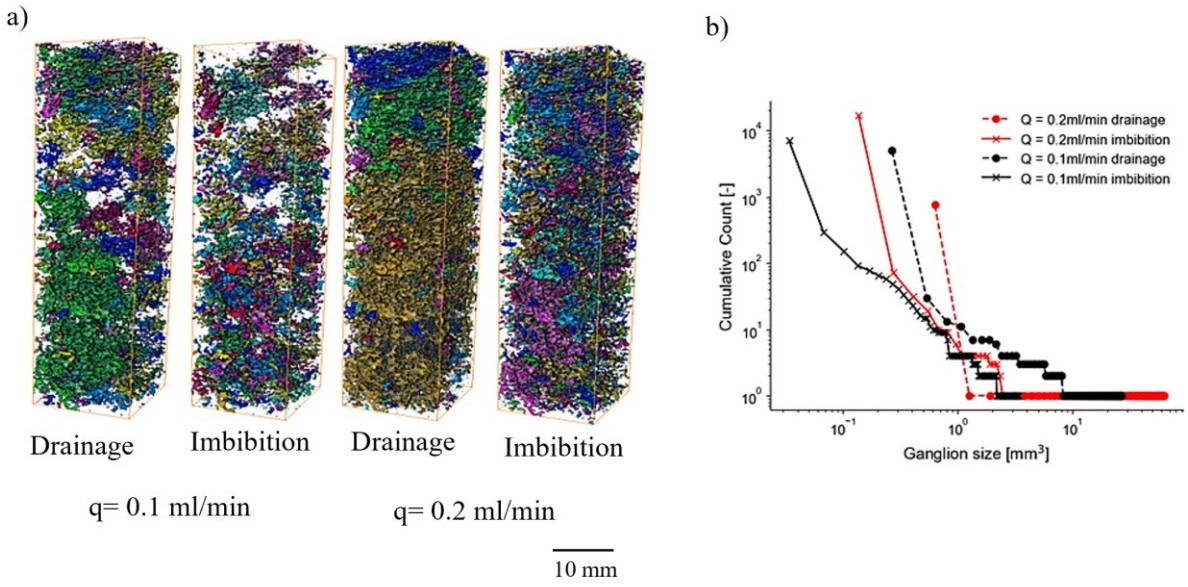


Figure B. 5 (a) Ganglia distribution across the sample in the low and high flow rates at the end of drainage and imbibition respectively. (b) A comparison of the ganglia size and cumulative count (frequency) between the low and high flow rates for drainage and imbibition. Red is the high flow rate while black is the low flow rate.

B.4. Investigation of wettability

Wettability variations, driven by mineralogical differences or diagenetic processes, lead to spatial changes in fluid preference. These variations influence capillary pressures, relative permeability, and displacement efficiency, creating complex flow patterns that challenge uniform fluid movement. Upon investigating the contact angle in both regions, the image was analysed at the end of drainage (100% gas flow). We found that it varies around 41° and there is no change in local wettability between the two regions. These results indicate no noticeable difference in wettability across the sample, which appears to be strongly water-wet (Al-Gabri, et al., 2025).

Al-Gabri, et al., 2025, presents an enhanced geometric algorithm for automated, pore-by-pore contact angle measurement from micro-CT images. This method achieves superior accuracy compared to previous approaches by enabling spatially resolved wettability characterization throughout the pore space, allowing researchers to identify and quantify local variations in wettability that may influence multiphase flow behaviour. The automated nature of the algorithm makes it possible to analyse large numbers of pores systematically, providing detailed maps of contact angle distributions within heterogeneous rock samples. This technique is particularly valuable for investigating whether wettability heterogeneity contributes to observed variations in capillary pressure, relative permeability, and trapping, as it can detect subtle spatial differences that conventional bulk measurements would miss.

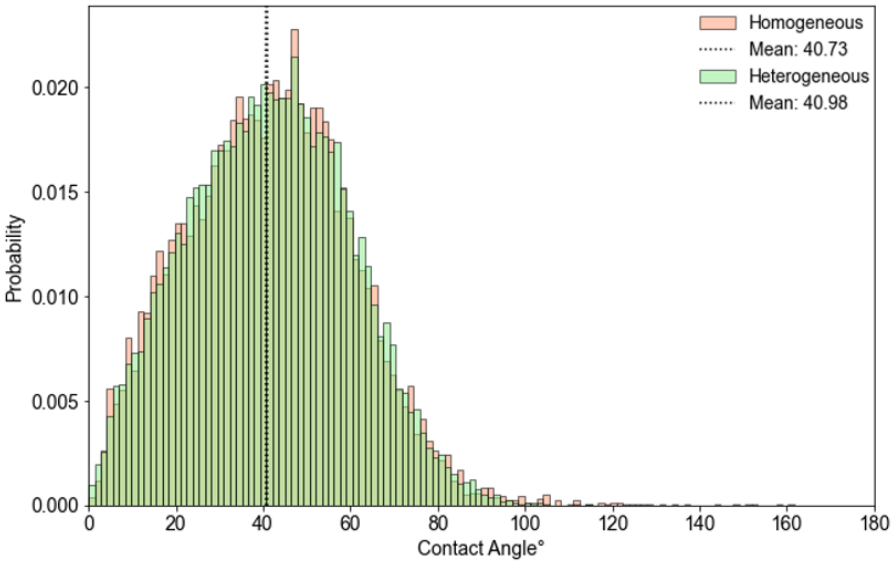


Figure B. 6 Contact angle histogram in both low and high entry pressure regions.

Appendix C: Supporting Chapter 6

(Supporting Chapter 6)

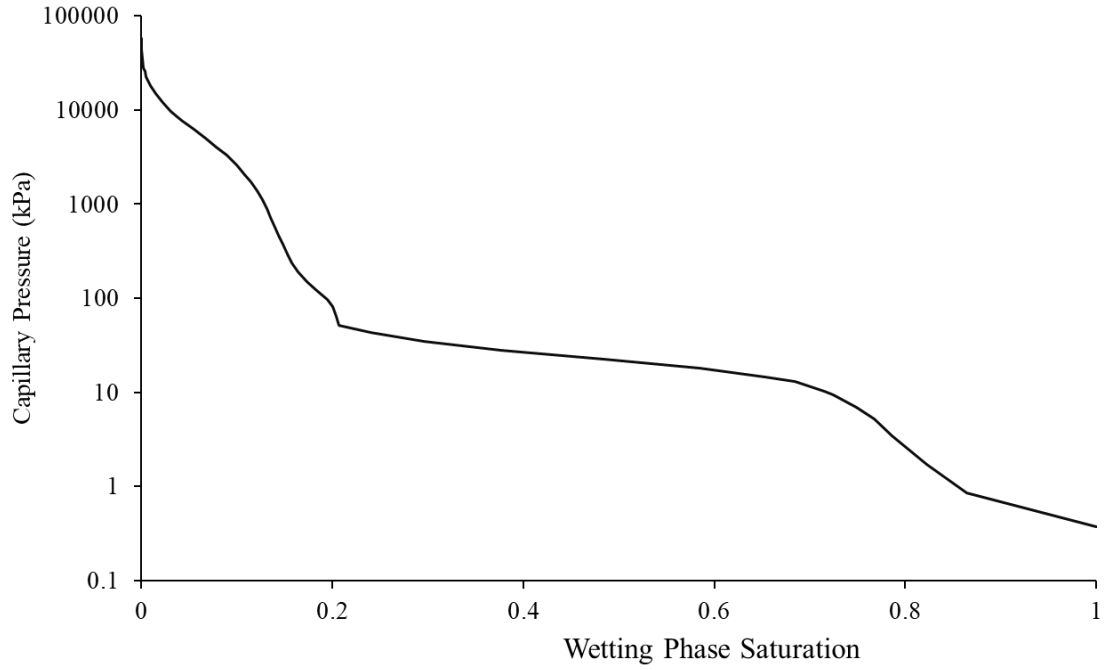


Figure C. 1 Mercury invasion capillary pressure (MICP). It highlights multiple entry pressure values.

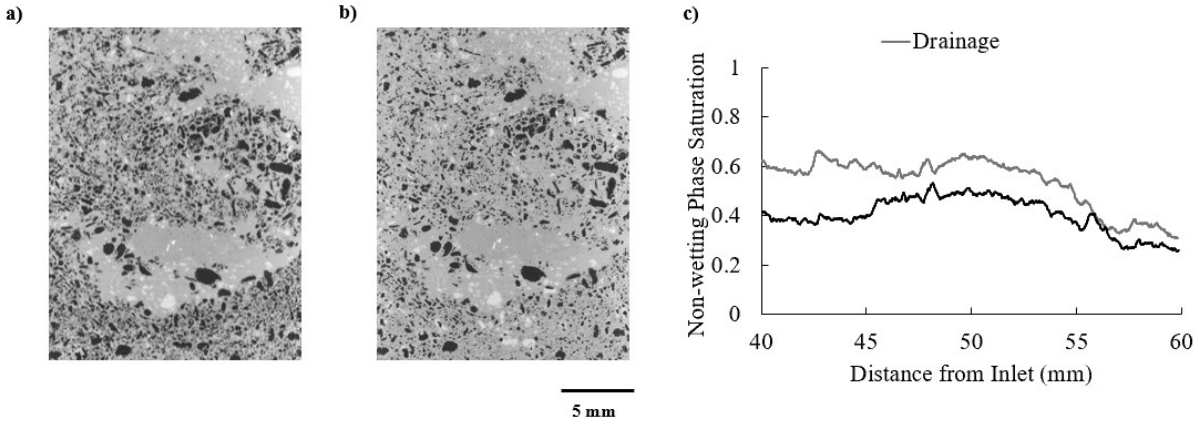


Figure C. 2 Two-dimensional cross-sections from a three-dimensional micro-CT image, zoomed in on the downstream heterogeneous region of the core. Panel (a) shows the fluid distribution at the end of drainage, while panel (b) captures the same region at the end of imbibition. Panel (c) displays the corresponding one-dimensional non-wetting saturation profile, illustrating the contrast in saturation before and after the heterogeneity. Notably, the non-wetting phase saturation remains unchanged within the heterogeneous zone, indicating limited displacement.

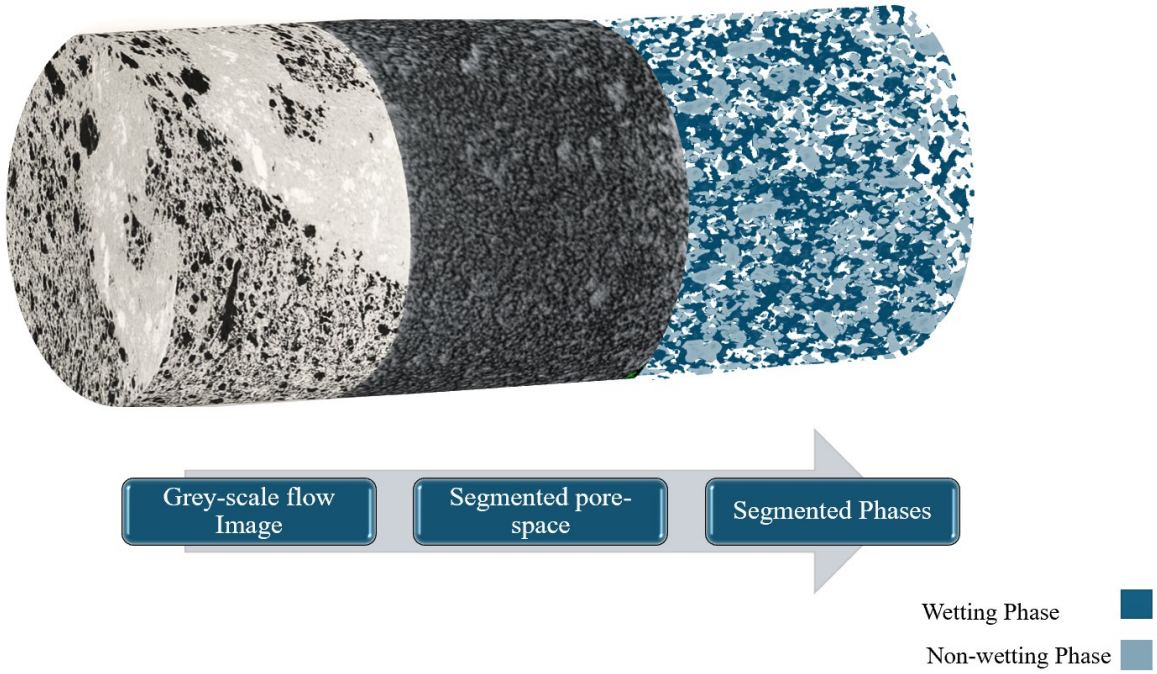


Figure C. 3 Segmentation workflow visualised for Edwards Brown dolomite. After imaging, the grey-scale image was segmented to separate pore space and grain phases. Finally, the fluid phases were segmented into wetting (dark blue) and non-wetting (light blue) phases and then calculated from the total pore-space to determine the saturation

C.1. Wavelet Analysis

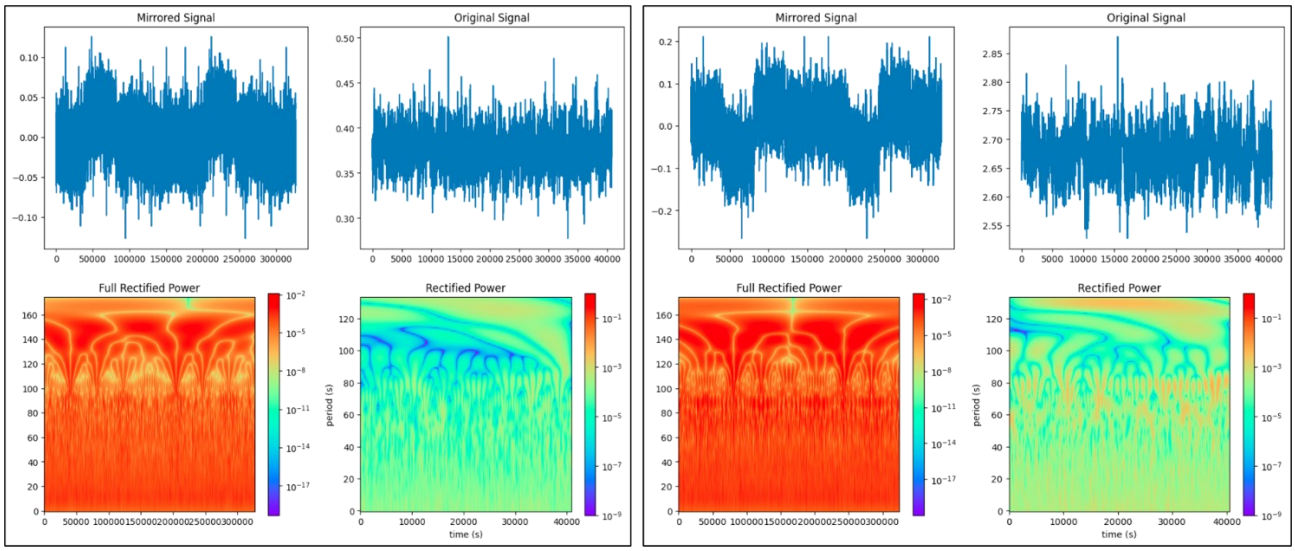
Wavelet analysis is a mathematical technique that decomposes signals into components at different time scales, making it particularly effective for detecting short-lived, localized events embedded within longer-term trends. In the context of pore-scale multiphase flow, rapid transient phenomena such as Haines jumps—sudden pore-filling events where fluid interfaces snap into adjacent pores—and the expansion or swelling of thin wetting films on pore walls occur on very short timescales. When pressure or saturation data are averaged over time or space, as is common in conventional measurements, these fast dynamics are smoothed out and effectively hidden within the aggregate signal.

Spurin et al. (2023) demonstrated that wavelet analysis can extract these transient features from core-scale pressure measurements, revealing pore-scale fluid displacement events that would

otherwise be obscured. This capability is valuable because such rapid, localized dynamics influence larger-scale flow behaviour and trapping mechanisms, yet they are not typically captured in continuum-scale models used for CO_2 storage or other subsurface applications. By resolving these pore-scale events, wavelet analysis provides deeper insight into the fundamental processes governing multiphase flow and trapping in porous media.

By decomposing pressure data into time–frequency space, discrete displacement events can be isolated and their intensity quantified. In our experiments, imbibition is associated with notably higher-pressure fluctuations and stronger dynamic events compared to drainage, consistent with the increased frequency of snap-off and enhanced trapping. Figures C.4 through C.7 shows the wavelet analysis of the pressure signal at drainage and imbibition for the same fractional flow.

It is notable that, when combined with dynamic imaging, wavelet analysis can provide a direct link between observable pore-scale events and pressure fluctuations, thereby bridging discrete displacement dynamics with macroscopic flow responses.



Drainage Imbibition

Figure C. 4 Wavelet analysis of the pressure signal for a brine fractional flow of 100% (f_w =1).

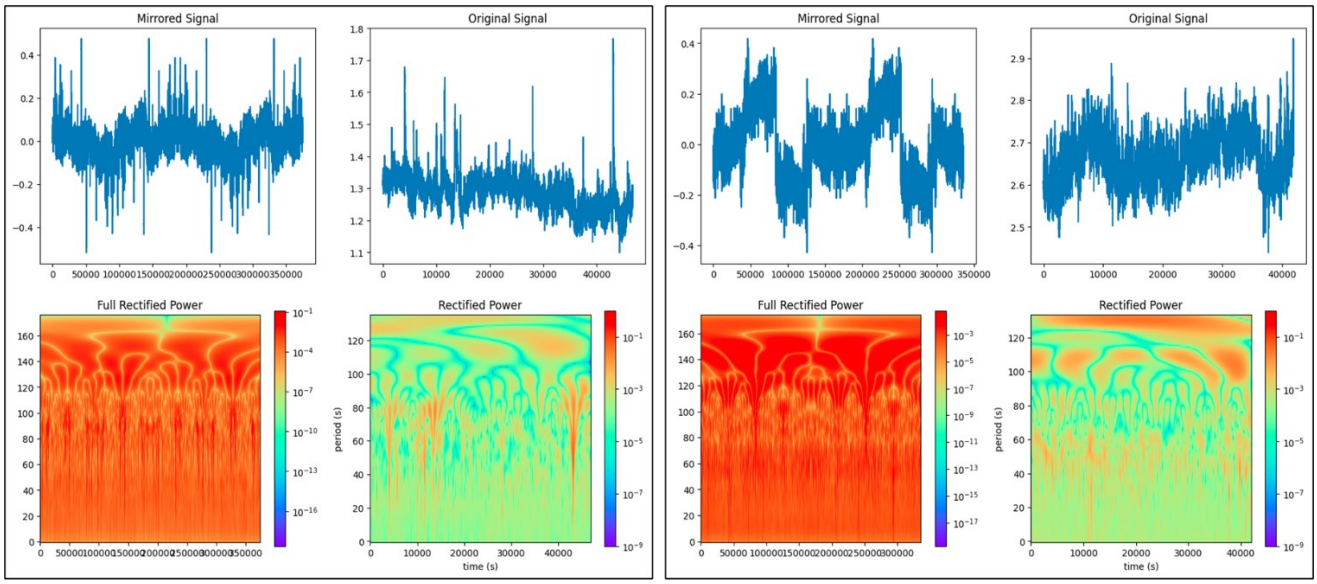


Figure C. 5 Wavelet analysis of the measured pressure signal for a brine fractional flow of 75% (f_w=0.75).

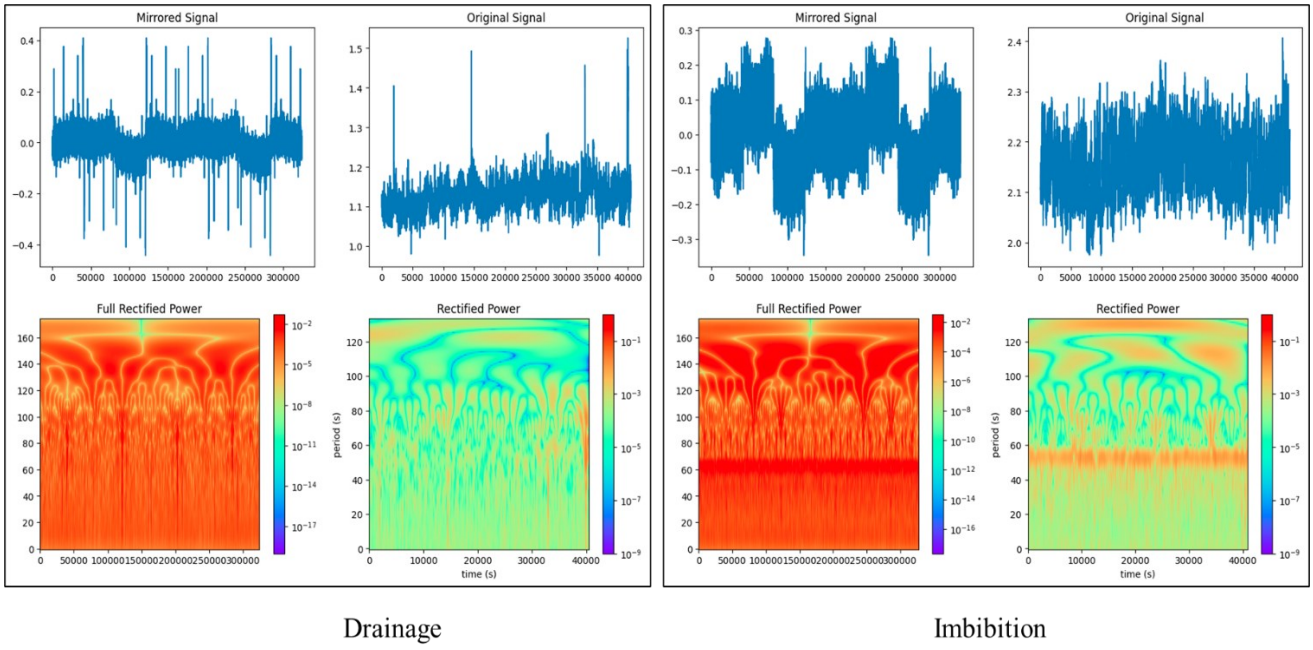


Figure C. 6 Wavelet analysis of the measured pressure signal for a brine fractional flow of 50% (f_w=0.5).

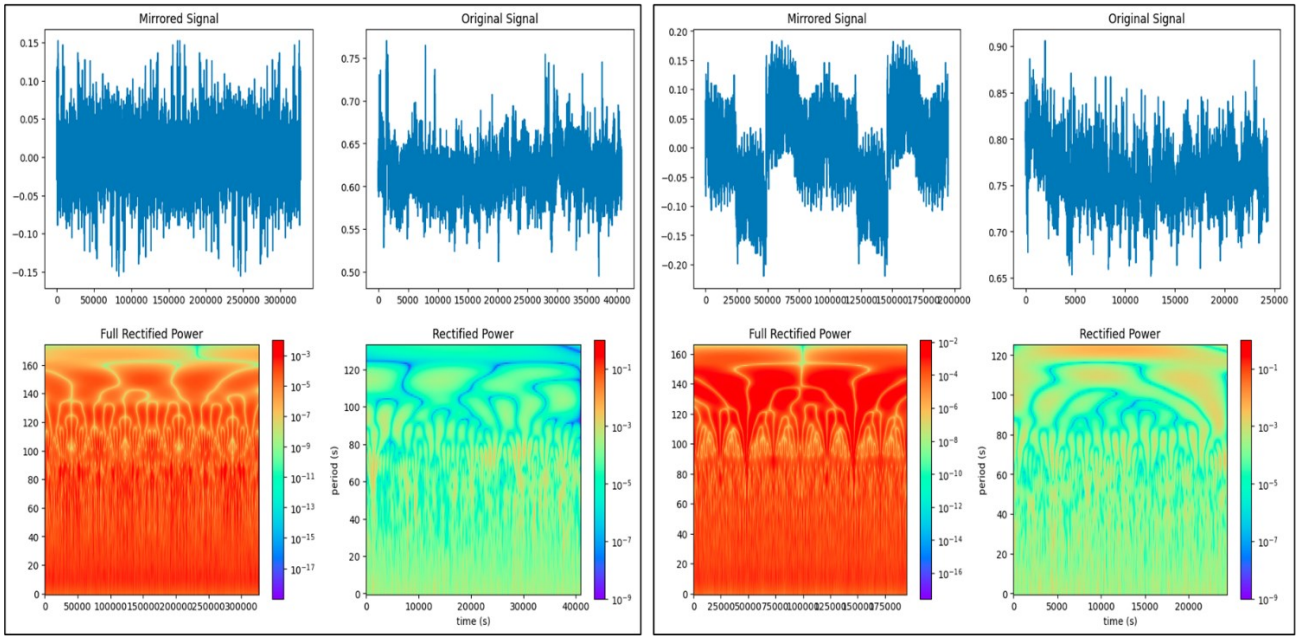


Figure C. 7 Wavelet analysis of the measured pressure signal for a brine fractional flow of 5% (f_w =0.05).